



POLITECNICO
MILANO 1863

SCUOLA DI INGEGNERIA INDUSTRIALE
E DELL'INFORMAZIONE

Characterization of titanium dioxide sol-gel coatings for self-cleaning surfaces

TESI DI LAUREA MAGISTRALE IN
MATERIALS ENGINEERING AND NANOTECHNOLOGY -
INGEGNERIA DEI MATERIALI E DELLE NANOTECNOLOGIE

Author: **Sara Lavino**

Student ID: 971054
Advisor: Prof. Maria Vittoria Diamanti
Academic Year: 2022-23

Abstract

This dissertation presents the development and evaluation of titania-based self-cleaning coatings, which, with proper formulations can be environment-friendly, transparent, highly adherent to the substrate, and can be deposited on any surface [1]. The primary objective of this study is to investigate the photocatalytic and wettability properties of TiO_2 -based coatings and their potential for creating self-cleaning surfaces that require less frequent cleaning and are easier to clean when needed.

Chapter 1 delves into the theory behind the self-cleaning mechanism, focusing on the photocatalytic and wettability properties of titanium dioxide. The chapter also introduces the anodization and sol-gel method for the production of TiO_2 coatings. Chapter 2 is dedicated to the employed materials and methods for the synthesis and characterization of the analyzed coatings, which are developed through sol-gel method and characterized by XRD and SEM. The photocatalytic activity of the coatings is evaluated through degradation tests of rhodamine B, whose results, commented in Chapter 3, indicate that the TiO_2 -based coatings exhibit moderate photocatalytic activity, provided that the solutions are aged for at least four months. Furthermore, the coatings demonstrate self-cleaning properties thanks to their hydrophilic behavior, effectively repelling dirt when exposed to abundant precipitation. The study also investigates the influence of solvent, substrate, deposition method, and calcination temperature on the coatings' properties and performance.

Additionally, the photocatalytic properties of coatings obtained through sol-gel and anodization methods were evaluated in collaboration with *Università degli Studi di Milano Statale*. The effectiveness of the coatings was tested through degradation experiments of tetracycline, a broad-spectrum antibiotic. Results indicate that both methods yield coatings able to degrade tetracycline, with the anodization method showing better performance and sample reusability, providing a more sustainable solution for wastewater treatment.

Keywords: self-cleaning coatings, photocatalytic, hydrophilicity, sol-gel method, titanium dioxide

Abstract in lingua italiana

La tesi presenta lo sviluppo e la caratterizzazione di rivestimenti autopulenti a base di ossido di titanio, che, con specifiche formulazioni, possono essere ecocompatibili, trasparenti, aderenti al substrato, e possono rivestire qualunque tipo di superficie [1]. L'obiettivo primario dello studio è indagare le proprietà fotocatalitiche e di bagnabilità dei rivestimenti necessarie per rendere le superfici autopulenti, che quindi richiederebbero una pulizia meno frequente e sarebbero più semplici da pulire.

Il primo capitolo è dedicato alla teoria dei rivestimenti autopulenti, e approfondisce le proprietà fotocatalitiche e di bagnabilità dell'ossido di titanio. Il capitolo introduce anche l'anodizzazione e il metodo sol-gel per la produzione dei rivestimenti. Il Capitolo 2 è dedicato ai materiali e metodi necessari per la sintesi e caratterizzazione dei rivestimenti, che sono stati prodotti tramite metodo sol-gel e sono caratterizzati mediante diffrazione a raggi X e microscopia elettronica a scansione. L'attività fotocatalitica dei rivestimenti è valutata tramite test di degradazione della rodamina B, i cui risultati, riportati nel terzo capitolo, indicano che i rivestimenti mostrano una moderata attività fotocatalitica, a condizione che le soluzioni siano invecchiate per almeno quattro mesi. Inoltre i rivestimenti presentano, grazie al comportamento idrofilico, proprietà autopulenti, poiché rimuovono efficacemente depositi organici sfruttando l'azione della pioggia. Lo studio esamina anche l'influenza del solvente, substrato, metodo di deposizione, e temperatura di calcinazione sulle proprietà ed efficacia dei rivestimenti.

Oltretutto, in collaborazione con l'*Università degli Studi di Milano Statale*, sono state confrontate le proprietà fotocatalitiche di rivestimenti ottenuti tramite metodo sol-gel e anodizzazione. L'efficacia dei rivestimenti è stata esaminata tramite test di degradazione di un antibiotico ad ampio spettro: la tetraciclina. I risultati indicano che benché entrambi i tipi di rivestimento siano efficaci nel degradare l'antibiotico, quelli ottenuti tramite anodizzazione mostrano prestazioni maggiori. Inoltre il rivestimento ottenuto tramite anodizzazione ha mantenuto la medesima attività fotocatalitica nei test di ripetibilità, consentendo il riutilizzo del campione e fornendo una soluzione più sostenibile per il trattamento delle acque reflue.

Contents

Abstract	i
Abstract in lingua italiana	iii
Contents	v
Introduction	1
1 Theory and state of the art	3
1.1 Titanium dioxide as a self-cleaning material	3
1.2 Self-cleaning coatings	4
1.2.1 Wettability	5
1.2.1.1 Hierarchical structure	6
1.2.1.2 Photoinduced hydrophilicity	7
1.2.2 Photocatalysis	11
1.2.2.1 Photolysis	11
1.2.2.2 Titanium oxide as a photocatalyst	12
1.2.2.3 Degradation mechanism	12
1.2.2.4 Suspended and immobilized photocatalyst	14
1.2.2.5 Influencing parameters	16
1.3 Production methods	20
1.3.1 Anodization	20
1.3.1.1 Mechanism of oxide growth	21
1.3.1.2 Influencing parameters	23
1.3.2 Sol-gel process	24
1.3.2.1 Processing steps	25
1.3.2.2 Influencing parameters	30
1.3.2.3 Reagents	31

2	Materials and methods	35
2.1	Sample preparation	35
2.1.1	Sol-gel solutions	35
2.1.2	Deposition techniques	36
2.1.2.1	Dip-coating	36
2.1.2.2	Spray-coating	37
2.1.3	Annealing	38
2.1.4	Corona treatment	39
2.1.5	Titanium meshes	40
2.1.5.1	Anodized mesh	40
2.1.5.2	Spray-coated titanium mesh	41
2.2	Characterization techniques	41
2.2.1	Photocatalytic tests	41
2.2.1.1	Photodegradation of rhodamine B	42
2.2.1.2	Photodegradation of tetracycline	44
2.2.2	Wettability tests	47
2.2.3	Soiling tests	48
2.2.3.1	Colorimetry theory	48
2.2.3.2	Accelerated soiling tests	51
2.2.3.3	Natural soiling	52
2.2.4	Adhesion tests	55
2.2.5	SEM morphological analysis	57
2.2.6	X-ray diffraction analysis	58
3	Results and discussion	59
3.1	Coating appearance	59
3.2	Photocatalytic performance	60
3.2.1	Processing of photocatalysis data	60
3.2.2	Preliminary tests	62
3.2.2.1	Photolysis tests	62
3.2.2.2	Adsorption tests	64
3.2.3	Ageing	65
3.2.4	Deposition technique	69
3.2.5	Substrate and consolidation	71
3.2.5.1	Glass substrate	71
3.2.5.2	PMMA substrate	75
3.2.6	Corona treatment	77

3.2.7	Solution reproducibility	79
3.3	Coating wettability	82
3.3.1	Dip-coated glass samples	82
3.3.2	Spray-coated glass samples	83
3.3.3	Spray-coated PMMA samples	87
3.3.4	Photoinduced hydrophilicity	90
3.4	Color variations	93
3.4.1	Coating deposition	93
3.4.2	Thermal treatment	95
3.5	Soiling	96
3.5.1	Accelerated soiling	97
3.5.2	Natural soiling	99
3.5.2.1	SCI and SCE mode	99
3.5.2.2	CIELAB coordinates	103
3.5.2.3	Meteorological data	107
3.6	Adhesion tests	109
3.7	Morphological analysis	113
3.7.1	Coating thickness	113
3.7.2	Thermal treatment	115
3.7.3	Choice of substrate	117
3.7.4	Deposition technique	118
3.8	XRD analysis	120
3.8.1	Photoactive samples	121
3.8.2	Thermal treatment	123
3.9	Comparison between sol-gel and anodized coatings	124
3.9.1	Photocatalytic activity	124
3.9.2	Reusability	128
3.9.3	Mineralization	131
3.9.4	Reaction rate constants	135
4	Conclusions and future developments	139
	Bibliography	141
A	Appendix A	151

A.0.1	Natural soiling	151
A.0.2	Annealing conditions	157
B	Appendix B	161
B.1	Dip-coater source code	161
B.2	LED	163
B.3	Calibration curves for T.O.C. Analyzer	163
	List of Figures	165
	List of Tables	171

Introduction

The interest for self-cleaning surfaces ranges among industries whose products functionality relies either on surface transparency or aesthetic appearance. The possible applications include, but are not limited to, glass buildings, photovoltaic panels, and automotive exteriors [1]. Particulate matter, a form of air pollution, hampers the decorative and functional purposes of these surfaces; hence, regular manual cleaning maintenance is required to restore their original state. The adoption of an alternative solution would not only decrease variable labor costs, but also avoid the pollution stemming from cleaning agents. Concerning the application on glass buildings, it would also reduce the perils to which skyscraper window cleaners are exposed.

Automatic cleaning methods are already on the market [1, 2]. Mechanical cleaning methods, which include air-blowing, water-blowing, ultrasonic vibrations, and robotic cleaning systems, are harsh on the surface often causing microcracks and defects [1, 2]. Furthermore, they require heavy and high-power demanding equipment [1, 2]. Electrostatic cleaning methods generate standing or travelling waves which drive dust particles away from the surface by overcoming cohesive and gravitational forces [1, 2]. Not only do they require high power input, but they also do not perform well on wet surfaces [1, 2].

Self-cleaning coatings, on the other hand, do not require energy input, do not scratch the surface during deposition, and remain efficient even with daily variations in weather conditions [1, 2]. With proper formulations they can be environment-friendly, transparent, highly adherent to the substrate, and can be deposited on any surface including glass, cement, and textiles [1, 2]. These advantages, compared to other cleaning methods, make it possible to meet the growing demand driven by air pollution. Nonetheless, they still require regular maintenance, although not as frequent as manual cleaning. Indeed, as the coatings are exposed outdoors, they are subjected to wear from harsh precipitation, sand-grains, UV radiation and more [2]. Nevertheless, self-cleaning coatings have recently been applied on historical monuments for their preservation.

The aim of this dissertation is to test the self-cleaning ability of TiO_2 films obtained by sol-gel method and deposited by either dip-coating or spray-coating, which is more suitable for

large scale applications. The self-cleaning ability was tested in natural conditions exposing the samples outdoor for five months and monitoring the surface color variations. As the self-cleaning ability is the result of the synergy between specific surface wetting properties and photocatalytic activity, samples were tested by monitoring the static water contact angle variations during exposure to UV radiation and the degradation of rhodamine B in low concentrations. Photocatalytic tests were also conducted to determine the most suitable thermal treatment. Furthermore, in collaboration with *Università degli Studi di Milano Statale*, a series of tests was carried out to compare the photocatalytic efficiency of TiO₂ sol-gel coatings and anodized titanium. Finally, tests were performed to evaluate and improve the adhesion of the coating to the substrate, such as glass and PMMA, to ensure a long service life.

1 | Theory and state of the art

1.1. Titanium dioxide as a self-cleaning material

Titanium dioxide (TiO_2) is a mineral that exists in three polymorphs at atmospheric pressure: rutile, anatase, and brookite [3, 4]. While other polymorphs, such as the cubic form, can exist at higher pressures, they are not significant for research and engineering applications [4]. The properties of these polymorphs can vary significantly and have been extensively studied for use in a wide range of applications, including catalysis, photovoltaics, sensors, and biomedical devices. Overall, TiO_2 is a widely adopted material owing to its chemical stability, biocompatibility, physical and electrical properties [3].

Rutile and anatase are the most commonly studied phases for engineering applications, while brookite is less researched due to its challenging synthesis and complex structural predictions [4–6] (Figure 1.1). Despite this, brookite has gained interest in the photovoltaic field due to its high photocatalytic activity compared to anatase and rutile phases [5]. Anatase is a metastable phase that evolves to rutile, a stable phase, at high calcination temperatures [3–5]. The transformation is reconstructive rather than displacive and occurs at temperatures ranging from 400°C to 1200°C depending on the synthesis conditions [4].

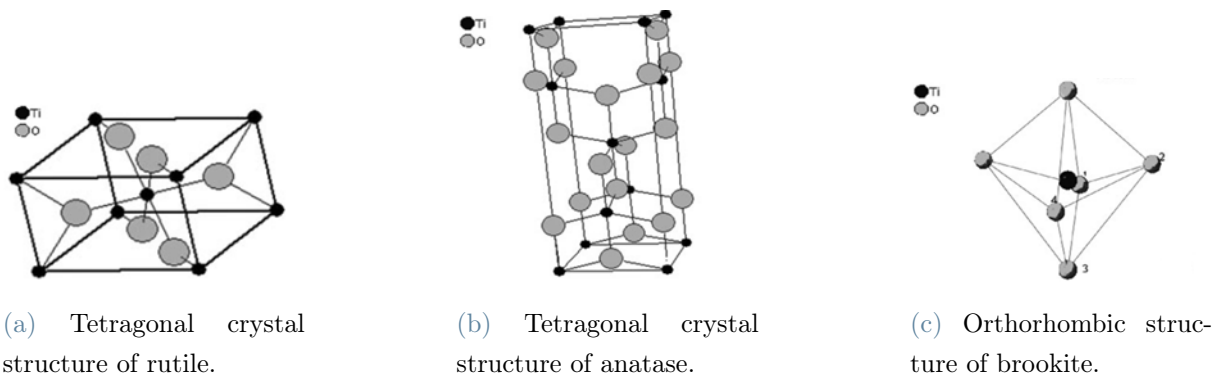


Figure 1.1: Crystal structures of TiO_2 polymorphs [3]

Titanium dioxide is often used in self-cleaning coatings because of its unique electrical, photocatalytic, and wettability properties. Compared to other self-cleaning coatings, these are potentially durable and environmentally friendly. Additionally, they can be applied to a wide range of surfaces, including glass, ceramics, and metals. As a result, they have numerous applications in industries such as construction, automotive, and healthcare, making them a promising technology for the future. Given the topic of this dissertation, only the properties that promote the material's photoactivity and hydrophilicity will be reported as to explain why it is an ideal material choice for self-cleaning surfaces.

1.2. Self-cleaning coatings

Self-cleaning films are able to remove pollutants, dust, or debris that is deposited on their surface. Hence, their application on modern buildings is desired for economic motives. Indeed, their application would reduce the need for routine maintenance tasks, such as facade cleaning, hence decreasing both the associated costs and the pollution caused by detergents and cleaning supplies.

Self-cleaning surfaces are either superhydrophobic or superhydrophilic [7, 8]. Superhydrophobic surfaces, which have a water contact angle (WCA) higher than 150° , induce the formation of spherical water drops which engulf dirt and remove it by rolling off the surface [7]. While superhydrophobic surfaces tend to be completely dry [7], superhydrophilic surfaces, which have a WCA lower than 10° , form a thin water film [7, 9, 10]. In both cases, the self-cleaning performance increases when the surface is exposed to water flow, e.g. rainfall [9, 11].

While hydrophobic surfaces are self-sufficient, hydrophilic surfaces do not rely solely on water flow [8]. Indeed, organic contaminants increase the WCA and disrupt the surface microstructure [10]. As a consequence, performant hydrophilic self-cleaning materials are also efficient photocatalysts able to mineralize organic pollutants and thus restore the original wettability of the surface [8, 10, 12]. Titanium dioxide, for example, is a self-cleaning material thanks to the synergistic effect of superhydrophilicity and photocatalysis, both triggered by UV irradiation [10, 12]. Indeed, the two behaviors enhance each other: hydrophilicity increases the adsorption of hydroxy groups on the surface, improving the photocatalytic activity [10]; while the continuous degradation of organic pollutants maintains the hydrophilicity of the surface [10].

1.2.1. Wettability

Surface wettability is most commonly determined by measuring the static WCA, i.e. the angle defined by the solid surface and the tangent to the drop surface [13, 14]. At thermodynamic equilibrium the WCA (θ) is defined by Young's equation (Equation 1.1), which relates θ to the interfacial energies per unit area ($\gamma_{SV}, \gamma_{SL}, \gamma_{LV}$) [13].

$$\gamma_{LV} \cdot \cos(\theta) = \gamma_{SV} - \gamma_{SL} \quad (1.1)$$

For θ larger than 90° the surface is hydrophobic, while it is hydrophilic for values smaller than 90° . Furthermore, for values exceeding 150° it is considered superhydrophobic; similarly, for θ smaller than 10° , the surface is deemed superhydrophilic. However, Young's equation is valid only for ideal solid surfaces, i.e. chemically inert, smooth, rigid, and homogeneous [13]. In real conditions metastable states are usually met, therefore the WCA changes across the surface and varies also according to drop deposition parameters [13, 14].

Real surfaces are characterized by contact angle hysteresis (CAH), for which the highest ($\theta_{advancing}$) and the lowest ($\theta_{receding}$) value of WCA differ [13, 14]. The real contact angle of the surface is often defined as a value in-between the advancing and receding contact angle [13]. To define the wettability of a surface it is necessary to define both static and dynamic contact angles. Static contact angle is an index of the liquid affinity to the surface, and it refers to the contact angle measured when there is no variation of the solid-liquid interface area after drop deposition [13–15]. Dynamic contact angle tests, on the other hand, are carried out by wetting and de-wetting the surface to gather both the advancing and receding contact angle [14]. Static contact angle tests are usually carried out by sessile drop method, while dynamic contact angle tests are carried out by one of the following: dynamic sessile drop method, Wilhelmy method, or sliding contact angle test [14]. These tests aim to measure the WCA hysteresis, which estimates the extent of drop mobility on the surface [14]. Concerning the self-cleaning ability of surfaces, it is of interest to also determine the sliding contact angle, i.e. the minimum surface tilting angle at which drops start to slide [14]. According to Parkin et al., superhydrophobic surfaces are more performing as the drops tend to roll off rather than slide off the surface, hence removing dirt more easily [8]. Ideally, self-cleaning surfaces should have very high static WCA, CAH close to zero, and very low roll-off angle [8].

1.2.1.1. Hierarchical structure

The WCA measured on a smooth surface is called *intrinsic contact angle* (θ_i) [14]. Real surfaces are rough and require suitable models to predict θ , such as the Wenzel's and the Cassie-Baxter's [13, 14]. The models mentioned above define the apparent contact angle (θ_{app}), i.e. the angle defined by the apparent solid surface and the tangent to the liquid surface [14]. According to the Wenzel model, the intrinsic WCA and the apparent contact angle have a linear relationship (Equation 1.2) [2, 13, 14].

$$\cos(\theta_{app}) = r \cdot \cos(\theta_i) \quad (1.2)$$

In Equation 1.2, r represents the *roughness ratio* defined as the ratio between the total and the projected surface area [14]. When the liquid on a surface is in a Wenzel state, that is the liquid-solid contact area is maximized (Figure 1.2), roughness amplifies the intrinsic wettability of the surface and hampers drop mobility due to the pinning effect of asperities [14].

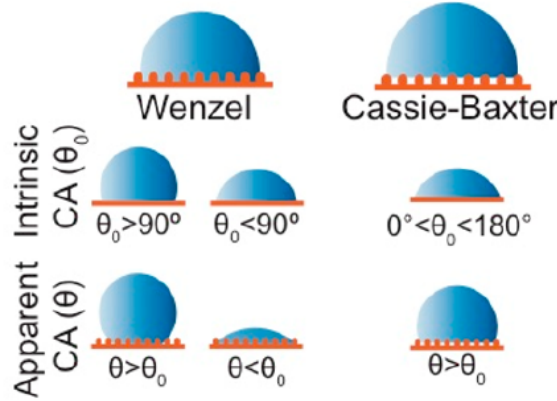


Figure 1.2: Comparison between Wenzel's and Cassie-Baxter's model [14]

Conversely, a liquid in the Cassie-Baxter state minimizes its contact area with the solid surface allowing air to be trapped between the asperities, such as in a highly porous material (Figure 1.2) [14]. According to this model θ_{app} and θ_i are related through the area fraction of the solid-liquid (f_{SL}) and liquid-vapour (f_{LV}) interface (Equation 1.3) [14].

$$\cos(\theta_{app}) = f_{SL} \cdot \cos(\theta_i) - f_{LV} \quad (1.3)$$

Therefore, a liquid that behaves according to the Cassie-Baxter model will always increase the hydrophobic character of a surface, and will have low CAH values due to the lack of

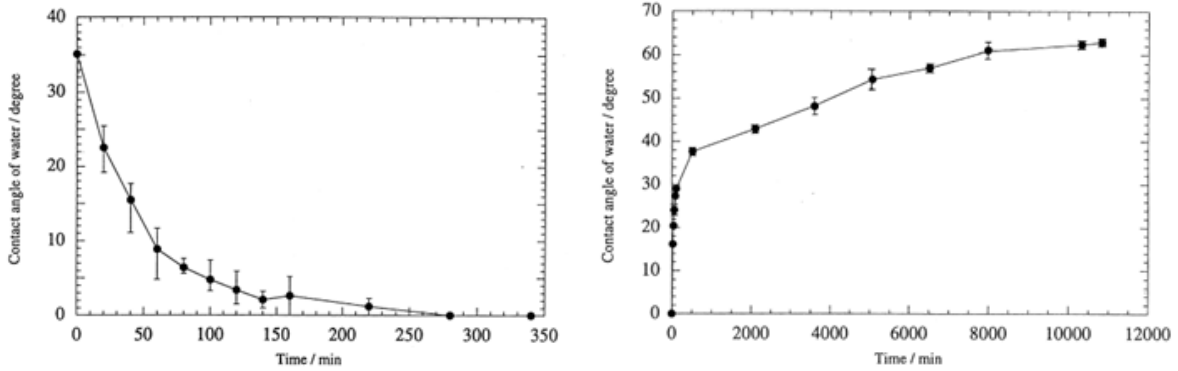
the pinning effect [14].

According to these models it is possible to control wettability by modifying the surface structure [15]. Self-cleaning surfaces are abundantly found in nature, where the wettability is controlled by the micro-nano structure of the surface rather than by chemical composition alone [15]. For example lotus leaves are self-cleaning owing to their textured surface consisting of hierarchical arrays of micro and nano-papillae [2]. Hierarchically structured surfaces are characterized by multi-scale roughness, e.g. the lotus leaf surface presents 10 μm and 100 nm papillae which highly increase its hydrophobic character [2]. The so-called *lotus effect* has pushed researchers to synthesize and improve bio-inspired wettability patterns to enhance the self-cleaning ability of surfaces [15, 16].

1.2.1.2. Photoinduced hydrophilicity

Titanium dioxide is studied for self-cleaning purposes partly owing to its ability to turn superhydrophilic when irradiated by UV light. Before irradiation the surface is hydrophilic with values of water contact angle ranging between 50° and 70° [17]. However, literature reports contradictory values as the material's wettability depends on multiple parameters, including surface roughness, surface treatment, and the method of preparation [17]. However, it is also possible to modify the surface properties of TiO_2 through various treatments, such as the addition of organic species in order to make it more hydrophobic and increase the water contact angle.

TiO_2 is a photoresponsive material, that, when it is irradiated by UV light, can become superhydrophilic thanks to a mechanism called *photoinduced hydrophilicity*. For example, Figure 1.3a shows that superhydrophilicity of anatase polycrystalline coatings is initiated by UV irradiation (1 mWcm^{-2}) [18]. The process is reversible simply by storing the sample in dark conditions (Figure 1.3b) [18].



(a) Water contact angle variation against irradiation time of anatase polycrystalline film synthesized by sol-gel method [18].

(b) Water contact angle variation in dark conditions [18].

Figure 1.3: Photoinduced hydrophilicity.

The theory behind the increase in hydrophilicity states that the metal ions present on the surface (Ti^{4+}) are photoreduced (Ti^{3+}) when irradiated by UV light [10, 18]. This phenomenon leads to the formation of oxygen vacancies and to water or dissociative water adsorption. Figure 1.4 portrays the just mentioned phenomenon [13].

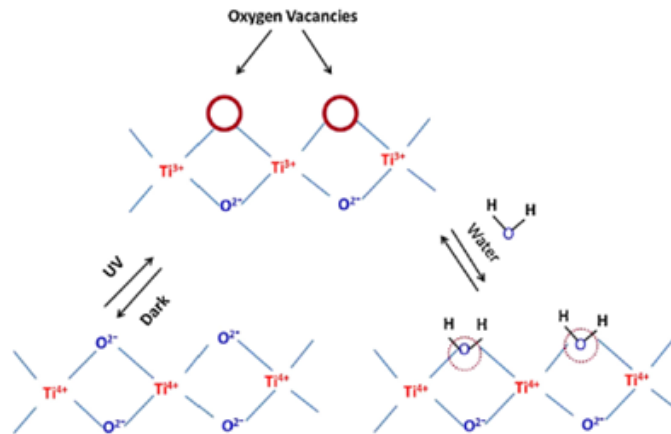


Figure 1.4: Superhydrophilic conversion phenomenon [13].

The adsorbed OH groups increase surface hydrophilicity enhancing the self-cleaning behavior of TiO_2 [10, 12, 18]. Indeed, thanks to the increased hydrophilicity, a layer of chemisorbed and physisorbed water forms on the surface preventing close contact with pollutants, which are easily removed by water sheeting [12].

To prove the *oxygen vacancies theory*, Wang et al. carried out WCA experiments on

rutile samples with different single crystal faces: (110) and (001) [18]. The (110) face has threefold coordinated oxygen atoms in the bulk and a bridging oxygen on the surface, which does not exist in the (001) face [18]. The bridging oxygen, being less coordinated, is more reactive and thus adsorption of dissociative water is more likely to occur. Indeed, under the same conditions, the hydrophilizing rate of (110) is faster (Figure 1.5a) [18]. Furthermore, as shown in Figure 1.5b, the bonds formed on the bridging site are more stable as represented by the lower hydrophobization rate [18].

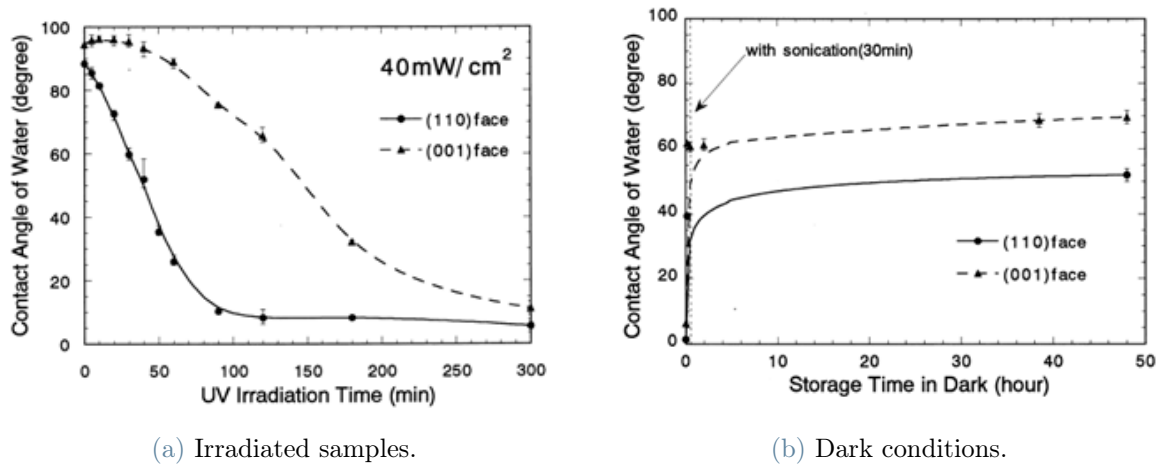


Figure 1.5: Water contact angle variation on different single-crystal rutile faces [18].

Sakai et al. demonstrated that hydrophilic conversion in titanium dioxide requires band gap excitation with the formation of a photogenerated hole [19]. They also reported that the plot of the reciprocal of the contact angle against UV irradiation time is a straight line, which allows to define a hydrophilic conversion rate independent of the initial contact angle but linearly dependent on UV irradiation intensity (Figure 1.6a and Figure 1.6b) [19].

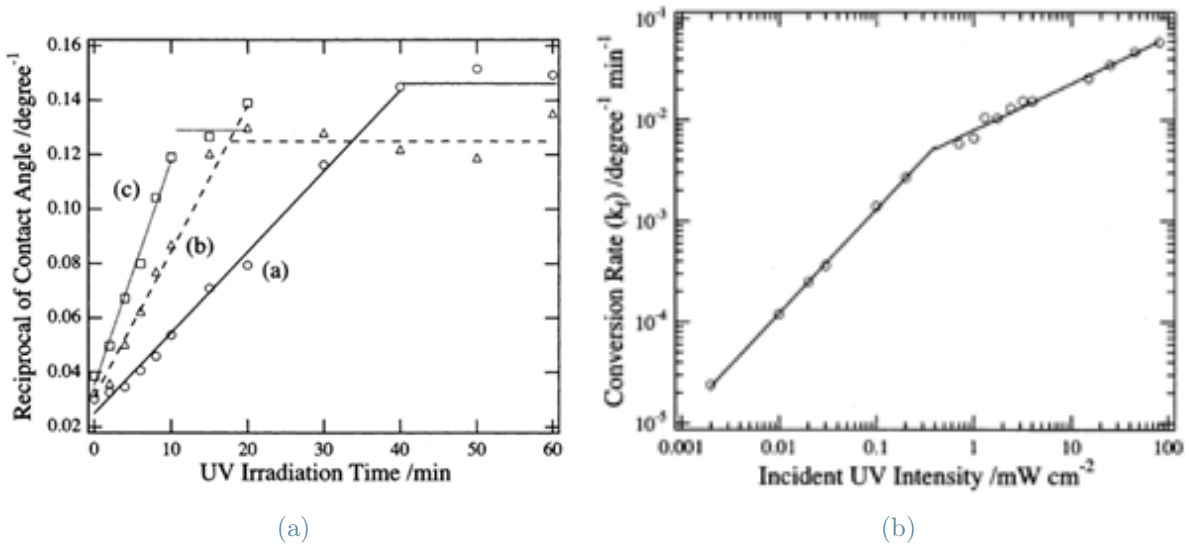


Figure 1.6:

- (a) Linear conversion rate under different UV irradiation intensities: (a) 0.2 (b) 0.7 (c) 1.0 mW/cm² [19];
 (b) Linear dependency between conversion rate and UV irradiation [19].

The variation in the slope values in Figure 1.6b is due to the onset of electron-hole recombination which limits the hydrophilic conversion [19]. The increase in the hydrophilic character with UV intensity, as shown in Figure 1.6a, is thought to happen according to the following model (Figure 1.7).

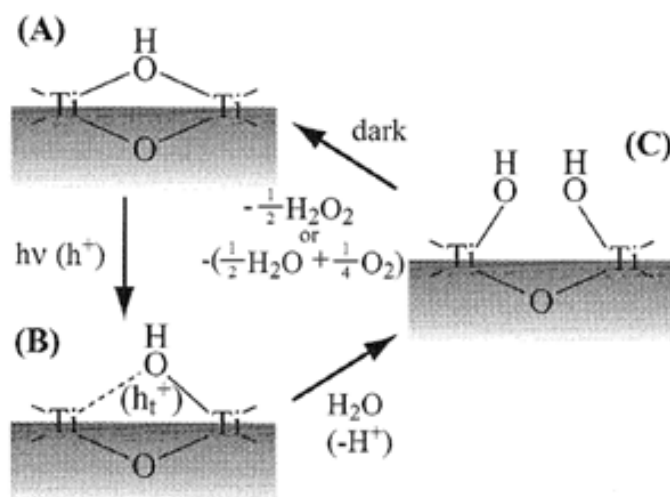


Figure 1.7: Hydrophilization model [19]

- (A) When the TiO₂ surface is excited by UV irradiation the photoexcited electrons are

captured by molecular oxygen [19]. (B) The corresponding hole is trapped at a lattice oxygen weakening its bond with titanium [19]. (C) A water molecule then is able to bind to Ti [19]. In the dark, hydrophilicity is lost due to release of $\text{H}_2\text{O} + \text{O}_2$ or H_2O_2 . In a nutshell, upon UV irradiation the density of hydroxyl groups increases accentuating the surface hydrophilic behavior [19]. As the process is triggered by photogenerated holes, the presence of holes scavengers will hinder the hydrophilic conversion of titanium oxide [19].

1.2.2. Photocatalysis

Photocatalysis is an accelerated photoreaction thanks to the presence of a catalyst. This dissertation focuses on the assessment of the self-cleaning ability of sol-gel coated samples, which is enhanced by the photodegradation of pollutants that promote hydrophobicity. Therefore, it was necessary to test the photocatalytic activity of the samples, which was performed by assessing the photodegradation of water pollutants, such as dyes and antibiotics. This chapter aims at introducing the theory behind the success of TiO_2 as a photocatalyst.

1.2.2.1. Photolysis

Photolysis is the degradation of a chemical compound, either organic or inorganic, following light absorption [20–22]. The reaction can be either direct or indirect:

- in direct photolysis the compound chemical bonds are broken as a consequence of direct absorption of radiation [20, 21];
- indirect photolysis involves the presence of photosensitizers (e.g. O_2 , OH^- , $\text{ROO}\cdot$) that absorb the radiation and then transfer the energy to the compound of concern [20, 21].

The probability of energy transfer between two molecules depends on the concentration of both chemical species [21]. Therefore, it is common to bubble oxygen in the photocatalysis reactor during laboratory tests.

Any photon with sufficient energy can break the chemical bonds of a compound [21]. Although, not every chemical species is prone to photodegradation as the necessary wavelength for degradation might not be present in the provided light radiation [22]. The photodegradation rate depends on the light absorption properties of the compound [21], its reactivity [21], its bond strength, intensity of the radiation [21], and test temperature [22].

The photolysis reaction follows three steps [22]:

1. Light absorption: as the molecule absorbs light it acquires an excited state which induces physical and chemical changes to the molecule [22];
2. Primary photochemical processes: the excited molecule reacts following different processes, such as luminescence, energy transfer, photoionization, photodissociation, rearrangement, and reaction [22];
3. Secondary thermal reactions: the intermediates formed in the previous step are further transformed, for example, by dissociating into radicals [22].

However, as photolysis reactions are rather slow photocatalysts are employed to accelerate and promote the degradation of pollutants.

1.2.2.2. Titanium oxide as a photocatalyst

Titanium dioxide photocatalysis is a reaction induced by a photon absorption event at the surface or in the bulk [23]. As its bandgap ranges between 3.0 and 3.2 eV it is able to absorb radiation between 387 nm and 413 nm, which amounts to only about 5% of the solar spectrum [23]. Its application at a commercial scale for water treatment is advantageous for the following reasons [24]:

1. The reaction occurs at room temperature;
2. Complete mineralization is feasible, thus the production of toxic intermediate products is limited;
3. Titanium dioxide is inexpensive;
4. It can be supported on various substrates allowing continuous re-use;
5. Photogenerated carriers are highly reactive favoring pollutant degradation through oxo-reduction reactions.

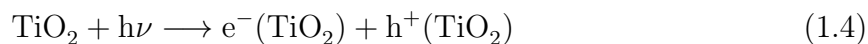
The photocatalytic activity of TiO_2 relies on multiple parameters: degree of crystallinity, morphology, particle size, phase composition, specific surface area, defect density, and more [25]. Some of these are explained in the following paragraphs.

1.2.2.3. Degradation mechanism

The semiconductor character of titanium oxide allows the degradation of pollutants thanks to the photogeneration of charge carriers and hence the formation of a redox environment [24].

Upon UV irradiation the photocatalyst absorbs energies equal or above its band gap value

inducing the excitation of electrons to the vacant conduction band and the photogeneration of holes in the valence band (Eq.1.4) [23, 24].



Photon absorption can occur directly by absorption of UV irradiation or by transfer of excited electrons from pollutants to the conduction band of TiO_2 [23]. These electron-hole pairs tend to recombine and dissipate the absorbed energy [24]. Generally recombination accounts for 90% of the photogenerated pairs, while only 10% remains available for photocatalysis reactions [23]. Recombination can be either radiative, i.e. the energy is emitted in the form of photons, or irradiative, i.e. through the emission of phonons, which is more common in TiO_2 [23]. Both high temperature and intrinsic defects, such as oxygen vacancies, interstitial, and substituted ions, favor charge carrier recombination as they introduce additional electronic states between the conduction and valence band [23]. Otherwise, if carrier separation is efficient, the energy can be used to drive downhill and uphill reactions [23]: in uphill reactions the photon energy is converted into chemical energy, e.g. during photocatalytic splitting of H_2O into H_2 and O_2 ; while in downhill reactions the absorbed energy is used to induce thermodynamically favored reactions, e.g. pollutant degradation [23]. Although, not all photon energy invested in charge carrier generation is available for redox reactions, as hot electrons and deep holes are subjected to thermalization and thus energy loss [23]. As a consequence, even if the photocatalyst is able to absorb photons with energies that exceed its band gap, the actual available energy for degradation is close to the band gap value.

To drive photocatalytic reactions the photogenerated carriers have to migrate to the surface of the catalyst where they can transfer to the adsorbed pollutant to perform reduction and oxidation reactions [23, 24]. Depending on the electron donor or acceptor character of the pollutant, degradation occurs by reaction with either the energized holes or electrons [24]. However, the charge carriers usually do not directly react with the pollutant, which is present in solution at low concentrations. Excited electrons combine with oxygen to form super oxide ions (O_2^-), while holes in the conduction band combine with hydroxyl ions to form hydroxyl radicals ($\text{OH}\cdot$). These reactive species then degrade organic molecules into smaller hydrocarbons up to complete mineralization (Figure 1.8) [26].

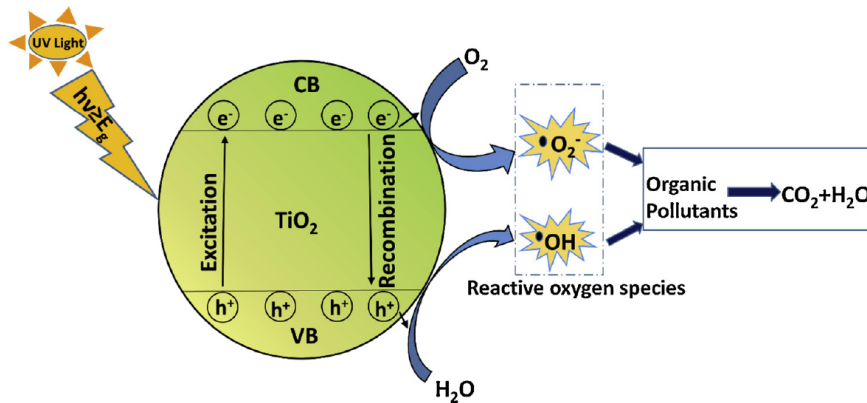


Figure 1.8: Representation of exciton generation, charge transfer, electron-hole recombination, electron and hole driven reactions at the surface of a photocatalyst particle [26]

1.2.2.4. Suspended and immobilized photocatalyst

The use of photocatalysts for the degradation of pollutants in water solutions can be achieved in two ways: either by suspending the photocatalyst powder in the solution, or by immobilizing it on a substrate. Literature shows that suspended photocatalysts employed in slurry type photocatalytic reactors are more efficient than immobilized particles [24].

For example, Manassero et al. compared the quantum and photonic efficiency of three different set-ups for the degradation of cofibric acid [27]:

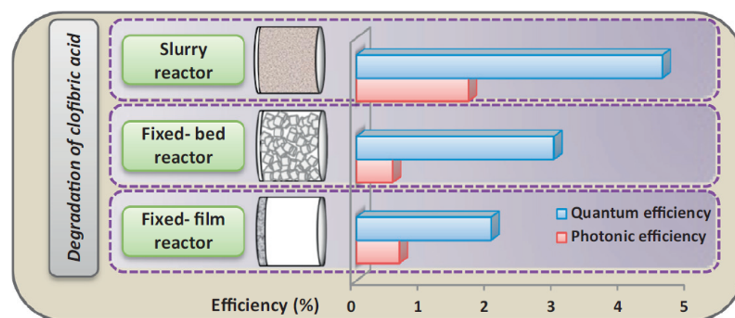
- Slurry reactor with suspended TiO₂ particles;
- Fixed film reactor with TiO₂ immobilized onto the reactor window;
- Fixed-bed reactor filled with TiO₂-coated glass rings.

The efficiencies were defined as follows:

$$\eta = \text{Photonic efficiency} = \frac{\text{Observed reaction rate}}{\text{Rate of incident radiation}} \quad (1.5)$$

$$\eta_{RXN} = \text{Quantum efficiency} = \frac{\text{Observed reaction rate}}{\text{Rate of photon absorption}} \quad (1.6)$$

The authors concluded that although the slurry reactor was the most efficient, the fixed-bed reactor had satisfactory results with the additional benefits related to the use of immobilized photocatalyst (Figure 1.9a and Figure 1.9b).



(a)

Efficiency evaluation among SR, FFR and FBR.

Reactor	Condition	Reaction rate $\times 10^9$ (mol s ⁻¹)	Photon absorption rate $\times 10^8$ (Einstein s ⁻¹)	η (%)	η_{Rxn} (%)
SR	0.5 g L ⁻¹	5.0	10.9	1.68	4.59
FFR	5 coatings	1.9	9.4	0.64	2.02
FBR	5 coatings	1.6	5.4	0.54	2.96

(b)

Figure 1.9: Efficiency comparison between suspended and immobilized TiO₂ photocatalysts [27].

Thus, while slurry reactors are the most commonly employed for research purposes, immobilized photocatalyst have more leverage for practical applications. The lower efficiency related to immobilized photocatalysts is due to mass transfer limitations which arise from the low surface area, characteristic of immobilized particle systems [24, 27, 28]. On the other hand, one drawback related to the use of suspended photocatalysts is their loss of efficiency in time. Indeed, degradation intermediates trigger particle coagulation thus decreasing the surface area [24].

Immobilized particle systems introduce several benefits that make it more suitable for engineering applications [24, 27, 28]:

1. they allow continuous operation;
2. catalyst recovery and reuse are easy and inexpensive;
3. the supports can be reused for several cycles;
4. the substrates can be functionalized to speed up the purification process;
5. catalyst separation and installation of a liquid-solid separator are unnecessary.

To ensure the highest efficiency, the substrate should be transparent to UV radiation, chemically inert, with a high surface area, it should strongly bind with the photocatalyst

without impacting its reactivity, and it should have strong adsorption affinity to the pollutants [24, 28].

1.2.2.5. Influencing parameters

Phase composition The photocatalytic activity of TiO_2 varies among its polymorphs due to variations in morphology and structure following phase transitions [26]. A study on the photocatalytic activity of different polymorphs was carried out by Singh et al., who tested the performance of TiO_2 nanoparticles obtained by sol-gel method [26]. The authors performed rhodamine B degradation tests on anatase and rutile both in single and mixed phases, respectively obtained at the following calcination temperatures: 400°C , 900°C , and 600°C [26]. The authors reported that the anatase phase shows better photocatalytic activity than rutile, which, on the other hand, does not show visible light-induced degradation (Figure 1.10).

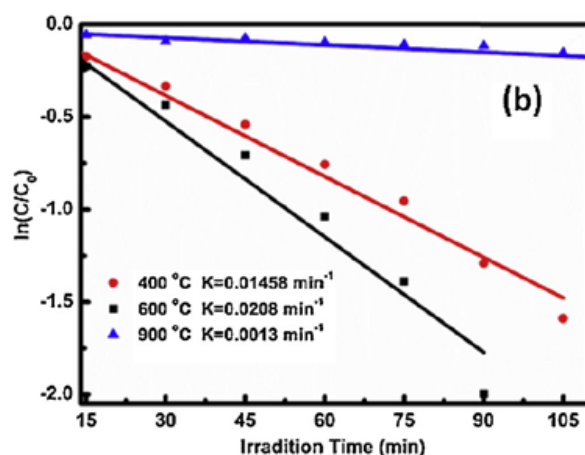


Figure 1.10: Photocatalytic activity difference among TiO_2 polymorphs [26]

Generally, the small electron and hole effective mass found in the anatase structure favors the migration of the charge carriers and thus increases its photocatalytic activity [26]. Furthermore, the phase transition from anatase to rutile induces an increase in particle size, reducing photocatalytic activity [26]. However, the mixed phase turned out to be the most performing as it completely degraded the compound in only 105 minutes [26]. The better photocatalytic performance of the mixed phase is due to the lower charge recombination rates [25]. Indeed, the 0.2-0.25 eV difference between the conduction band energies of the single phases induces the transfer of photogenerated charge carriers [25, 29]. Electrons flow from the rutile phase to the anatase phase, while holes proceed in the opposite direction [29]. Therefore, charge carrier separation is improved [25]. The best

conditions are met when the mixed phase is anatase dominant [25]. Additionally, it was proven that higher degrees of crystallinity enhance the photocatalytic activity of titanium dioxide [30].

Calcination temperature and particle size Behnajady et al. also performed tests on the photocatalytic activity of different TiO_2 polymorphs [31]. The tests were performed by varying the calcination temperature of synthesized TiO_2 nanoparticles. In Figure 1.11 the authors have summarized the phase content and crystallite size of the tested samples.

Calcination temperature ($^{\circ}\text{C}$)	Amount of each phase %	Crystallite size (nm)
350	A: 100, R: -	D_A : 5, D_R : -
450	A: 95, R: 5	D_A : 15, D_R : 12
750	A: -, R: 100	D_A : -, D_R : 22

Figure 1.11: Influence of calcination temperature on phase and crystallite size [31].

With increasing temperature the amorphous sample obtained at 350°C crystallizes into anatase (A), which then completely transforms into rutile (R) at 750°C . Additionally, the increase in temperature stimulates crystallite growth, which is detrimental to photocatalytic activity.

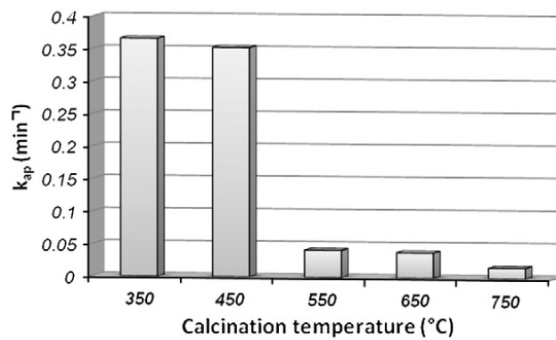
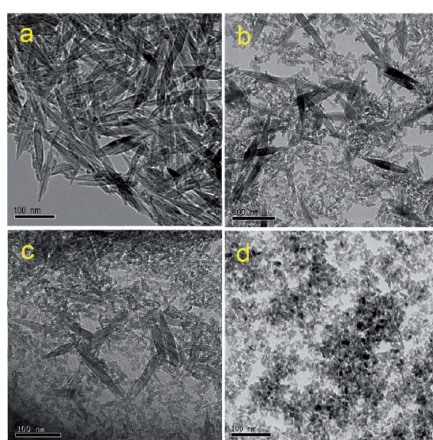


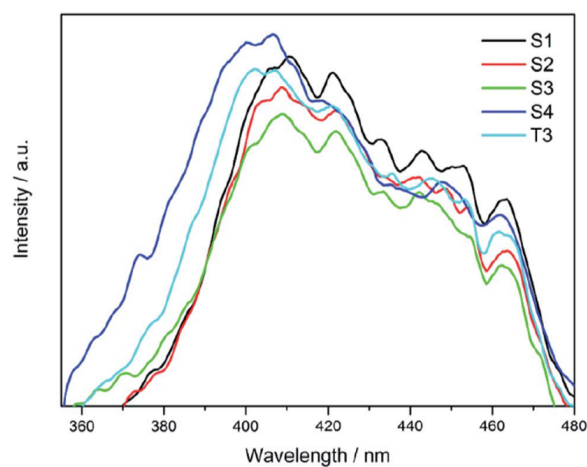
Figure 1.12: Influence of calcination temperature on photocatalytic activity [31].

The decline in photocatalytic activity is attributed to particle agglomeration, particle growth, and rutile phase increase [31]. Smaller particle sizes in the order of 1-10 nm are thought to be better for photocatalytic purposes as quantum size effects are introduced, which widen the semiconductor band gap [31]. Hence, the excited electrons and the corresponding holes have a higher redox ability and thus photocatalytic activity increases [31].

Morphology and specific surface area As the degradation of pollutants occurs on the surface of the photocatalyst, both morphology and specific surface area directly influence the reaction. Generally, large surface areas are preferred as they provide multiple active sites for the adsorption of pollutants and for the generation of oxidative radicals needed for the degradation [25]. Not only is the specific surface area related to the catalyst particle size, but also to the morphology. Cheng et al. studied the influence of these two parameters in the photocatalytic activity of titanium oxide obtained by soft-chemical strategy [25]. The research focused on the comparison between the photocatalytic activity of nanoparticles (0D) and nanorods (1D). The research concluded that composite structures (0D/1D) combine the benefits of the two morphologies, and thus performed better than the single structures. It was proved that while the 0D structures have higher surface-to-volume ratio, the 1D structure inhibits electron-hole recombination [25]. The authors compared the photoluminescence spectra of different morphologies to determine the ones with the lowest carrier recombination rates, and thus lowest heat generation and photon emissions.



(a) TEM images of different sample morphologies: a) S1, b) S2, c) S3, d) S4 [25].



(b) Photoluminescence spectra of different sample morphologies [25].

Figure 1.13: Comparison of photocatalytic efficiency between different TiO_2 nanostructures.

As shown in Figure 1.13 the S1, mainly composed of 1D structures, performs better than S4, mainly composed of nanoparticles. On the other hand, S3, a composite structure dominated by nanoparticles, had the lowest charge recombination rate. The authors justify the result stating that the composite structure introduces fewer contact barriers and

accordingly fewer electron trap sites, which otherwise would trigger trap-assisted recombinations [25]. Nevertheless, both bulk and surface recombination can occur. Surface recombination is typical of high surface-to-volume ratio structures, such as 0D. As a consequence, although high surface areas benefit the photocatalytic activity of TiO_2 , the improvement is offset by the resulting higher recombination rate [25]. Therefore, morphology and specific surface area provide a synergistic effect on the photocatalytic activity of titanium oxide [25].

According to theoretical predictions and experimental results, nanotubes tend to have higher photocatalytic activity than nanoparticles [32]. The reason is attributed to the higher specific surface areas of nanotubes, prolonged lifetime, and thus efficient separation, of photogenerated electron-hole pairs, and stronger reduction ability thanks to the higher conduction band minimum [32]. However, the photocatalytic activity of nanotubes highly depends on their morphology: such as length [33], pore diameter [34], and top morphology [35]. While generally a wider pore diameter promotes higher degradation efficiency [34], length presents a more complex relationship. Indeed, there is an ideal length for which photocatalytic activity reaches a maximum level due to the compromise between pollutant diffusion and light absorption, as generally long nanotubes present thinner walls and thus low amounts of TiO_2 (Figure 1.14).

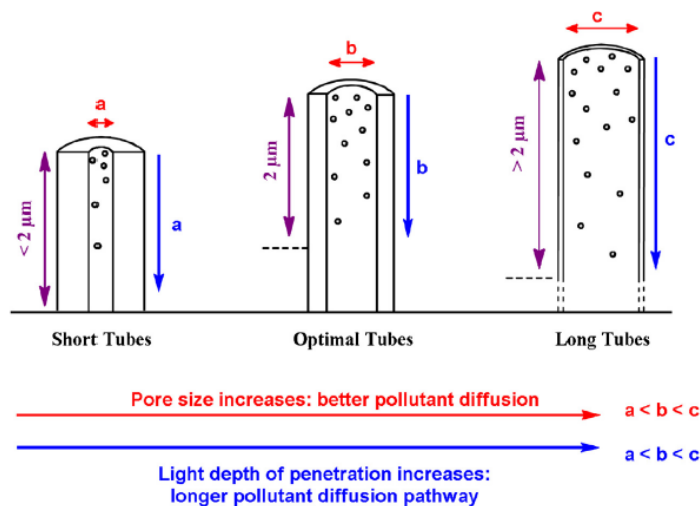


Figure 1.14: Illustration and interpretation of the correlation between photocatalytic activity and anodized TiO_2 nanotubes [33].

Thus, in long nanotubes, light has to travel a longer distance to be absorbed by the semiconductor, but in doing so the electron-hole pairs necessary for degradation are generated deeper in the nanotubular channels and thus are less accessible to the pollutants [33]. Too

long nanotubes, therefore, induce a diffusion controlled degradation mechanism whose efficiency is decreased compared to shorter structures [33]. However, short nanotubes, having thicker walls, present small inner diameters that impede pollutant diffusion. Generally, research papers report that higher photocatalytic activity is yielded by nanotubes in the order of 5 to 7 μm [33, 35].

Due to the importance of pollutant diffusion in the tubular channels, top morphology strongly influences the photoactivity of the semiconductor. Generally, four different morphologies can be formed following anodization [35]:

- initiation layer, which forms in the early stages of anodization and partially blocks the nanotube mouth;
- open tubes, whose initiation layer is removed by etching;
- nanotubes with connected interpore space, which resemble a porous layer;
- *grassy tubes*, which are nanotubes covered by nanodimensional wires originating from extended etching.

Comparing the photocatalytic activity of titanium oxide nanotubes with different top morphologies, but same diameter and tube length, the *grassy tubes* are by far the less efficient as they impede contact between pollutants and the oxide layer [35].

1.3. Production methods

Titanium dioxide is synthesized via different methods, such as anodization, sol-gel, hydrothermal, and vapour deposition techniques [36]. This dissertation, however, is focused only on the first two methods, which are carried out at ambient pressure and temperature.

1.3.1. Anodization

The anodization process yields titanium oxide coatings highly adherent to the substrate, and whose thickness varies according to the process parameters. This technique is an electrochemical process in which the workpiece is immersed in an anodizing solution and acts as anode of an electric circuit under potentiostatic conditions. Different coating morphologies are achieved by varying electrolyte formulation, applied voltage, processing time, and temperature. According to the employed process parameters, two different coatings are obtained: either a barrier or a tubular type film [36]. The morphology highly depends on the electrolyte, indeed nanotubes are formed only when the oxide is moderately soluble, such as when employing solutions containing fluoride ions; although, similar results

can be obtained even when using perchlorate, chloride, and bromide ions [36]. Barrier films are instead formed when using aqueous solutions containing sulphuric, phosphoric, or acetic acid [36]. While the thickness of barrier films is limited to a few hundred nanometers, nanotubes can reach up to $1000 \mu\text{m}$ [36]. The growth of barrier films is driven by field-assisted oxidation alone, which requires the application of an electric field to induce the movement of ions across the film, hence the oxidation process ceases when the electrical resistance of the coating, and thus its thickness, exceeds a certain limit [36]. The electric field drives Ti^{4+} ions from the substrate to the electrolyte, while OH^- and O^{2-} , originating from field-assisted water dissociation, are driven towards the substrate: hence the coating grows at the metal/oxide interface. Tubular structures, instead, grow by field-assisted oxidation and dissolution, according to which the oxide is preferentially dissolved where the electric field is strongest, i.e. at the tube base [36].

1.3.1.1. Mechanism of oxide growth

The mechanism necessary for the formation of nanostructured oxide follows three stages (Figure 1.15 and Figure 1.16):

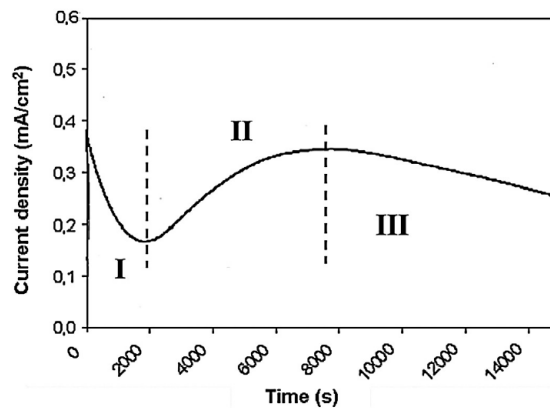
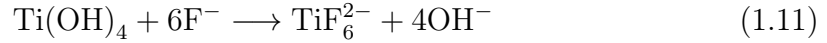
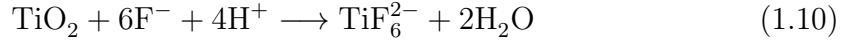


Figure 1.15: Current density variation registered during anodization of titanium in glycerol/NaF [36].

- Initially, a thin barrier film forms at the metal/oxide interface thanks to the applied electric field which drives Ti^{4+} and O^{2-} ions towards the electrolyte and towards the substrate, respectively (Equation 1.7, Equation 1.8, and Equation 1.9) [36]. The process generates hydrogen evolution at the cathode and oxygen evolution at the anode [36]. As the oxide thickens the current density decays due to the increase in the electric resistance (Stage I) [36];



- F^- ions are also involved in the process combining with Ti^{4+} to form a stable complex ($[\text{TiF}_6]^{2-}$) (Equation 1.10, Equation 1.11, and Equation 1.12) [36];



Pits and cracks form at the surface, where nanotubes start developing thanks to the combined action of the stronger electric field, which weakens the bonds between Ti and O, and the presence of fluoride ions, which dissolve the oxide layer at the electrolyte interface [36]. Due to oxide dissolution, current density increases (Stage II) [36];

- The formation of nanotubes is enhanced by the formation of a pH gradient between the pore base and mouth [36]. Current density drops to a constant value as a steady-state condition is reached for which the oxide dissolution and growth rate are equal (Stage III) [36].

However, a too high dissolution rate inhibits the growth of nanotubes:

- first generation nanotubes reached a maximum thickness of $0.5 \mu\text{m}$ because fluoride ions were supplied by hydrofluoric acid [36];
- fluorine salts, which were employed for the synthesis of second generation nanotubes, yielded nanotubes up to $5 \mu\text{m}$ long [36];
- third generation nanotubes can reach $1000 \mu\text{m}$ because the employed electrolyte is

not water-based but organic [36]. Indeed, fluoride ions in organic solutions are less aggressive than in water-based electrolytes, however, as oxygen is strongly bonded to carbon, it is necessary to extend the anodization time to achieve thick coatings [36].

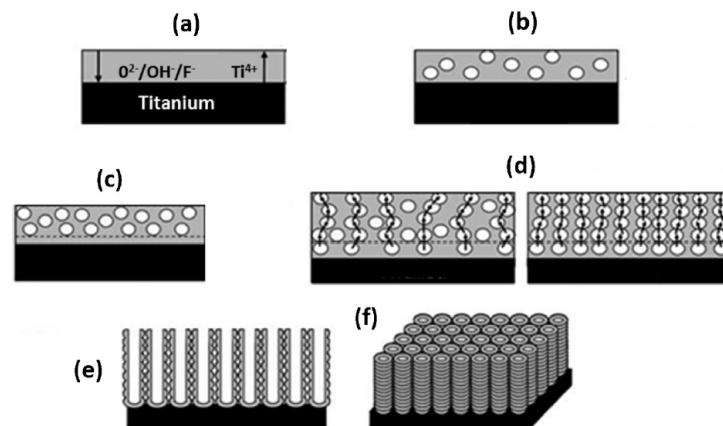


Figure 1.16: Illustration of titanium oxide growth mechanism[36]: a) formation of the barrier film; b) formation of pits on the surface due to dissolution induced by fluoride ions; c-d) alignment of the cavities which leads to the formation of self-ordered nanotube arrays; e) formation of longer channels due to the collapse of adjacent cavities; f) final structure.

1.3.1.2. Influencing parameters

Oxide growth is influenced by multiple parameters, some of which are described in the following paragraphs.

pH and temperature Low pH and high temperature induce higher dissolution rates. Therefore the use of fluoride salts rather than hydrofluoric acid is ideal to reduce oxide dissolution and promote growth of nanotubes [36]. Nanotubes are usually formed at room temperature, however, organic electrolytes may require up to 40°C to facilitate the formation of nanotubes [36].

Solution ageing Oxide growth is promoted when using the electrolyte in multiple anodization cycles [36]. Indeed, ageing induces both moisture absorption from the environment, which increases the presence of O^{2-} and OH^- ions, and the build-up of $[TiF_6]^{2-}$ species which lower chemical dissolution and increase the electrolyte conductivity [36].

Applied voltage In barrier type films the anodizing ratio defines the maximum coating thickness per unit volt: thus higher voltage yields thicker coatings as a stronger electric

field is generated [36]. Additionally, in tubular coatings nanotube diameter, as well as length, and applied voltage follow a positive linear relationship [37]. Usually, organic solutions require higher potential difference, i.e. 10-60 V, compared to water-based ones, i.e. 5-30 V [36]. Higher applied potential difference is also correlated to thicker nanotube walls [37].

Processing time Organic electrolytes require long processing times due to slow oxide growth despite the lower dissolution rates: therefore, anodization is carried out up to 24 hours to ensure the formation of long nanotubes [36]. On the other hand, by adopting water-based solutions, although the oxide reaches its ultimate thickness in a few minutes, the processing time ranges from 30 minutes to a few hours to allow the arrangement of self-ordered nanotubular arrays [36]. Overall, longer anodizing time enhances tube length and regularity [37].

Electrolyte Third generation nanotubes are formed in organic electrolytes to promote their growth. While water-based electrolytes can form nanotubes up to 0.5 μm in length, those grown in organic electrolytes can reach up to 1000 μm [36]. However, organic solutions, usually based on ethylene glycol, need a small water volume percent to promote nanotube growth, which may otherwise be slow. With increasing volume concentrations of ethylene glycol the morphology of the oxide shifts from porous layer (10%), to the formation of irregular nanotubes (70%), and to the formation of packed nanotubes (80-90%); furthermore, with increasing concentration of ethylene glycol the film thickness increases [38].

1.3.2. Sol-gel process

Titanium dioxide based self-cleaning coatings are synthesized by sol-gel method, hydrothermal and solvothermal method, layer-by-layer self-assembly, electrochemical methods, electrospinning, and plasma treatment [39]. This dissertation focuses on the sol-gel method due to its advantages [40]:

- it is simple and cost-effective;
- it requires low processing temperature;
- it forms complex structures;
- it is versatile.

The sol-gel process is a bottom-up wet chemical synthesis method that occurs at low

temperatures under heating and stirring conditions [41, 42]. It is aimed at the production of nano and microstructures that can be employed for different purposes [41, 42]: synthesis of metallic oxide nanoparticles [42], water or oil-repellent self-cleaning and antibacterial surfaces [43], substrate catalysis [44], filters [44], and more.

1.3.2.1. Processing steps

The synthesis is based on a two-step reaction involving both hydrolysis and condensation of metal alkoxides or metal chlorides by the action of a proper solvent [45]. Additional reagents can be added, such as catalysts, to increase the hydrolysis rate, surfactants, to stabilize the sol, and chelating agents, to slow down the hydrolysis rate. The steps involved in sol-gel synthesis are the following:

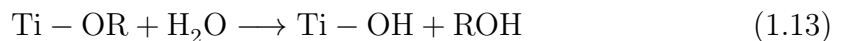
1. Preparation of a homogeneous solution:

Precursor and solvent are mixed in a container to obtain a homogeneous solution. Some precursors might require the dilution in a water soluble organic solvent and then a subsequent dissolution in water or alcohol, necessary for the hydrolysis step [41, 42].

2. Hydrolysis and sol formation:

Molecular precursors react with either water or alcohols to form a colloidal solution, in which fine disperse solid particles are suspended in liquid [41–44, 46, 47]. This is possible only if the particle size does not exceed 100 nm, in this condition the Brownian motion of the particles overcomes the force of gravity and prevents the particles from settling [41, 42].

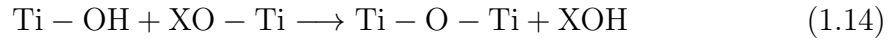
The hydrolysis reaction, necessary for the sol formation, replaces an alkoxide ligand (R) with either a hydroxyl ligand (OH^-) or an oxo ligand (O^{2-}) (Equation 1.13) [42].



Regardless of whether an aqueous or non-aqueous sol-gel method is chosen, the oxygen necessary to carry out the reaction and produce hydroxyl groups is provided by the solvent, i.e. either water or alcohol [40, 44]. Complete hydrolysis leads to the formation of a rigid gel, useful for powder synthesis; while partial hydrolysis leads to the formation of a viscous fluid which can be processed to obtain crystalline films [42]. Nevertheless, for this to occur the solution has to gelate.

3. Gelation:

Sol gelation occurs thanks to the polycondensation reaction triggered by the addition of the appropriate solvent [41]. During condensation, adjacent molecules form oxide linkages which trigger the formation of a polymeric network, with release of water (water condensation) or alcohol (alcohol condensation) [40, 42]. Polycondensation involves the hydroxyl groups formed in the hydrolysis reaction and the residual alkoxy groups [44]. The bond that is formed between the molecules is created either by olation, where a hydroxyl bridge is formed between two metal centers (Ti-OH-Ti), or by oxolation, where an oxygen atom acts as a bridge instead (Ti-O-Ti) [40].



Equation 1.14, where X denotes either a hydrogen atom or an alkyl group, represents the condensation reaction which induces the formation of metal-oxygen-metal links and the release of either water or alcohol [40–43].

The final product is called a *wet-gel*, i.e. an oxide network of metal oxide clusters branching in a liquid [41, 46, 47]. Three-dimensional networks with close packing are formed when titanium alkoxide is present in excess, as it triggers the inorganic polymerization of the precursor at low hydrolysis rates. Loosely packed networks are formed when there is insufficient development of the three dimensional network, leading to the formation of $\text{Ti}(\text{OH})_4$ [46].

4. Ageing:

The ageing step might take a few hours or a few days. Ageing induces continuous changes in the polymeric structure thanks to the ongoing polycondensation, which strengthens the links between particles and stabilizes the pore structure [40, 42, 43]. The sol-gel properties thus evolve accordingly [42, 43].



Figure 1.17: Effects of aging on a sol-gel formula

Figure 1.17 is a visual representation of the consequences of four months aging on the same sol-gel formula.

5. Application:

Sol-gel solutions can be used to form thin-films on a wide variety of substrates. For this purpose, there are several techniques that can be used, although not all of them are suitable for large-scale productions. Here are explained the three coating methods most used in laboratory for research purposes:

- Dip-coating:

The process requires the immersion of the substrate in the solution of interest, and its subsequent withdrawal (Figure 1.18).

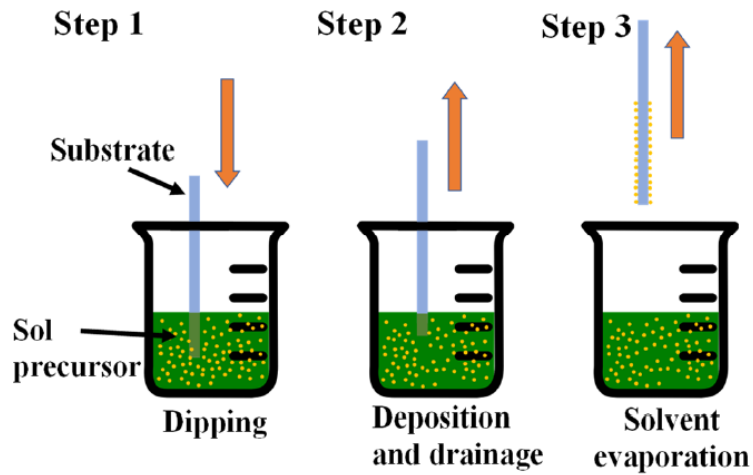


Figure 1.18: Dip-coating method for thin film deposition [48].

Both movements should be carried out at constant speed to ensure the deposition of uniform coatings [48]. Multiple variables influence the final outcome, such as number of cycles performed, viscosity of the solution, speed of immersion and withdrawal, inclination angle, sol concentration, temperature, and more [48]. The wide variety of parameters forces researchers to identify the best combination to achieve the required thin-film properties. Overall, film thickness and uniformity are mostly influenced by viscosity. Highly viscous solutions form non-homogeneous coatings, hence it is usually better to use less viscous solutions and to perform multiple cycles [48]. As capillary action and viscous drag are responsible for the solution distribution on the substrate, high rates of immersion, which increase viscous forces, lead to thicker layers [48]. Disadvantages related to this method include the limited dimension of products that can be coated, and the large quantity of solution needed compared to the actual deposited volume.

– Spray-coating:

Contrary to dip-coating, spray-coating requires small volumes of solution and it allows easier deposition on large surfaces. For the deposition a spray-gun is needed, which consists of a tank, where the solution is loaded, an air-compressor, which atomizes the solution, and the spray-gun nozzle, which sprays the solution onto the substrate (Figure 1.19).

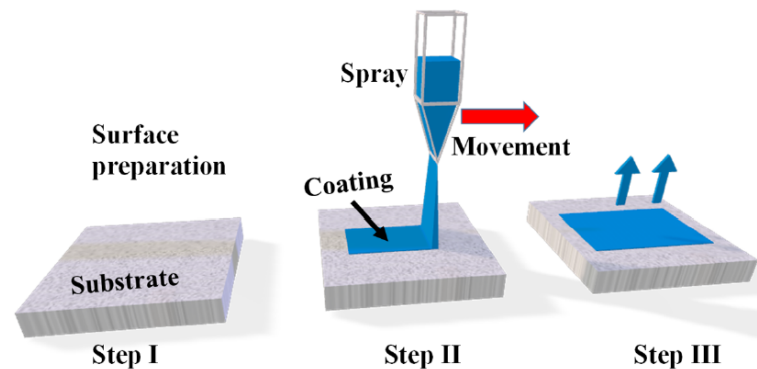


Figure 1.19: Spray-coating method for thin film deposition [48].

Therefore, the solution is atomized and deposited on the substrate surface thanks to the high flow rate supplied by the air compressor. The process variables include applied air pressure, and thus flow rate, substrate temperature, duration of the deposition, number of layers, distance between the substrate and spray gun nozzle, and so forth [48]. Solution viscosity also influences the final coating properties, as at constant pressure viscous solutions form larger droplets that do not adhere well to the substrate.

– Spin-coating:

According to this method, a drop of solution is deposited at the centre of the surface which is then rotated at high speed (Figure 1.20).

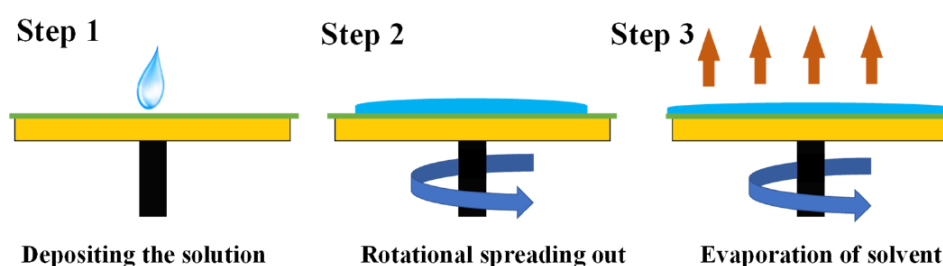


Figure 1.20: Spin-coating method for thin film deposition [48].

The centrifugal force and the liquid surface tension push the drop from the center to the surface edges, thus covering the whole surface [48]. Although an extremely uniform film is formed, the process wastes 95-98% of the employed solution as the high-speed rotation expels excess material [48]. Furthermore, the technique can only be applied on flat surfaces with limited dimension due to the difficulties associated to rotating large objects [48]. The main variables

that influence film thickness are the viscosity of the liquid and the rotation speed.

- Other methods:

Several other methods can be employed for thin-film deposition. These include, along with others, blade-coating, roll-coating, slot-die coating, bar-coating, and brushing.

6. Drying:

The drying step is required to remove the solvent and obtain a solid product. Different drying methods lead to microstructures with varying degrees of porosity. Drying under ambient conditions leads to the formation of *xerogel*, which is characterized by low porosity due to volume shrinkage between 5 to 10 times [40–42, 44]. On the other hand, *aerogels* are formed by supercritical drying which minimizes changes in the solid network ensuring low density, high pore volume, and high surface area [40–42, 44]. Instead, freeze drying reduces the shrinkage that is witnessed during spontaneous drying: the obtained product is called *cryogel* [40].

7. Annealing:

High temperature consolidation treatments are performed to remove solvent residues, to improve the structural stability and mechanical properties of the film, and to increase its adhesion to the substrate [40, 42, 43]. The chosen temperature will determine the phases, pore size, and density of the obtained xerogel [40]. For example, in titanium based sol-gels the anatase-rutile phase transformation is triggered at 600-800°C [40].

1.3.2.2. Influencing parameters

The sol-gel method is a chemical process, and as such it is susceptible to several variables, some of which are described in the following paragraphs.

Temperature and ageing time Higher reaction temperature accelerates the hydrolysis reaction of alkoxides [43]. As a consequence, the oxide network forms earlier in the process and the sol-gel requires less time to properly age. However, extended ageing might lead to particle precipitation and the loss of photocatalytic activity.

Catalyst and pH Similarly to high reaction temperatures, the presence of a catalyst accelerates the hydrolysis rate [43]. Usually, acid (e.g. HCl and HF) and basic (e.g.

ammonia) catalysts are used [43, 49]. However, it is important to note that pH highly influences the final microstructure of the sol-gel [49, 50].

Water content Higher volumes of water, up to the stoichiometric value, increase the number of alkoxide molecules that are hydrolyzed, and that can then polycondensate [43]. Hence, with higher water content the degree of crosslinking increases thus increasing the sol-gel viscosity [43]. However, when the water content exceeds the stoichiometric amount, the concentration of polycondensate is reduced, along with the solution viscosity [43]. Furthermore, during the drying step the high amounts of solvent induce high volume shrinkage and internal stresses [43].

Reagents The type of precursor, chelating agent, and solvent used to produce the sol-gel highly influence the final microstructure [43]. Countless papers have been published to determine the differences that arise when using different reagents, such as porosity, surface area, phase composition, crystallinity and so forth [31, 51–60].

1.3.2.3. Reagents

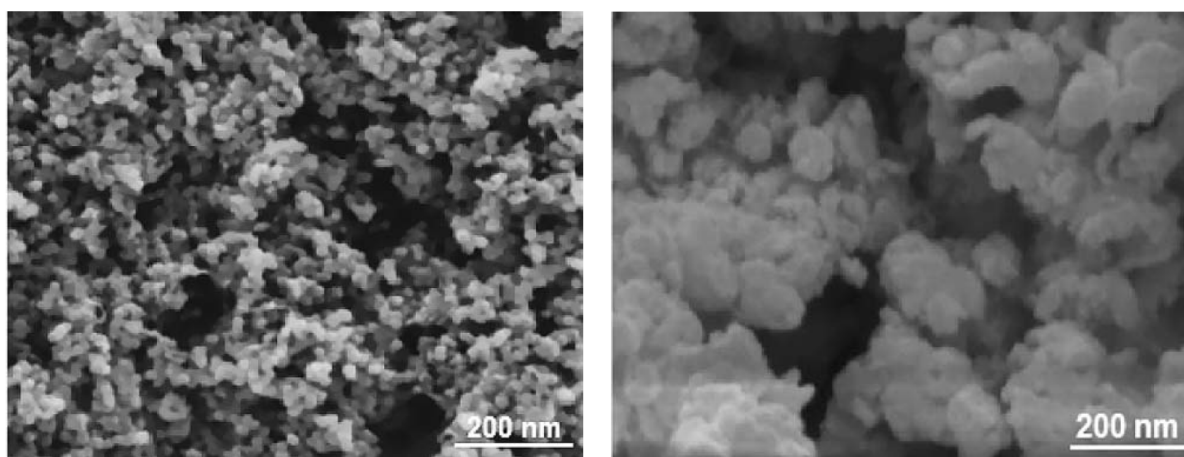
Precursor Titanium(IV) isopropoxide (TTIP) is widely reported in literature as a precursor for the production of titania based sol-gels, as it produces stable solutions at low hydrolysis ratio and it favors the production of anatase rich phases [52, 61]. Furthermore, TTIP forms TiO_2 nanoparticles with the highest surface area compared to other precursors [51]. For examples, in a comparison between TTIP and titanium n-butoxide (TBOT), the former yielded nanoparticles with higher degree of crystallinity of the anatase phase, the formation of a multiphase system where the anatase and rutile phase respectively amounted to 95% and 5%, and reduced crystallite size [31]. All these characteristics resulted in seven times higher photocatalytic activity than the nanopowder produced via TBOT [31]. Furthermore, the use of TTIP as a precursor avoids toxic by-products and chlorine contamination like it is observed with TiCl_4 [54].

Chelating agent Precursor and chelating agent react to form a stable complex which limits the available groups able to hydrolyze and condense [54]. For example, acetic acid is used to control the degree of the hydrolysis-condensation reaction and hence the oligomerization of TTIP [54–56]. The complex has the following molecular formula, where the acetate group acts as a bidentate [54]:



The limited available groups, restricted by the formation of bidentate ligands, lead to partial hydrolysis which promotes the formation of anatase, hence the final product is more favorable for photocatalysis purposes [54, 56, 57]. Complete hydrolysis, on the other hand, favors the formation of the rutile phase [54, 56]. On the other hand, replacing acetic acid with hydrochloric acid leads to a mixture of anatase, brookite, and rutile phases [56]. Indeed, the use of strong acids supports the continuous dissolution-precipitation of Ti-O-Ti bridges that favour particle agglomeration and the crystallization of the rutile phase [54, 55, 58].

As shown in Figure 1.21a and Figure 1.21b, TiO_2 nanoparticles obtained with acetic acid as chelating agent are narrow and spherical, whereas without the addition of a chelating agent, and under the same conditions, the particles are formless and highly agglomerated [55]. Increasing concentrations of acetic acid lead to smaller particles and higher surface area than non-chelated solutions [57]. However, high concentration of acetic acid are proven to be detrimental to the overall photocatalytic activity of TiO_2 , probably due to increases in the crystallite sizes [55, 58].



(a) SEM image of acetic acid modified nanopowder. (b) SEM image of nanopowders obtained without chelating agent.

Figure 1.21: Effect of chelating agent on powder microstructure [55].

Furthermore, the addition of a chelating agent improves the thermal stability of the powder [55, 58]. The complex prevents crystallization hence it triggers the rutile to anatase transition at temperatures higher than 400° [55]. Overall, the molar ratios of acetic acid and water have the highest impact on the properties of the final product than all the other process variables [58].

Solvent During sol-gel synthesis it is necessary to add a solvent to trigger hydrolysis and condensation reactions, which can be either aqueous or non-aqueous. Several organic solvents can be used, but the choice will inevitably influence the structure and morphology of the resulting film and therefore its photocatalytic activity [31, 53]. For example, it has been reported that solvents have a clear impact on particle size and the percent of anatase and rutile phase [31, 59]. Methanol, for example, highly promotes the photocatalytic activity of TiO_2 nanopowders [31], as it favors the formation of high percentages of anatase phase (95%), induces the formation of small crystallites [31, 60], as well as, higher surface roughness, larger pore size, and greater hydrophilic behavior compared to other organic solvent-modified nanopowders [60]. However, when ethanol is compared with other organic solvents it often performs as second best after methanol, thus making it a viable option for photocatalytic purposes [10, 31, 60]. Furthermore, according to safety datasheets, ethanol is a safer alternative to methanol.

Water is the more environmentally-friendly alternative, however, given the faster hydrolysis-condensation reaction rates, sol-gel synthesis is more difficult. Indeed, instantly after the addition of water, the mixture clumps and gels and it requires intervention by the operator to break up the gel and homogenize the solution. Water-based sol-gels, after a proper ageing period, tend to be more viscous than ethanol-based solutions.

2 | Materials and methods

The aim of this dissertation is to determine the self-cleaning ability of three different sol-gels. The studied solutions have already been tested for their photocatalytic activity in previous dissertations, which, however, lacked the characterization necessary to deem them self-cleaning [62]. Therefore, the solutions have been tested on different substrates assessing their adhesion and determining their wettability and photocatalytic activity. Furthermore, their self-cleaning ability was tested both in real and accelerated conditions. The ensuing paragraphs will elucidate on the synthesis of the mentioned solutions, the adopted deposition techniques, and the sample characterization methods.

2.1. Sample preparation

2.1.1. Sol-gel solutions

Three different solutions have been prepared and characterised continuing an ongoing work of previous students (Table 2.1) [62, 63].

Table 2.1: Formula of sol-gel solutions, where *WB* and *EB* stand for water- and ethanol-based solutions, respectively.

Solution ID	Precursor [g]	Solvent [g]	Chelating agent [g]
WB-1	TTIP 5.68	Distilled water 36.00	Acetic Acid 6.00
EB-1	TTIP 5.68	Ethanol alcohol 92.14	Acetic Acid 6.00
WB-2	TTIP 5.68	Distilled water 36.00	Acetic Acid 6.00

The solutions were prepared at room temperature in a beaker by slowly adding the chelating agent to the precursor. The mixture was stirred at moderate velocity, and, subsequently, the solvent was slowly added. As the addition of this reagent induces mixture gelation, it was necessary to use a spatula to break down the clumps and to ensure

the correct stirring of the solution. WB-1 and EB-1 were then covered with parafilm and stirred for 15 minutes, whereas solution WB-2 was stirred for 6 hours. Finally, the stir bar was removed and the beakers containing the solutions were sonicated for one hour while in contact with ice to prevent further gelation and formation of clumps.

An additional sol-gel solution (*EB-2*) was used as prepared by Meroni et al. [64]. This solution was only used to spray-coat titanium meshes, and as a consequence it is introduced separately from the other sol-gels. In brief, 28.13 g of titanium isopropoxide 97% were mixed with ethanol to form a 0.6 M solution. After thorough stirring, 12 mmol of HCl 37% were added to the mixture. In a separate beaker 0.47 g of Lutensol ON70 (BASF) were dissolved in 130 ml of ethanol to form a stabilizing solution, which was then poured in the sol. The so obtained solution was then stirred for one hour at room temperature, and finally deposited after ageing for 48 hours. While this solution was used as reference in a published research paper, the solutions described in Table 2.1 are environmentally friendly and were expected to yield self-cleaning coatings.

Reagents

- Titanium(IV) isopropoxide (TTIP) 97% - Sigma-Aldrich [65];
- Glacial acetic acid $\geq 99\%$ - Sigma-Aldrich [66];
- Ethanol $\geq 99.8\%$ - Sigma-Aldrich [67];
- Hydrochloric acid - Sigma Aldrich;
- Lutensol ON 70 - D-BASF, 50070761.

2.1.2. Deposition techniques

The following paragraphs are dedicated to the employed deposition techniques, namely dip-coating and spray-coating. Before coating deposition each solution was sonicated for 15 minutes, and the substrates were properly cleaned with ethanol and distilled water.

2.1.2.1. Dip-coating

The dip-coating method is one of the most used in laboratories for research purposes. Indeed, it is easy and there are few variables that influence the process, namely the immersion speed and the sample tilt angle. The dip-coater used for deposition was manufactured in-house and it is controlled by an Arduino source code file (Appendix B.1), which allows to change the pulse time [μs] and thus the immersion speed. The conver-

sion values for the two parameters are reported in Table 2.2, where ascent pulse time is indicated as longer than descent pulse time to offset the gravitational force.

Table 2.2: Unit conversion values for the dip-coater [62].

Immersion speed	$[mm\ min^{-1}]$	Ascent pulse time	$[\mu s]$	Descent pulse time	$[\mu s]$
60		12 577		10 375	
120		5 280		5 040	
180		3 180		3 302	
240		2 217		2 447	

However, it was not necessary to vary the parameters as previous studies stated that an immersion speed of $120\ mm\ min^{-1}$ consistently yielded samples with the highest photocatalytic activity [62]. The samples were secured to the dip-coater with a 90° tilt angle, and they were coated twice, making sure that the surface was completely dry before applying a new layer. The samples were then dried horizontally for 5-20 minutes depending on the employed solution. One of the disadvantages associated with this method is the limit on the sample dimension, due to the size of the dip-coater and the size of the beakers. Therefore, only 2.5 cm x 2.5 cm samples could be used.

2.1.2.2. Spray-coating

Dip-coating has been extensively used in previous dissertations to deposit sol-gels on glass substrates. However, spray-coating is a more suitable deposition method for large surfaces, e.g. windows; furthermore, the necessary equipment can be easily transported to the site of interest. The technique is versatile, meaning that the deposition parameters can be adapted according to the surface to be coated and the employed solution. For these reasons, the author proposed to compare the properties of dip-coated and spray-coated samples, as to understand whether significant differences arise. To this purpose, a dual action airbrush compressor kit (Abest, AC06-32K) was employed with the following operating variables:

- during deposition the spray-gun nozzle was kept at about 10 cm from the substrate surface. However, as the solutions have different viscosity, the author recommends finding the ideal distance for each solution;
- the air compressor operated at its maximum capacity: 25 PSI (≈ 1.7 bar). Although

the air pressure is adjustable, the air compressor does not provide information on the actual outlet pressure. As a consequence, to ensure repeatability, it was decided to use it at its maximum capacity;

- to better compare the results with the dip-coated method, the samples were kept vertically during deposition and they were dried horizontally;
- the samples were coated twice on each side, ensuring that the previous coating was completely dry before applying a new layer;
- to guarantee uniform deposition the solution was sprayed following a zigzag pattern, as showed in Figure 2.1;

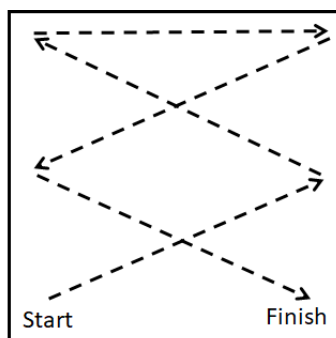


Figure 2.1: Spray-coating deposition pattern.

- the deposition was carried out as long as it was necessary to cover the whole surface, without allowing the solution to pool;
- the substrate was always kept at room temperature.

The method was used to coat glass samples (2.5 cm x 2.5 cm), PMMA samples (2.5 cm x 2.5 cm and 10 cm x 7.5 cm), and titanium mesh samples (5 cm x 15 cm).

2.1.3. Annealing

Thermal treatment was necessary to crystallize the deposited amorphous TiO_2 , to increase its adhesion to the substrate, and to further remove solvent residues. Glass and titanium samples were annealed for two hours at 500°C in a muffle furnace (Zetalab, Z-A) as, according to previous dissertations, this treatment results in high photocatalytic activity [62]. As PMMA is characterized by low glass transition temperature ($85\text{-}165^\circ\text{C}$) it was necessary to adopt an alternative thermal treatment [68]. Since the product details of the purchased PMMA sheets specified the softening point at 105°C , it was decided to perform annealing tests at 90°C for two, three, and four hours. The temperature was chosen as

to be as close as possible to the softening point, both to avoid sample deformation due to the release of internal stresses and to optimize the benefits of the thermal treatment. Therefore, PMMA samples were annealed at 90°C for two, three, and four hours in a thermostatic oven (Galli, M710) to determine the most effective treatment. The same treatment was then repeated on glass to serve as a reference.

2.1.4. Corona treatment

Coatings should be highly adherent to the surface to ensure long service life, performance, and avoid release of fragments, as the nanoparticles which constitute the coatings are potentially toxic to the environment. Therefore, PMMA samples (2.5 cm x 2.5 cm) were subjected to corona treatment, aimed at increasing the hydrophilicity of the surface in order to promote the adhesion of the coating. Four samples per solution (Table 2.1), aged for about 190 days, were prepared. Half of them were annealed for two hours at 90°C, to determine whether the benefits of the corona treatment could supplement the benefits of annealing.



Figure 2.2: Corona treatment.

To this purpose, a handheld and portable corona plasma treater (Electro-Technic Products, BD-20AC) was employed operating at about 25 000 V with an output frequency of 4.5 MHz (Figure 2.2). Twelve PMMA samples were treated for one minute on each side, making sure to evenly treat the whole surface. Within 30 minutes from the treatment, the samples were spray-coated.

2.1.5. Titanium meshes

Two commercially pure grade 2 ASTM titanium meshes were prepared to assess the photocatalytic activity difference between two different types of immobilized TiO_2 semiconductors. One was anodized to obtain nanotubes, while the other was spray-coated with *EB-2*, whose formula is reported in Chapter 2.1.1.

2.1.5.1. Anodized mesh

Two titanium mesh strips (15 cm x 2.5 cm) were cleaned by sonication for 15 minutes in ethanol and for 5 minutes in distilled water. Once completely dry, each titanium strip was anodized for 30 minutes at 45 V with a linear ramp of 2.0 V min^{-1} (Potentiostat LTC-Caoduro). The employed anodizing solution is described in Table 2.3.

Table 2.3: Employed reagents for the anodizing solution.

Reagent	Molarity [mol l^{-1}]	Weight [g]
Ethylene Glycole	17.23	532.38
Distilled Water	2.00	18.00
NH_4F	0.20	3.70

The sample was then gently rinsed with distilled water and dried vertically at room temperature. Finally, the sample was annealed for two hours at 500°C . Before starting photocatalysis tests, the two strips were tied together with three titanium wires (Figure 2.3).

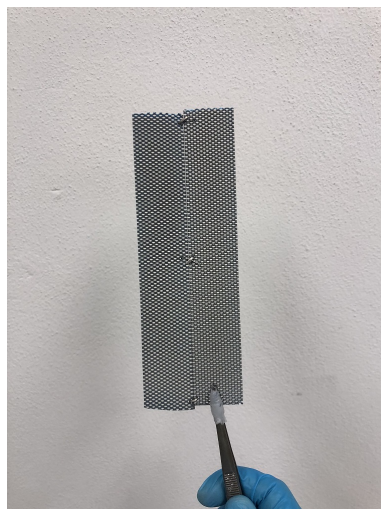


Figure 2.3: Anodized mesh sample.

2.1.5.2. Spray-coated titanium mesh

Two additional mesh strips were properly cleaned and spray-coated twice with solution *EB-2*, which is described in Chapter 2.1.1. Nitrogen gas was used to dry the meshes to ensure quick drying and avoid the influence of air moisture on the coating morphology. Finally, the strips were annealed at 500°C for two hours, and tied together with titanium wires.

2.2. Characterization techniques

2.2.1. Photocatalytic tests

The following paragraphs illustrate the set-ups which were employed to determine the photocatalytic activity of coatings deposited on glass, PMMA, and titanium samples. To this purpose, their efficiency was measured by monitoring the light-induced degradation of pollutants, such as rhodamine B and tetracycline.

Rhodamine B is a fluorescent dye commonly used in photocatalysis tests to determine the efficiency of semiconducting catalysts. Although the standard recommends the use of methylene blue [69], this proved to be too unstable to make comparable photocatalysis predictions. Furthermore, literature often reports the use of rhodamine B in photocatalytic experiments [70–73], as it is a common pollutant found in wastewater [74]. Indeed, rhodamine B is used in several industries, including paper, plastic, and most importantly textile [74]. Its use is prohibited in food industries as it is mutagenic and carcinogenic, but it is nonetheless found in wastewater posing both environmental and health risks [74].

Tetracycline is a broad-spectrum family of antibiotic drugs commonly used in human and animal therapy [75]. However, only 20-50% is correctly metabolized while the remainder accumulates in wastewater systems [75]. Tetracycline pollution in water systems is an hazard to both human and environmental health, as it increases bacterial resistance and causes ecological imbalances in the environment by causing fluctuations in soil and water microflora [75]. As both pollutants are not easily degradable in the environment, researchers are focused on finding suitable photocatalysts and degradation techniques.

2.2.1.1. Photodegradation of rhodamine B

The batch reactor employed to test glass and PMMA samples (2.5 cm x 2.5 cm) consists of a 100 ml beaker and a 3D printed PLA support, which not only isolates the solution from the environment but also supports the LED necessary for UV irradiation. The employed LEDs (Nichia, NCSU033C UV SMD LED), whose dimensions are 6.8 mm x 6.8 mm x 1.93 mm, emit 750 mW at 365 nm (Figure 2.4) [76].

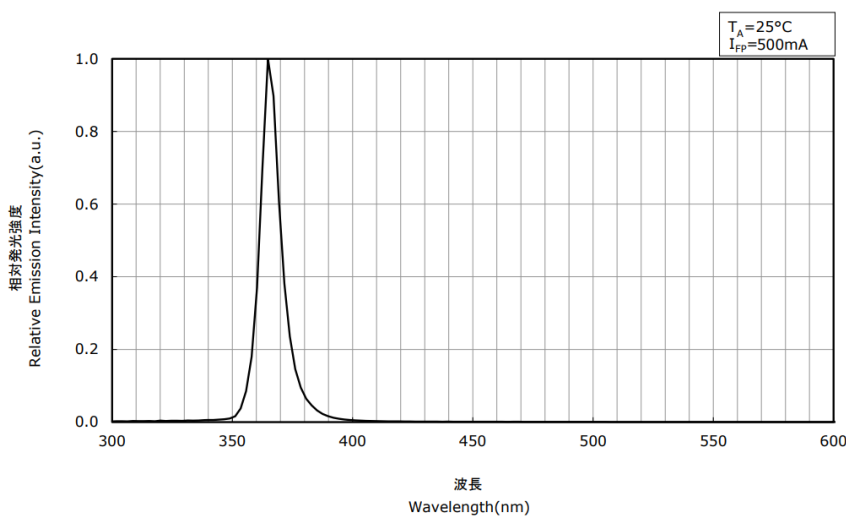


Figure 2.4: Emission spectrum of employed UV-LED [76].

As LED emission is highly directional (Figure B.1), the sample surface was placed parallel to the LED at about 3 cm with the aid of a titanium net, which also kept the sample 0.5 cm below liquid level (Figure 2.5). Each beaker was filled with 40 g of 10^{-5} M rhodamine B aqueous solution to test the degradation efficiency of coatings deposited either on glass or PMMA. As the reaction occurs close to the double layer of the surface, it is necessary to continuously stir the solution to guarantee uniform and efficient degradation, therefore each beaker was equipped with a stir bar and was placed on a magnetic stirrer (VELP Scientifica, F203A0177). As the magnetic stirrer provided six positions each photocat-

alytic session allowed to test six samples simultaneously, therefore six batch reactors were connected in series and powered by a general-purpose potentiostat (AMEL Instruments, 2049) operating at 0.5 A in galvanostatic conditions.

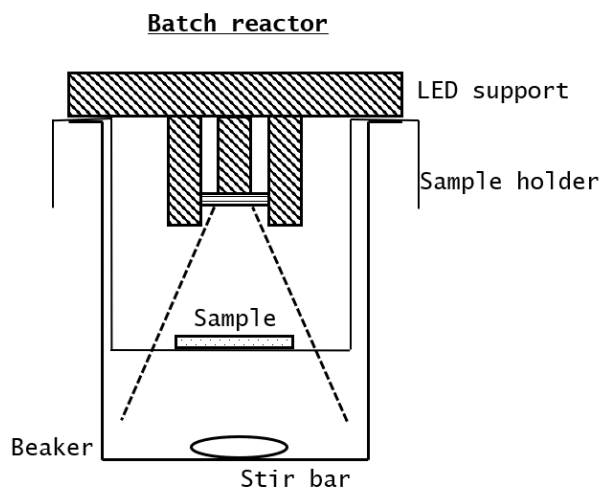


Figure 2.5: Design of the employed batch reactor.

To ensure that every sample received the same irradiation during the photocatalytic tests, the LEDs were switched on different beakers every hour. The test was carried out for six hours withdrawing about 3 ml every hour to measure the absorbance with a spectrophotometer (Thermo Scientific, Spectronic 200). The values were taken at the peak of rhodamine B absorption spectrum, i.e. 555 nm. Each withdrawn sample was then poured back in the corresponding beaker.

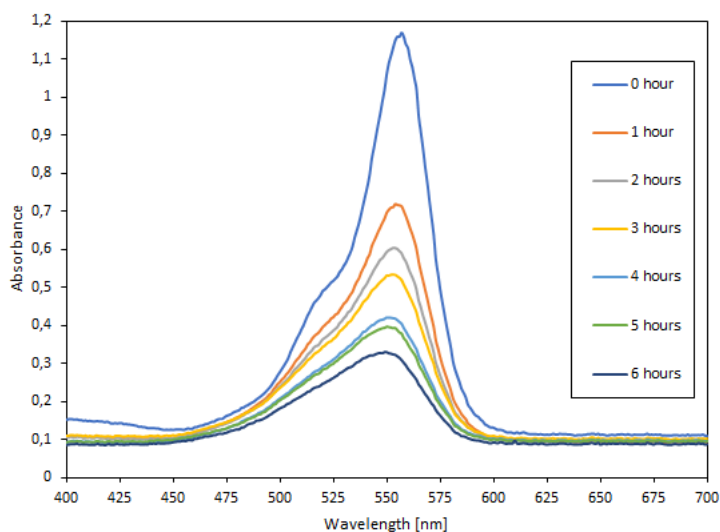


Figure 2.6: Absorbance spectrum of degrading rhodamine B.

As Figure 2.6 shows, during the test the absorbance peak gradually decreases indicating the successful degradation of the dye. By knowing the absorbance value it is possible to derive the variation of dye concentration in time through the Lambert-Beer law, which correlates the absorbance (A) to dye concentration (C), its molar attenuation coefficient (ϵ), and light pathlength (l):

$$A = \epsilon \cdot C \cdot l \quad (2.1)$$

As ϵ is considered constant for every material at a given wavelength, and as l is constant given the test conditions, it is possible to obtain the percentage concentration variation in time:

$$\Delta C[\%] = \frac{C - C_0}{C_0} \% = \frac{A - A_0}{A_0} \% \quad (2.2)$$

Most importantly, adopting the Langmuir-Hinshelwood kinetics, it is possible to derive the reaction rate constant (k). Indeed, the graph obtained by plotting $\ln(CC_0^{-1})$, where C_0 represents the initial dye concentration, against time is a linear graph, whose slope is equal to k [77].

$$\ln\left(\frac{A}{A_0}\right) = \ln\left(\frac{C}{C_0}\right) = -k \cdot t \quad (2.3)$$

Langmuir-Hinshelwood kinetics, which describes pseudo-first-order reactions, is commonly used to explain the kinetics of heterogeneous catalytic processes [77]. The values of k were obtained by applying the REGR.LIN function in the Italian version of Excel (which is equivalent to the LINEST function in the English version), with the constant term equal to zero.

2.2.1.2. Photodegradation of tetracycline

Photocatalytic tests were also carried out on titanium meshes to compare the performance of sol-gel coatings and anodized TiO_2 . The photocatalytic activity of the samples was assessed by monitoring the degradation of 20 ppm tetracycline solutions, which were prepared either in MilliQ-water or in a complex water matrix which simulates tap water (Table 2.4).

Table 2.4: List of reagents necessary to synthesize two liters of the tap water solution [78].

Salt	Molarity [$mol\ l^{-1}$]	Weight [g]
$NaHCO_3$	$4 \cdot 10^{-3}$	0.3360
$MgSO_4(7H_2O)$	$0.76 \cdot 10^{-3}$	0.1873
$CaCl_2$	$2.24 \cdot 10^{-3}$	0.2486

Before every photocatalytic test the titanium meshes were exposed to UV irradiation for 30 minutes on each side to activate the semiconductor. An HG 500 UV lamp with a maximum emission peak at 365 nm was used, as it was positioned at about 40 cm from the sample it irradiated about $120\ Wm^{-2}$ [79]. The mesh was then placed in a jacketed photocatalytic reactor with 500 ml of the aforementioned solution, which was magnetically stirred for the whole test to ensure its homogeneity, and was kept at a constant temperature of $25^\circ C$ with the aid of a heated immersion circulator (ThermoScientific, Haake E52) (Figure 2.7). To enhance the degradation of tetracycline, the solution was oxygenated at a rate of $5\ nL\ h^{-1}$.

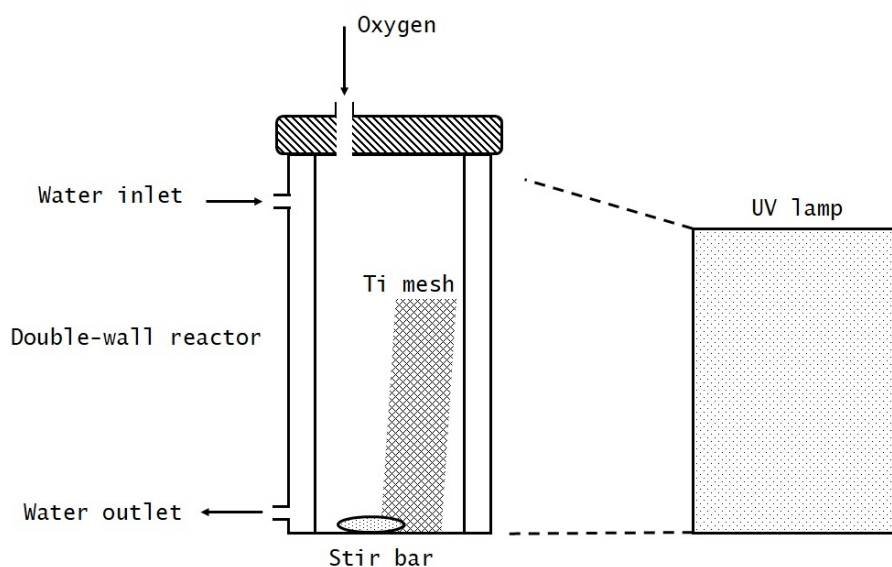


Figure 2.7: Set-up of photocatalytic test.

In the first 30 minutes of the test the reactor is kept in the dark to to achieve adsorption-desorption equilibrium. Following adsorption, the reactor is irradiated with a HG 500 UV lamp placed at about 20 cm from its axis. To evaluate the photocatalytic activity,

5 ml of the solution are drawn at 0, 10, 20, 30, 45, and 60 minutes in the first hour, and then once every hour up to 240 minutes. The samples are then analysed with a UV-VIS spectrophotometer (Shimadzu, UV-2600 240V IVDD) obtaining the absorption spectrum from 200 to 800 nm. The data was analyzed through the Lambert-Beer law and by adopting pseudo-first order kinetics as explained in Chapter 2.2.1.1.

To evaluate the mineralization efficiency of the mesh, 20 ml were drawn every hour and analyzed with a Total Organic Carbon Analyzer (Shimadzu, TOC-VCPN). The calibration curves needed for the TOC are reported in appendix B (Figure B.2, Figure B.3, and Figure B.4). As a consequence, at the end of the photocatalytic test 355 ml of the initial solution were left in the reactor, and the mesh sample was not completely submerged anymore. Data was collected both by Non-Purgeable Organic Carbon (NPOC) and Total Organic Carbon (TOC) mode: the former is more suitable when testing solutions in complex water matrix, as TOC may overestimate organic carbon content in the presence of high dissolved inorganic carbon. Mineralization (Min.%) was computed as follows, where X denotes either NPOC or TOC values and X_0 represents the initial value:

$$Min.\% = \frac{X - X_0}{X_0} \% \quad (2.4)$$

Mineralization error was computed according to the rules of propagation of uncertainty:

$$\frac{\sigma_{Min.\%}}{Min.\%} = \sqrt{\left(\frac{\sqrt{\sigma_0^2 + \sigma_x^2}}{y_0 - y_x}\right)^2 + \left(\frac{\sigma_0}{y_0}\right)^2} \quad (2.5)$$

σ represents the standard deviation, y stands for the actual measurement, the subscript $_0$ and $_x$ respectively stand for the initial and current measured value. Equation 2.6 shows the relation between TOC (or NPOC) values and tetracycline concentration (C):

$$C [ppm] = \frac{X/12}{22} \cdot 444.435 \quad (2.6)$$

Where, 22 is the number of carbon atoms in tetracycline, whose molecular mass is $444.435 \text{ g mol}^{-1}$, and 12 is the average atomic mass of carbon. Following the test, the mesh was cleaned with Milli-Q water and placed under UV irradiation for 30 minutes on each side to remove leftover adsorbants, such as tetracycline and its intermediate degradation products.

2.2.2. Wettability tests

As mentioned in previous chapters, self-cleaning surfaces rely on specific wetting properties, namely hydrophilicity and hydrophobicity. Consequently, WCA tests were crucial to understand the self-cleaning ability of the analysed coatings. The test was performed on dip-coated glass, spray-coated glass, and spray-coated PMMA (2.5 cm x 2.5 cm). The aim was not only to determine the wettability of the coatings, but also to determine whether substrate material, deposition technique, and thermal treatment influence the values of static water contact angle. To evaluate the expected photoinduced hydrophilicity, each sample was irradiated by UV light for 30 minutes on each side. Preliminary tests were carried out on dip-coated glass samples by measuring the WCA before and after UV irradiation (0.5 mW cm^{-2} emitted by a Disano, 6401 Rapid System lamp). Further tests were instead carried out by using a lamp designed to simulate sunlight to better reproduce real conditions: the emission intensity in the UV-A range is about 1.1 mW cm^{-2} (Osram, Ultra Vitalux 300 W 230 V E27). Photoinduced hydrophilicity was thus monitored by taking measurements every 20 minutes for one hour. Following irradiation, the samples were placed in dark conditions monitoring the recovery of the initial water contact angle. Specifics on deposition technique, thermal treatment, and sol-gel aging time are summarized in the corresponding result chapters.

The test was performed following the directives in the BS EN 15802:2009 standard [80], which instructs to use distilled water, to place the sample on a horizontal surface, and to deposit water drops with a micro-pipette as the required volume is comprised between 5 and 10 μl . After deposition the drops were photographed showing the three-phase interface.

The reported WCA values were obtained from the average of three measurements performed on each sample. Each measurement was carried out via a plugin of ImageJ (Java 1.8), a software widely used in the scientific field for image processing. The plugin was made available by the *Biomedical Imaging Group of the École Polytechnique Fédérale de Lausanne* [81], along with the instructions to use it. Before employing it a few tests were carried out to assess whether the tool yielded reliable results: three arbitrary papers on WCA measurements were downloaded and the WCA was measured with the plugin [82–84]. As the percentage change between the reported and the measured WCA is below 2.7%, the tool was considered appropriate. Figure 2.8 shows the software interface and how the WCA is measured. The aim is to adjust the toggles, that vary height, diameter, and position, so that the green line follows the drop outline.

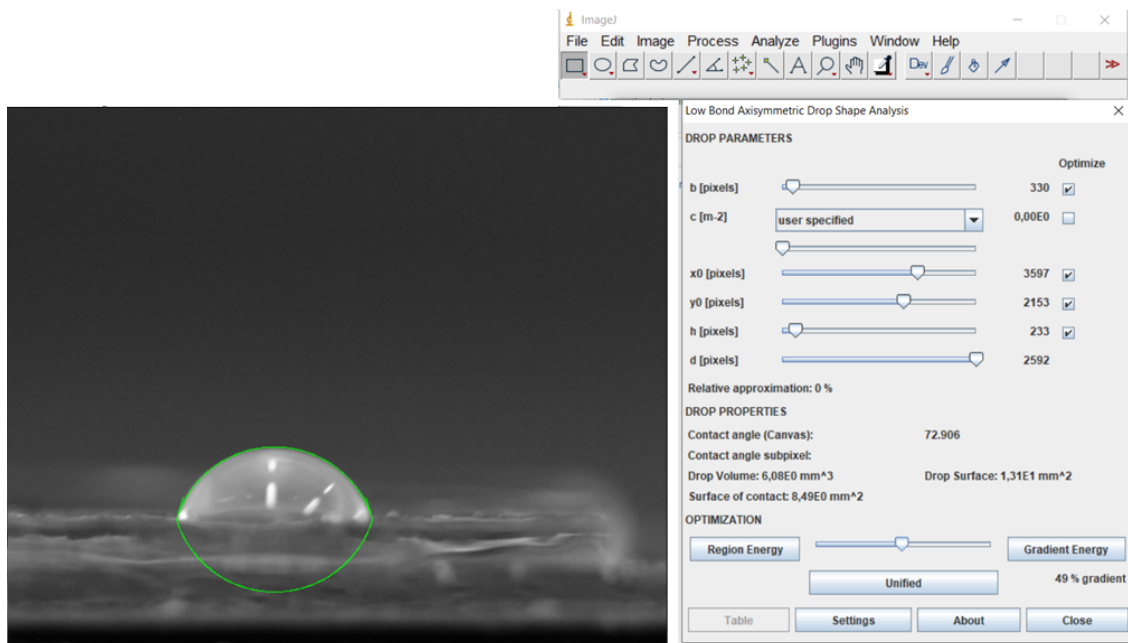


Figure 2.8: ImageJ software interface.

Thanks to a collaboration with Università degli Studi di Milano Statale it was possible to use a Krüss EasyDrop analyzer to photograph high quality images of distilled water drops ($5 \mu l$) deposited on spray-coated glass samples. The photographs were taken before and after irradiation, which was carried out for one hour with a HG 500 UV lamp emitting about $120 mW cm^{-2}$ [79].

2.2.3. Soiling tests

2.2.3.1. Colorimetry theory

Colorimetry replaces the subjective response to colour with an objective numerical system, allowing the standardization of colour measurements [85]. Indeed, mere sample observation does not allow for objective colour description as the results highly depend on light source, on the observer, and obviously on the optical properties of the material [85]. As humans have three different cone cells able to define colours as a mixture of red, green, and blue, the CIE (Commission Internationale de l'Éclairage) used to express colour in the RGB space [85]. However, to better approximate human vision the CIE defined a new space: CIELAB [85]. The space is represented by three color coordinates, which are mathematically defined from the absorbance spectra of human cone cells [86].

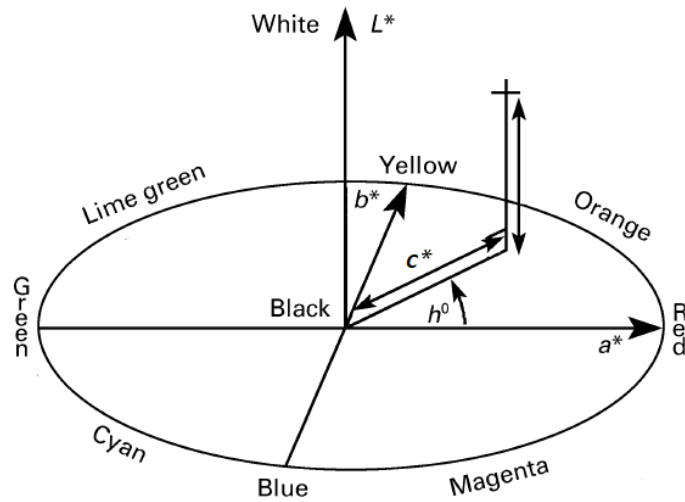


Figure 2.9: Representation of Cartesian and polar coordinates in the CIE $L^*a^*b^*$ color space [85].

Figure 2.9 represents the CIELAB color space, identified by the following coordinates:

- L^* identifies the lightness, it ranges on a 0 to 100 scale, which correspond to pure black and pure white, respectively [86];
- a^* indicates the red-green component of color, where negative values represent green hues while positive values represent red hues [86];
- b^* indicates the yellow-blue component, hence yellow hues for positive values and blue hues for negative ones [86].

From these values it is possible to identify two other parameters useful for color description [87]:

1. Chroma, defined in Equation 2.7, is often used interchangeably with saturation and it describes the intensity and the colorfulness of a color.

$$C^* = \sqrt{a^{*2} + b^{*2}} \quad (2.7)$$

It ranges from 0 to 100, which correspond to dull and intense colors [87], respectively. For example, values between 0 and 5 identify neutral grey colors [85].

2. Hue describes the hue angle in the CIELAB space (Equation 2.8).

$$H^* = \tan^{-1} \frac{b^*}{a^*} \quad (2.8)$$

Each angle range identifies the dominant hue of the surface:

- $0 < H^* < 90^\circ$: red hue;
- $90^\circ < H^* < 180^\circ$: green hue;
- $180^\circ < H^* < 270^\circ$: blue hue;
- $270^\circ < H^* < 360^\circ$: purple hue.

To monitor the color difference that occurs after coating deposition and soiling, it is necessary to evaluate the Euclidean distance between two points in the 3D space (Equation 2.9) [85, 87].

$$\Delta E = \sqrt{(\Delta L^*)^2 + (\Delta a^*)^2 + (\Delta b^*)^2} \quad (2.9)$$

For $\Delta E < 1$, the color difference in grayscale images is not perceptible by human eye; whereas, the same holds true for any other color for $\Delta E < 3$. Hence, for $\Delta E < 1$ colors match.

To acquire the necessary CIELAB coordinates a spectrophotometer is needed. Spectrophotometers with an integrating sphere work according to two operating modes: Specular Component Included (SCI) and Specular Component Excluded (SCE). SCI includes both diffused and specular reflectance, which is the reflected light from the specimen that has the reflection angle equal to the incident angle [88]. To obtain the SCE values, the specular light is excluded by a light trap in the spectrophotometer [89]. It is thus necessary to specify whether the values have been obtained through the SCI or the SCE mode. The SCI mode measures the true color of the surface, as it is unaffected by the surface conditions [88]: thus, two objects painted with the same dye but with different surface finish generate the same coordinates in the color space. As a consequence, the SCI mode does not simulate the surface appearance as perceived by the human eye. On the other hand, the SCE mode is more sensitive to surface roughness and thus it is an objective alternative to visual inspection [88], according to which matte surfaces appear duller, and thus lighter, than glossy ones. In this dissertation both SCE and SCI values have been reported to better evaluate the color change that surfaces undergo following coating deposition and soiling. In the author's opinion the SCE values are more suitable to this application as human perception of the surface is paramount in the context of

self-cleaning surfaces, as ideally they should maintain the same aesthetic appearance and degree of transparency.

In this dissertation a portable spectrophotometer (Konica Minolta, CM-2500d), equipped with SpectraMagic NX software, was used to collect CIELAB coordinates both in SCI and SCE method. As the employed substrates are transparent, printing paper has been used as a background to collect data. The results are reported in terms of ΔE (Equation 2.9) to indicate color variation during soiling tests. To better understand which parameter affects the color variation the most, the results have also been reported as ΔL^* , Δa^* , and Δb^* . The color variations resulting from coating deposition and thermal treatment were computed as the change between the parameters collected before and after the process, as displayed in Equation 2.10 and Equation 2.11, where X stands for the coordinate taken into consideration.

$$\Delta X = X_{coated} - X_{uncoated} \quad (2.10)$$

$$\Delta X = X_{annealed} - X_{coated} \quad (2.11)$$

2.2.3.2. Accelerated soiling tests

Tests in real conditions are time-consuming, therefore an accelerated soiling test was designed to obtain faster results that could be used as preliminary test in the future. The test was performed by employing a soiling solution designed by Mokhtarifar et al. to simulate the soiling of metallic roofings in highly polluted areas and assess the self-cleaning behavior of coated samples [90]. The adopted soiling solution was composed of the following mixtures:

- 12 vol% carbon black mixture, obtained by mixing 1 g of carbon black in 200 ml of distilled water;
- 36 vol% of humic acid mixture, obtained by mixing 1 g of humic acid in 200 ml of distilled water;
- 24 vol% of salt mixture, obtained by mixing 1 g of NaCl, Na₂SO₄, and CaSO₄·2H₂O in 200 ml of distilled water;
- 28 vol% of dust mixture, obtained by mixing 1 g of bentonite and montmorillonite in 200 ml of distilled water.

The so obtained solution should be magnetically stirred before every soiling test to ensure

homogeneity and correct composition. The test was performed on dip-coated glass samples (2.5 cm x 2.5 cm) with solutions aged for about 110 days. The samples were then subjected to UV irradiation for two hours ($0.5 \mu W cm^{-2}$) to activate the surface. Following irradiation, the specimens were immersed in the just mentioned soiling solution at $120 mm min^{-1}$ with the aid of a dip-coater and an inclination angle of 10° . The samples were then dried horizontally in room conditions. To evaluate the degree of soiling L^*a^*b values have been acquired before and after soiling.

2.2.3.3. Natural soiling

To determine the self-cleaning ability of the coatings, 12 samples were exposed outdoors from October (2022) to April (2023). Indeed, in Italy heating systems are turned on around October, hence a higher concentration of PM10 in air was expected which would enhance the soiling of the samples (Figure 2.10).

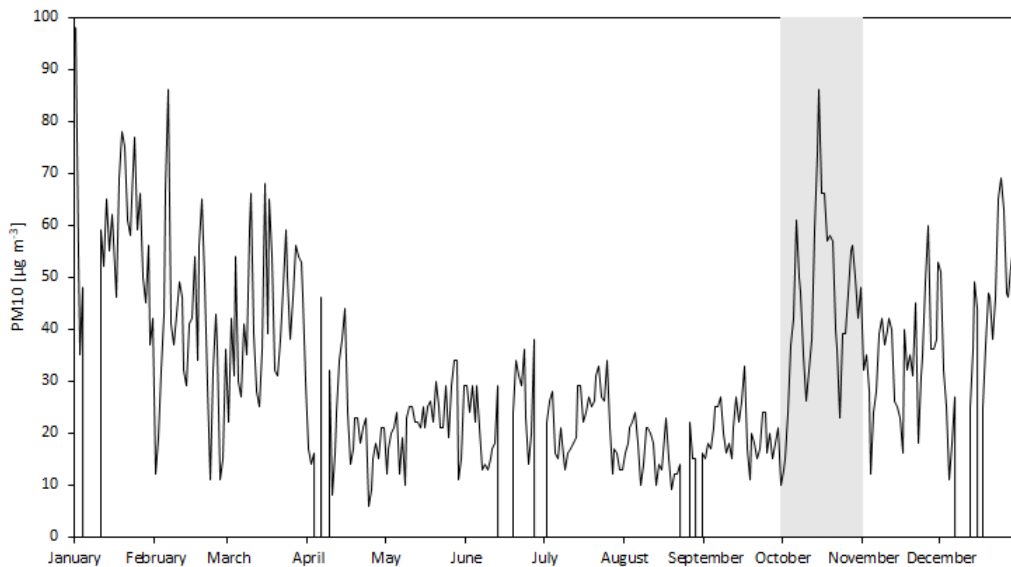


Figure 2.10: Evolution of PM10 concentration in air in 2022.

The samples were fixed on a rack inclined at 45° and facing south, so that they were exposed to cycles of shadow, direct sunlight, and precipitations (Figure 2.11b).

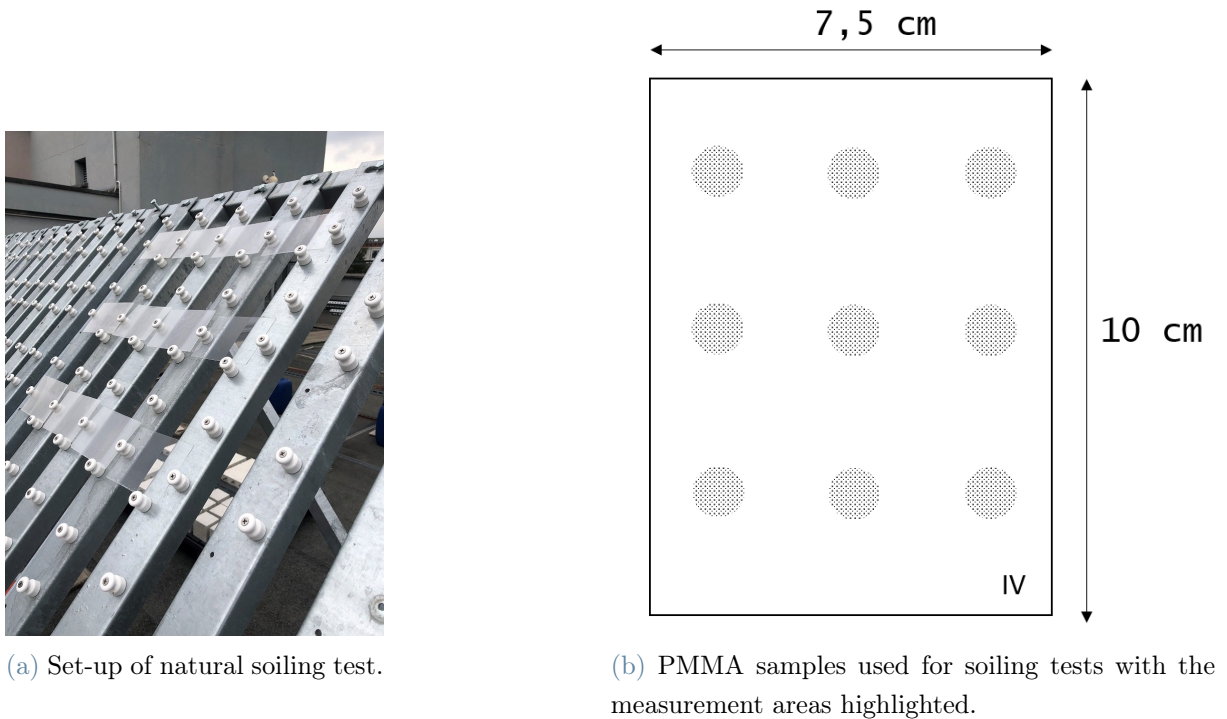


Figure 2.11: Set-up and samples used for the natural soiling tests.

To this purpose, each solution reported in Table 2.1, and aged for about 160 days, was sprayed on three PMMA samples (10 cm x 7.5 cm). The samples were then annealed for two hours at 90°C, numbered, and placed on the rack. Three samples were left uncoated as reference. The color of the sample's surface was monitored weekly by taking nine measurements with a portable spectrophotometer (Konica Minolta, CM-2500d) equipped with the SpectraMagic NX software (Figure 2.11a).

The self-cleaning ability was evaluated in terms of color difference, i.e. ΔE in accordance with colorimetry theory. To determine which meteorological factors have a higher influence on the coating performance, data were compared with values of relative humidity [%] (Figure 2.12), precipitation [mm] (Figure 2.13), temperature [°C], and global radiation [$W m^{-2}$] (Figure 2.14). However, temperature is highly correlated with global radiation hence it has been discarded as it did not provide further insight on the self-cleaning ability of the samples. The mentioned data was obtained through a direct request to INEMAR-ARPA Lombardia. Meteorological data was collected from the weather station located on *Via Juvara*, while PM10 data was collected from the *Milano Pascal Città Studi* weather station.

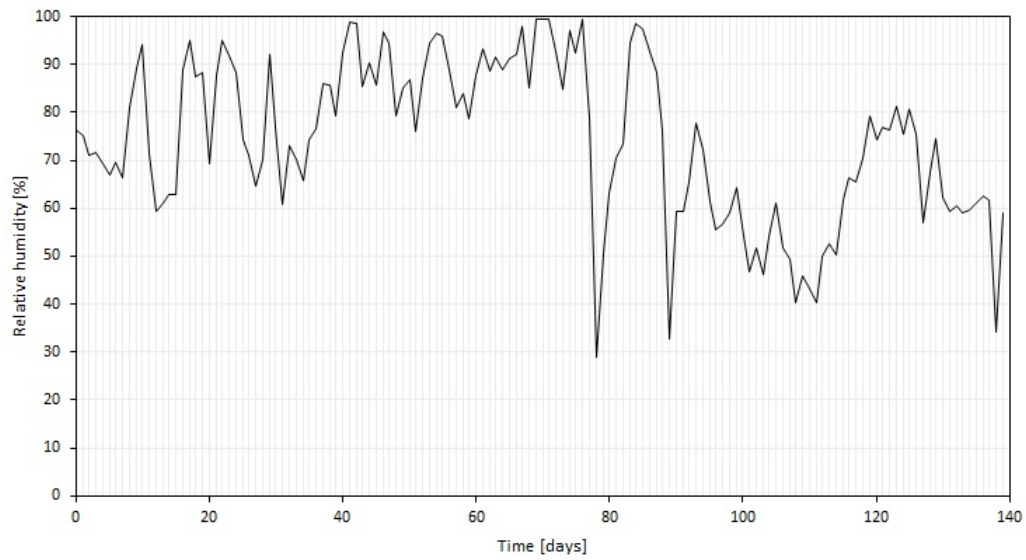


Figure 2.12: Relative humidity data acquired during the natural soiling test.

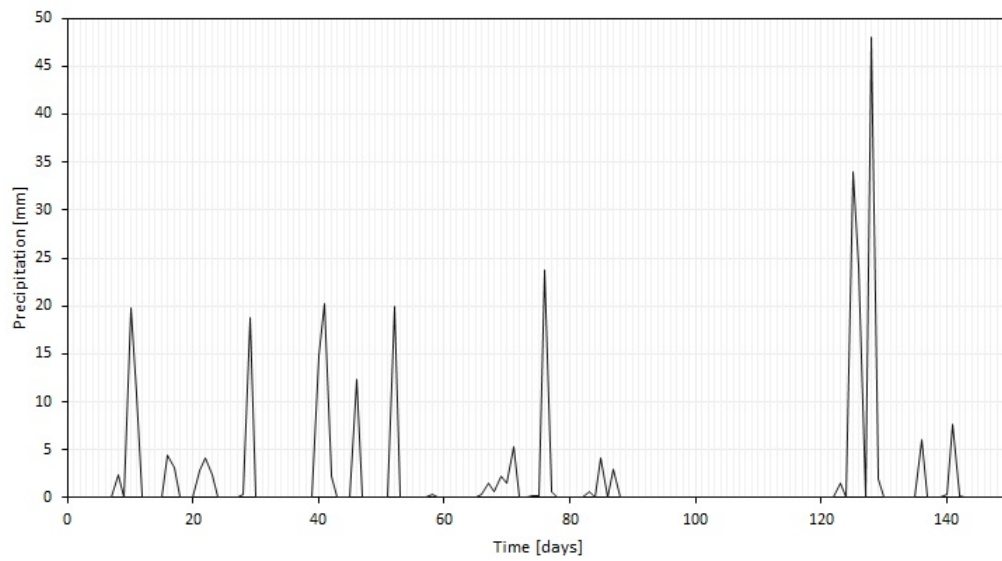


Figure 2.13: Precipitation data acquired during the natural soiling test.

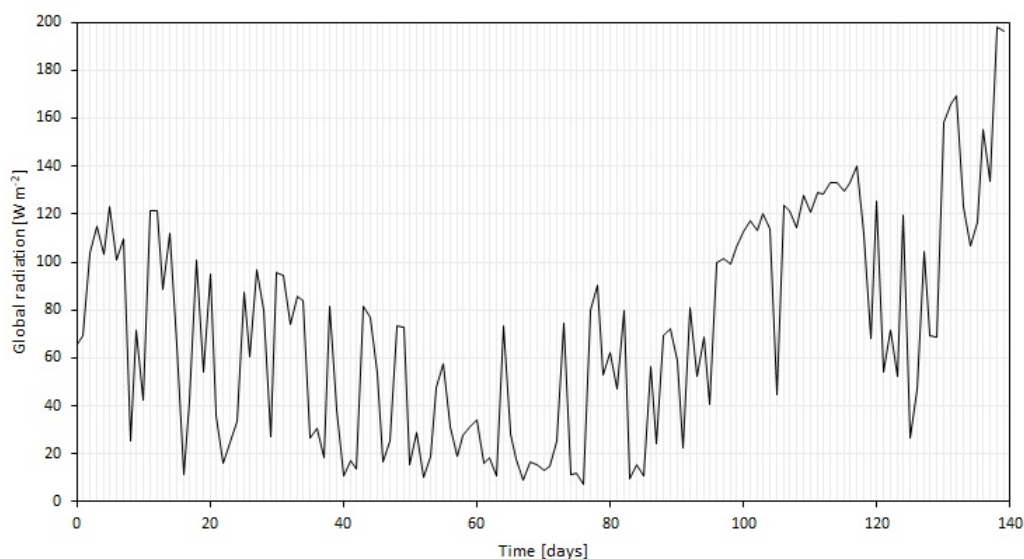


Figure 2.14: Global radiation data acquired during the natural soiling test.

2.2.4. Adhesion tests

For the product to be marketable it is necessary to assess the adhesion of the coating to the substrate. Correct adhesion would provide multiple benefits including, but not limited to, low maintenance costs, high efficiency, and high durability. Last but not least, it would avoid loss of coating particles in the environment that would require filters to prevent water contamination. The author proposed to run adhesion tests as the coating flaked during routine sample handling and it was visibly worn after photocatalytic experiments.

As quantitative methods were not accessible, the author carried out qualitative tests, such as the cross-cut and the X-cut test, which are evolutions of the tape-and-peel test [91]. The ASTM D3359 standard, albeit aimed at the adhesion assessment of ductile coating films to metallic substrates, was chosen. The standard itself states that the reported methods have been used by researchers to measure adhesion of coatings on non-metallic substrates [91–93]. The drawback is that the error, precision, and bias data resulting from non-metallic substrates have not been studied, and thus the standard is theoretically only aimed at metallic ones [91]. As the test result is qualitative and highly dependent on several parameters including the operator, the standard recommends that the variables and employed method should be decided by the interested parties [91]. These tests evaluate lower levels of adhesion, are economical, and quick to perform, however they are highly subjective and their ranking does not make fine distinctions between adhesion levels.

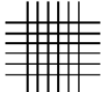
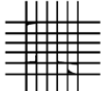
The standard introduces two methods that are performed equivalently, but for the incision

pattern performed by the operator. The *X-cut adhesion test* is intended for use in the field, however it was carried out as a trial for the set-up of the more appropriate *cross-cut test*. Before the test, the coated samples were cleaned with compressed air to remove any flakes and dust that could hinder the success of the experiment. According to the standard, the X-cut was performed with a snap-off blade making two cuts about 40 mm long with an incident angle between 30° and 45° [91]. Both the X-cut and the cross-cut test require that a piece of pressure sensitive tape (25 mm wide) should be firmly pressed on the surface ensuring homogeneous contact with the substrate [91]. In the X-cut test the tape should be running in the same direction as the smaller angles. Within a minute of application the tape should be quickly removed by pulling the free end at 180° [91]. For both testing methods, the surface has to be closely inspected by the operator who should make note of the coating areas that have been removed [91]. Accordingly, the operator will rate the adhesion following the instructions reported on the rankings in Figure 2.15 and Figure 2.16 [91]. The test should then be repeated on two more samples to estimate repeatability [91].

5A	No peeling or removal,
4A	Trace peeling or removal along incisions or at their intersection,
3A	Jagged removal along incisions up to 1.6 mm ($\frac{1}{16}$ in.) on either side,
2A	Jagged removal along most of incisions up to 3.2 mm ($\frac{1}{8}$ in.) on either side,
1A	Removal from most of the area of the X under the tape, and
0A	Removal beyond the area of the X.

Figure 2.15: Classification of X-cut test results [91]

Concerning the cross-cut test, the standard differentiates the testing method according to the thickness of the coating: below 50 μm and between 50 μm and 125 μm [91]. The former instructs the operator to make eleven parallel cuts 1 mm apart, while the latter specifies to make six cuts 2 mm apart. Figure 2.16a depicts the final appearance of the samples [91]. The cuts should be 2 cm long and deep enough so that the substrate is clearly visible [91].

CLASSIFICATION OF ADHESION TEST RESULTS		
CLASSIFICATION	PERCENT AREA REMOVED	SURFACE OF CROSS-CUT AREA FROM WHICH FLAKING HAS OCCURRED FOR SIX PARALLEL CUTS AND ADHESION RANGE BY PERCENT
5B	0% None	
4B	Less than 5%	
3B	5 - 15%	
2B	15 - 35%	
1B	35 - 65%	
0B	Greater than 65%	

(a)
(b)

5B The edges of the cuts are completely smooth; none of the squares of the lattice is detached.

4B Small flakes of the coating are detached at intersections; less than 5 % of the area is affected.

3B Small flakes of the coating are detached along edges and at intersections of cuts. The area affected is 5 to 15 % of the lattice.

2B The coating has flaked along the edges and on parts of the squares. The area affected is 15 to 35 % of the lattice.

1B The coating has flaked along the edges of cuts in large ribbons and whole squares have detached. The area affected is 35 to 65 % of the lattice.

0B Flaking and detachment worse than Classification 1B.

Figure 2.16: Classification of cross-cut test results [91].

A total of 12 samples were prepared, half of which intended for either the X-cut or the cross-cut test method. Each glass sample (2.5 cm x 4 cm) was dip-coated with one of the solutions, aged for 30 days, described in Table 2.1. Half of the samples were annealed at 500°C for two hours to test the effects of thermal treatment on the degree of adhesion. As the dried coating thickness was expected to be thinner than 500 nm, the first procedure of the cross-cut test was chosen.

Furthermore, adhesion was also assessed by subjecting samples to repetitive photocatalytic tests and monitoring the decline in photoactivity. The decline is due to the detachment of the coating from the substrate, thus lower variations in photoactivity are correlated with higher coating adhesion.

2.2.5. SEM morphological analysis

The morphology of the deposited titanium oxide layer was analyzed by scanning electron microscopy analysis (Carl Zeiss AG, EVO Series 50). The characterization was carried out to identify which differences arise when employing different sol-gels, thermal treatments, deposition techniques, and substrates. Furthermore, the analysis was also performed to

verify the morphological variation before and after photocatalysis tests of anodized and spray-coated titanium meshes.

2.2.6. X-ray diffraction analysis

Despite the same sol-gels were used, test results changed according to deposition parameters, aging time, and annealing treatments. XRD analysis was carried out to determine the presence of anatase in a selected number of samples to determine why some were more photoactive or hydrophilic than others, and to determine the variations induced by different thermal treatments. X-ray spectra carry the following information:

- peak position gives information on the present material phases and crystal orientations;
- peak intensity highlights the preferred crystal orientations;
- peak width points to the crystallinity of the sample, as well as, through the Scherrer equation (Equation 2.12), the dimension of crystallites.

$$\tau = \frac{K\lambda}{\beta \cos(\theta)} \quad (2.12)$$

- τ = mean size of crystallites;
- K = dimensionless shape factor usually equal to 0.9;
- λ = X-ray wavelength;
- β = peak width at half the intensity (FWHM);
- θ = Bragg angle.

In the presence of multiple materials, the peaks in XRD spectra overlap. This was the case of the present dissertation, as the samples consisted of titanium oxide deposited on glass. According to data retrieved from the I.C.S.Database, glass presents peaks around 23°, 26°, and 27° [94]; while the anatase peak forms around 25°. However, glass was expected to be *X-ray amorphous*, thus showing a wide peak. A disadvantage to this phenomena is the fact that low amounts of anatase are not detectable as the peaks are concealed by the glass peak. The test was carried out with an Empyrean X-ray Diffractometer from Malvern PANalytical.

3 | Results and discussion

3.1. Coating appearance

While the following pictures provide a representation of the coatings' appearance, it is important to note that it can vary depending on factors such as solution ageing and viscosity. To highlight both transparency and any white opaque defects, the pictures were taken using a black background.

Dip-coated films are often nonuniform, appearing mostly transparent but with white opaque defects where the solution has shrunk during the drying process (Figure 3.1). However, *EB-1* consistently yielded perfectly transparent coatings.

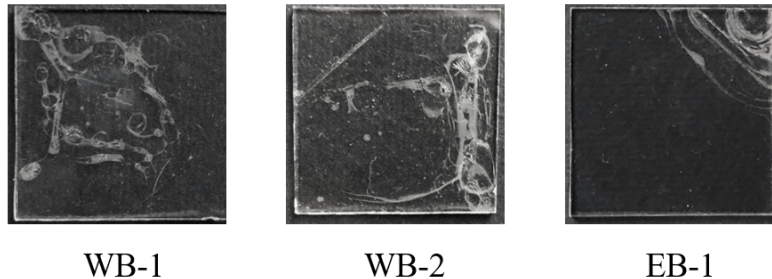


Figure 3.1: Appearance of dip-coated glass samples.

Unlike dip-coating, the appearance of spray-coated films can vary significantly depending on the solution used. While they tend to be translucent rather than transparent, this is likely due to the deposition of larger amounts of sol-gel. For instance, water-based sol-gels typically yield white translucent coatings, while ethanol-based solutions often produce coatings with a more uniform appearance, where the white color changes gradually (Figure 3.2).

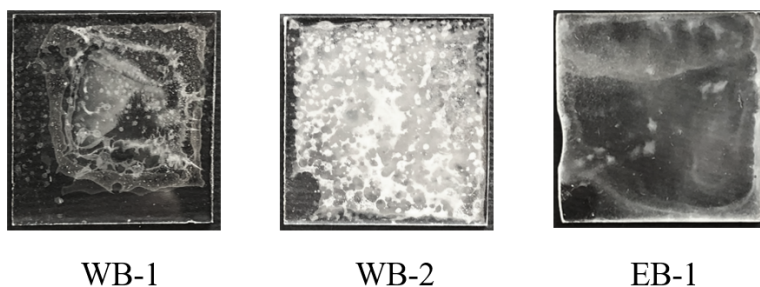


Figure 3.2: Appearance of spray-coated glass samples.

Despite the challenges in achieving coating uniformity, spray-coated PMMA samples were successfully prepared for natural soiling tests, as a satisfactory level of coating uniformity was achieved (Figure 3.3).

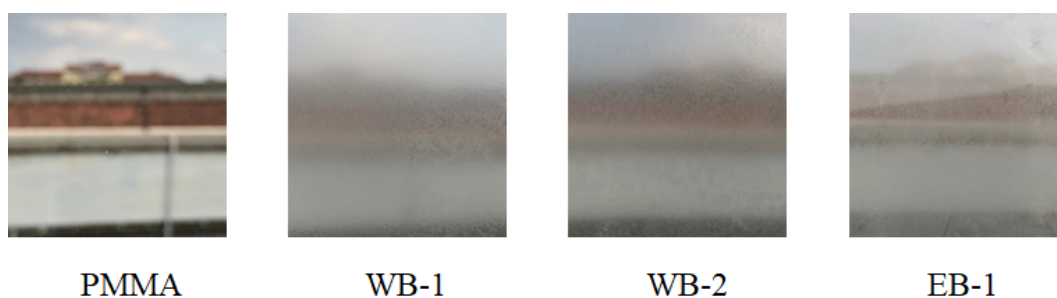


Figure 3.3: Appearance of spray-coated PMMA samples.

3.2. Photocatalytic performance

Tests on the photocatalytic activity of the sol-gels were carried out routinely to assess their performance. Furthermore, they were used as a benchmark to determine which process variables yielded better coatings. For example, photocatalytic tests were useful to determine the adhesion degree of the coating on different substrates, the best annealing conditions, and to compare the activity of spray-coated and dip-coated samples. The following paragraphs summarize the results of the above mentioned tests.

3.2.1. Processing of photocatalysis data

Data acquired during photocatalysis tests consisted of absorbance values collected every hour (Figure 3.4).

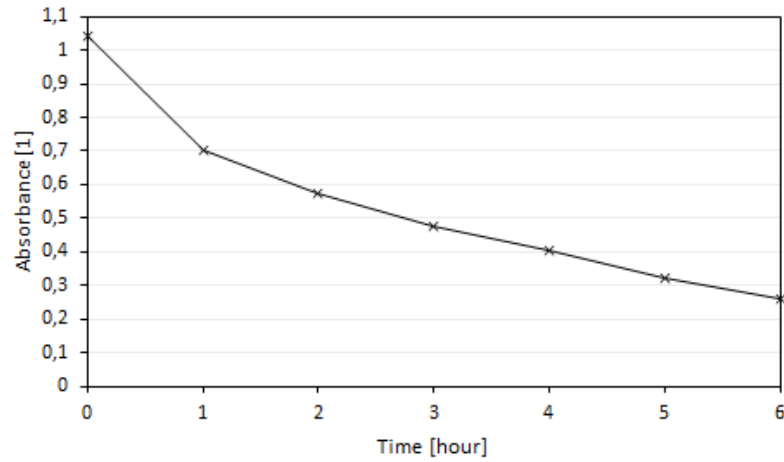


Figure 3.4: Example of absorbance variation during photocatalysis tests.

The percentage change in pollutant concentration was computed from the absorbance values by exploiting the Lambert-Beer law (Equation 2.1 and Equation 2.2). The values, which are usually reported in graphs like in Figure 3.5, give insight on the efficiency of the coating in degrading pollutants.

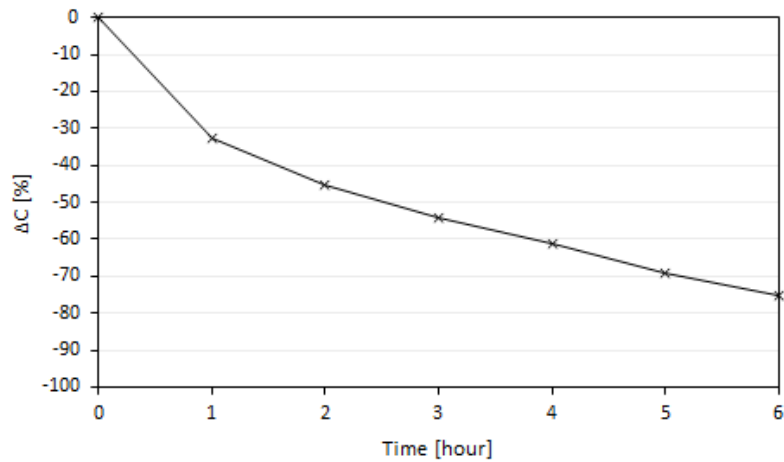


Figure 3.5: Example of concentration variation during photocatalysis tests.

However, it is by applying the pseudo-first order kinetic model that one can obtain objective and comparable data (Equation 2.3). Indeed, the slope of the curves obtained by plotting $\ln(CC_0^{-1})$ against time, like the one portrayed in Figure 3.6, represents the reaction rate constant k .

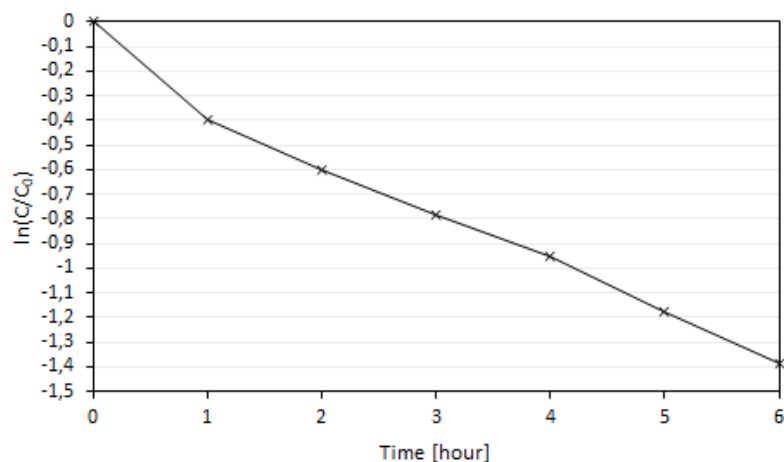


Figure 3.6: Example of application of the pseudo first-order kinetic model on photocatalysis data.

The upcoming considerations will rely on the two latter representations, as well as on the evaluation of reaction rate constants.

3.2.2. Preliminary tests

The use of catalysts is necessary to increase the reaction rate of photolysis. For this reason, before evaluating the photocatalytic activity of the analyzed samples, it is necessary to determine the photolysis reaction rate. Indeed, catalysts increase the light-induced degradation rate of pollutants, hence to evaluate their efficiency it is necessary to determine a reference value. Furthermore, tests were also performed in dark conditions to gauge rhodamine B adsorption and determine whether it is negligible.

3.2.2.1. Photolysis tests

Tests were performed according to the guidelines described in Chapter 2.2.1.1, albeit without introducing a coated sample. Data was collected from six batch reactors:

- three batch reactors were prepared as explained in Chapter 2.2.1.1, by also introducing an uncoated glass sample (2.5 cm x 2.5 cm);
- the other reactors, instead, were only filled with the rhodamine B solution.

The purpose was to establish whether the accessories contributed to the decrease of absorbance, for example either by providing adsorption sites or by furthering light-induced degradation.

Figure 3.7 reports the concentration variation relative to each batch reactor, where Ref_# and Ref_G# represent the reactors with and without glass samples, respectively. As shown in the graph, there is negligible difference between the two set-ups, suggesting that the additional equipment does not contribute to the decrease of absorbance. On average, photolysis drives the degradation of about 20% of rhodamine B.

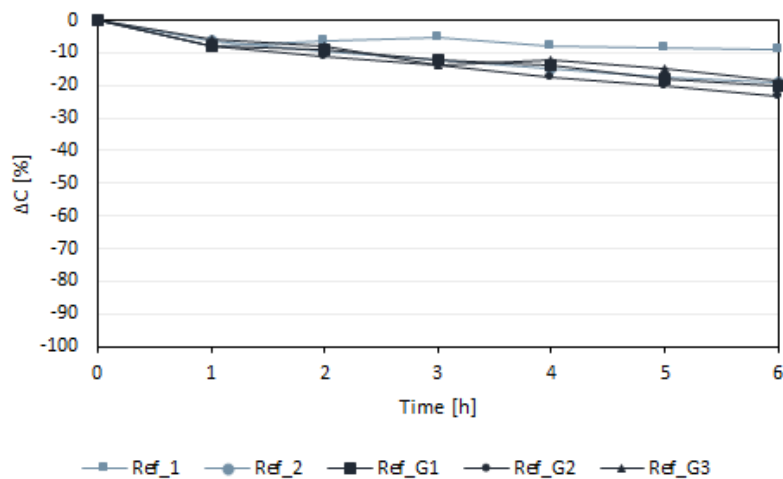


Figure 3.7: Concentration variation during preliminary photolysis tests.

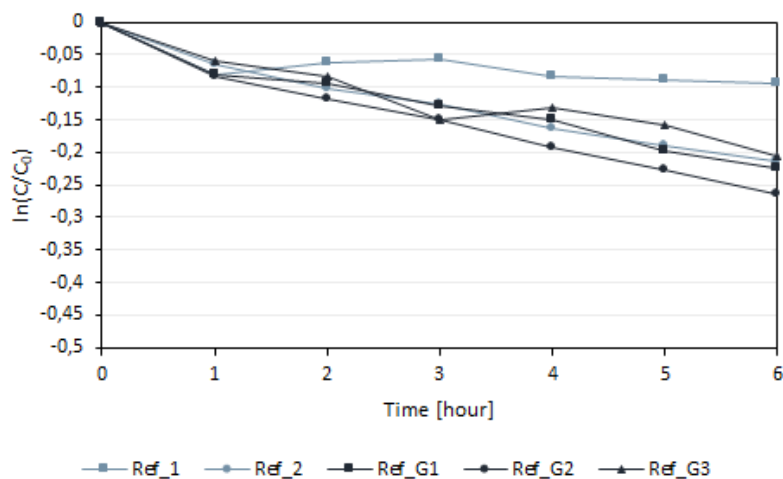


Figure 3.8: Application of the pseudo-first order kinetic model on preliminary photolysis tests.

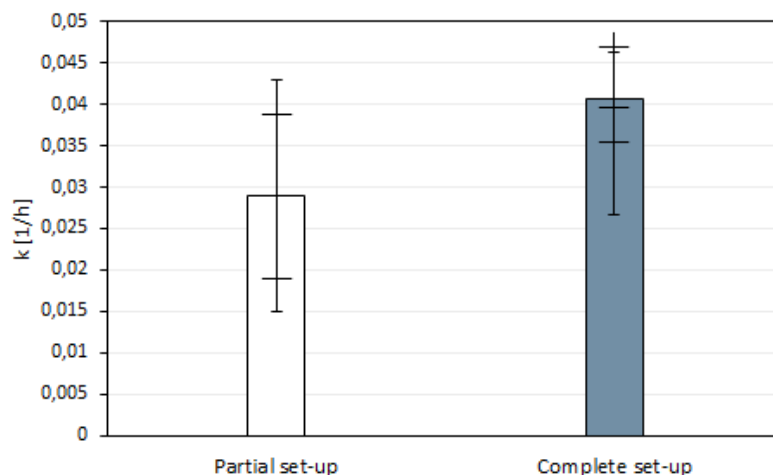
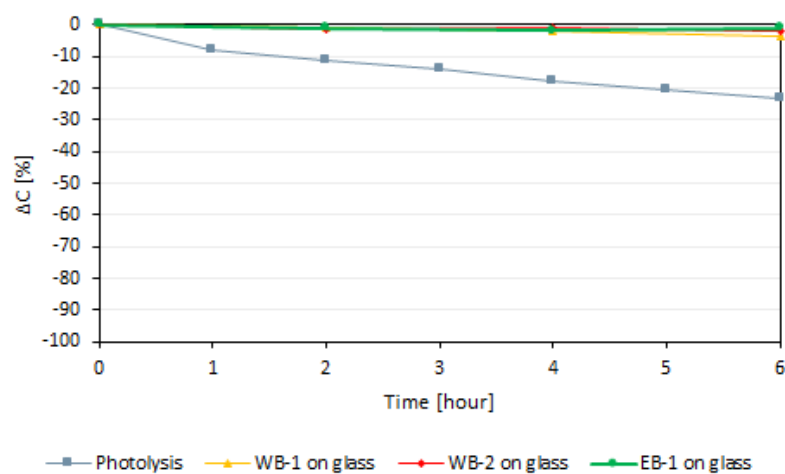


Figure 3.9: Average rate coefficients of preliminary photolysis tests.

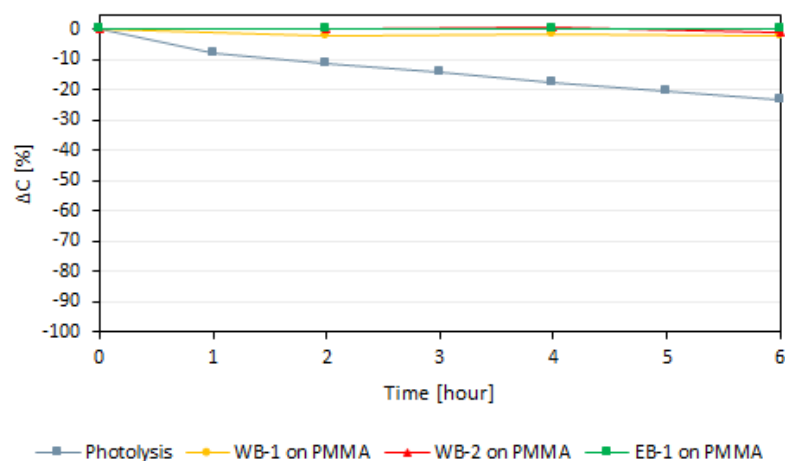
Figure 3.9 represents the average values of the reaction rate constants obtained by applying the pseudo first-order kinetic model. Overall, the results do not vary considerably between the two set-ups suggesting that the introduction of additional equipment in the solution has negligible influence on the variation of rhodamine B concentration. In conclusion, the average rate coefficient obtained from the complete set-up (0.04 h^{-1}) was used as reference value for future photocatalysis test.

3.2.2.2. Adsorption tests

Six batch reactors were prepared according to the description made in Chapter 2.2.1.1 to determine the degree of rhodamine B adsorption on coated glass and PMMA samples (2.5 cm x 2.5 cm). Each sample was dip-coated with one of the solutions reported in Table 2.1, however as the tests were carried out on different dates the solutions aged for a longer period before being deposited on PMMA. For reference, the solutions aged for about 60 and 180 days before being deposited on glass and PMMA, respectively.



(a)



(b)

Figure 3.10: Comparison of concentration variations induced by photolysis and adsorption tests.

The results shown in Figure 3.10, suggest that the adsorption of rhodamine B onto glass and PMMA is negligible: indeed concentration variation did not exceed 5%, while it amounted up to 20% during photolysis tests. Therefore, adsorption is deemed negligible and it will not be considered henceforth.

3.2.3. Ageing

The photocatalytic activity of sol-gel solutions is time-dependent as they require ageing to consolidate the gel. However, as prolonged ageing is detrimental to the solution, it is important to routinely monitor its photocatalytic activity. To represent the change over

time of photocatalytic activity relative to each solution described in Table 2.1, the results are plotted as $\ln(C/C_0^{-1})$ against time.

WB-2, whose results are represented in Figure 3.12, was considered the most performing photocatalyst as it reached the highest value of k after a dwell period of about four months. Indeed, at the top of its performance, it could degrade 94% of rhodamine B ($10^{-5}M$) (Figure 3.11). As the graph shows, in the first four months the photocatalytic activity slowly developed thanks to the ongoing polycondensation reaction. However, merely 10 days after the maximum activity was reached the solution showed a sudden decrease in its performance. This abrupt change in photoactivity is a drawback as it allows a small time window, compared to the required ageing period, in which the sol-gel can be deposited. On the other hand, there is good test repeatability as the coatings performed similarly.

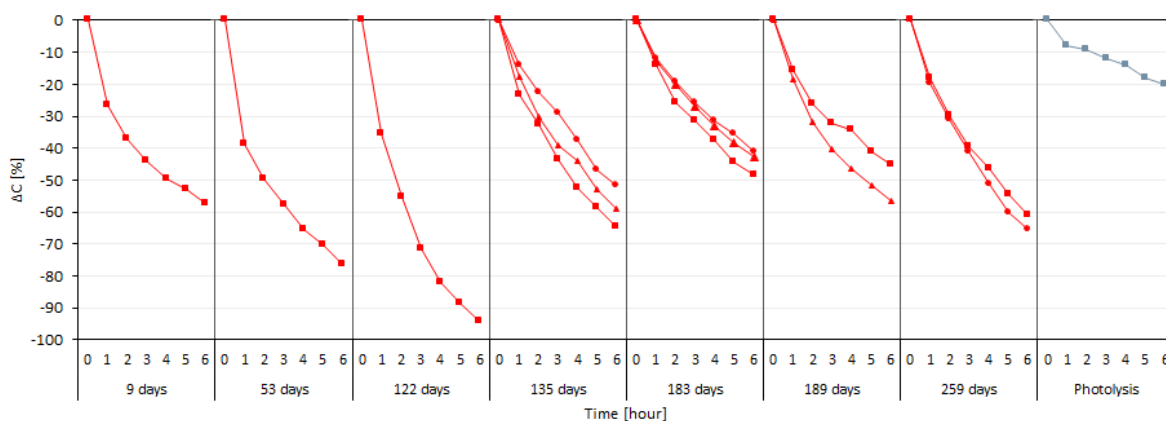


Figure 3.11: Concentration variation during degradation of rhodamine B ($10^{-5}M$) performed by WB-2.

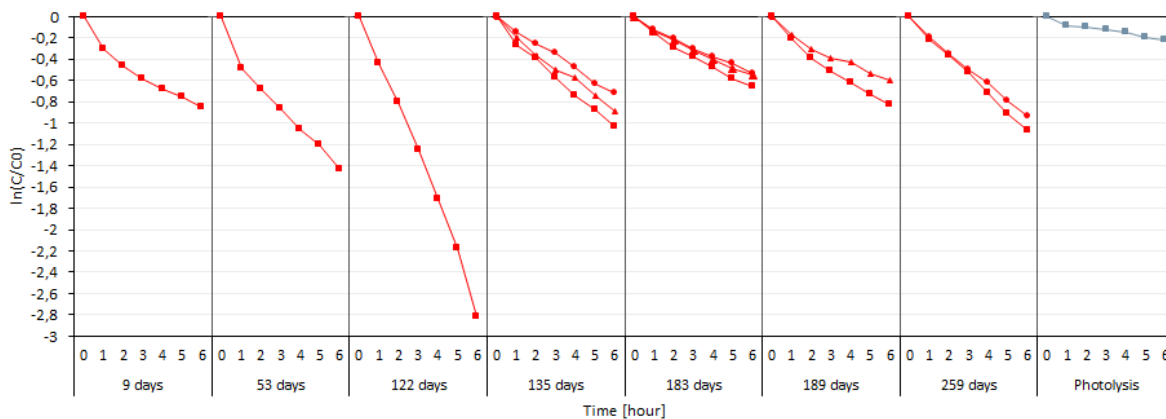


Figure 3.12: Photocatalytic activity variation in time of WB-2.

Solution WB-1, although it initially showed a similar increase in performance, was not as photoactive as WB-2 since it could not degrade more than 75% of the pollutant (Figure 3.13). However, contrary to WB-2, it showed a lower rate of performance loss, which would allow a better prediction of its photocatalytic activity (Figure 3.14).

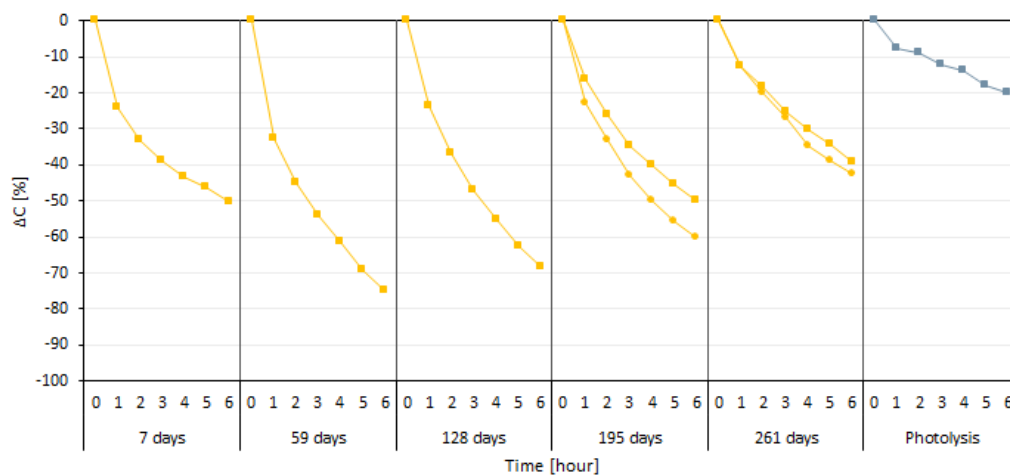


Figure 3.13: Concentration variation during degradation of rhodamine B ($10^{-5}M$) performed by WB-1.

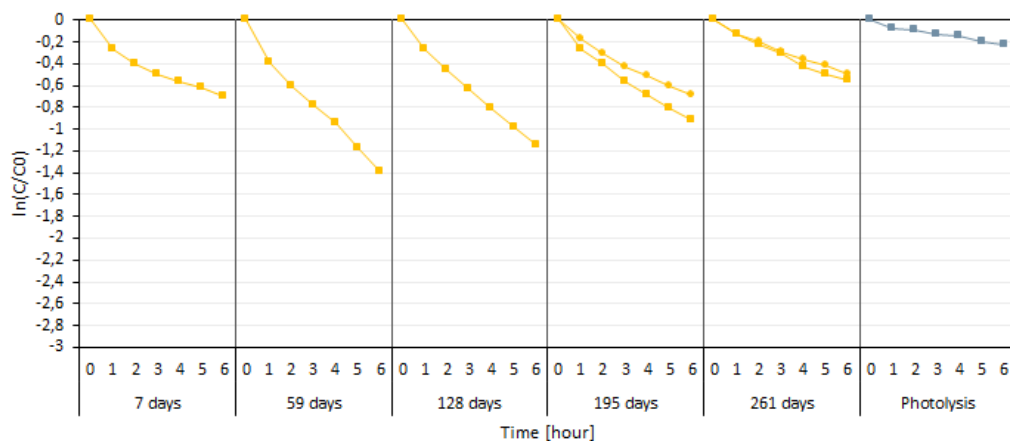


Figure 3.14: Photocatalytic activity variation in time of WB-1.

Lastly, EB-1 showed an initial delayed activation as after 60 days it could degrade only 43% of the dye, remarkably lower than WB-1 and WB-2. Nevertheless, it was routinely monitored expecting a slow increase in photoactivity given the low hydrolysis rate of ethanol compared to water. Indeed, while the water-based solutions gradually became

more viscous and turned white (Figure 1.17), EB-1 remained virtually the same. This could suggest why its photoactivity quickly disappeared as the following tests proved.

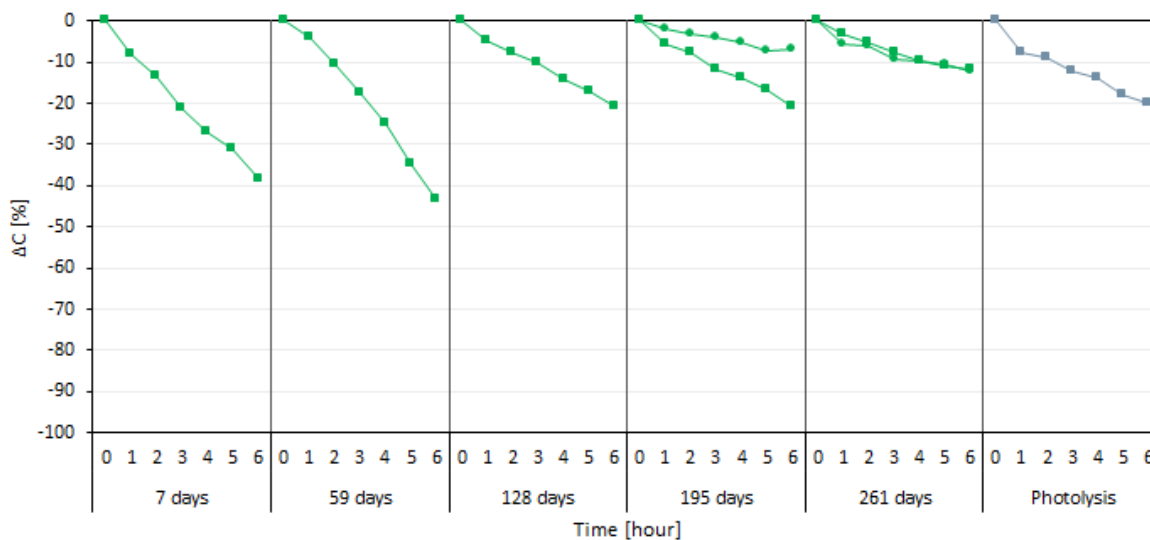


Figure 3.15: Concentration variation during degradation of rhodamine B ($10^{-5}M$) performed by EB-1.

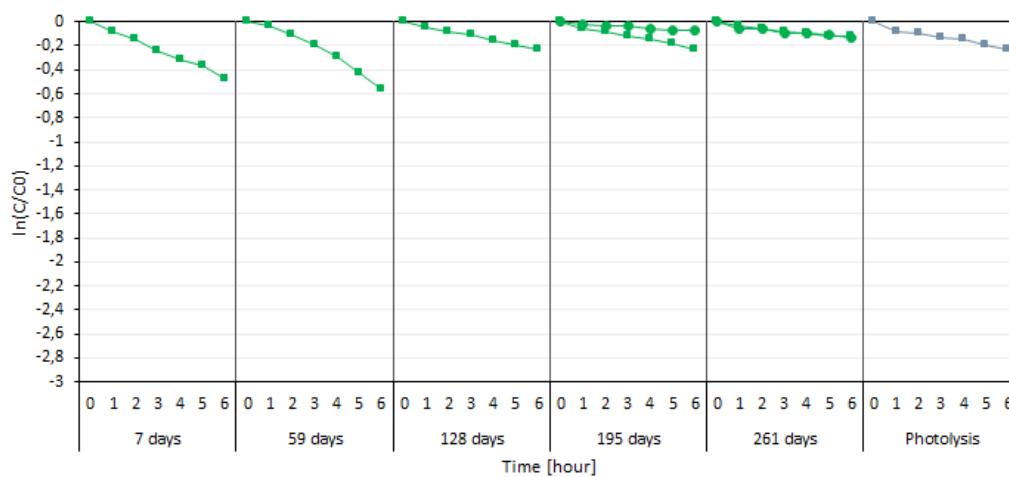


Figure 3.16: Photocatalytic activity variation in time of EB-1.

To better compare the photocatalytic activity variation in time of each sol-gel, the reaction rate constants derived from the graphs shown above are represented in Figure 3.17. As the coefficient of determination (R^2) was always above 0.95, data closely follow pseudo first-order kinetics, as expected. The ethanol-based solution remained inert despite a long ageing period, indeed the reported k values are comparable with that obtained in

photolysis tests (0.04 h^{-1}). The water-based solutions, save for the higher peak obtained by *WB-2* at 122 days, performed similarly. Indeed, their activity increased in the first four months and then gradually decreased.

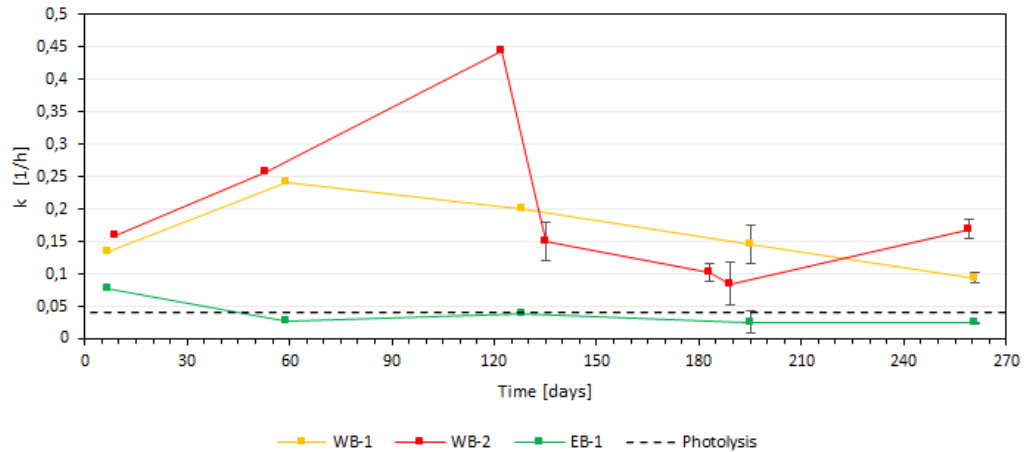


Figure 3.17: Evolution of photocatalytic activity in time.

3.2.4. Deposition technique

Photocatalytic tests were carried out to compare the photocatalytic activity of spray- and dip-coated samples, and to determine whether spray-coating is a viable deposition technique. The aim was to obtain similar values of k , the first step towards determining whether the two deposition techniques yield samples with similar self-cleaning ability. As previously mentioned, there are multiple advantages to substituting dip-coating with spray-coating, for example the possibility to coat surfaces in situ.

Six PMMA samples (2.5 cm x 2.5 cm) were coated with WB-1, WB-2, and EB-1 (Table 2.1), aged for approximately 60 days, either by spray or dip-coating.

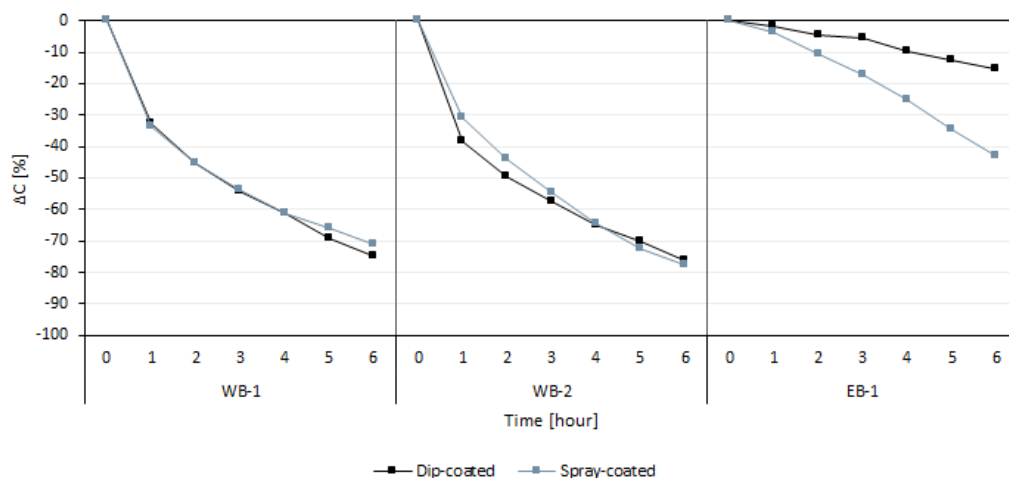


Figure 3.18: Comparison of degradation efficiency between spray- and dip-coated samples.

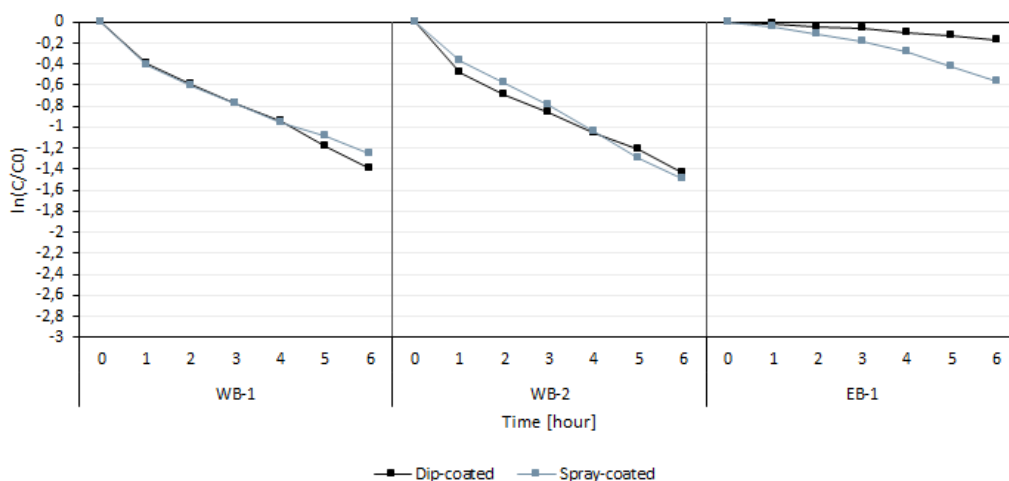


Figure 3.19: Comparison of photocatalytic activity between spray- and dip-coated samples.

Results show that the deposition technique does not influence photocatalytic activity (Figure 3.18 and Figure 3.19). Indeed, the curves which correspond to the two deposition techniques overlap thus confirming good reproducibility even when using two different coating techniques. Only solution *EB-1* showed considerable deviation, however, given its negligible activity, it is not significant.

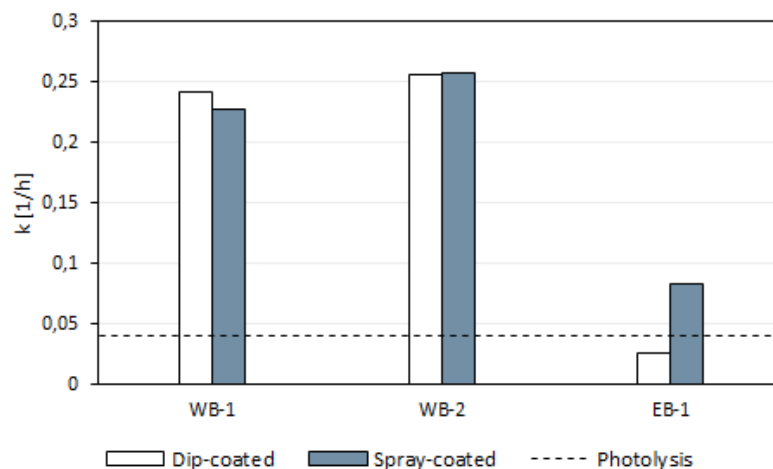


Figure 3.20: Reaction rate constants of spray- and dip-coated samples.

Figure 3.20 compares the values of k related to spray- and dip-coated samples. The percentage change between the two deposition techniques corresponds to 0.5% and -5.9% for *WB-2* and *WB-1*, respectively. On the other hand, the sample dip-coated with solution *EB-1* was not active, as shown by its value of k similar to photolysis, hence it is futile to compute the percentage change and to determine whether the new deposition technique is a viable option for this solution. However, given the good results reported by *WB-1* and *WB-2*, it was decided to adopt this new technique and to continue testing.

3.2.5. Substrate and consolidation

The standard thermal treatment, performed on coated glass samples, was chosen according to the results of previous dissertations [62], which reported highest photocatalytic activity for samples treated at 500°C for two hours. However, this dissertation employs different substrate materials: glass, titanium, and PMMA. While titanium was thermally treated in the standard way, PMMA cannot withstand such high temperatures as its glass transition temperature ranges between 85°C and 165°C [68]. The following paragraphs report the results associated to the influence of thermal treatment on photocatalytic activity and adhesion, which was assessed by conducting repeatability tests.

3.2.5.1. Glass substrate

Standard treatment The effects of thermal treatment on the photocatalytic activity of dip-coated glass samples are summarized in Figure 3.21. For reference, the solutions used were aged for about 125 days. The results show that annealing the samples after

coating deposition improves the photocatalytic activity of both *WB-1* and *EB-1*. On the other hand, solution *WB-2 An.* showed lower photocatalytic activity than *WB-2*. However the difference is reasonably comparable with experimental error. The treatment was particularly effective for solution *WB-1*, as it increased the degradation of rhodamine B from 68% to 85% (Figure 3.21a).

Figure 3.22 reports the variation of reaction rate constants of the corresponding solutions. Each percentage change indicates the variation of k when repeating photocatalysis tests: the annealing treatment does not considerably increase coating adhesion, as the variation is in the same order of non-annealed samples. However, as annealing improves photoactivity, the results obtained in repeated tests are comparable to the results obtained in the first run of the non-annealed samples.

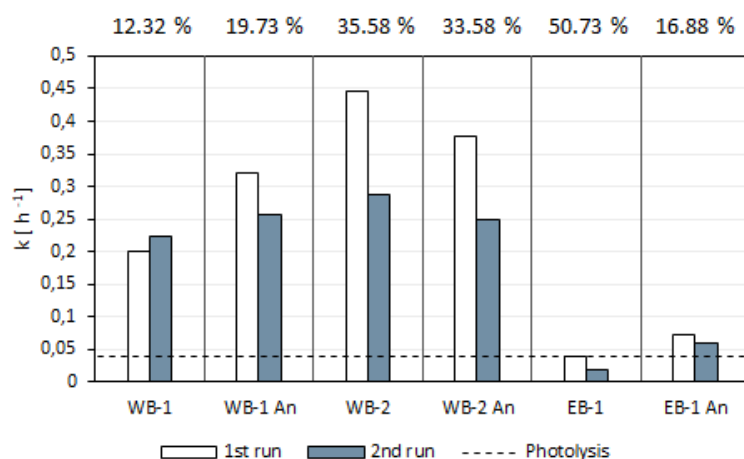
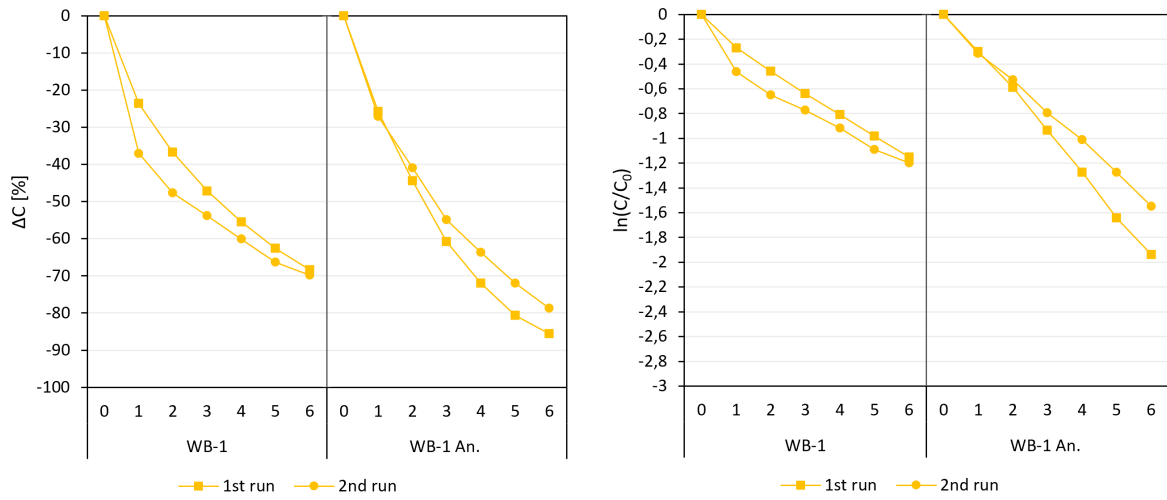


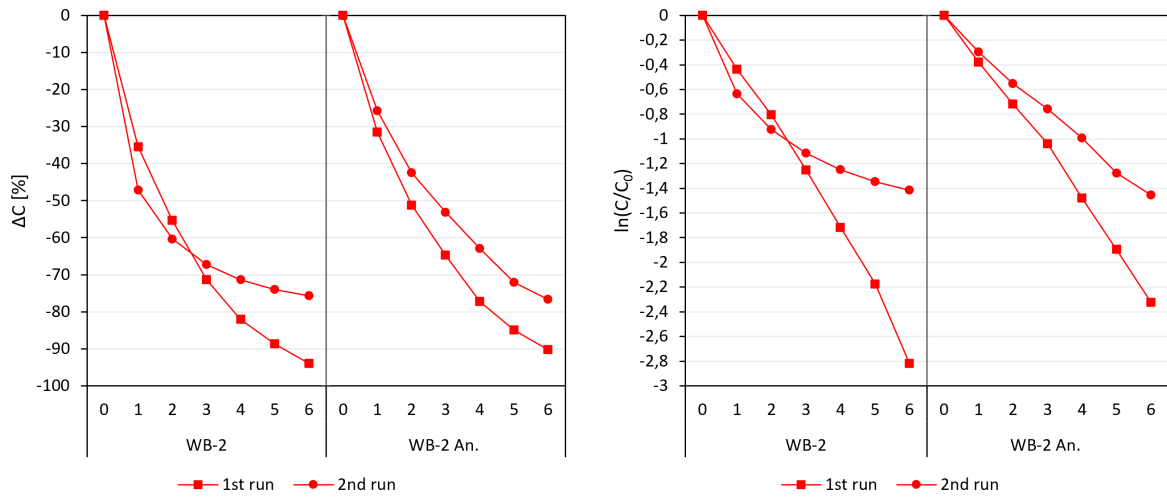
Figure 3.22: Comparison of reaction rate constants of untreated and annealed dip-coated glass samples.

Alternative treatment As PMMA necessitates an alternative annealing treatment to be performed at around 90° , spray-coated glass samples were prepared to evaluate how different annealing treatments influence photocatalytic activity.

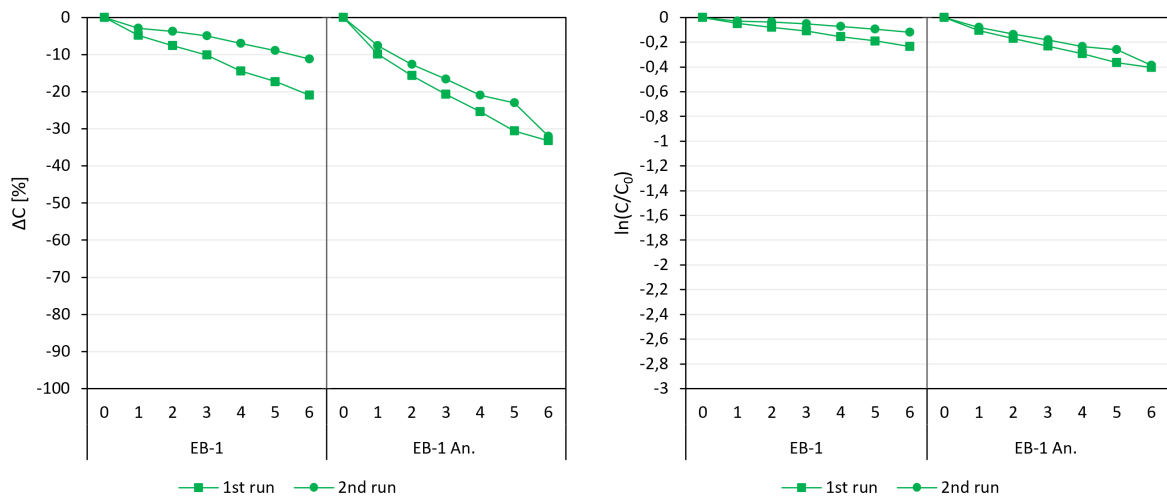
To this purpose, *WB-2*, the most performing sol-gel, which was aged for about 183 days, was employed. As three samples were tested for each annealing condition, for the sake of simplicity and readability, Figure 3.23 and Figure 3.24 show only one curve for each annealing condition. The complete graphs are reported in Appendix A (Figure A.9). Final observations were made on the average values of k , which show that with increasing annealing treatment the photoactivity of the coating decreases (Figure 3.25). Nonetheless, conclusions on the best thermal treatment were made on the results obtained from spray-coated PMMA samples.



(a) Comparison of photocatalytic activity between annealed and untreated *WB-1* coatings.



(b) Comparison of photocatalytic activity between annealed and untreated *WB-2* coatings.



(c) Comparison of photocatalytic activity between annealed and untreated *EB-1* coatings.

Figure 3.21: Effects of annealing treatment, performed at 500°C for two hours, on the coatings' photocatalytic activity.

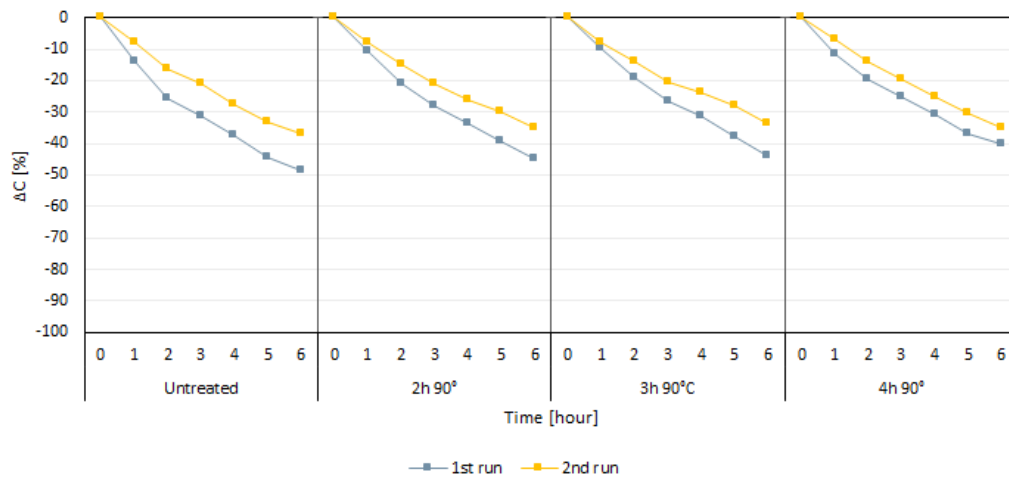


Figure 3.23: Influence of duration of annealing treatment on the degradation efficiency of spray-coated glass samples.

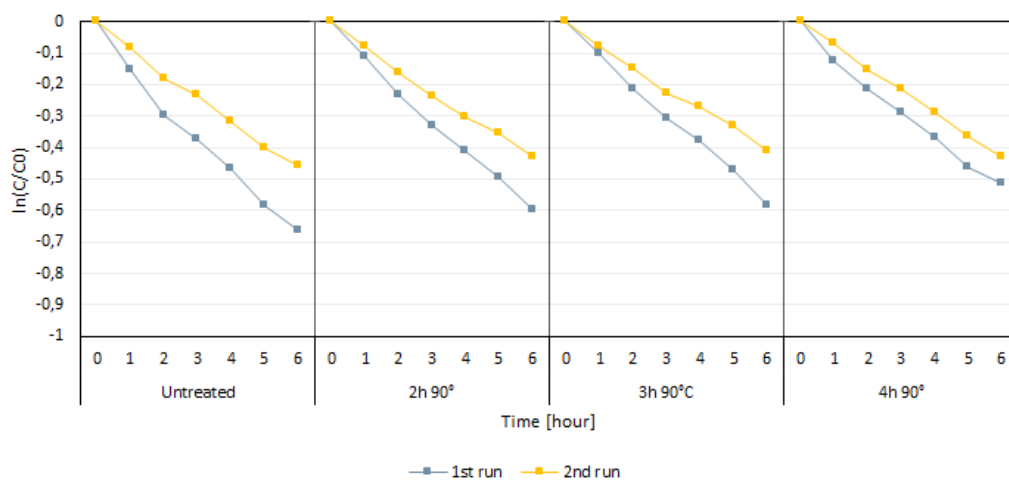


Figure 3.24: Influence of duration of annealing treatment on the photocatalytic activity of spray-coated glass samples.

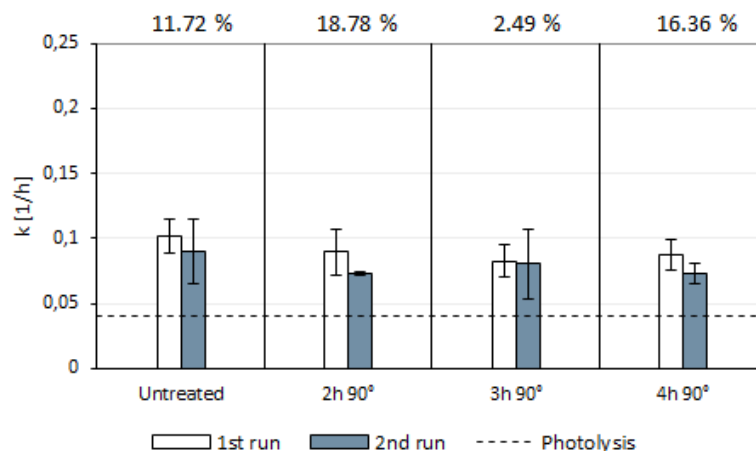


Figure 3.25: Thermal treatment assessment of coated glass samples.

3.2.5.2. PMMA substrate

Three samples (2.5 cm x 2.5 cm) were prepared for each thermal treatment and were tested twice to assess repeatability. To run the tests *WB-2* was chosen, as it yielded the best results in previous tests. The sol, aged for 135 days, was spray-coated on PMMA. The complete graphs are reported in Appendix A (Figure A.10), while Figure 3.26 and Figure 3.27 report only one curve per tested condition for the sake of simplicity. The best thermal treatment was evaluated by computing the average of the rate coefficients (Figure 3.28). Samples that were treated for two hours at 90°C reported the highest photocatalytic activity in both the first and second test run. However, as the percentile variation of k is high, ranging between 40% and 50%, it is necessary to find ways to improve the adhesion of the coating to the substrate. Indeed, glass samples subjected to the same annealing treatment showed an average variation of 15%, therefore the adhesion of the sol-gel coating to glass is stronger than to PMMA. Following these results, all the PMMA samples were annealed at 90°C for two hours.

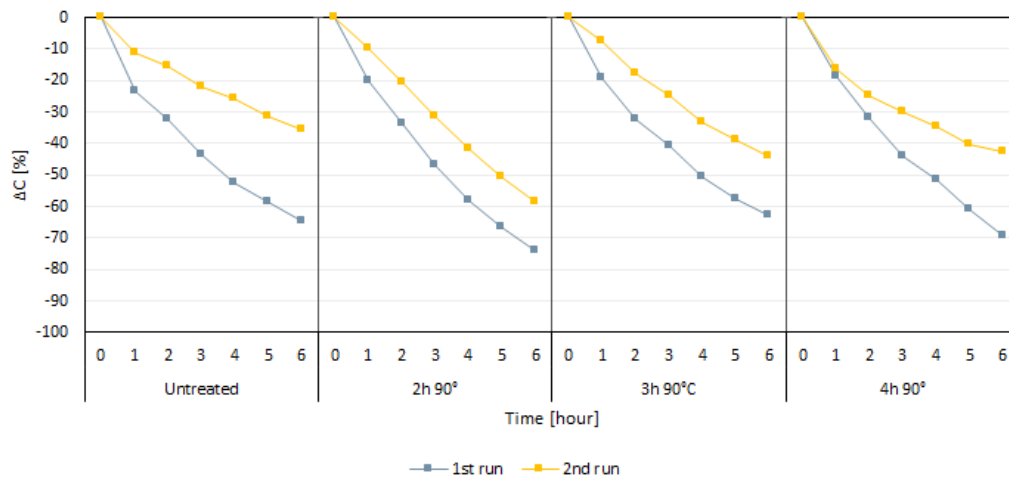


Figure 3.26: Influence of annealing treatment on the degradation efficiency of spray-coated PMMA.

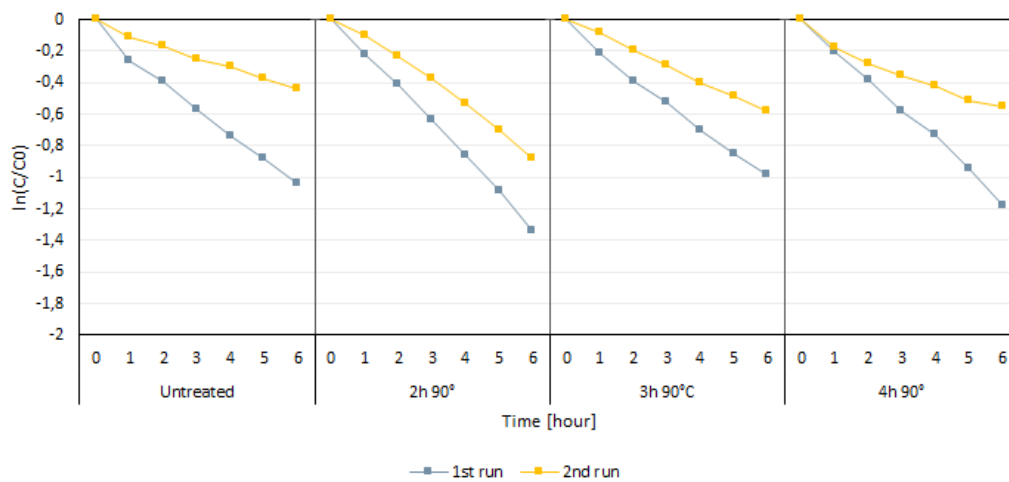


Figure 3.27: Influence of annealing treatment on the photocatalytic activity of spray-coated PMMA.

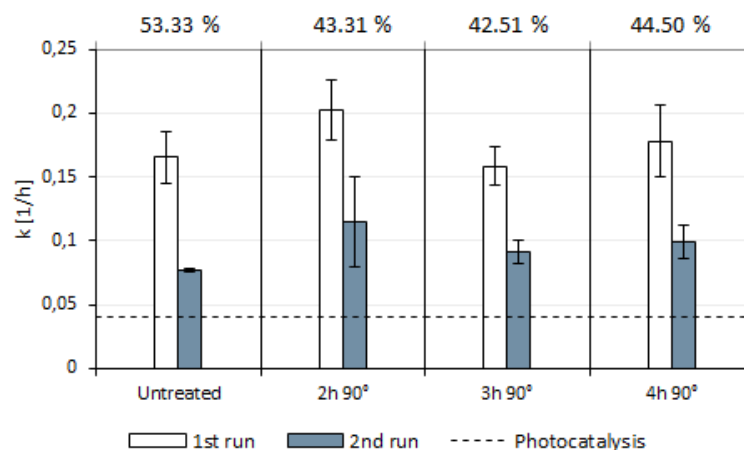
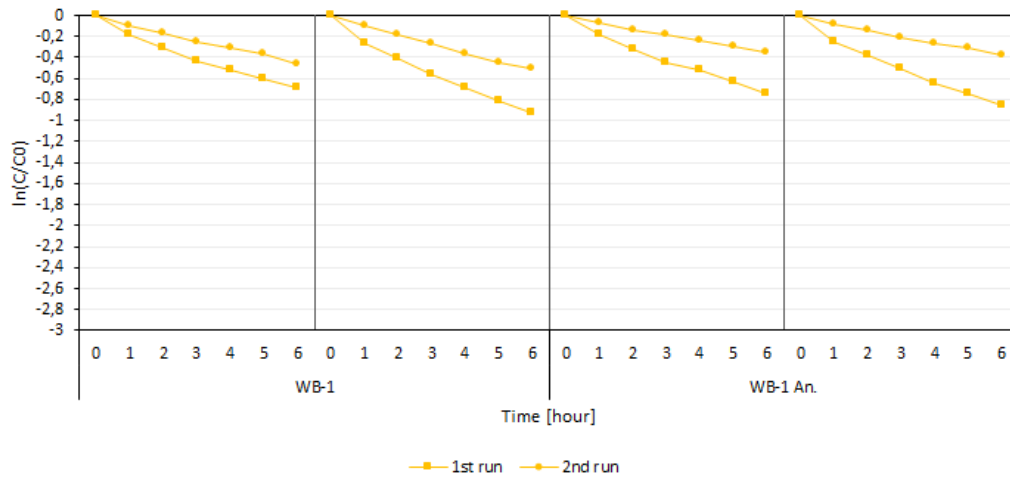


Figure 3.28: Thermal treatment assessment of coated PMMA samples.

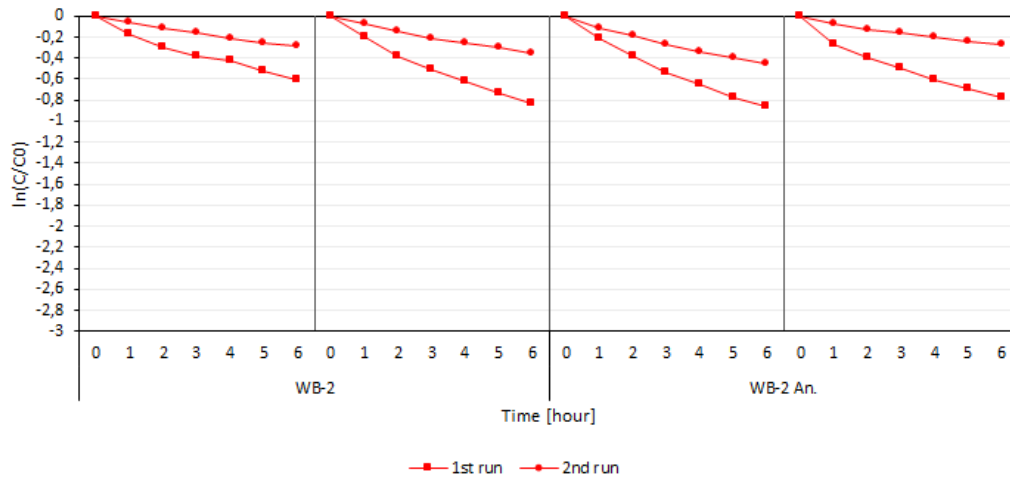
The reaction rate constants, portrayed in Figure 3.28, show that the photocatalytic activity of coated PMMA samples is remarkably higher than the values obtained from the glass samples subjected to the same thermal treatment. As the glass samples were tested 50 days after the PMMA ones, the reason is probably due to the longer ageing period which caused the solution to lose part of its effectiveness when sprayed on glass samples. Therefore, it is not possible to assess whether the choice of the substrate material influences the photoactivity of the coating. However, according to the abovementioned results, it influences adhesion and thus reusability.

3.2.6. Corona treatment

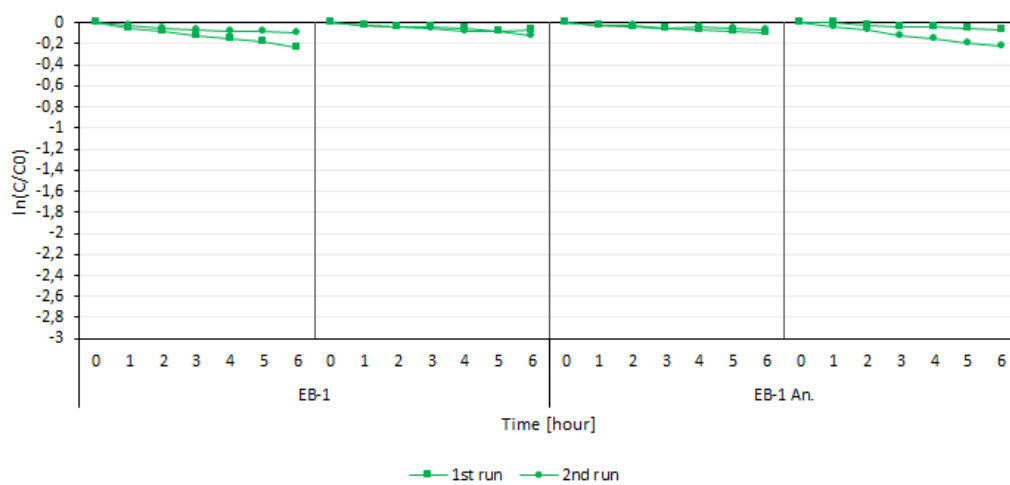
To increase the adhesion of the coating on PMMA, a few substrates were subjected to corona treatment before coating deposition (sol-gel ageing period: 190 days). To determine whether the treatment inhibited the loss of coating, the photocatalytic activity of each sample was tested twice (Figure 3.29).



(a)



(b)



(c)

Figure 3.29: Assessment of corona treatment on the degradation efficiency of PMMA samples spray-coated with (a) *WB-1*, (b) *WB-2*, and (c) *EB-1*.

The results in Figure 3.29 and Figure 3.30, show that the treatment was not successful as the percentage change between the first and second run of the test is between 43% and 57%, hence close to the variations obtained without corona treatment (Figure 3.28). The results relating to sample *EB-1* and *EB-1 An.* have been ignored as they are not active.

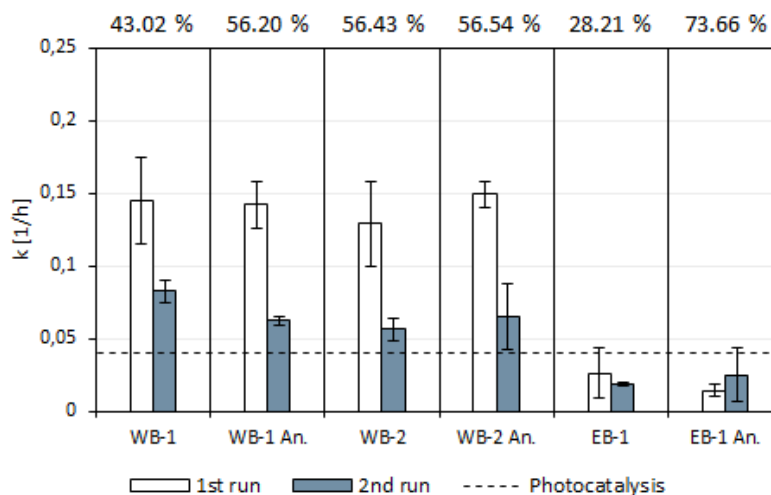


Figure 3.30: Assessment of corona treatment.

Therefore, corona treatment was deemed unsuccessful on PMMA samples. Future studies should either aim at finding alternatives to increase the adhesion to PMMA, or finding more suitable substrates.

3.2.7. Solution reproducibility

Given the gradual change in performance of the studied solutions with ageing time, a new batch was synthesized to continue testing. The new solutions were tested after four months expecting high photocatalytic activity.

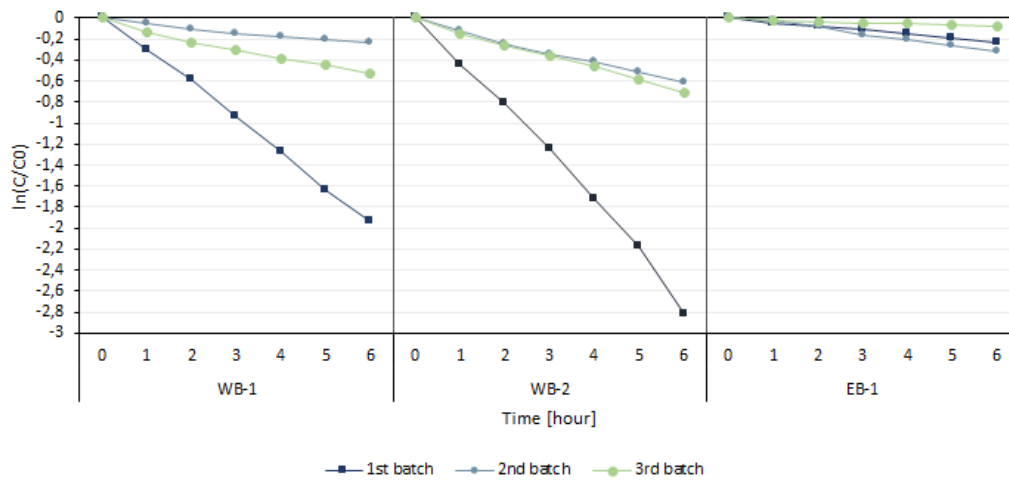


Figure 3.31: Comparison of photocatalytic activity of different batches after a 4 month aging process.

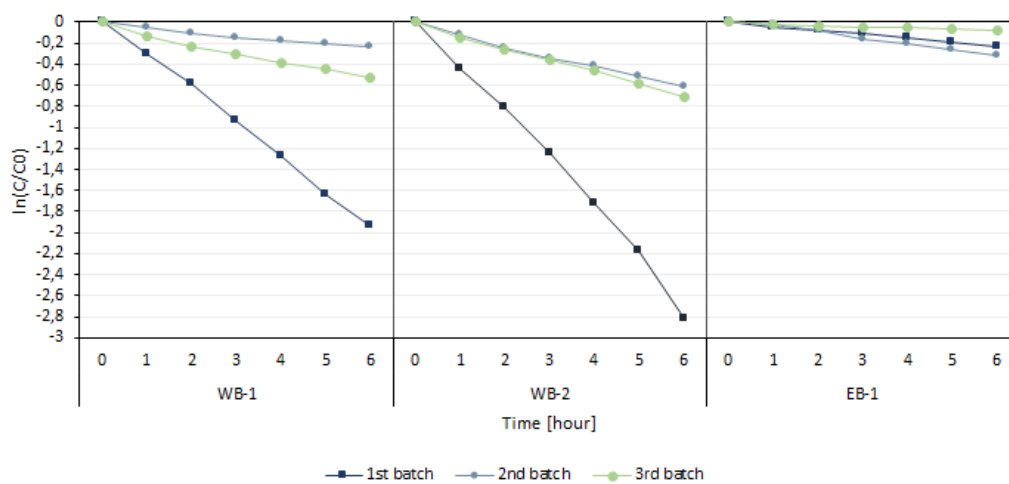


Figure 3.32: Application of pseudo-first order kinetics on the degradation efficiency of different batches after a 4 month aging process.

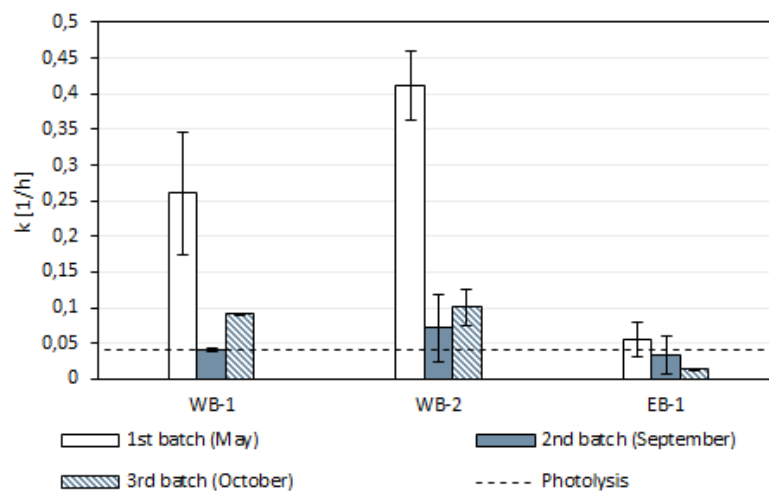


Figure 3.33: Reaction rate constants of different batches after a 4 month aging process.

The results, reported in Figure 3.31, Figure 3.32, and Figure 3.33, show that the photocatalytic activity of the same solutions obtained from different batches highly varies. These results bring into question the reproducibility of the solutions. Further tests are needed to determine whether environmental parameters, such as temperature and humidity, during sol-gel synthesis and deposition influence the performance of the coating. Indeed, the batches were prepared at different times of the year, i.e. May and October, therefore higher temperature observed during summer could have accelerated the hydrolysis-condensation rate promoting higher photocatalytic activity. Another motivation could also be related to the frequency with which the solutions were employed. Indeed, while the first batch was routinely tested for 9 months, and thus was routinely subjected to 15 minutes of ultrasonication, the second batch had never been tested so far. Further studies could determine whether routinely exposing the solutions to ultrasonication could prolong the time in which the samples are photoactive. Indeed, ultrasonication raises the solution temperature and promotes homogeneity, thus promoting hydrolysis-condensation reactions.

3.3. Coating wettability

Water contact angle tests were carried out for each sol-gel solution described in Table 2.1. The tests were performed on both glass and PMMA to determine whether the substrate influences the wettability of the coating, and thus its self-cleaning ability. Furthermore, the tests were repeated to determine how different deposition techniques and thermal treatments influence the WCA.

3.3.1. Dip-coated glass samples

Seven glass samples (2.5 cm x 2.5 cm) were prepared as follows:

- one was used as a reference;
- three glass samples were coated with the solutions reported in Table 2.1 (ageing time 7 days);
- three glass samples were coated with the abovementioned solutions and annealed for two hours at 500°C.

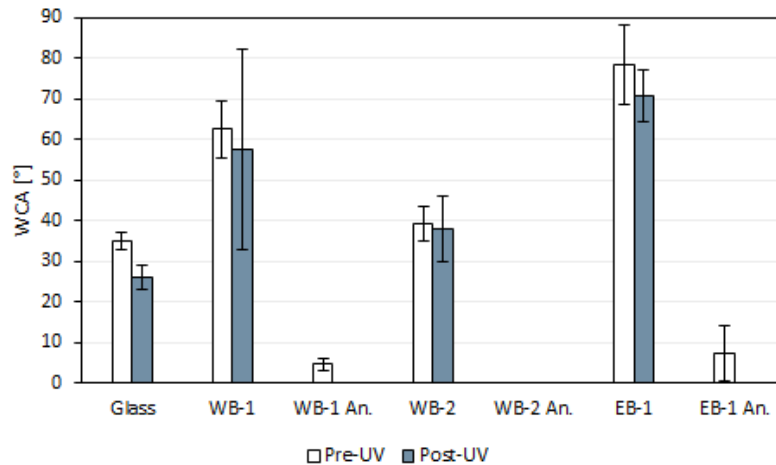


Figure 3.34: Wettability before and after UV irradiation of dip-coated glass samples.

Through the results showed in Figure 3.34 it is possible to make the following observations:

- the coatings were found to increase the hydrophobicity of the glass, with the highest values observed for the alcohol-based sol-gel coating (*EB-1*);
- irradiation induces a slight increase in hydrophilicity as the samples reported decreasing average WCA values. However, the variation never exceeded 9°, hence it

is negligible considering the aim of obtaining a superhydrophilic and self-cleaning surface;

- annealed samples are superhydrophilic with WCA below 10° , thus ideal for self-cleaning purposes. After UV irradiation, the WCA was not measurable as the deposited water drop spread evenly on the whole surface, in these instances a WCA of 0° was assigned. The large difference between annealed and regular samples cannot be found in the occurring phase transitions as their structure is not different enough to induce such a variation; whereas, the high temperature treatment not only induces the evaporation of solvent residues, but also the degradation of organic contaminants that promote hydrophobicity;
- finally, the reported standard deviations further prove that the coatings are inhomogeneous. Indeed, the standard deviation of uncoated glass never exceeded 3° , whereas the one of coated samples, ignoring sample *WB-1* post thermal treatment, ranged between 4° and 10° .

3.3.2. Spray-coated glass samples

The test was repeated on spray-coated glass samples to determine whether deposition technique and thermal treatment influence the wettability of the coating. Seven samples were prepared for both the test under UV irradiation and the test in dark condition. Thirteen glass samples (2.5 cm x 2.5 cm) were prepared as follows:

- one was used as a reference;
- six glass samples were coated with the solutions reported in Table 2.1 (ageing time 190 days);
- six glass samples were coated with the above mentioned solutions and annealed for two hours at 90°C .

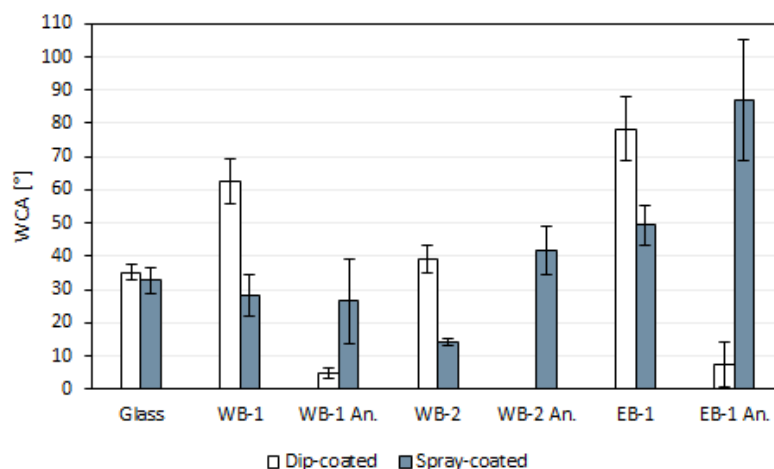


Figure 3.35: Comparison between wettability of coatings deposited with different methods.

Figure 3.35 shows the difference that arises when varying the deposition technique, although it could also be due to the different ageing period of the solutions. However, the results are consistent and show that contrary to the dip-coated samples, the spray-coated coatings enhance glass hydrophilicity. The deposition technique, on the other hand, does not improve the homogeneity of the surface as the standard deviation values are comparable. Surprisingly, while dip-coated annealed samples were superhydrophilic, the thermal treatment of spray-coated samples increased the values of WCA. Although higher values were expected given the thermal treatment performed at lower temperature, one would nevertheless have anticipated lower values than the non-treated samples. However, Figure 3.35 shows that spray-coated annealed samples have higher WCA values than untreated samples. Further research is needed to determine the reason behind this behavior.

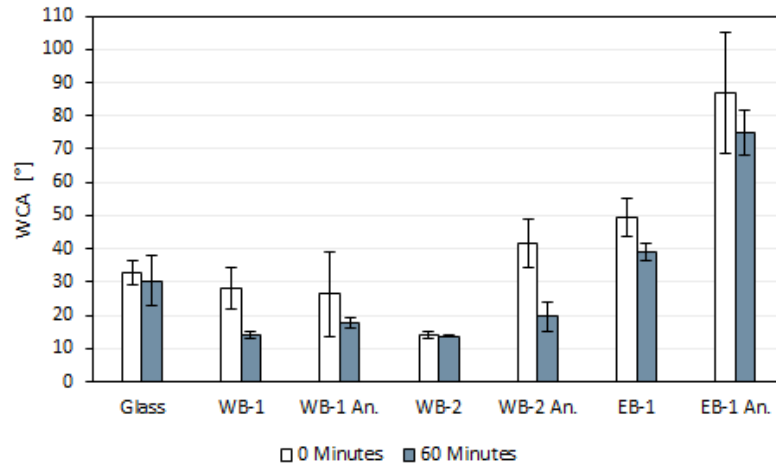


Figure 3.36: Wettability before and after UV irradiation of spray-coated samples.

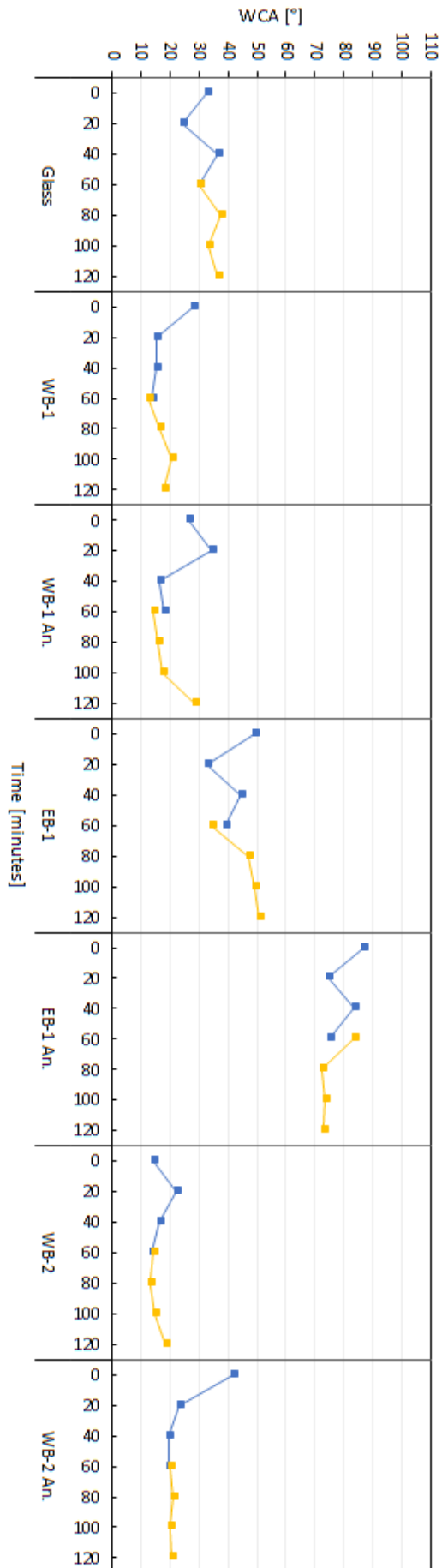
Photoinduced hydrophilicity is also found in spray-coated glass samples (Figure 3.36). Although a different radiation intensity was applied, 1.1 mW cm^{-2} instead of 0.5 mW cm^{-2} , the variation in WCA is comparable to the dip-coated samples. Indeed, while the dip-coated samples showed a variation upto 9° after UV irradiation, spray-coated samples showed variations between 9° and 20° . The slightly higher variation in wettability allows to monitor the hydrophilization of the coatings during UV irradiation (Figure 3.37a).

The results, besides the data shown in red in Figure 3.37b, do not show a clear trend. The reasons for this are twofold:

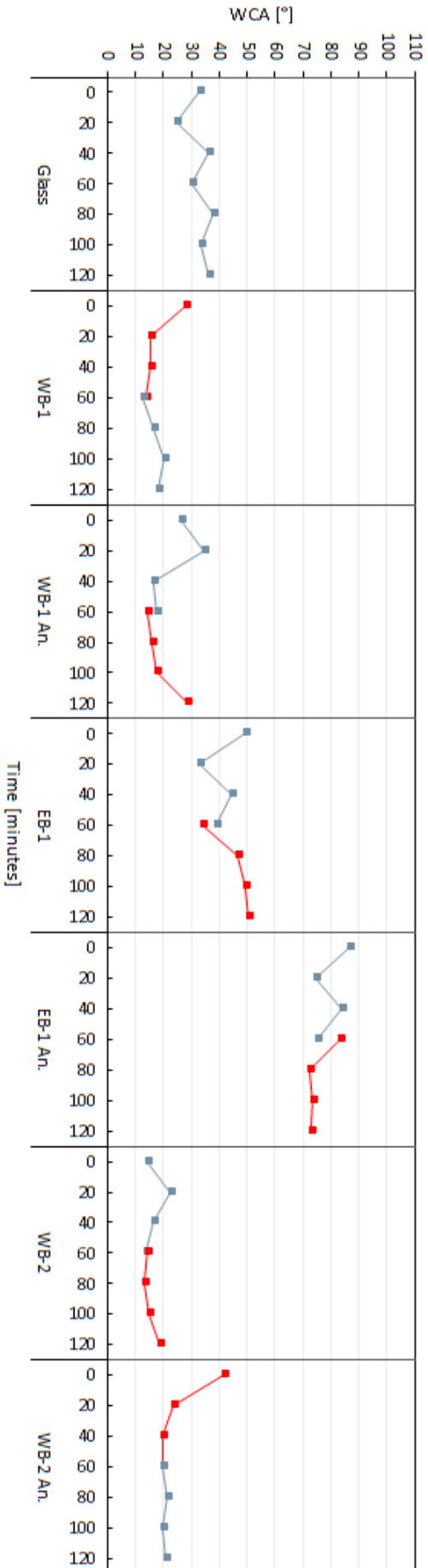
- the coatings are inhomogeneous, thus WCA varies considerably across the surface;
- the photoinduced hydrophilicity is not significant enough to offset the errors arising from the previous point.

However, it is possible to make the following observations:

- although different samples were used for the test under UV irradiation and for the test in dark conditions, the data, besides sample *EB-1* and *EB-1 An.*, show good correspondence between the two values measured at 60 minutes. This shows both good coating reproducibility and good software employment;
- however, the photoinduced hydrophilicity is not significant as literature reports variations around 35° in one hour (Figure 1.3a) [18];
- storing the samples for one hour in the dark is enough to recover the initial conditions;



(a)



(b)

Figure 3.37: Photoinduced hydrophilicity of spray-coated glass samples.

- samples *EB-1* and *EB-1 An.*, although visually more homogeneous, report the most erratic data due to lack of photoactivity;
- as reported in the previous paragraph, the alcohol based sample (*EB-1*) is considerably more hydrophobic than the water-based samples.

3.3.3. Spray-coated PMMA samples

The test described in Chapter 3.3.2 was repeated on PMMA samples to determine whether the choice of substrate influences wettability. The solutions used were aged for about 165 days (Table 2.1).

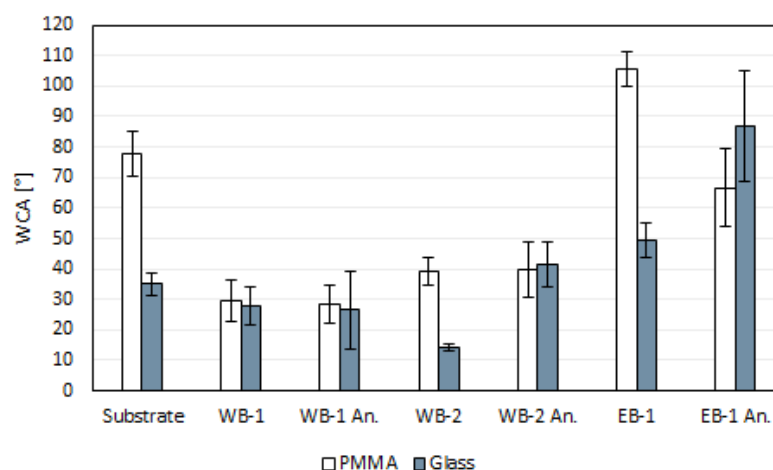


Figure 3.38: Substrate influence on wettability.

Through the results showed in Figure 3.38 it is possible to make the following observations:

- as expected, PMMA is more hydrophobic than glass;
- coating *WB-1*, *WB-1 An.*, and *WB-2 An.* show similar WCA values on the two different substrates;
- instead, coating *WB-2*, *EB-1*, and *EB-1 An.* show large variations of wettability on the two substrates;
- therefore, it is not possible to state that substrates have poor influence on wettability: indeed, coated PMMA has higher values of WCA compared to coated glass.

Notably, the water contact angle measured on glass and coated glass samples reveals a small difference, indicating that glass is moderately hydrophilic with comparable wettability to the applied coating. This observation initially raised doubts about the uniformity of

spray-coated coatings and their effectiveness in altering the substrate wettability. On the other hand, PMMA is more hydrophobic, and thus the difference between the coated and uncoated samples is more visible: indeed, the applied coating reduces the water contact angle to values close to those of glass. This confirms the coatings' efficacy in modifying the substrate wettability.

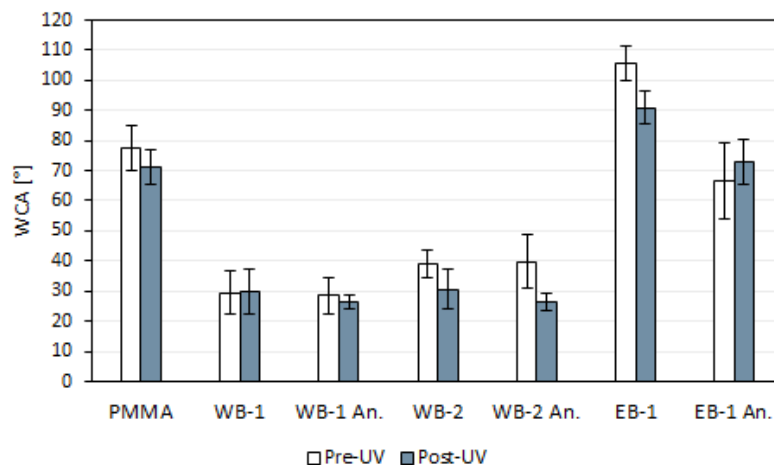


Figure 3.39: Wettability before and after UV irradiation of spray-coated PMMA samples.

Figure 3.39 reports the values of WCA on coated PMMA before and after UV irradiation. The average variation in hydrophilicity is within the experimental error (5°), therefore the coatings showed poor or absent photo-activation.

These poor results are further confirmed in Figure 3.40, which reports the hydrophilization and WCA recover of spray-coated PMMA samples. The results are erratic and it is not possible to make concluding comments. The behavior is indeed unpredictable, owing to the small variations observed which, as said, fall within the experimental error.

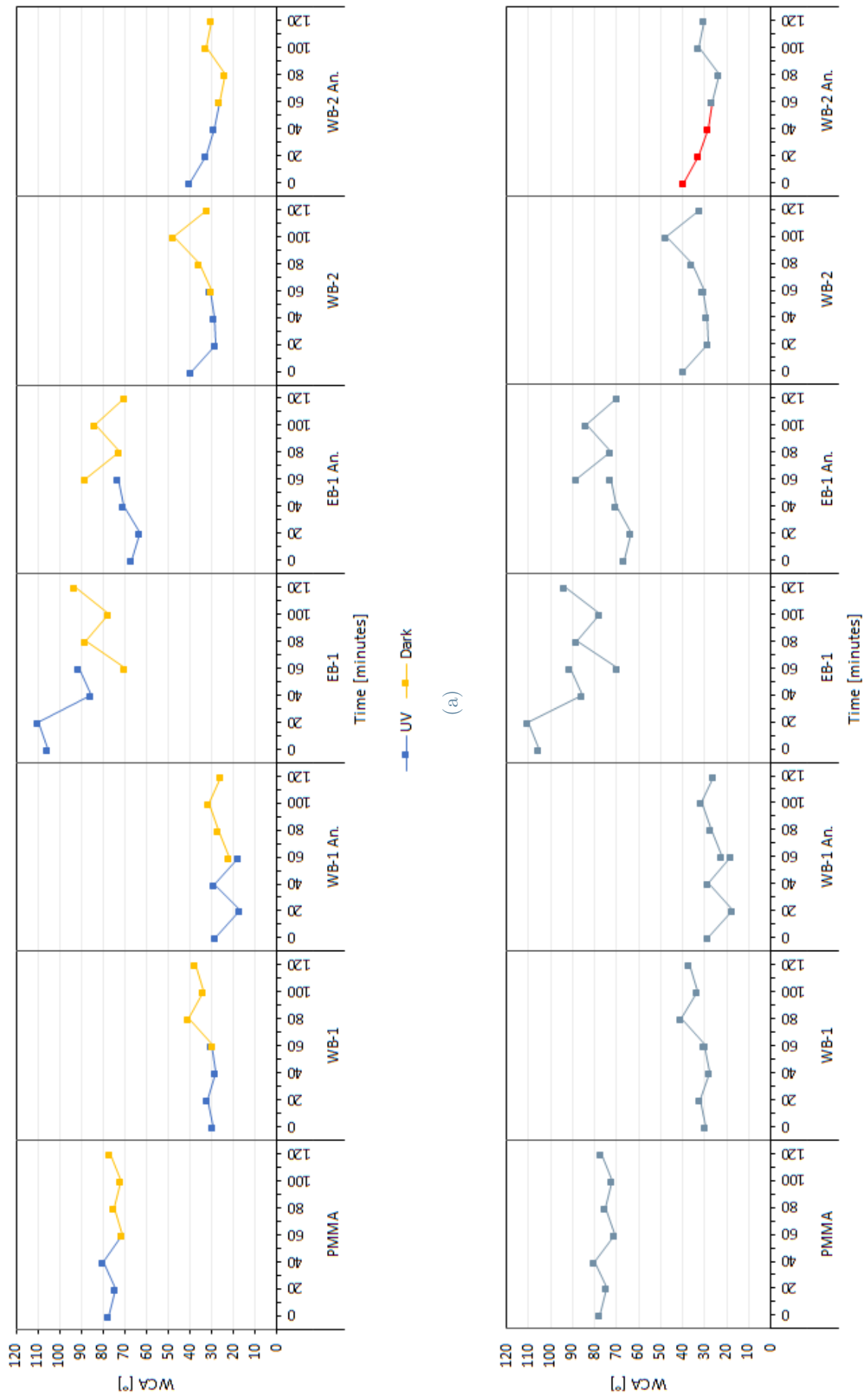
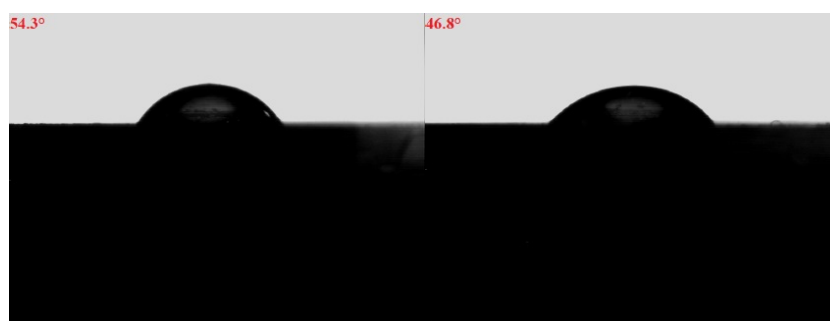


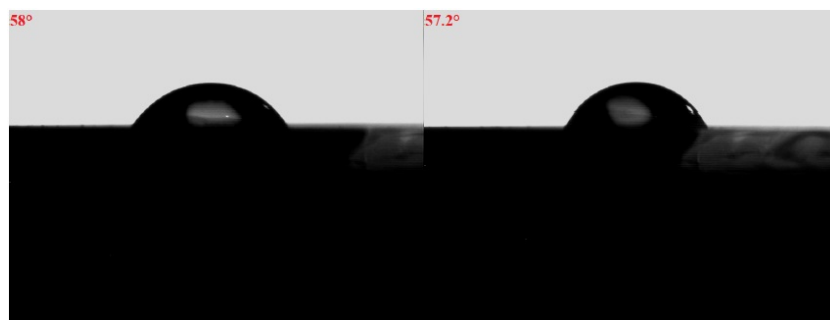
Figure 3.40: Photoinduced hydrophilicity of spray-coated PMMA samples.

3.3.4. Photoinduced hydrophilicity

The following images, which portray spray-coated glass samples, serve as an aid to visualize the occurring photoinduced hydrophobicity. The *An.* specimens were annealed following coating deposition for two hours at 90°C. To show the effects of photoinduced hydrophobicity, each sample was irradiated for one hour with a HG 500 UV lamp emitting about 120 mW cm^{-2} [79].



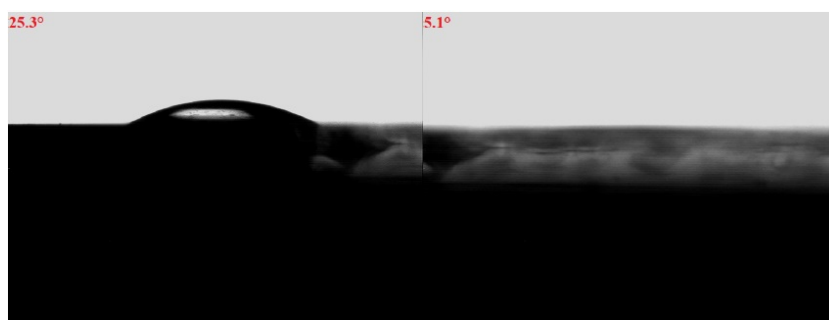
(a) EB-1



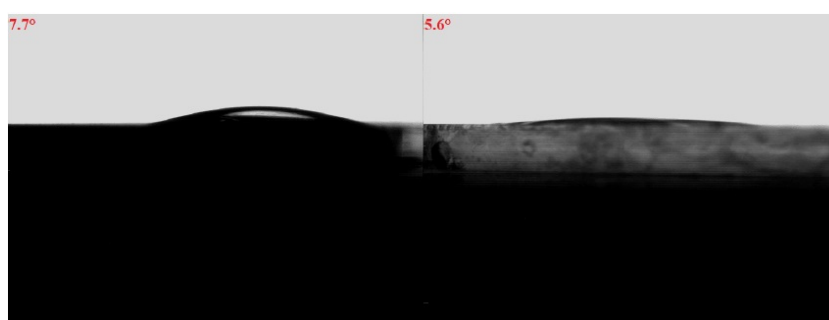
(b) EB-1 An.

Figure 3.41: Photoinduced hydrophobicity of glass spray-coated with *EB-1*.

Deposition of the ethanol-based sol-gel increases the static water contact angle of the substrate (Figure 3.41). This is likely due to the use of ethanol as solvent, which could have formed a hydrophobic complex with titanium. The annealing treatment, carried out at 90° for two hours, does not considerably influence wettability.

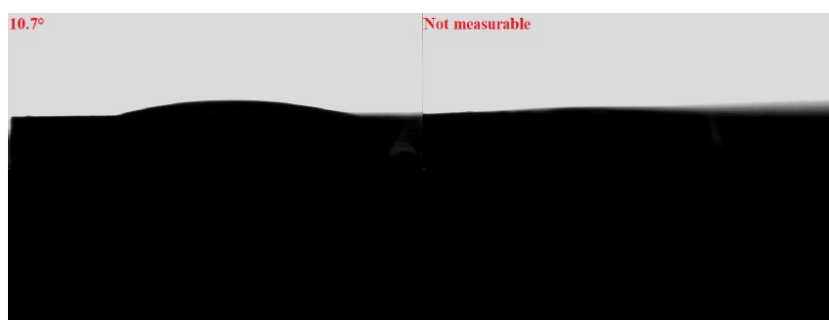


(a) WB-1

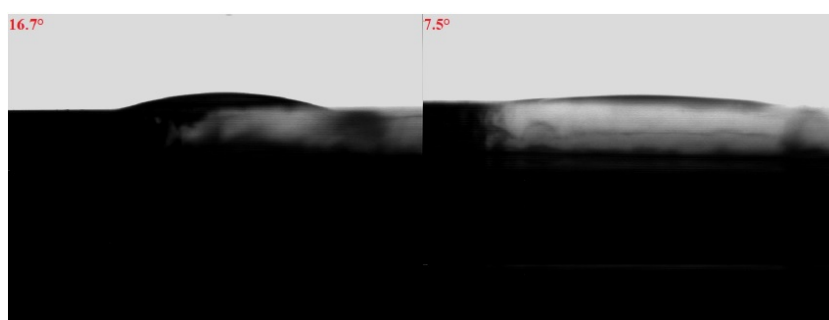


(b) WB-1 An.

Figure 3.42: Photoinduced hydrophilicity glass sprat-coated with WB-1.



(a) WB-2



(b) WB-2 An.

Figure 3.43: Photoinduced hydrophilicity of glass spray-coated with WB-2.

As shown in Figure 3.42 and Figure 3.43, water-based coatings allow to reach superhydrophilicity following UV irradiation. Once again, the annealing treatment, carried out at low temperature (90°C), does not considerably influence the water contact angle.

3.4. Color variations

In an ideal scenario the applied coating should be transparent, so that the aesthetic appearance of the substrate is maintained. It is especially important when considering the application on transparent substrates, such as windows, so that their primary function is preserved. Sol-gel solutions employed in this dissertation formed translucent non-homogeneous coatings, therefore it was necessary to quantify the color variation that followed coating deposition and thermal treatment. To this purpose, each sol-gel solution (Table 2.1), aged for 160 days, was sprayed on three PMMA samples (10 cm x 7.5 cm), which were then annealed for two hours at 90°C.

3.4.1. Coating deposition

Table 3.1: CIELAB coordinates of PMMA samples following coating deposition by spray-coating and annealing treatment (SCI mode).

Sample ID	WB-2			WB-1			EB-1		
Coordinates	L*	a*	b*	L*	a*	b*	L*	a*	b*
Background	90.74	1.73	-11.37	90.74	1.73	-11.37	90.74	1.73	-11.37
Virgin sample	90.13	0.62	-7.81	89.77	0.63	-7.64	89.79	0.65	-7.69
Spray-coated sample	87.12	0.24	-6.02	86.87	0.29	-6.21	87.96	0.16	-5.61
Annealed sample	86.74	0.27	-5.94	86.12	0.31	-5.87	87.84	0.06	-4.88

The method for coating deposition follows the guidelines reported in Chapter 2.1.2.2, while the results have been analysed as explained in Chapter 2.2.3.3 and Chapter 2.2.3.1.

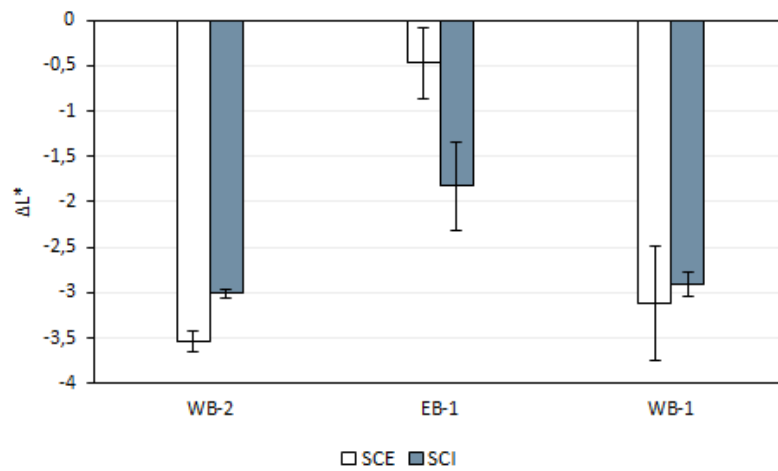


Figure 3.44: Variation in the L^* coordinate following coating deposition.

The sol-gel application led to a decrease in the L^* coordinate, hence as per definition it induces a loss of lightness. As the variation is higher than 1 the difference is clearly perceivable by the human eye.

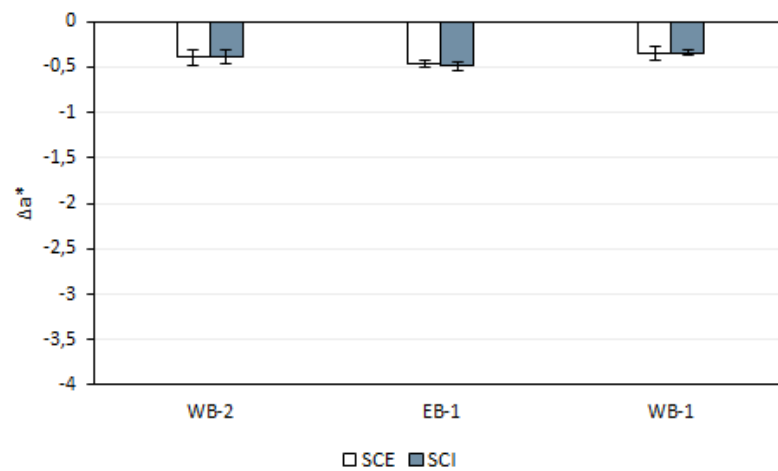


Figure 3.45: Variation in the a^* coordinate following coating deposition.

The decline in coordinate a^* is below 1 so the color difference is not perceptible.

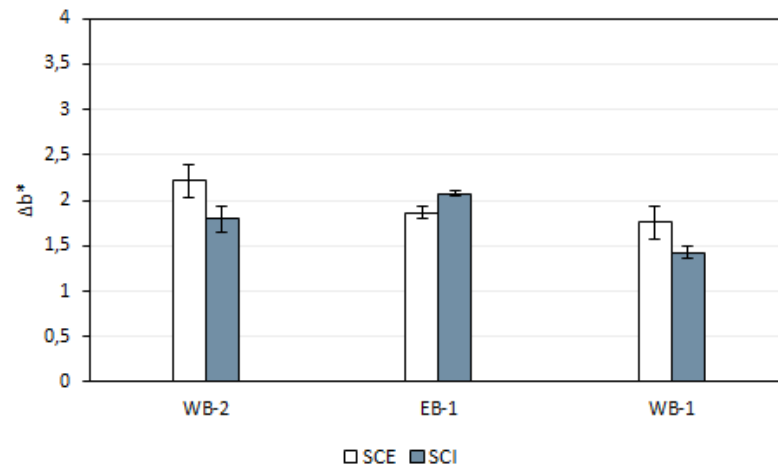


Figure 3.46: Variation in the b^* coordinate following coating deposition.

The increase of b^* , on the other hand, is associated with sample yellowing. Although perceivable, the color variation is slight, as portrayed in Table 3.1. The values are representative of each sol-gel and are computed as an average of the SCI values acquired from three different samples.

3.4.2. Thermal treatment

Following coating deposition, the samples were annealed at 90°C for two hours. The following graphs report the color variations induced by the thermal treatment (Figure 3.47, Figure 3.48, Figure 3.49).

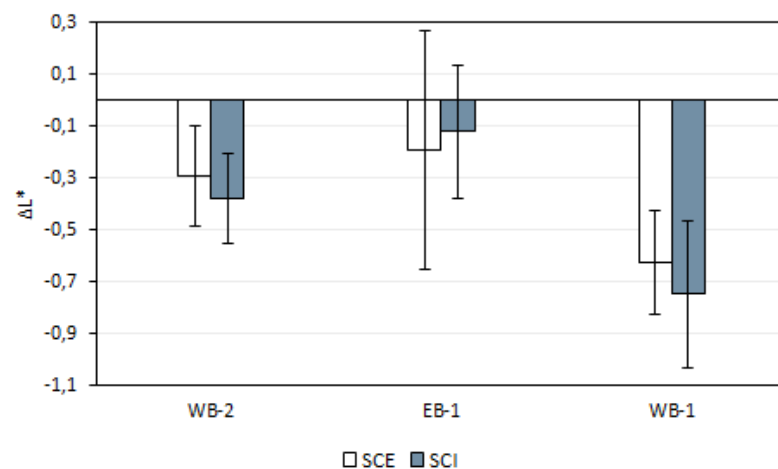


Figure 3.47: Variation in the L^* coordinate following thermal treatment.

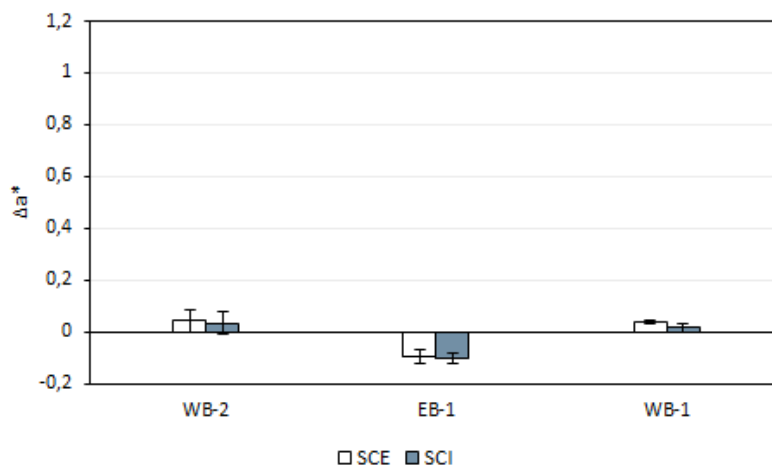


Figure 3.48: Variation in the a* coordinate following thermal treatment.

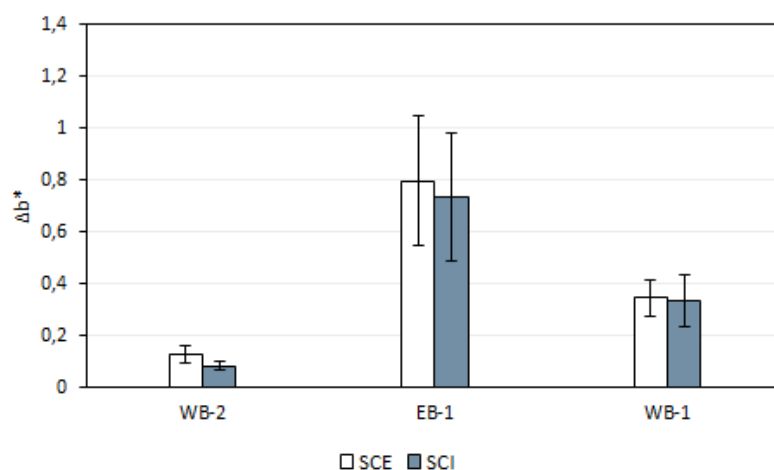


Figure 3.49: Variation in the b* coordinate following thermal treatment.

As the variations are below 1 for all coordinates, the color variations that follow sample annealing are negligible as they are unperceivable by the human eye. Table 3.1 summarizes the average values of the CIELAB coordinates for each sol-gel type.

3.5. Soiling

The self-cleaning ability of the coatings was evaluated by subjecting them to soiling tests and monitoring their color variations. Coatings with a more pronounced self-cleaning ability were expected to display negligible color variations, as the water-sheeting effect would remove the deposited dirt.

Accelerated tests were carried out as preliminary tests to determine whether the coatings potentially displayed self-cleaning ability. Natural soiling tests were, instead, carried out to determine the real performance of the coatings as well as their resistance when exposed to weathering.

3.5.1. Accelerated soiling

Table 3.2: CIELAB coordinates following accelerated soiling tests (SCI mode).

Coordinates	Background			Sample			Soiled sample		
	L*	a*	b*	L*	a*	b*	L*	a*	b*
WB-1	90.74	1.73	-11.37	88.29	0.06	-6.83	79.20	2.00	-1.04
WB-1 An.	90.74	1.73	-11.37	86.21	-0.35	-5.38	74.27	2.07	2.37
WB-2	90.74	1.73	-11.37	88.51	-0.05	-6.68	77.80	1.53	-0.28
WB-2 An.	90.74	1.73	-11.37	86.04	-0.24	-5.81	76.56	1.5	1.18
EB-1	90.74	1.73	-11.37	87.43	0.053	-3.67	80.85	1.08	2.16
EB-1 An.	90.74	1.73	-11.37	87.75	0.52	-6.93	80.41	1.11	-2.40
Glass	90.74	1.73	-11.37	89.37	0.86	-9.54	80.08	2.17	-4.16

The results of the accelerated soiling test are portrayed in Table 3.2, where each coordinate represents the average of three measurements. Due to the small difference between values obtained by SCI and SCE mode, only SCI values are reported. As portrayed in the last column of Table 3.2, and in Figure 3.50, soiling decreases L^* but increases the value of b^* , while the variations in a^* , as they are below 3, are not perceptible. Therefore, the samples became darker and acquired a yellow-hue.

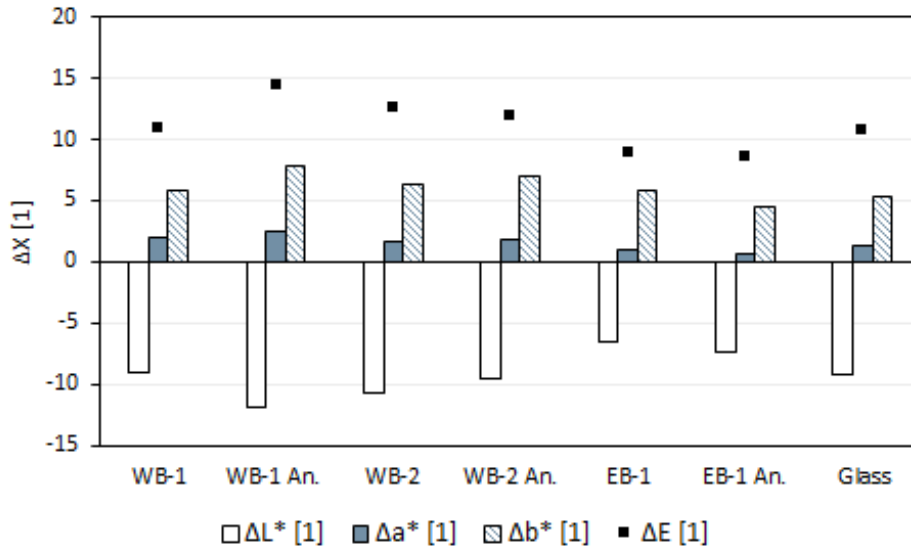


Figure 3.50: Variation of CIELAB coordinates following sample soiling (SCI mode).

Samples with stronger self-cleaning ability were expected to show small values of ΔE . Therefore, according to the results, the best self-cleaning coatings are *EB-1* and *EB-1 An.*, whose ΔE values are 8.85 and 8.64, respectively. Unexpectedly, glass performed better than any water-based coating. The author proposes the following motivations:

- glass and ethanol-based coatings are both smooth and regular, while water-based coatings present a rougher surface. Although water-based coatings are more hydrophilic, the surface roughness could trigger a pinning-effect that prevents the water droplets from sliding. The smoother surface of glass and *EB-1*, instead, enhances water flow and thus the surface self-cleaning ability;
- the soiling effect could have increased the surface hydrophobicity. Thus, *EB-1*, which already had higher WCA than the other coatings, could have become hydrophobic. Hydrophobic surfaces, which rely on drop-rolling rather than drop-sliding, have been reported to be more efficient than hydrophilic ones;
- according to the author the test should have included a second stage in which the surfaces should have been exposed to high humidity, or water-spray, and UV irradiation. The irradiation, as previously reported in the introduction, would have triggered the photocatalytic reaction, restoring the initial hydrophilicity of the surface. Whereas, the water-spray would have promoted water-sheeting and thus the self-cleaning ability of the surface.

For these reasons the author believes the test is incomplete and biased, as it ad-

vantages coatings with higher hydrophobicity. Following these considerations, the better performance of glass and *EB-1* is inevitable.

3.5.2. Natural soiling

Samples subjected to natural soiling were monitored weekly. However, during the five-month test, the coating was subjected to environmental wear, indeed, as shown in Figure 3.51, it partially detached from the substrate. Therefore, the reported results not only take into account the color variation due to soiling, but also due to the loss of coating.

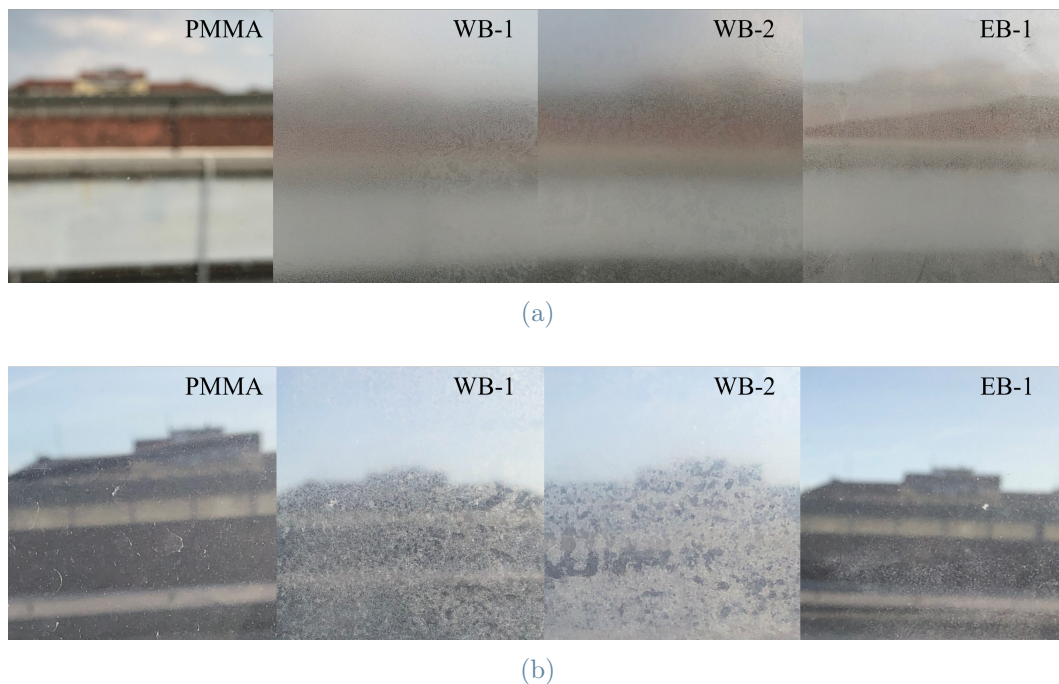


Figure 3.51: Coating appearance at the beginning (a) and at the end (b) of the natural soiling tests.

3.5.2.1. SCI and SCE mode

The results pertaining to color variation are reported in both SCI and SCE mode, as significant differences were observed between the two modes. As shown in Figure 3.52, the values obtained in SCI mode demonstrate the remarkable self-cleaning functionality of the coated PMMA samples. In contrast, the uncoated PMMA samples exhibited higher values of ΔE , which linearly increased over time. The curves representing the PMMA samples are visibly distant from those of the coated specimens, thus emphasizing the distinct self-cleaning abilities of the two groups of samples.

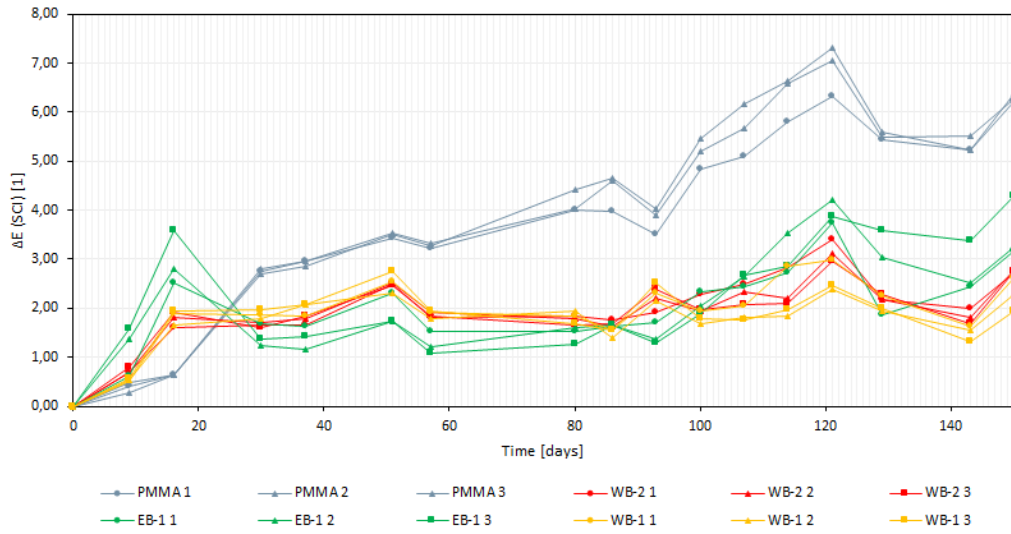


Figure 3.52: Color variation during natural soiling (SCI mode).

Data obtained in SCE mode provides valuable information about the appearance of the coating, as this mode accounts for specular reflectance and is therefore sensitive to variations in surface finish. Indeed, soiling due to dust and particulate matter not only alters the surface color but also transforms the PMMA surface from glossy to matte, thus affecting the acquired data. Thus, SCE mode is a better representation of human color perception and is more suitable for evaluating the self-cleaning ability of surfaces. Figure 3.53 displays the data acquired in SCE mode and shows that the curves representing the uncoated and coated PMMA samples are closer together than in Figure 3.52. This suggests that the self-cleaning ability of the different samples is not clearly discernible using this mode. For example, the curves representing the uncoated samples and the water-based coatings overlap during the first two months, but then diverge, potentially indicating the coatings' resistance to soiling. Since the data acquired in SCI mode demonstrates the self-cleaning functionality of the coatings, it is important to investigate the source of the large difference between the data obtained in the two modes. As ΔE provides limited information about how two colors differ, the phenomenon will be further analyzed by examining each color coordinate as well as the meteorological conditions.

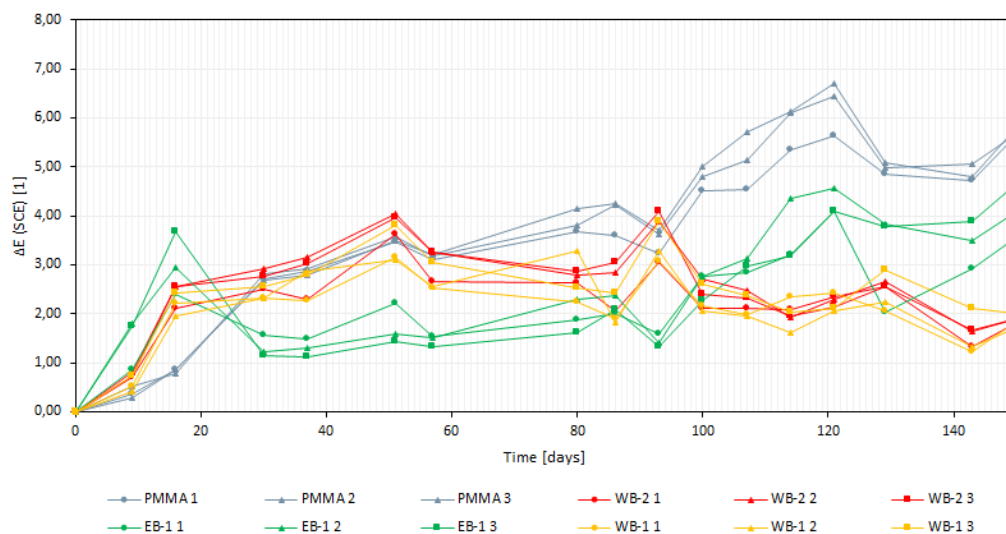


Figure 3.53: Color variation during natural soiling (SCE mode).

The behavior of the coating samples under soiling and weather conditions reveals two significant phenomena. First, the curves representing the same sample type exhibit similar patterns (Figure 3.54, Figure 3.55, Figure 3.56 and Figure 3.57), indicating that coating deposition is a repeatable process: coatings obtained from the same solutions and deposited in the same manner yield surfaces that behave similarly. Second, each coating type exhibits a unique self-cleaning behavior, reacting differently to soiling and weathering. Notably, water-based coatings demonstrate similar self-cleaning patterns, suggesting that the choice of solvent highly influences the self-cleaning mechanism. Therefore, to simplify the following analysis only one curve was selected from each batch. The graphs representing the pattern behavior acquired in SCE mode are portrayed in Appendix A (Figure A.1, Figure A.2, Figure A.3 and Figure A.4).

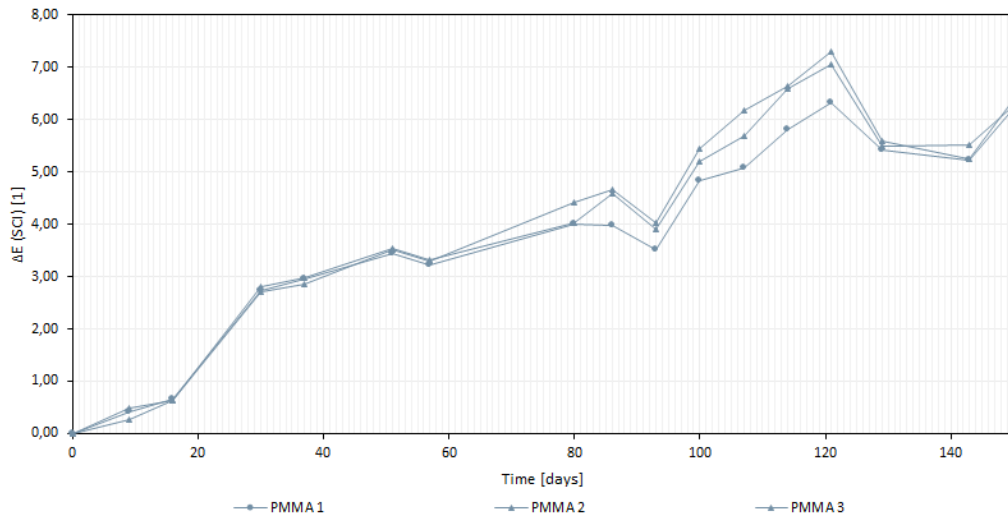


Figure 3.54: Pattern behavior of PMMA samples exposed to natural soiling (SCI).

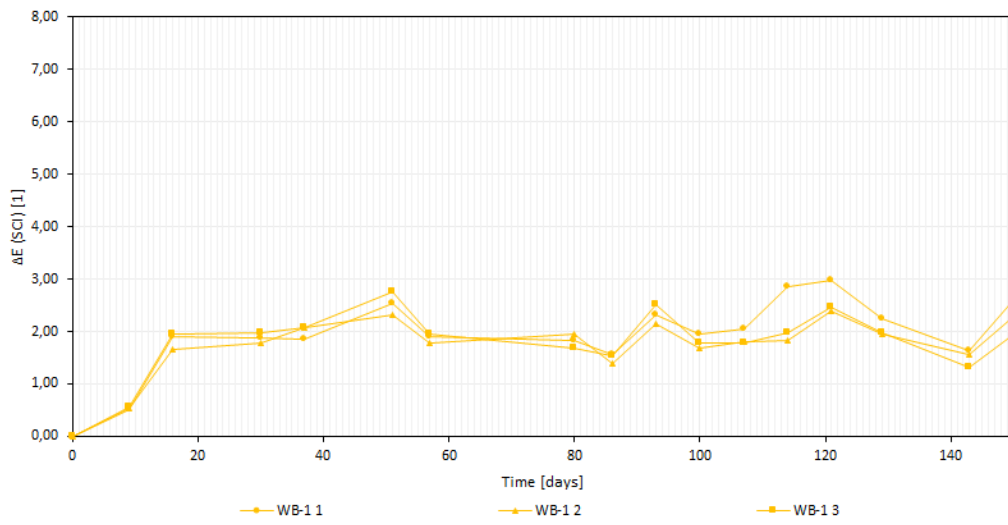


Figure 3.55: Pattern behavior of WB-1 exposed to natural soiling (SCI).

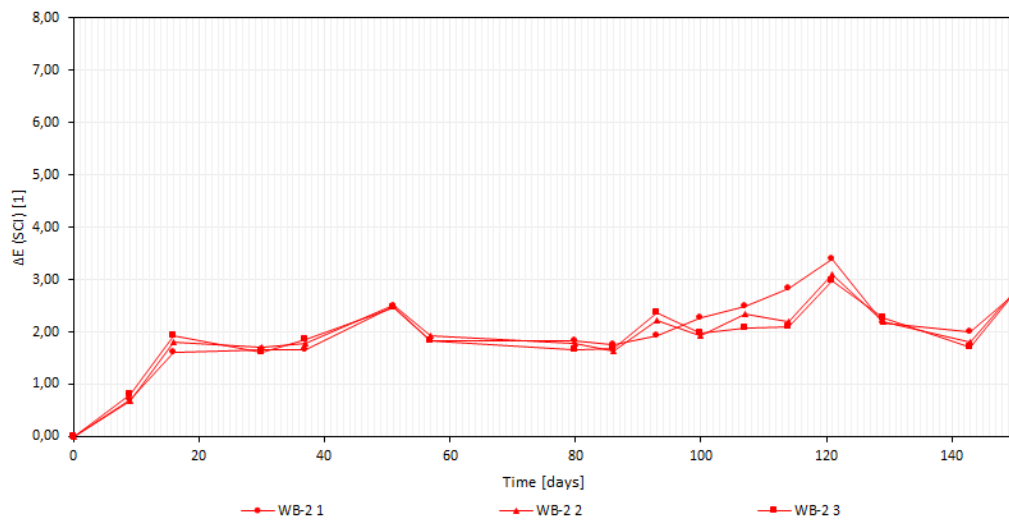


Figure 3.56: Pattern behavior of *WB-2* exposed to natural soiling (SCI).

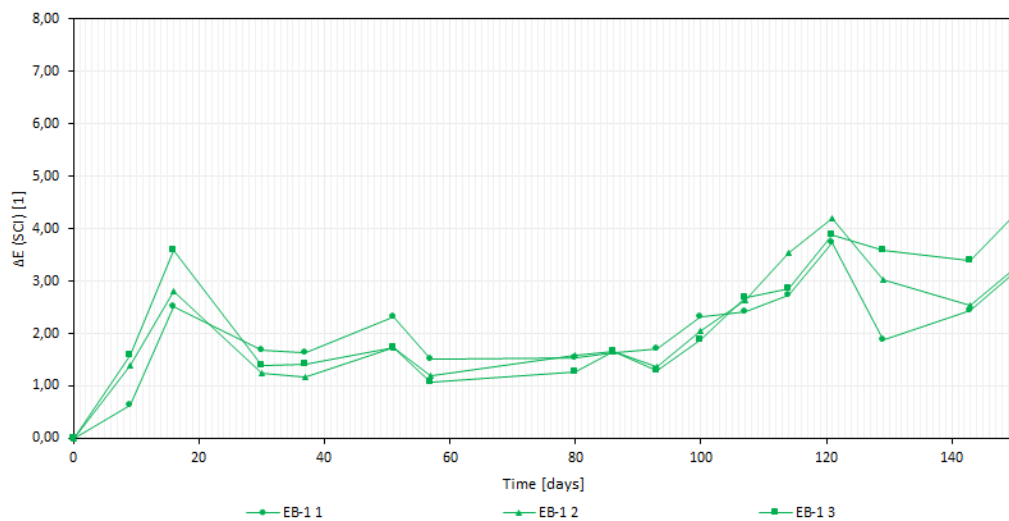


Figure 3.57: Pattern behavior of *EB-1* exposed to natural soiling (SCI).

3.5.2.2. CIELAB coordinates

To understand which coordinates most closely represent either soiling or the loss of coating, three additional graphs, which represent the variations in the single coordinates, were prepared. Overall, the soiling test induced larger variations in the L^* and b^* coordinates, which respectively showed progressive darkening and yellowing of the samples (Figure 3.58 and Figure 3.59). The a^* coordinate, however, did not show any variation (Figure A.7 and Figure A.8). The graphs representing data acquired in SCI mode are in Appendix A (Figure A.5 and Figure A.6).

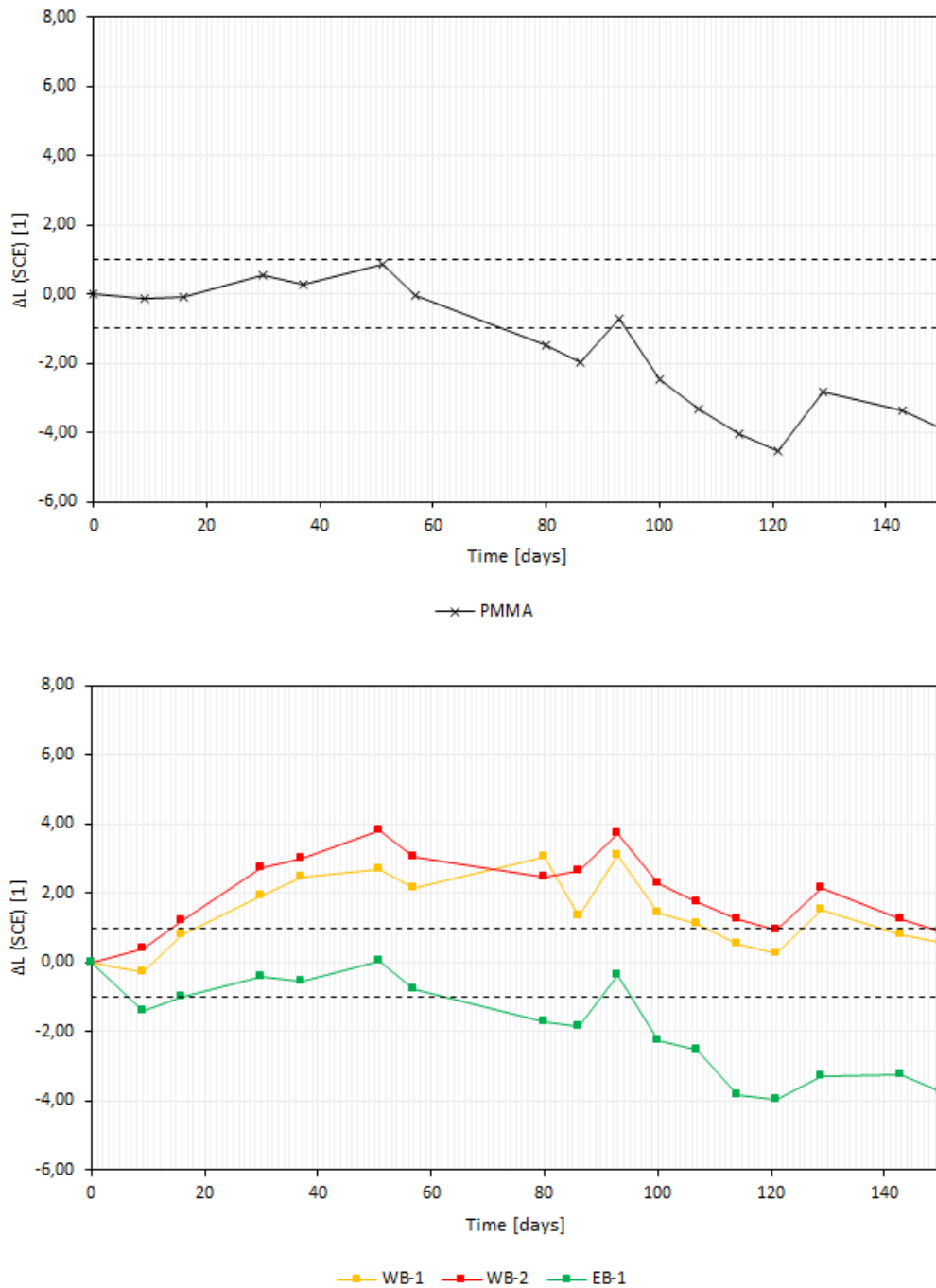


Figure 3.58: Variation of the L^* coordinate during natural soiling (SCE).

The reference sample showed negligible variation of the L^* coordinate in the first three months of the test, as the ΔL^* value was always below 1. Following this period, the sample became progressively darker proving that particulate matter and dust accumulated on the surface. On the other hand, the water-based coated samples portrayed a positive variation in ΔL^* , while the ethanol-based one behaved similarly to the reference samples, as its value

remained unchanged and became negative at the 100-day mark. The positive variation could be due to both coating detachment and soiling:

- although the coatings are deposited on a transparent substrate, and therefore the loss of coating should not increase the value of L^* , the measurements were taken using white printing paper as background. Since the coating is translucent, the white background partially influences the CIELAB coordinates acquired during measurements. Considering perfectly adherent coatings, when computing ΔL^* the background contribution is eliminated. However, when the coating is partially detached, the influence from the background increases as the material becomes partially more transparent, thus when computing the difference there still is some contribution left which overall increases the luminosity of the color. In addition, the contribution from the background cannot be eliminated a priori from the acquired data, as the contribution increases with the coating's transparency. Opaque coatings would virtually have no contribution, however, the present dissertation deals with translucent coatings and it is not possible to estimate how much the substrate influences the acquired data;
- although soiling predominantly influences luminosity, it also turns the surface from glossy to matt, thus further increasing the ΔL^* value when data is acquired through the SCE mode. Additionally, the weathering effect of precipitations likely increased the surface roughness, further affecting the acquired data.

Variations in the b^* coordinate are due to three reasons:

1. soiling: as introduced in the results of the accelerated test, soiling increases the b^* coordinate endowing the samples of a yellow hue;
2. chemical degradation: polymer materials, such as PMMA, are subjected to chemical degradation induced by UV irradiation, which induces a yellowing-effect;
3. coating deposition: as previously demonstrated, coating deposition increases the b^* coordinate: therefore negative Δb^* values could indicate the loss of coating.

As shown in Figure 3.59, the reference sample shows a consistent increase in Δb^* , which could be do to soiling and chemical degradation. Whereas, in the coated samples, Δb^* increased in the first month and remained constant around 1.0 and 2.0. As the coatings are translucent, and their coating thickness is below 1 μm , for simplicity one can assume that all the samples were subjected to the same amount of chemical degradation, and the variations in Δb^* are attributable to either soiling or coating loss. Nonetheless, it is not possible to separate the two effects. However, given the current analysis, the L^*

coordinate most closely represents the soiling effect on the tested samples, as in the 90 to 120-day range, when no precipitation occurred, ΔL^* decreased considerably, while Δb^* , despite increasing, showed negligible variation.

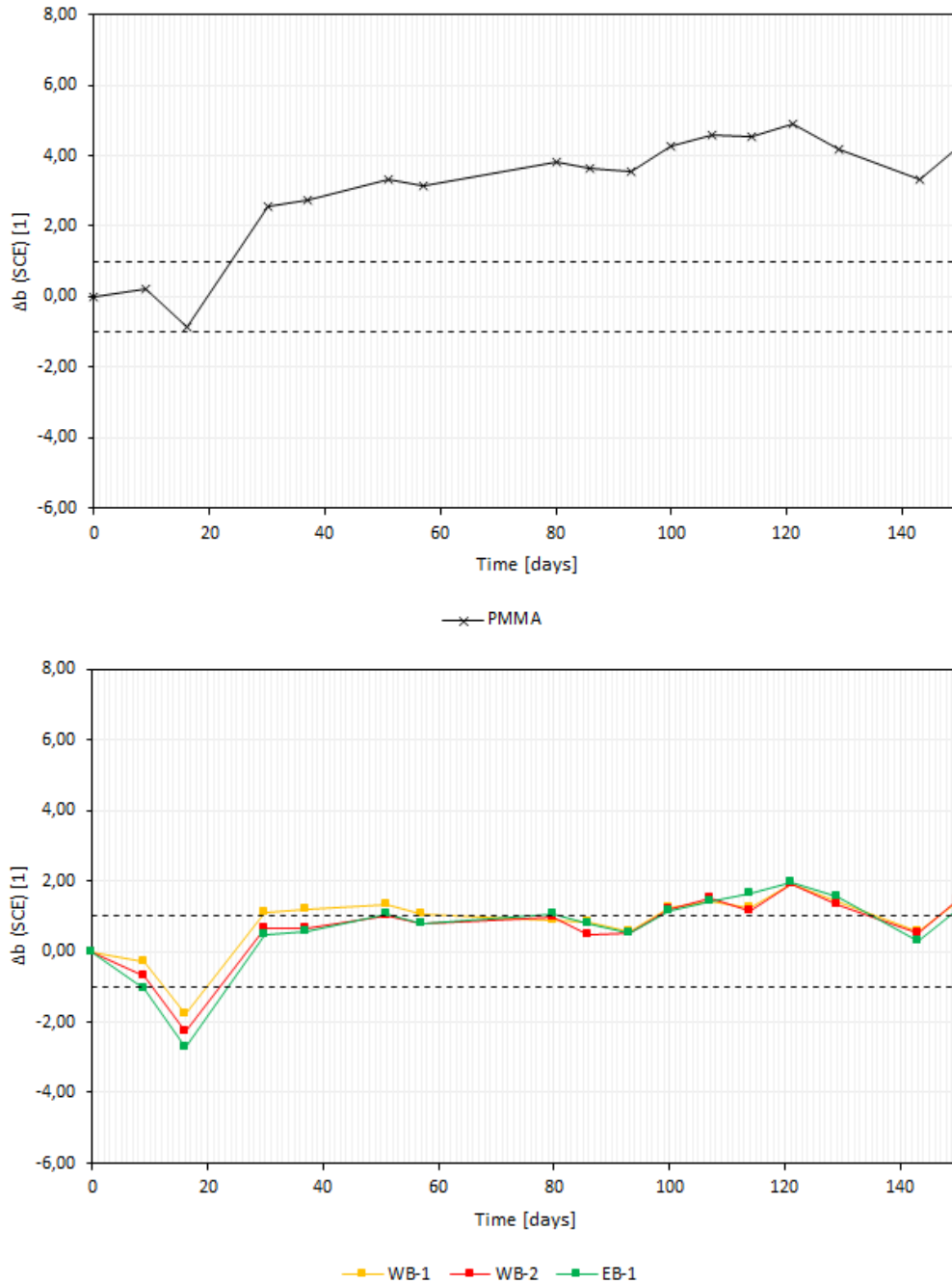


Figure 3.59: Variation of the b^* coordinate during natural soiling.

3.5.2.3. Meteorological data

As previously stated, only one curve was chosen from each batch to simplify the analysis on the correlation between meteorological phenomena and color variation.

Figure 3.60 shows the soiling curves, which represent each sol-gel batch, and the precipitation data; furthermore, different periods have been highlighted to help visualize when considerable color variations were witnessed: positive variations, which indicate soiling, were highlighted in blue, while negative ones in green,

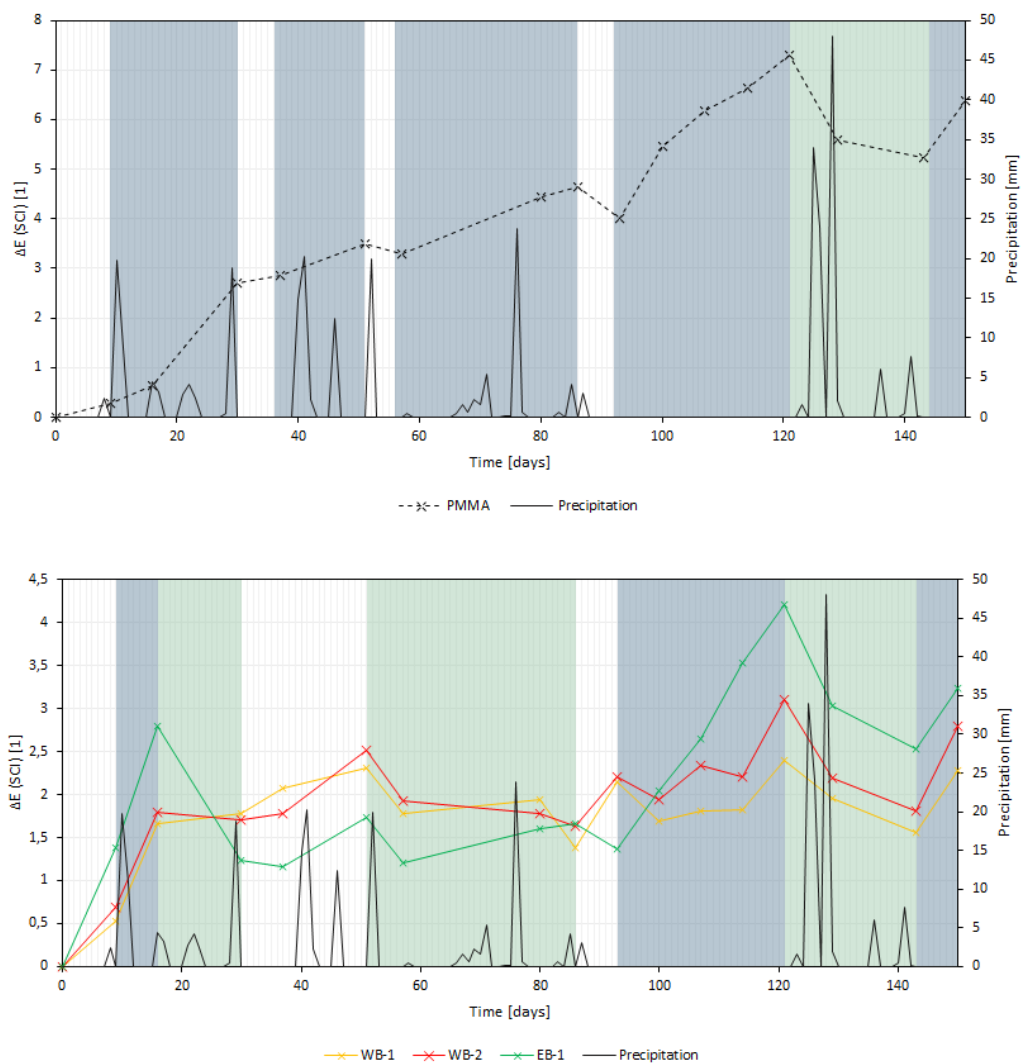


Figure 3.60: Correlation between precipitation and sample soiling (SCI).

Data representing the reference samples shows how the sample progressively gets more soiled. As the highlighted areas show, the color variation increases regardless of the amount of precipitation witnessed by the sample. Through the highlighted area ranging

between 90 and 120 days, given the extensive time in which no precipitation was witnessed, it is possible to compute the soiling rate, approximately equal to $0.117 \Delta E \text{ days}^{-1}$. On the other hand, in the same period, *WB-1*, *WB-2*, and *EB-1*, had the following rates 0.009, 0.031, $0.088 \Delta E \text{ days}^{-1}$, respectively. Indeed, as shown by the green highlighted areas, precipitations either diminish the values of ΔE or hamper further soiling in coated samples. The water-based coatings, which show similar behavior with close values of ΔE , are more efficient than the ethanol-based coatings.

Global radiation alone cannot enhance the self-cleaning functionality of surfaces, but it is necessary to hydrophilize the coating and induce the necessary photocatalytic reaction. Therefore, data should show considerable loss of ΔE when abundant precipitations were anticipated by high values of global radiation. However, as shown in Figure 3.61, these instances were infrequent and the ΔE variations too inconsistent to draw any definitive conclusions. This may be because the study was conducted during autumn and winter, when global radiation is moderate. Further investigation during spring and summer could provide more insight into the influence of solar radiation on the coatings' self-cleaning mechanism.

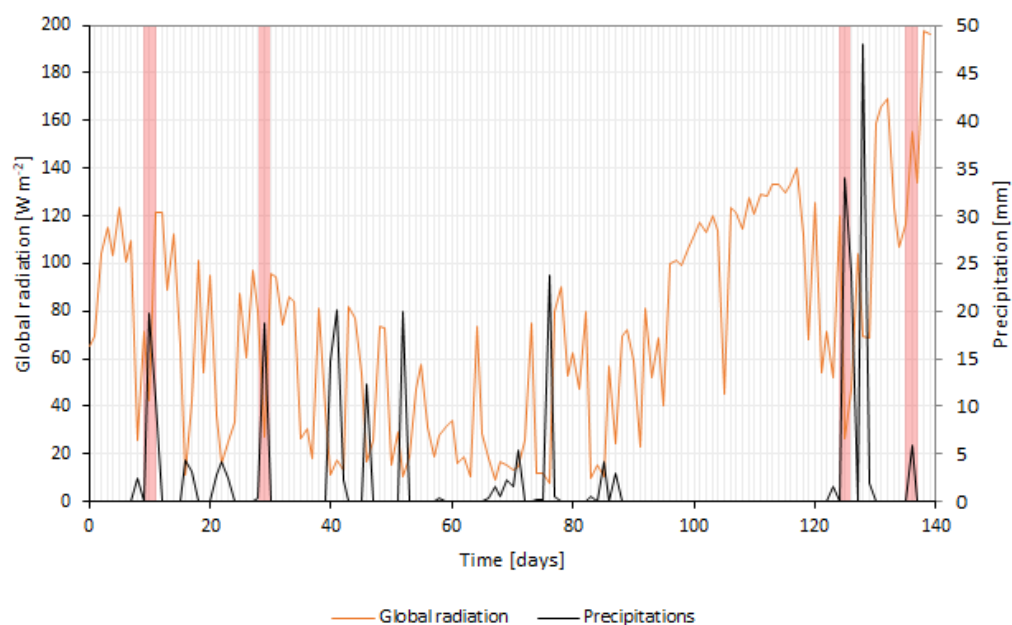


Figure 3.61: Global radiation and precipitation data, with highlighted the areas where precipitations is anticipated by high global irradiation.

In the region from 95 to 115 days, high and constant radiation was reported with small variations in ΔE for the coated samples compared to the uncoated ones. The author

hypothesized that the lower variation in ΔE could be due to the coating self-cleaning behavior induced by the synergy between high solar radiation and high relative humidity. However, as shown in Figure 3.62, although high global radiation was reported, the relative humidity was low compared to the previous months. Indeed, in the highlighted period, relative humidity fluctuates between 40% and 60%, not enough to wet the surface.

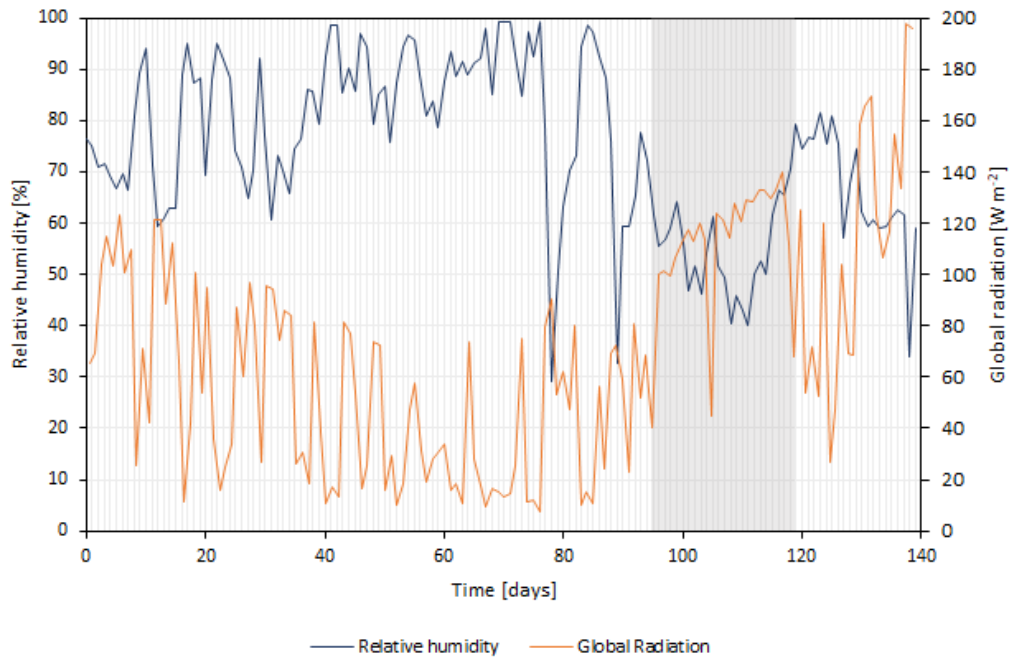


Figure 3.62: Global radiation and relative humidity data, with highlighted the area where no precipitation was recorded.

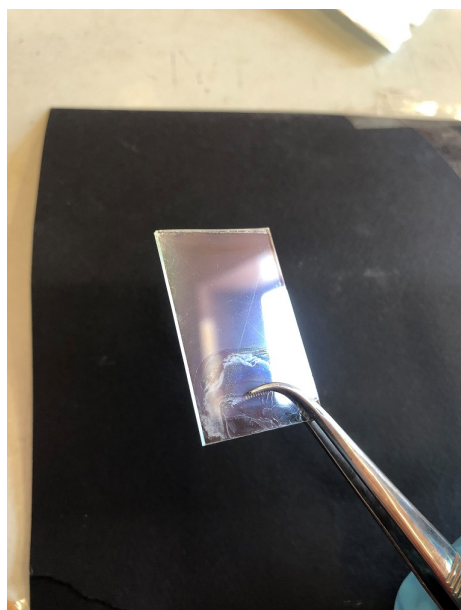
3.6. Adhesion tests

The following paragraph summarizes the results of the qualitative adhesion test, which was carried out to evaluate the level of adhesion between coating and glass. As shown in Table 3.3 the water-based samples (*WB-1* and *WB-2*) performed poorly in both tests, while *EB-1* showed excellent adhesion.

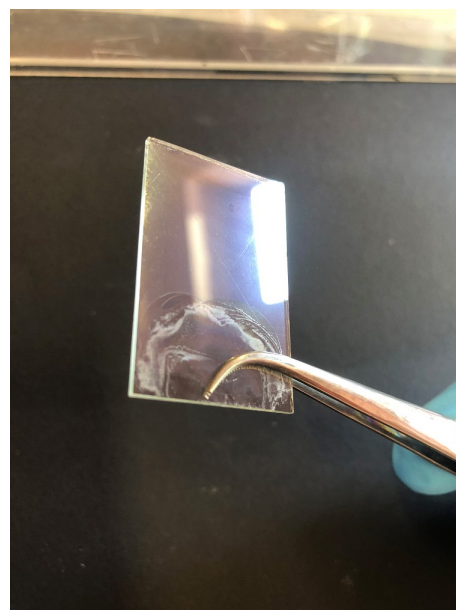
Table 3.3: Adhesion test results.

Sample ID	Test method	Ranking
WB-1	X-Cut	N/A or 0A
	Cross- Cut	N/A or 0B
WB-1 An	X-Cut	N/A or 0A
	Cross- Cut	N/A or 1B
EB-1	X-Cut	5A
	Cross- Cut	4B
EB-1 An.	X-Cut	5A
	Cross- Cut	5B
WB-2	X-Cut	N/A or 0A
	Cross- Cut	N/A or 0B
WB-2 An.	X-Cut	N/A or 0A
	Cross- Cut	N/A or 0B

The ethanol-based coatings, for example like the one shown in Figure 3.63, remained intact after tape removal regardless of coating homogeneity. On the other hand, the water-based samples performed poorly and, according to the standard instructions, they were not classifiable. Not only were the samples subjected to major material loss in areas beyond the incised surface, but the tape glue partially transferred onto the surface (Figure 3.64).



(a) Before tape application.



(b) After tape removal.

Figure 3.63: X-Cut adhesion test results for sample EB-1.



(a) Before tape application.



(b) After tape removal.

Figure 3.64: X-Cut adhesion test results for sample WB-1.

This phenomenon occurred categorically for each water-based sample regardless of the adopted method. Figure 3.65 clearly shows both the transfer of coating onto the tape

and the transfer of glue onto the sample. Regardless, the samples were classified with the lowest rank owing to the extended loss of material.



Figure 3.65: Comparison between tested sample and removed tape.

This phenomenon was also reported by Retolaza et al. who performed cross-cut tests on TiO_2 coatings deposited on PMMA [93]. The authors concluded that performing the test immediately after coating deposition results in the adhesion of the glue onto the surface, whereas when the test is performed months after deposition the phenomenon does not occur [93]. They postulate that right after deposition the coating has high surface energy and it is thus prone to adhere to other materials. Indeed, their results support this theory as wettability tests showed high hydrophilicity just after deposition, followed by gradual increase in the water contact angle up to 6 weeks [93]. This hypothesis, however, does not explain why the phenomenon did not occur on the alcohol based samples as well.

During testing, the tape removal was smoother and easier on the ethanol-based samples; whereas, testing on the water-based samples was more challenging as the tape clung to the surface and a greater force was needed to peel off the tape. The non-homogeneous surface of the samples seemed to be the reason of this behavior, as the tape seemed to be more adherent to the white portions of the coating. Indeed, after abrading the white defects with a paper towel the tape removal was smoother and less glue adhered to the surface. On the other hand, abrading the alcohol based samples did not result in material loss, once again proving the high adherence of the coating to the substrate.

In conclusion, this test was not successful in determining the adhesion of the coating to the surface for it was necessary to apply a different force to each type of coating, as a consequence, per standard instructions, the results are not comparable. Rather than

assessing the level of adhesion of the coating to the substrate, the test seemed to establish the level of adhesion of the tape to the coating. Alternative adhesion tests should be performed in the future, as, nonetheless, the ranking system is limited and the difference among annealed and non-annealed samples is not appreciable.

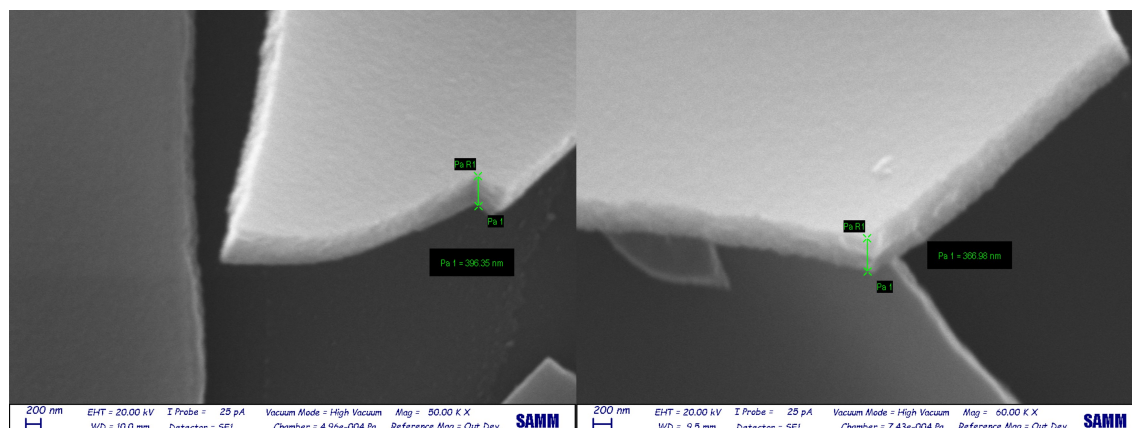
3.7. Morphological analysis

Given the different performance of *WB-1*, *WB-2*, and *EB-1*, morphological analysis was carried out to determine the surface appearance of a selected number of samples, since both photocatalytic activity and wettability are influenced by surface roughness and coating porosity.

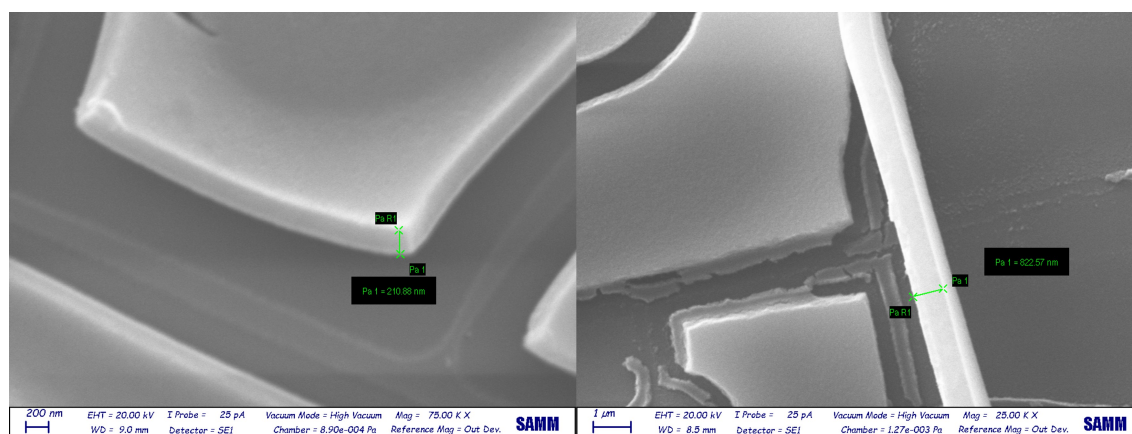
Twelve samples were analysed with a scanning electron microscope to determine the influence on morphology of multiple parameters, such as the use of different solvents in sol-gel formulations, the effect of different annealing treatments, and deposition techniques. The following chapters summarise the observations and comments that were made during the analysis.

3.7.1. Coating thickness

Coating thickness was assessed to determine whether spray- and dip-coating deposit different amounts of solution. First of all, as shown in Figure 3.66a, thermal treatment slightly influences coating thickness. Indeed, the coating (*WB-1*), which was deposited on glass by immersion, had a thickness of about 400 nm and of 370 nm before and after annealing, respectively. This reduction in thickness after annealing is consistent with the removal of solvent molecules and the densification of the coating. In both pictures showed in Figure 3.66a it is also possible to distinguish the two deposited layers, therefore it is safe to assume that each layer deposited by dip-coating is about 190 nm thick.



(a) Thickness of WB-1 before (left) and after (right) annealing at 500°C for two hours.



(b) Thickness of EB-1 (left) and WB-2 (right) after annealing at 500°C for two hours.

Figure 3.66: Thickness of sol-gel coatings deposited by immersion.

The thickness of coatings obtained by immersion of *EB-1* and *WB-2* is of 210 nm and 822 nm, respectively (Figure 3.66b). The reduced thickness of *EB-1* compared to the water-based solutions explains why, contrary to the coatings yielded by the water-based sol-gels, the coatings were homogeneous and transparent. The small thickness could be explained by the low viscosity of *EB-1*, which did not properly age as its viscosity did not vary in the months following synthesis. The thickness of the coating obtained by deposition of *WB-2* is unusually high: on one hand it could explain its higher photocatalytic activity, on the other it probably does not represent average coating thickness but rather a localized build-up of material.

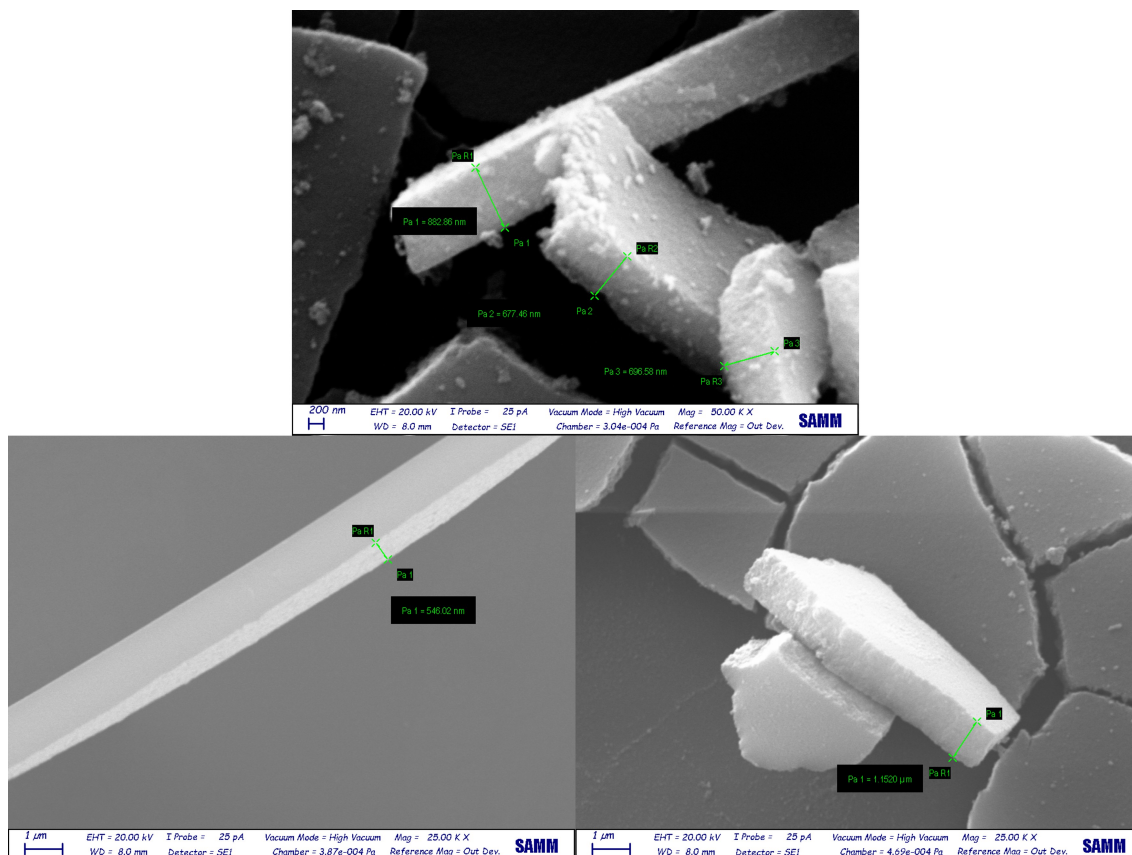


Figure 3.67: Thickness of *WB-1* (top), *EB-1* (left), *WB-2* (right), deposited by spray-coating on glass and annealed at 90°C for two hours.

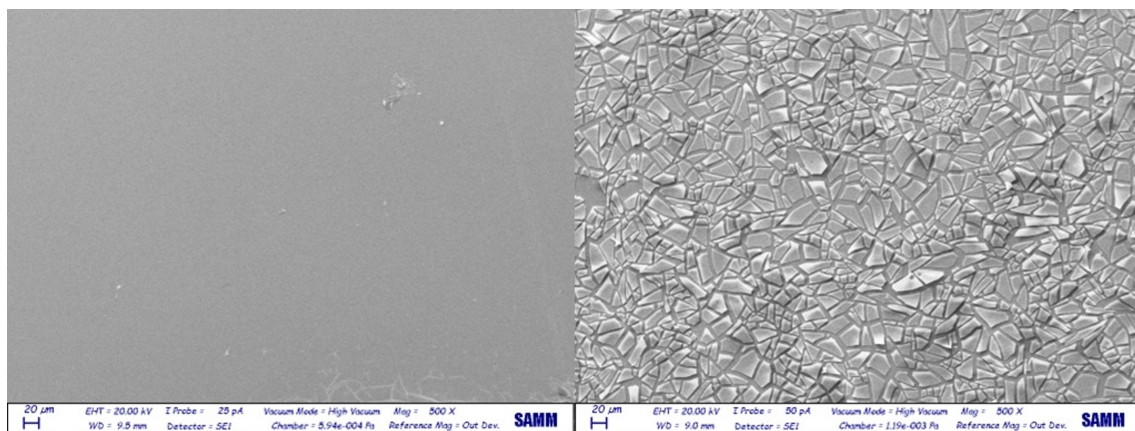
Spray-coating yielded coatings with greater thickness, as shown in Figure 3.67. Indeed, even solution *EB-1*, which yielded transparent coatings when deposited by immersion, was translucent when deposited by spray-coating. The reported thicknesses are about 750 nm, 546 nm, and 1.15 μm for *WB-1*, *EB-1*, and *WB-2*, respectively. Once again, *WB-2* reported the greatest thickness.

It was not possible to determine whether the choice of substrate material influences the final coating thickness as PMMA melts at high SEM magnifications.

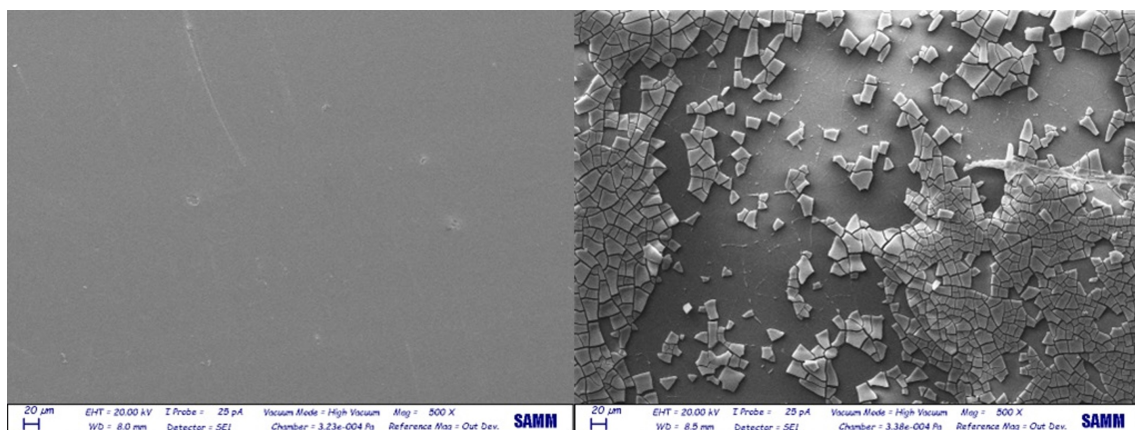
3.7.2. Thermal treatment

To determine the differences that arise when using different thermal treatments two glass samples, coated with *WB-1*, were annealed for two hours at 500°C and 90°C. As showed in Figure 3.68, the deposition of *WB-1* on glass yields smooth and uniform coatings regardless of the employed deposition technique. However, subjecting the samples to a thermal treatment completely cracks the surface regardless of the reached temperature. The for-

mation of cracks is probably due to internal stresses arising from solvent evaporation.



(a) WB-1 dip-coated on glass before (left) and after (right) annealing at 500°C for two hours.



(b) WB-1 spray-coated on glass before (left) and after (right) annealing at 90°C for two hours.

Figure 3.68: Influence of annealing treatment on coating morphology.

WB-2 and *EB-1*, on the other hand, seem to be more resistant as the coating fissures following thermal treatment rather than cracking (Figure 3.69).

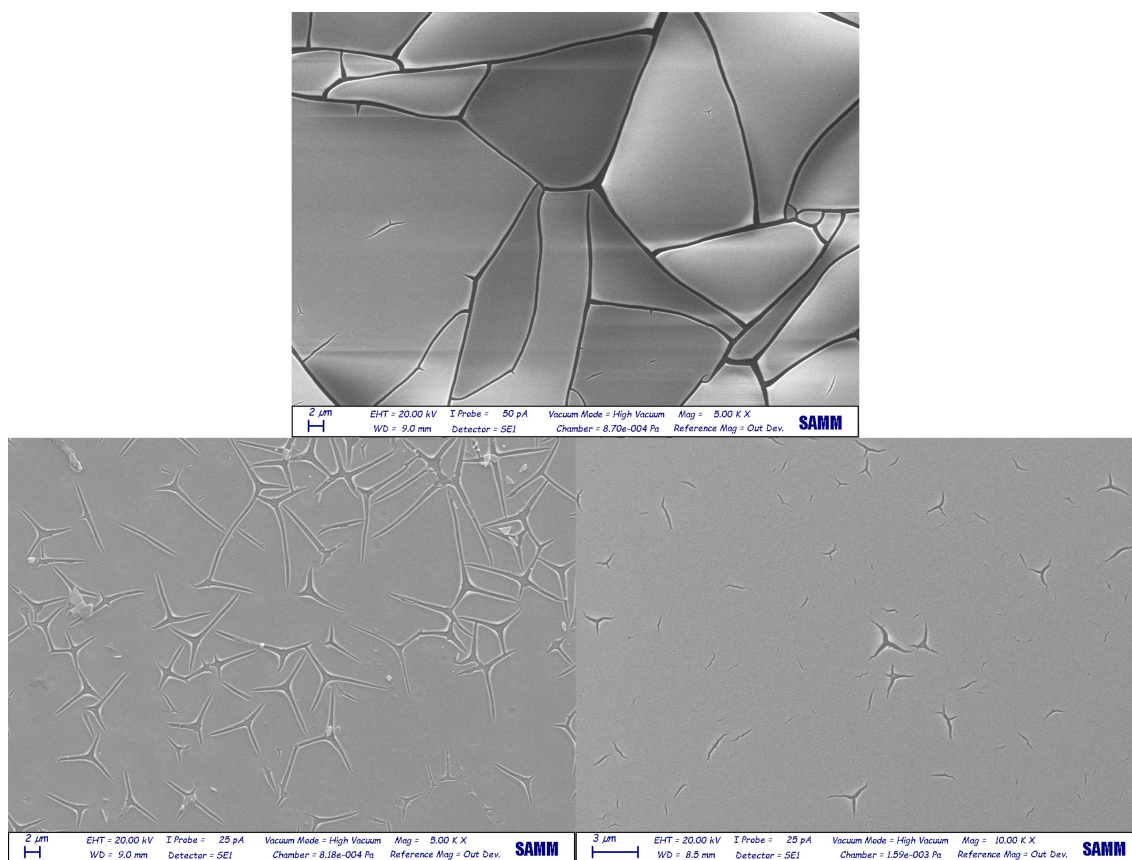


Figure 3.69: WB-1 (top), EB-1 (left), WB-2 (right) dip-coated on glass and annealed at 500°C for two hours.

3.7.3. Choice of substrate

As explained in previous chapters, coatings tend to adhere poorly to PMMA compared to glass. Figure 3.70 further proves so, as while the coating deposited on glass is completely smooth, the one deposited on PMMA is irregular, partially cracked and detached. This is probably due to the lack of adhesion that promotes coating detachment even when the sample is not thermally treated.

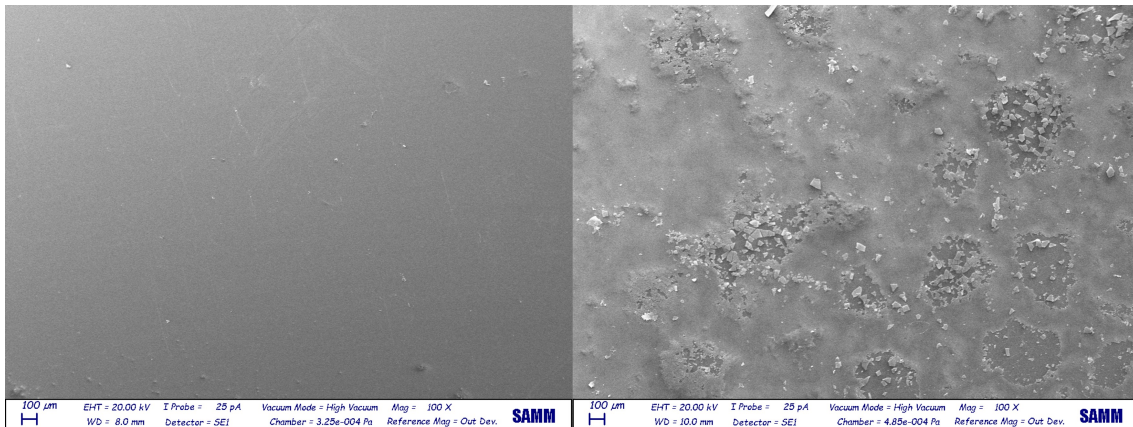


Figure 3.70: WB-1 spray-coated on glass (left) and PMMA (right).

3.7.4. Deposition technique

Dip-coating yields smooth and compact coatings in all the analyzed solutions, as shown in Figure 3.71. Although, a few defects are present on the surface, such as craters, shrinkage, and blistering.

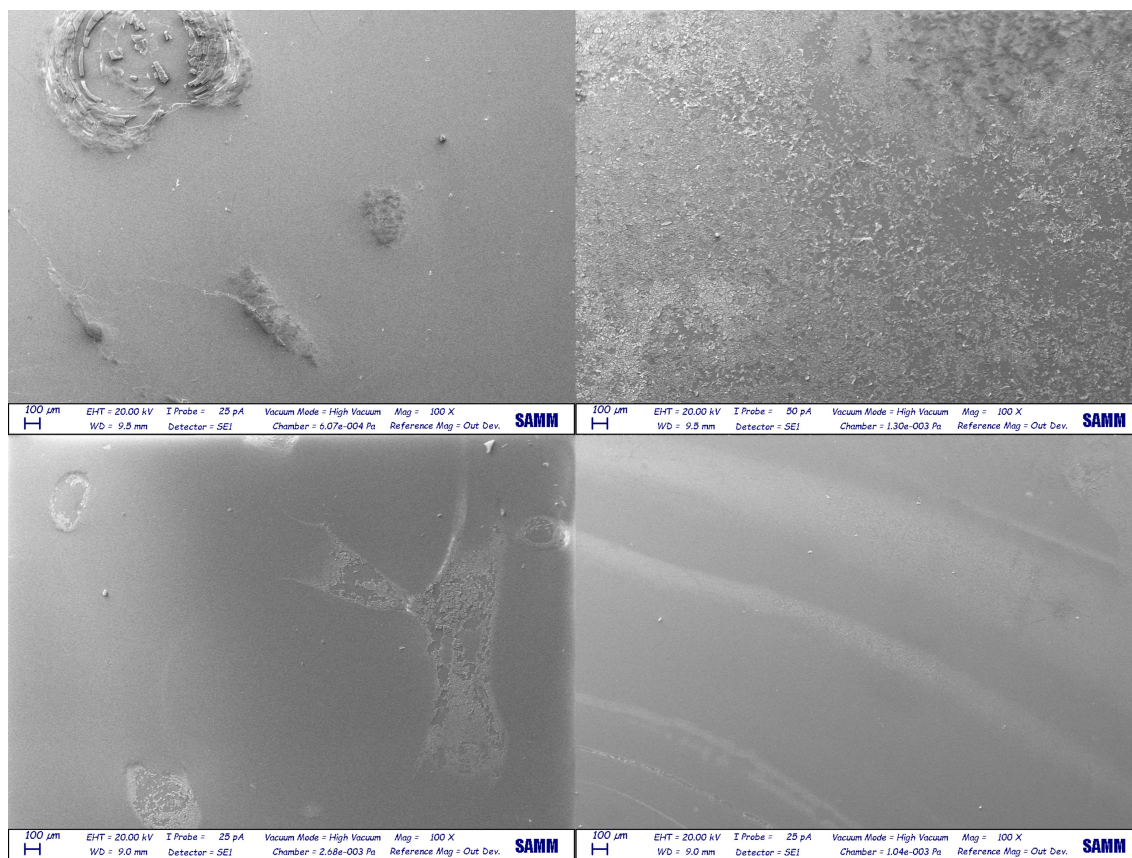


Figure 3.71: Dip-coated glass with solutions WB-1 (top left), WB-1 An. (top right), WB-2 An. (bottom left), EB-1 An. (bottom right). The An. samples were annealed for two hours at 500°C.

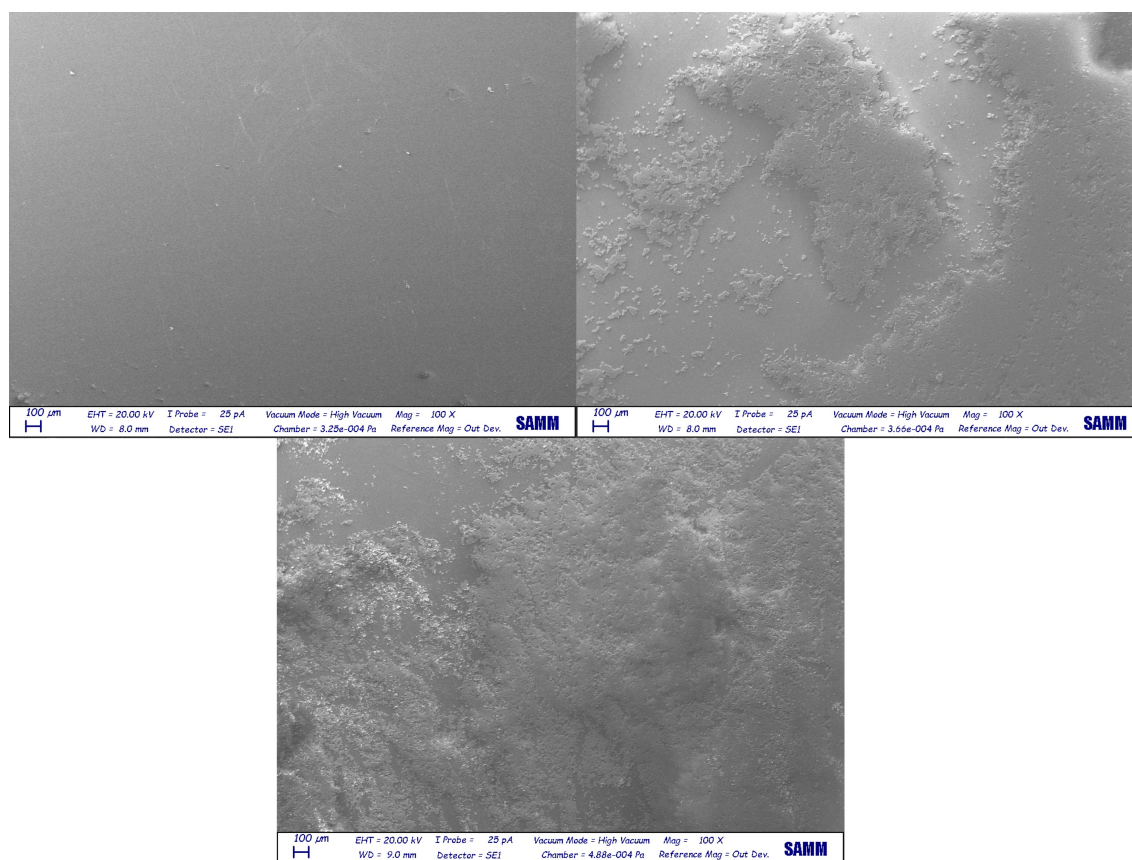


Figure 3.72: Spray-coated glass with solutions WB-1 (top left), WB-1 An. (top right), and WB-2 An. (bottom). The An. samples were annealed for two hours at 90°C.

Spray-coating, on the other hand, yields non-uniform coatings as the film seems to be concentrated in localized areas while leaving other areas bare (Figure 3.72)

3.8. XRD analysis

The following paragraphs summarize the results obtained during XRD analysis, which aimed at verifying the presence of anatase on coated glass samples. Given the different results obtained in photocatalytic and wettability tests, despite similar deposition parameters were adopted, the paragraphs are divided accordingly to evaluate whether coating performance and anatase concentration are correlated. Furthermore, the effect of different thermal treatments has been addressed. In all the analysed samples the rutile phase could not be detected.

3.8.1. Photoactive samples

The analysis was performed on previously tested samples to show the difference between photoactive and inert coatings. All the water-based coatings, whose results are reported in Figure 3.73 and Figure 3.74, presented an anatase peak at about 25° which corresponds to (101) crystal plane (ICSD: 98-007-6173). Anatase is thus present both prior and after annealing, probably due to the presence of anatase nanocrystals in the sol [62]. However, following thermal treatment, carried out at 500°C for two hours, the anatase peak intensifies suggesting an increase in the phase amount. The wider bump, ranging from 15° to 30° , corresponds to amorphous glass, i.e. the substrate.

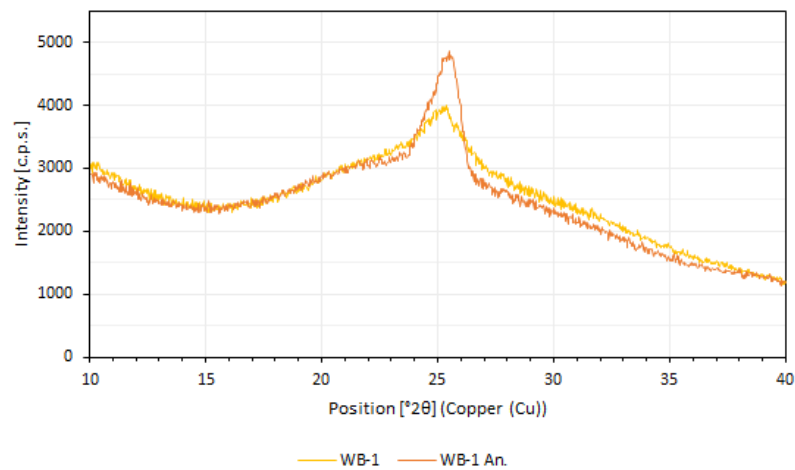


Figure 3.73: XRD spectrum of WB-1 deposited on glass.

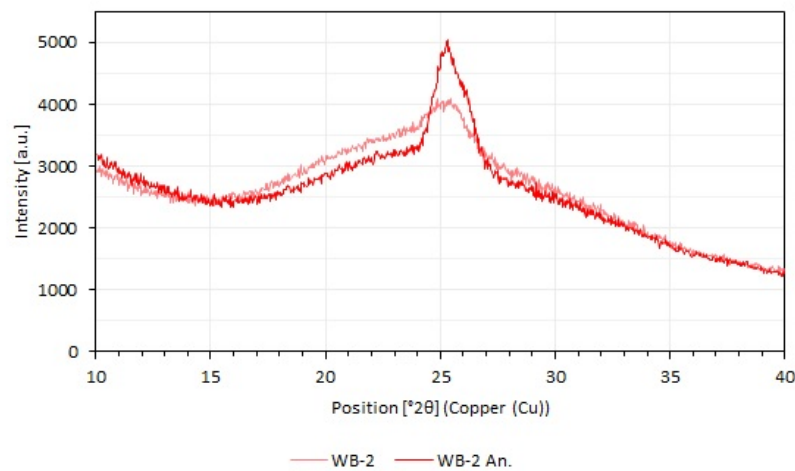


Figure 3.74: XRD spectrum of WB-2 deposited on glass.

The annealed ethanol-based coating, on the other hand, showed a small anatase peak. Furthermore, prior to annealing, the sample did not present any peak related to TiO_2 (Figure 3.75). It is not possible to determine whether a small amount of anatase was present as the peak related to amorphous glass conceals less intense peaks. However, given that during photocatalysis tests EB-1 was inert as it showed a reaction rate constant equal to photolysis (0.04 h^{-1}), one can assume that either the coating was amorphous or too thin to be photoactive.

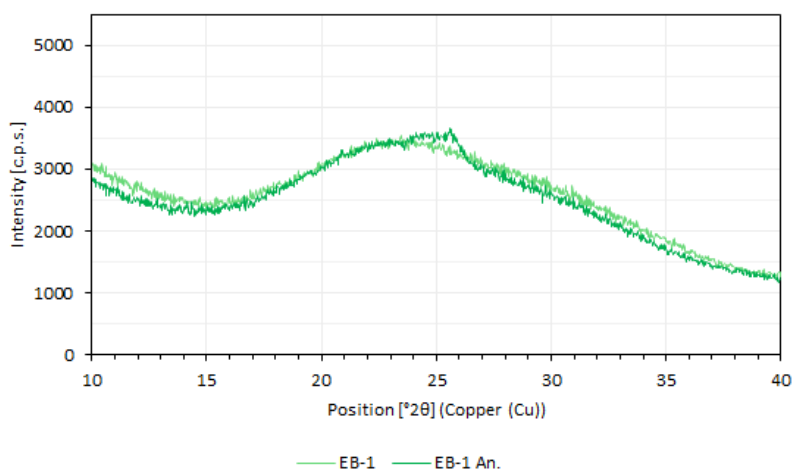


Figure 3.75: XRD spectrum of the ethanol-based coating (EB-1).

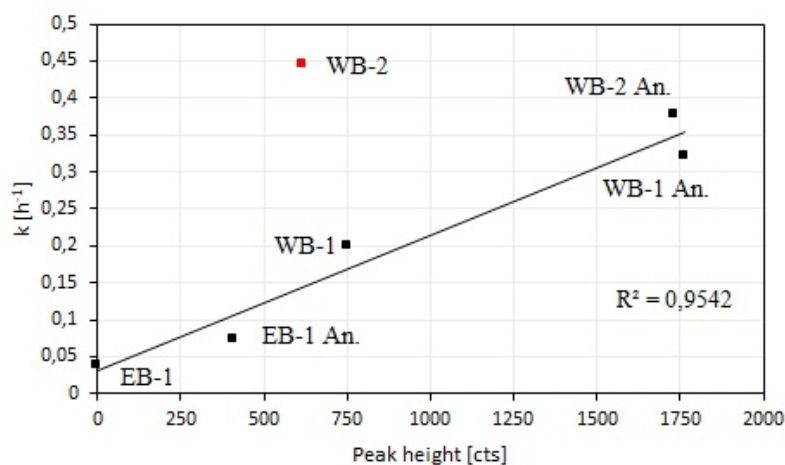


Figure 3.76: Correlation between peak intensity and photoactivity.

Finally, it was noticed that the coating photoactivity correlates with the intensity of the anatase peak. Indeed, EB-1, which did not present any peak was inert, while the water-based coatings were active. Overall, annealing improves the photoactivity of the samples

as well as increasing the anatase phase content. Figure 3.76 shows that, neglecting the outlier reported in red, the two parameters are highly correlated as the coefficient of determination has a value of 0.95. The high photocatalytic activity of *WB-2* could be ascribed to the formation of a thicker coating, as it was mentioned in the chapter on morphological analysis.

3.8.2. Thermal treatment

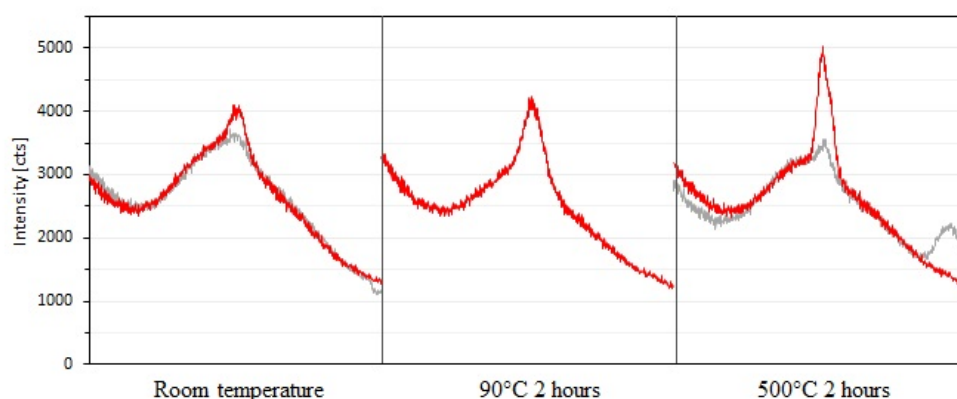


Figure 3.77: XRD spectra of *WB-2* coatings subjected to different thermal treatments.

The results shown in red in Figure 3.77 are straightforward: increasing the temperature of the annealing treatment increases the intensity of the anatase peak at 25° . This is fundamental for photocatalysis purposes, and as a consequence the author recommends to always anneal the samples before testing their activity. However, as shown by the results in grey, the thermal treatment did not yield consistent results. The cause is probably due to the different ageing periods: indeed the results in grey represent samples aged for one week, while the samples showed in red were aged for about four months. Therefore, proper ageing is fundamental to form coatings with high quantities of TiO_2 nanoparticles, which can then be converted to anatase phase by annealing. Without proper ageing the annealing treatment is not efficient.

3.9. Comparison between sol-gel and anodized coatings

The following paragraphs summarize the results obtained by testing the degradation efficiency of sol-gel and nanostructured anodized coatings. Direct comparison between the two techniques is rarely investigated, however given that they offer distinct advantages it is valuable to explore their performance differences. Therefore, this study aims to evaluate and compare the effectiveness of these two methods for degradation efficiency, providing insights into their respective benefits and limitations

3.9.1. Photocatalytic activity

The initial test was conducted in Milli-Q water to establish a reference point, while repeatability tests were performed under more realistic conditions, i.e. in simulated tap water, to take into account the effect of ions on the photocatalytic process.

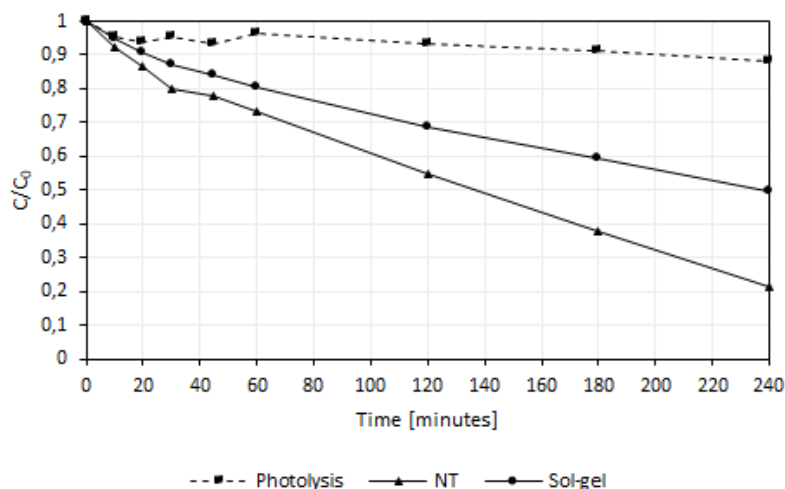


Figure 3.78: Monitored degradation of tetracycline in Milli-Q water.

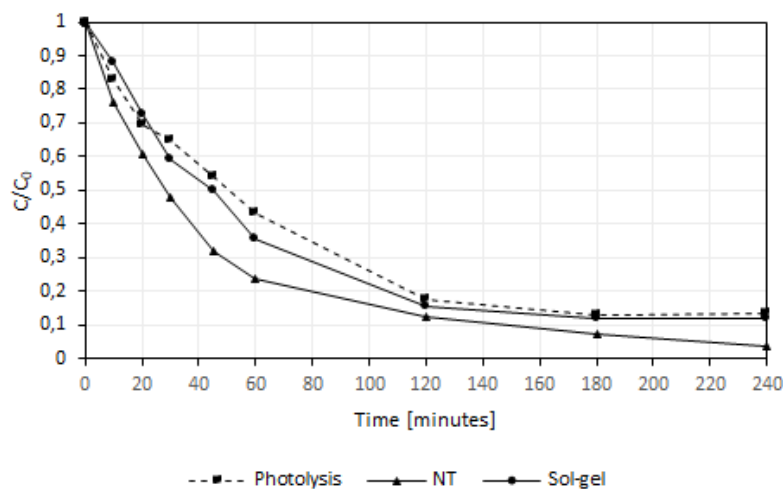


Figure 3.79: Monitored degradation of tetracycline in simulated tap water.

As shown in Figure 3.78 and Figure 3.79, both techniques yield photoactive coatings. The represented curves are relative to the best performing values.

While both mechanisms are linear, the degradation process in simulated tap water occurs at a faster rate compared to the process in Milli-Q water. For instance, in the latter, the anodized film degrades 80% of the concentration within 240 minutes, whereas in the former, it takes only 60 minutes to achieve the same level of degradation. However, in the tap water system, the degradation efficiency slows down after about 120 minutes, probably to the accumulation of intermediary products on the semiconductor surface that hinder the degradation mechanism. The increase in the degradation efficiency is witnessed also during photolysis, hence the presence of ions facilitates the degradation of tetracycline.

Concerning the test conducted in Milli-Q water, the nanostructured coating exhibits stronger photocatalytic activity than the coating obtained by the sol-gel method. Specifically, the anodized coating was able to degrade 80% of the antibiotic, whereas the sol-gel coating only achieved a 50% degradation rate. However, the difference between the two coatings in the complex water matrix is not as noticeable, as they are both comparable with photolysis. The difference between the three degradation mechanisms is better represented by the absorbance spectra.

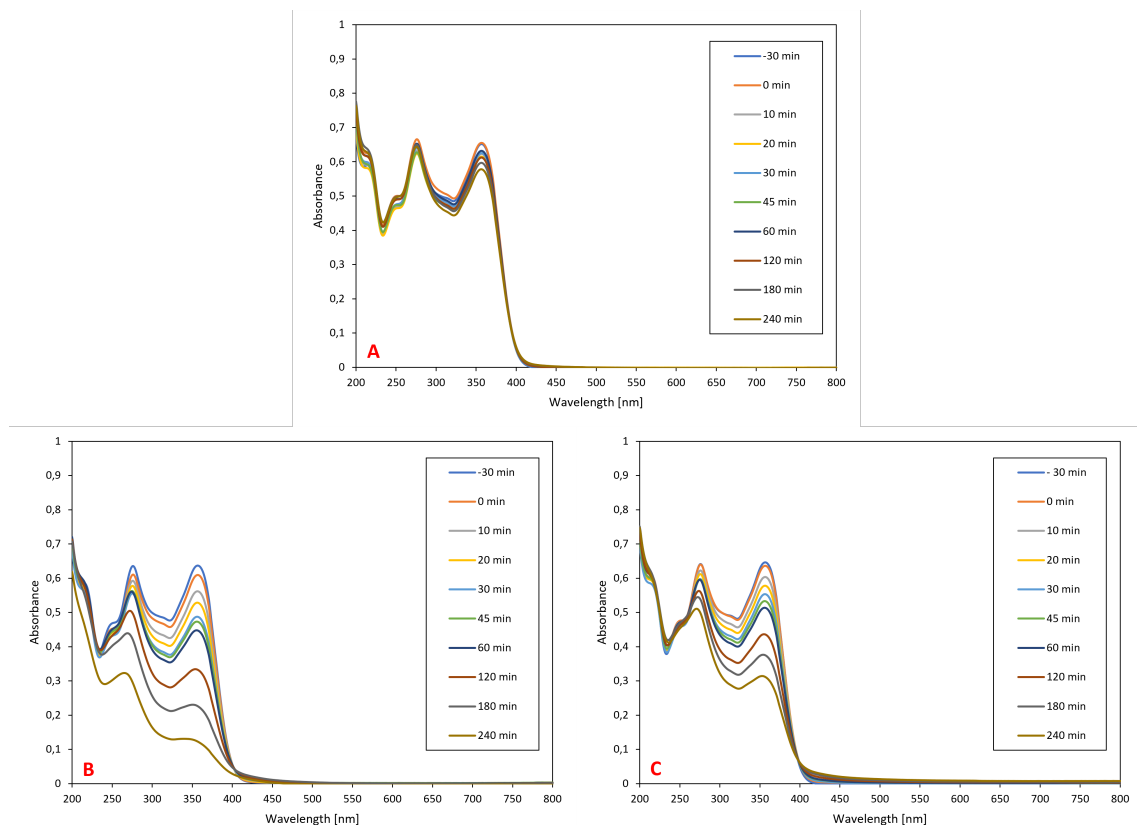


Figure 3.80: Absorption spectra of the monitored degradation of tetracycline in Milli-Q water promoted by (A) photolysis, (B) anodized coating, and (C) sol-gel coating.

The displayed absorbance spectra are relative to the abovementioned curves. Figure 3.80 clearly shows how the photocatalytic films increase the degradation of tetracycline, as the coatings drive lower values of absorbance in both peaks. However, the anodized coating is more efficient than the sol-gel coating obtaining higher variations in the absorbance values.

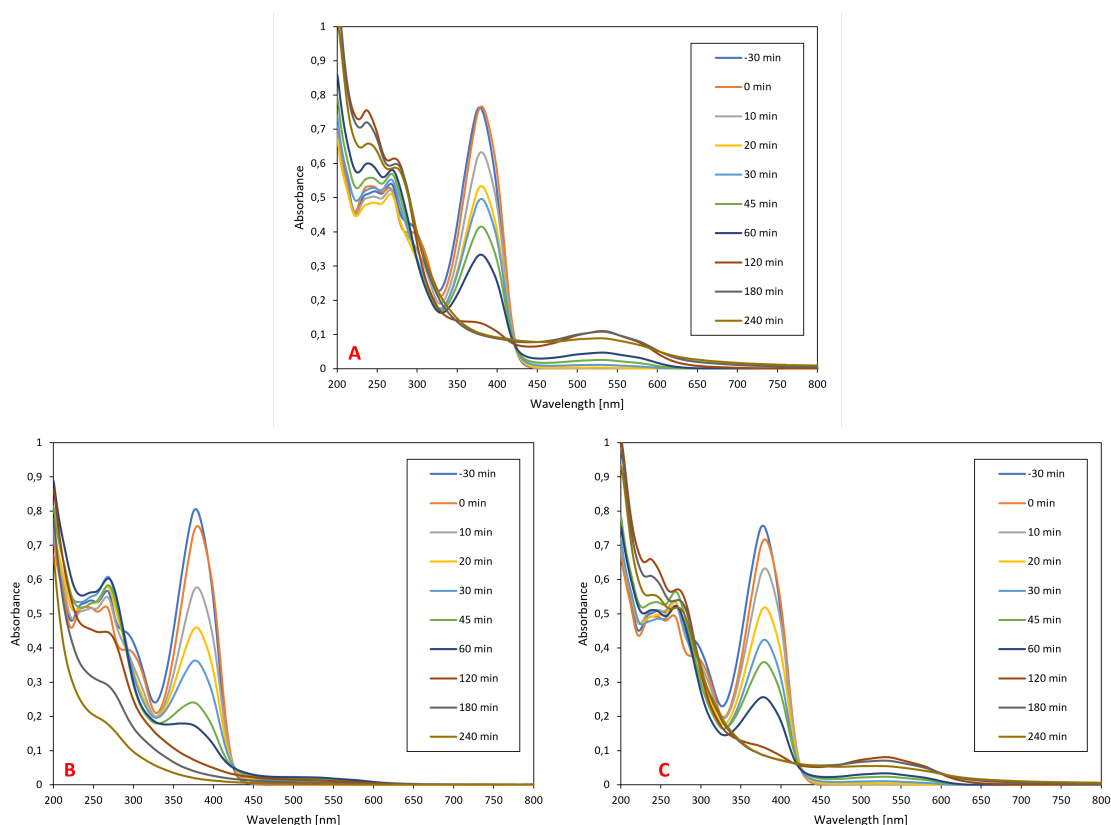


Figure 3.81: Absorption spectra of the monitored degradation of tetracycline in simulated tap water promoted by (A) photolysis, (B) anodized coating, and (C) sol-gel coating.

The absorbance spectra of the solution in simulated tap water differs from the one in Milli-Q water, due to the presence of salts in solution. While the solution in Milli-Q water appeared transparent, the one prepared in simulated tap water had a clearly visible yellow hue. This difference was reflected in the absorbance spectra, which showed a higher peak at 380 nm in the tap water solution, indicating greater absorption of blue light. Additionally, during the degradation test the tap water solution also exhibited a peak at 550 nm, which absorbs green light and caused the solution to turn slightly pink after 60-120 minutes. However, after 180 minutes, both the 550 nm and 380 nm peaks disappeared, and the solution became transparent. The explanation for this phenomenon was not investigated, but as tetracycline antibiotics chelate calcium salts to form complex compounds, the degradation mechanism could form different intermediary products than when degraded in distilled water. In terms of photocatalyst efficiency, the anodized coating showed greater degradation than photolysis, as evidenced by the higher variations induced in the peaks at 200-250 nm and the slightly stronger variation in the 380 nm peak. In contrast, the absorbance spectrum of the sol-gel coating did not differ significantly from the spectrum obtained during photolysis, suggesting that the coating was likely inert.

3.9.2. Reusability

To ensure the reliability and longevity of the workpiece, repeatability tests were conducted to assess the consistency and reproducibility of the coating's performance under controlled conditions, as well as the adhesion of the coating. Such tests are crucial to determine the suitability of the product for engineering applications, where durability and performance over time are critical factors.

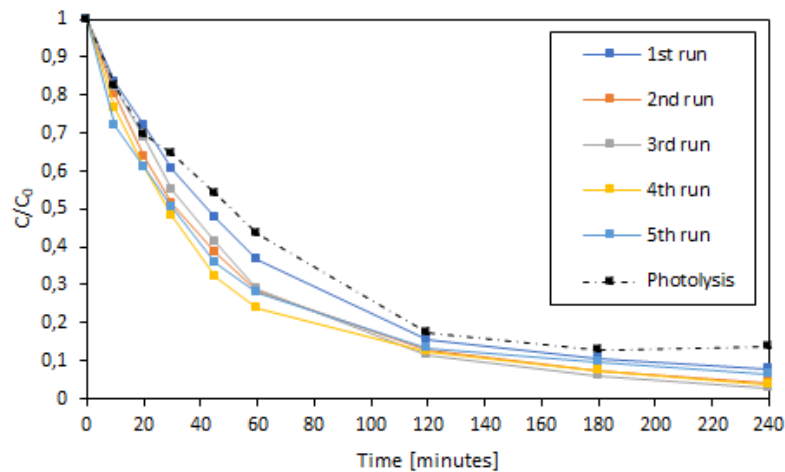


Figure 3.82: Repeatability tests conducted on the anodized coating and carried out in simulated tap water.

The results reported in Figure 3.82 indicate that the anodized sample shows good reusability, as each test reported the degradation of more than 99.8% of the concentration of tetracycline. The small variations are consistent with experimental error.

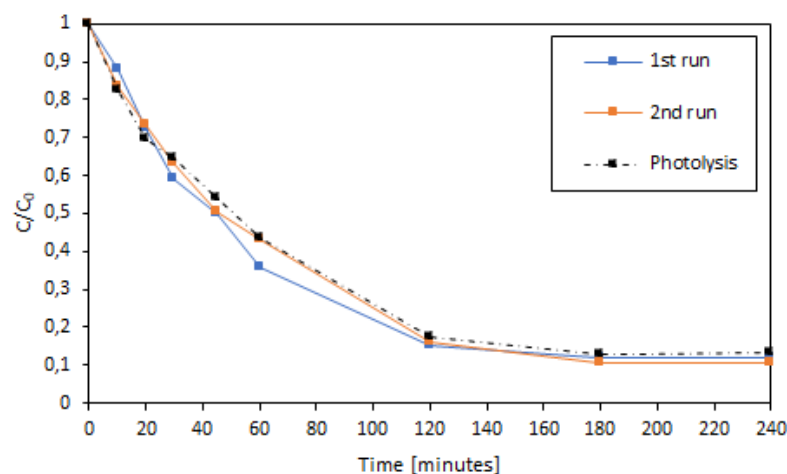
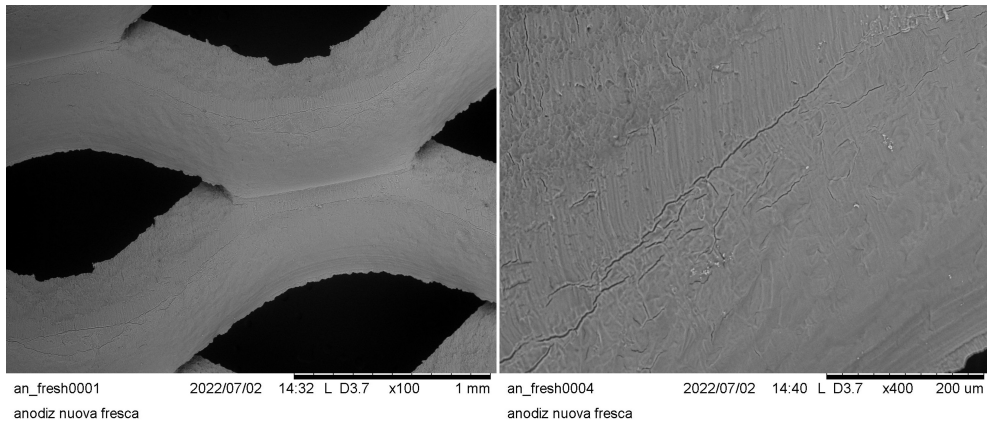


Figure 3.83: Repeatability tests conducted on the sol-gel coating and carried out in simulated tap water.

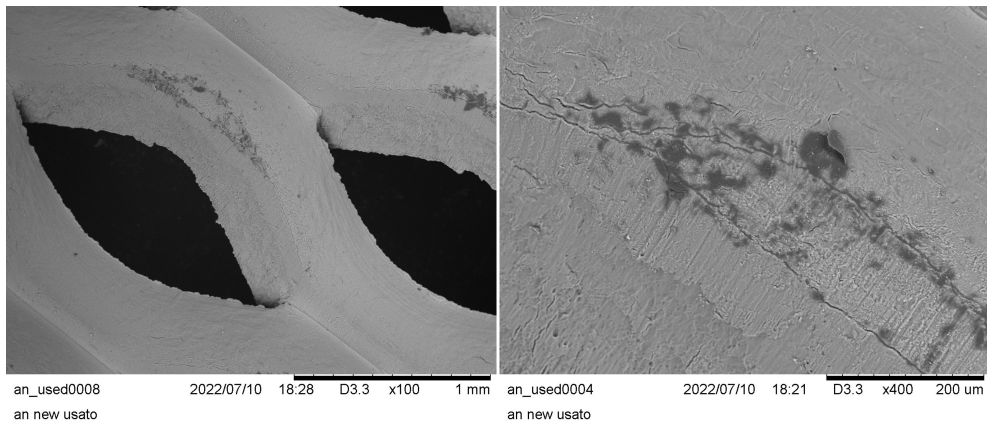
The sol-gel coated sample, despite the initial good photoactivity reported during the test in Milli-Q water, showed poor performance in the complex water matrix (Figure 3.83). Since the results obtained during the second test were comparable to those of photolysis, the test was discontinued as it was not providing any additional insights. The reason to the poor performance of the sol-gel coated samples is attributable to two causes:

1. contrary to the anodized coating, the sol-gel coating produced high amounts of intermediary products that covered the surfaces in the batch reactor. The accumulation of these species hindered light transmission and covered the semiconductor hampering the degradation of tetracycline;
2. additionally, sol-gel coatings are poorly adherent to the substrate. Hence, following three photocatalytic tests it is safe to assume that the coating partially detached from the substrate thus explaining the lack of photoactivity.

The following pictures are obtained by scanning electron microscopy, and show the coating appearance before and after the degradation tests. The reader is reminded that the anodized coating was subjected to six photocatalytic tests while the sol-gel coating only to three.



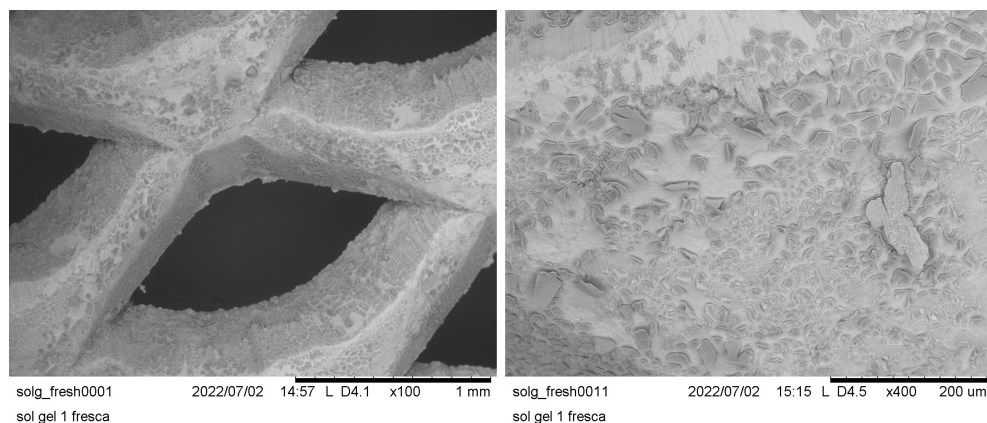
(a) Before repeatability tests.



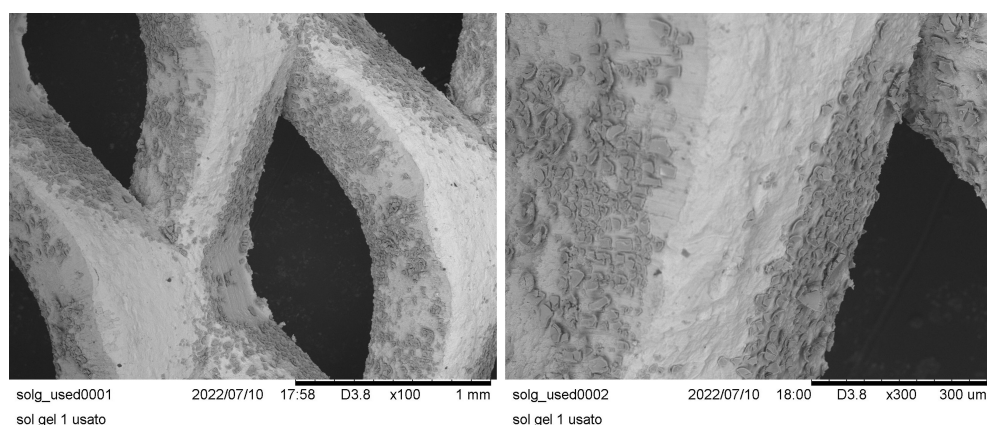
(b) After repeatability tests.

Figure 3.84: SEM images of the anodized coating.

The anodization process formed a dense and homogeneous coating with minimal cracking. Although the morphology of the coating remained largely unchanged after the repeatability tests, dark spots were observed which may be attributed to the deposition of intermediary degradation products (Figure 3.84). However, it is important to note that at this stage of the research, this hypothesis has not been confirmed.



(a) Before repeatability tests.



(b) After repeatability tests.

Figure 3.85: SEM images of the sol-gel coating.

In contrast to the anodized coating, the sol-gel coating exhibited extensive cracking and partial detachment, as shown in Figure 3.85. As it was previously discussed, the cracks are due to the annealing treatment that was carried out at 500°C for two hours. During the repeatability tests, the coating further detached, exposing the underlying metallic surface. The images demonstrate that a large portion of the sample area remains uncoated. This confirms the initial hypothesis that the decreased performance was due to the loss of semiconducting material during the degradation tests.

3.9.3. Mineralization

While the coatings are photoactive, it is important to evaluate their mineralization efficiency, as incomplete mineralization may result in the formation of intermediary degradation products potentially more toxic than the original pollutant. Therefore, to ensure the effectiveness of a semiconductor for the treatment of wastewater it is necessary to

determine the mineralization efficiency to prevent the release of hazardous species into effluents. To determine the mineralization efficiency in the complex water system and Milli-Q water, NPOC and TOC methods were employed, respectively. Because the employed T.O.C. analyzer has low sensitivity at these concentrations levels, the acquired data have high error. Therefore, it is recommended that readers focus on the general trend rather than the individual values.

Figure 3.86 and Figure 3.87 show representative curves of the most successful results, which also correspond to the highest degradation efficiency.

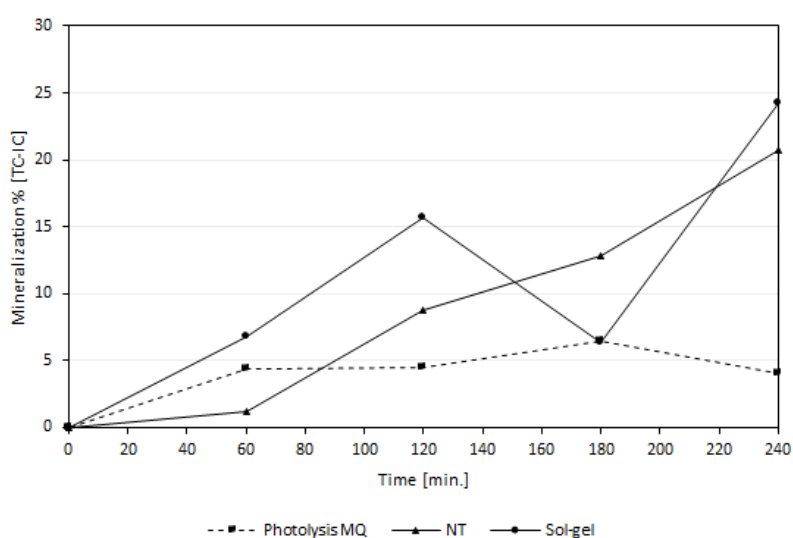


Figure 3.86: Mineralization values acquired during the degradation of tetracycline in Milli-Q water.

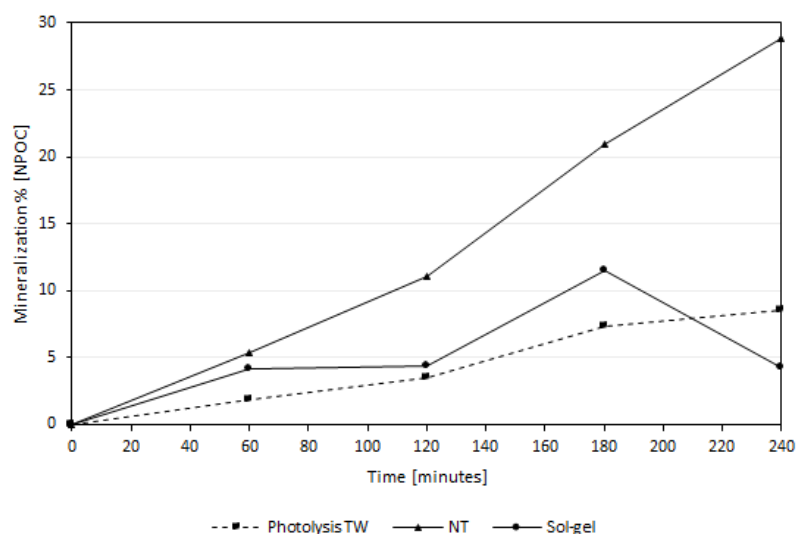


Figure 3.87: Mineralization values acquired during the degradation of tetracycline in simulated tap water.

Despite photolysis showed comparable degradation efficiency with the coatings tested in simulated tap water, it mineralizes only 5% to 10% of the solution (Figure 3.86 and Figure 3.87). Therefore, the use of photocatalysts not only increases the degradation rate of pollutants, but also improves mineralization. In fact, the coatings showed higher mineralization rates, ranging between 20% and 30%. Figure 3.88 and Figure 3.89 report the mineralization values acquired during the repeatability tests. However, due to the high variations, it is not clear whether mineralization is affected by the sample reuse. While the anodized sample reported values around 25% and 30%, the sol-gel coating performed similarly to photolysis confirming that the coating probably detached after the degradation test in Milli-Q water, which instead showed comparable values with the anodized coating. To determine whether the mineralization efficiency of the anodized coating is affected by the water medium, the author recommends to run further tests as the reported values are too similar to determine whether the difference is due to experimental error or to different degradation pathways.

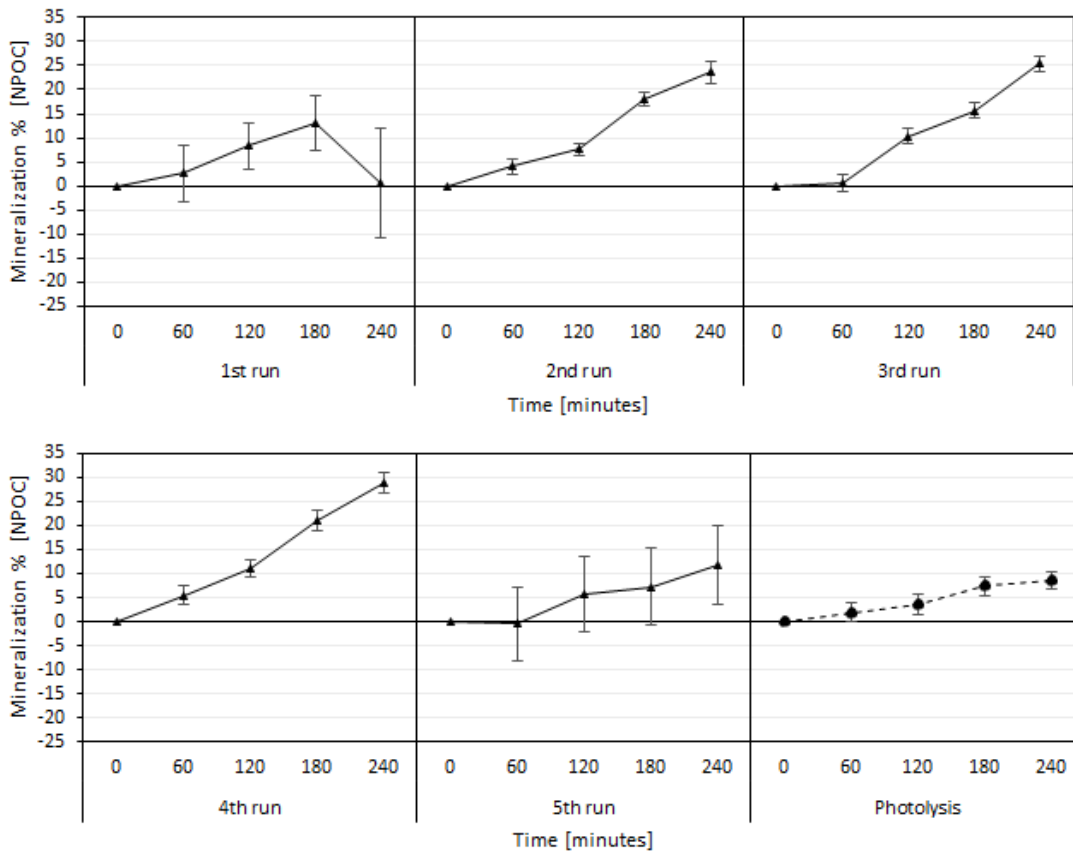


Figure 3.88: Mineralization values acquired during repeatability tests conducted on the anodized coating and carried out in simulated tap water.

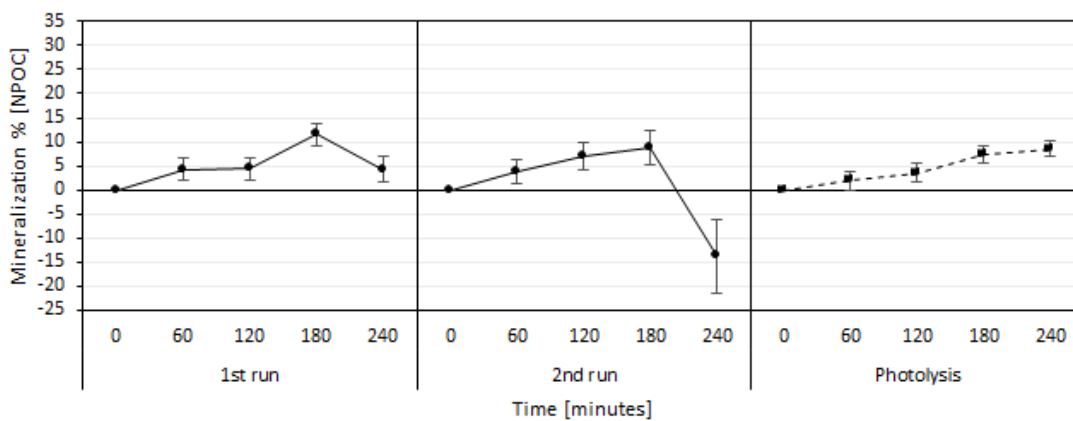


Figure 3.89: Mineralization values acquired during repeatability tests conducted on the sol-gel coating and carried out in simulated tap water.

3.9.4. Reaction rate constants

The reaction rate constants were calculated using the pseudo first-order kinetics model. However, during the degradation tests carried out in simulated tap water, some deviations from the expected linear behavior were observed. To address this, a decision was made to report only the initial reaction rate constants. This involved excluding a few data points, which are highlighted in red, from the computation (Figure 3.90, Figure 3.92, and Figure 3.91).

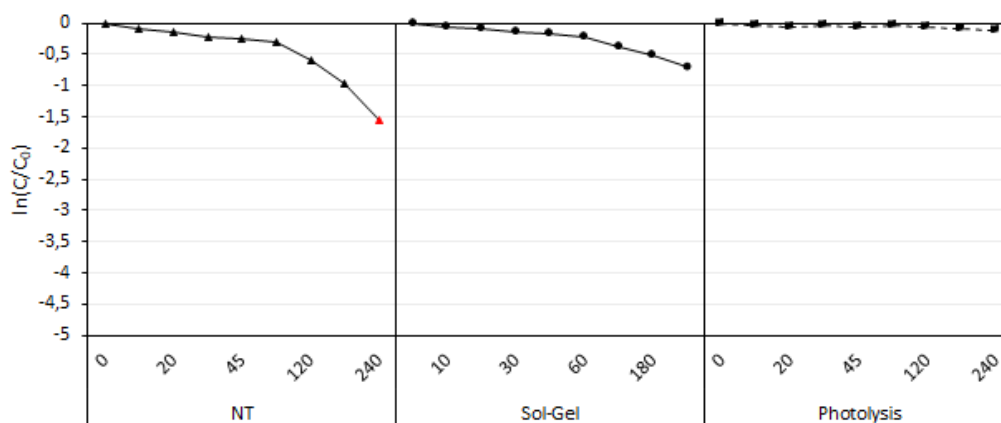


Figure 3.90: Application of the pseudo first-order reaction kinetic model on the data acquired during degradation tests conducted on the Milli-Q water solution.

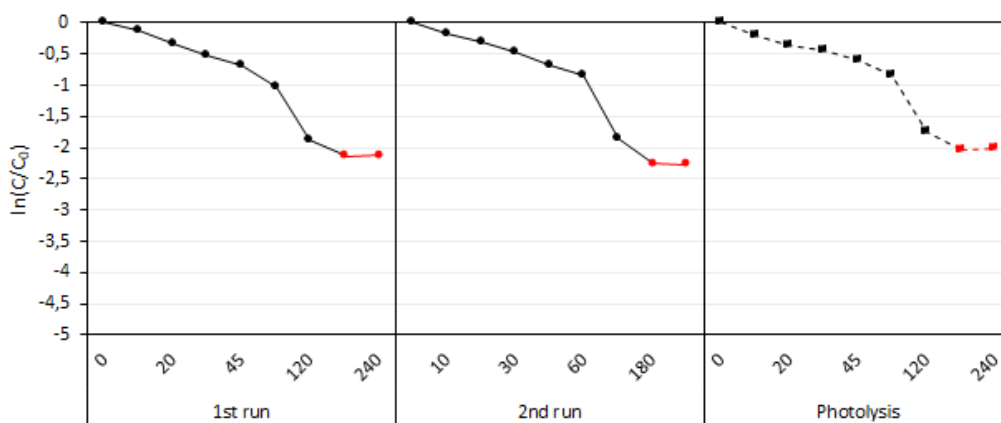


Figure 3.91: Application of the pseudo first-order reaction kinetic model on the data acquired during repeatability tests conducted on the sol-gel coating and carried out in simulated tap water.

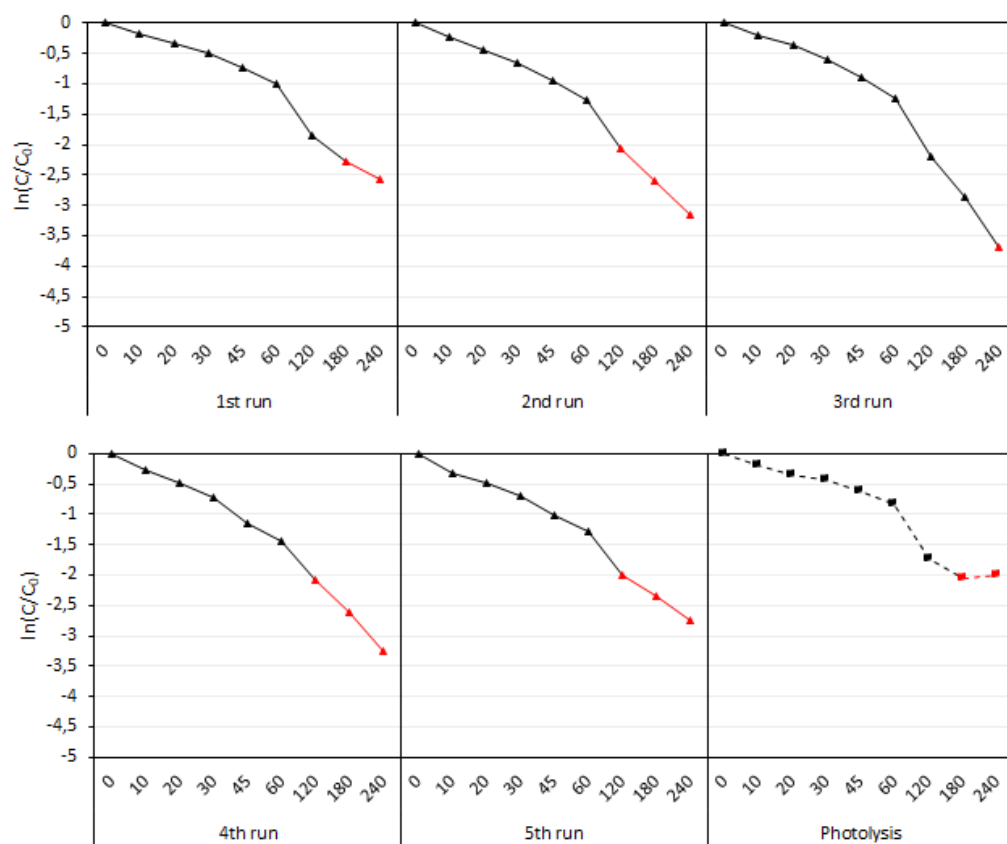
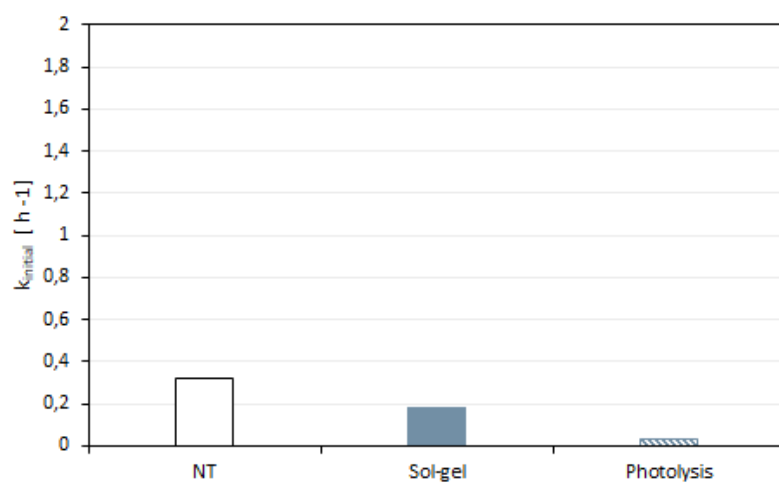
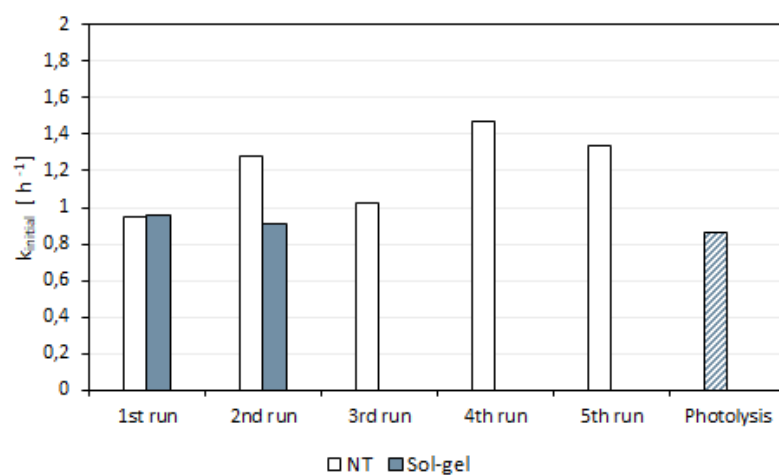


Figure 3.92: Application of the pseudo first-order reaction kinetic model on the data acquired during repeatability tests conducted on the anodized coating and carried out in simulated tap water.

Each reported k value was obtained with a coefficient of determination (R^2) above 0.99, save for the curve representing photolysis of tetracycline in Milli-Q water (0.83). Figure 3.93 shows that the reaction rate constants computed for the degradation of tetracycline in Milli-Q water, do not differ considerably from the photolysis value. However, readers are reminded that the anodized coating had degraded 80% of the concentration while photolysis only 10%. The difference between the two reaction rate constants is although comparable to the variations encountered during the reusability tests on the anodized coating, which always degraded more than 99.9% of the concentration. Therefore, the author hypothesizes that the initial reaction rate constant is not a suitable parameter to compare the degradation efficiency of a photocatalyst. Instead, mineralization and concentration variation allow for clearer comparisons.



(a) Reaction rate constants obtained from the degradation of tetracycline in Milli-Q water.



(b) Reaction rate constants obtained from the degradation of tetracycline in simulated tap water.

Figure 3.93: Reaction rate constants computed from the slope of the curves plotted as $\ln(CC_0^{-1})$ against time.

4 | Conclusions and future developments

The purpose of this dissertation is to characterize titanium dioxide-based coatings for self-cleaning surfaces. The coatings were evaluated for their photocatalytic and wettability properties, and the concluding remarks are discussed below.

The photocatalytic activity of the water-based coatings was found to be moderate, effectively degrading 70-85% of rhodamine B concentration provided that the solutions were aged for at least four months. The ethanol-based coating, on the other hand, was inert despite it was subjected to proper ageing. Indeed, the degradation of rhodamine B in presence of samples coated with the ethanol-based coating was dominated by photolysis. Despite the morphology of the coatings was affected by the deposition technique, the photocatalytic activity was not influenced. Dip-coated samples were nonuniform, transparent but with white opaque defects where the solution pooled and dried; spray-coated samples were uniform but translucent. Therefore, future studies should focus on developing solutions and deposition techniques that yield transparent and uniform coatings to maintain the aesthetic appearance of the coated surfaces. Additionally, given the poor sol-gel reproducibility, the influence of temperature and humidity during synthesis and coating deposition on the photocatalytic activity should be investigated.

XRD analysis showed that coatings with a higher anatase content were more photoactive, and higher annealing temperatures yielded higher anatase amounts. However, literature reports that mixed rutile-anatase phases are more photoactive: it is unclear whether the analyzed coatings contained a rutile phase due to overlapping peaks with the glass substrate. Future studies should consider using an alternative substrate or depositing additional coating layers to enhance the relative intensity of TiO_2 .

The coatings' poor adhesion on PMMA compared to glass was addressed by corona treatment, but repeated tests showed that the treatment was unsuccessful. Future studies should explore alternative treatments or substrate materials to improve adhesion. Literature reports that when corona treatments are unsuccessful, plasma systems can be used as

they produce higher and longer lasting surface effects than corona. However, the benefits should offset equipment investment and operational costs.

Wettability tests were carried out to determine the water contact angle and photoinduced hydrophilicity of the analysed coatings. Given the lack of time and resources, it is unclear whether the coating's wettability depends on deposition technique, ageing period, or environmental parameters. The required superhydrophilicity was obtained for solutions aged for one week, dip-coated on glass samples, which were then annealed for two hours at 500°C. In the remainder samples, photoinduced hydrophilicity, although present, was not enough to induce superhydrophilicity. Future studies should determine the influence of solution ageing period on wettability and investigate whether superhydrophilicity is only achieved with high anatase content.

Soiling tests, which were conducted by exposing coated PMMA samples outdoors, demonstrated the effective self-cleaning ability of the coatings. Precipitation data retrieved from ARPA Milano overlapped with decreasing ΔE values, thus highlighting the self-cleaning working mechanism. However, data representing color variations included the effects of coating loss and yellowing induced by chemical degradation. Future studies should use non-polymeric substrates and find ways to single out the effects of coating loss. Overall, the ethanol-based coating demonstrated lower performance probably due to the more pronounced loss of coating.

Qualitative adhesion tests were inconclusive, thus alternative methods should be investigated to determine the coating's durability and suitability for engineering applications. The author discourages the adoption of peel testing and suggests finding alternative adhesion tests. Poor coating adhesion would undermine the benefits provided by self-cleaning coatings, e.g. lower maintenance costs.

In summary, the water-based sol-gel solutions analyzed in this study exhibited moderate self-cleaning functionality. However, incorporating surfactants and dopants could improve the photocatalytic properties of the coating. The main limitation of the current formulation is its poor adhesion to the substrate, which needs to be addressed in future research. Despite this drawback, sol-gel coatings have the potential to match the performance of nanostructured anodized coatings, as demonstrated by their initial degradation test results on tetracycline solutions. The versatility of the sol-gel deposition method, which can be applied to any type of surface and performed in situ, is a significant advantage over anodization. If the adhesion issue can be resolved, sol-gel coatings would become a promising option for a wide range of engineering applications.

Bibliography

- [1] Amirul Syafiq, Vengadaesvaran Balakrishnan, Mohd Syukri Ali, Sanjay J Dhoble, Nasrudin Abd Rahim, Azimah Omar, and Ab Halim Abu Bakar. Application of transparent self-cleaning coating for photovoltaic panel: a review. *Current Opinion in Chemical Engineering*, 2022. doi: <https://doi.org/10.1016/j.coche.2022.100801>.
- [2] A. Syafiq, A.K. Pandey, N.N. Adzman, and Nasrudin Abd Rahim. Advances in approaches and methods for self-cleaning of solar photovoltaic panels. *Solar Energy*, pages 597–619, 2018. doi: <https://doi.org/10.1016/j.solener.2017.12.023>.
- [3] D. P. Macwan, Pragnesh N. Dave, and Shalini Chaturvedi. A review on nano-TiO₂ sol-gel type syntheses and its applications. *J Mater Sci*, pages 3669–3686, 2011. doi: DOI10.1007/s10853-011-5378-y.
- [4] Dorian A. H. Hanaor and Charles C. Sorrell. Review of the anatase to rutile phase transformation. *J Mater Sci*, pages 855–874, 2011. doi: DOI10.1007/s10853-010-5113-0.
- [5] M H Samat, M F M Taib, O H Hassan, M Z A Yahya, , and A M M Ali. Structural, electronic and optical properties of brookite phase titanium dioxide. *Mater. Res. Express*, 2017. doi: [https://doi.org/10.1088/Mater.Res.Express4\(2017\)0440032053-1591/aa67b3](https://doi.org/10.1088/Mater.Res.Express4(2017)0440032053-1591/aa67b3).
- [6] Jinfeng Zhang, Peng Zhou, Jianjun Liub, and Jiaguo Yu. New understanding of the difference of photocatalytic activity among anatase, rutile and brookite TiO₂. *Phys.Chem.Chem.Phys.*, 2014. doi: DOI:10.1039/c4cp02201g.
- [7] Minna Piispanen and Leen Hupa. Comparison of self-cleaning properties of three titania coatings on float glass. *Applied Surface Science*, pages 1126–1131, 2011. doi: doi:10.1016/j.apsusc.2011.09.048.
- [8] Ivan P. Parkin and Robert G. Palgrave. Self-cleaning coatings. *J. Mater. Chem.*, pages 1689–1695, 2005. doi: DOI:10.1039/b412803f.
- [9] Andre L. da Silva, Michele Dondi, and Dachamir Hotza. Self-cleaning ceramic tiles

- coated with Nb₂O₅ – doped – TiO₂ nanoparticles. *Ceramic International*, pages 11986–11991, 2017. doi: <http://dx.doi.org/10.1016/j.ceramint.2017.06.049>.
- [10] Mehdi Alzamani and Ebrahim Eghdam. Sol–gel synthesis of TiO₂ nanostructured film on SiO₂ pre-coated glass with a comparative study of solvent effect on the film properties. *J Sol-Gel Sci Technol*, pages 19–29, 2016. doi: DOI10.1007/s10971-016-4064-6.
- [11] T. Kemmitt, N.I. Al-Salim, M. Waterland, V.J. Kennedy, and A. Markwitz. Photocatalytic titania coatings. *Current Applied Physics*, pages 189–192, 2004. doi: doi:10.1016/j.cap.2003.11.006.
- [12] Kaishu Guan. Relationship between photocatalytic activity, hydrophilicity and self-cleaning effect of TiO₂/SiO₂ films. *Surface & Coatings Technology*, pages 155–160, 2005. doi: doi:10.1016/j.surfcoat.2004.02.022.
- [13] Swagata Banerjee, Dionysios D. Dionysiou, and Suresh C. Pillai. Self-cleaning applications of tio2 by photo-induced hydrophilicity and photocatalysis. *Applied Catalysis B: Environmental*, pages 396–428, 2015. doi: <http://dx.doi.org/10.1016/j.apcatb.2015.03.058>.
- [14] Zhangxin Wang, Menachem Elimelech, and Shihong Lin. Environmental applications of interfacial materials with special wettability. *Env. Sci. Technol.*, pages 2132–2150, 2016. doi: DOI:10.1021/acs.est.5b04351.
- [15] Sabri Alamri, Alfredo I. Aguilar-Morales, and Andrés F. Lasagni. Controlling the wettability of polycarbonate substrates by producing hierarchical structures using direct laser interference patterning. *European Polymer Journal*, pages 27–37, 2018. doi: <https://doi.org/10.1016/j.eurpolymj.2017.12.001>.
- [16] Junjie Chi, Xiaoxuan Zhang, Yuetong Wang, Changmin Shao, Luoran Shang, and Yuanjin Zhao. Bio-inspired wettability patterns for biomedical applications. *Mater. Horiz.*, pages 124–144, 2021. doi: DOI:10.1039/d0mh01293a.
- [17] N. Stevens, C. I. Priest, R. Sedev, , and J. Ralston. Wettability of photoresponsive titanium dioxide surfaces. *Langmuir*, pages 3272–3275, 2003. doi: <https://doi.org/10.1021/la020660c>.
- [18] T. Watanabe, A. Nakajima, R. Wang, M. Minabe, S. Koizumi, A. Fujishima, and K. Hashimoto. Photocatalytic activity and photoinduced hydrophilicity of titanium dioxide coated glass. *Thin Solid Films*, pages 260–263, 1999.
- [19] Nobuyuki Sakai, Akira Fujishima, Toshiya Watanabe, and Kazuhito Hashimoto. Quantitative evaluation of the photoinduced hydrophilic conversion properties of

- TiO₂ thin film surfaces by the reciprocal of contact angle. *J. Phys. Chem. B*, pages 1028–1035, 2003.
- [20] Prateek Sharma, Lata Rani, Ajmer S.Grewal, and Arun Lal Srivastav. Chapter2 - impact of pharmaceuticals and antibiotics waste on the river ecosystem: a growing threat. *Ecological Significance of River Ecosystems*, pages 15–36, 2022. doi: <https://doi.org/10.1016/B978-0-323-85045-2.00015-7>.
- [21] Dr.James G.Speight. Chapter 7 - chemical transformations in the environment. *Environmental Organic Chemistry for Engineers*, pages 305–353, 2017. doi: <https://doi.org/10.1016/B978-0-12-804492-6.00007-1>.
- [22] James G.Speight. Chapter 7 - redox transformations. *Reaction Mechanisms in Environmental Engineering*, pages 231–267, 2018. doi: <https://doi.org/10.1016/B978-0-12-804422-3.00007-9>.
- [23] Qing Guo, Chuanyao Zhou, Zhibo Ma ND, and Xueming Yang. Fundamentals of TiO₂ photocatalysis: Concepts, mechanisms, and challenges. *Advanced Materials*, pages 1–26, 2019. doi: <https://doi.org/10.1002/adma.201901997>.
- [24] Gianluca Li Puma, Awang Bono, Duduku Krishnaiah, and Joseph G. Collin. Preparation of titanium dioxide photocatalyst loaded onto activated carbon support using chemical vapor deposition: A review paper. *Journal of Hazardous Materials*, pages 209–2019, 2008. doi: [doi:10.1016/j.jhazmat.2008.01.040](https://doi.org/10.1016/j.jhazmat.2008.01.040).
- [25] Hao Cheng, Jingyu Wang, Yizhi Zhaob, and Xijiang Han. Effect of phase composition, morphology, and specific surface area on the photocatalytic activity of tio2 nanomaterials. *RSC. Adv.*, pages 47031–47038, 2014. doi: [DOI:10.1039/c4ra05509h](https://doi.org/10.1039/c4ra05509h).
- [26] Mrityunjay Kumar Singh and Mohan Singh Mehata. Phase-dependent optical and photocatalytic performance of synthesized titanium dioxide (tio2) nanoparticles. *International Journal of Light and Electron Optics*, 2019. doi: <https://doi.org/10.1016/j.ijleo.2019.163011>.
- [27] Agustina Manassero, María Lucila Satuf, and Orlando Mario Alfano. Photocatalytic reactors with suspended and immobilized tio2:comparative efficiency evaluation. *Chemical Engineering Journal*, pages 29–36, 2017. doi: <http://dx.doi.org/10.1016/j.cej.2017.05.087>.
- [28] M. Bideau, B. Claudel, C. Dubien, L. Faure, and H. Kazouan. On the "immobilization" of titanium dioxide in the photocatalytic oxidation of spent waters. *Journal of Photochemistry and Photobiology A. Chemistry*, pages 137–144, 1995.

- [29] David O. Scanlon, Charles W. Dunnill, John Buckeridge, Stephen A. Shevlin, Andrew J. Logsdail, Scott M. Woodley, C. Richard A. Catlow, Michael J. Powell, Robert G. Palgrave, Ivan P. Parkin, Graeme W. Watson, Thomas W. Keal, Paul Sherwood, Aron Walsh, and Alexey A. Sokol. Band alignment of rutile and anatase TiO₂. *Nature Materials*, pages 798–801, 2013. doi: DOI:10.1039/c4ra05509h.
- [30] V.A. Lebedev, D.A. Kozlov, I.V. Kolesnik, A.S. Poluboyarinov, A.E. Becerikli, W. Grünert, and A.V. Garshev. The amorphous phase in titania and its influence on photocatalytic properties. *Applied Catalysis B: Environmental*, pages 39–47, 2016. doi: <http://dx.doi.org/10.1016/j.apcatb.2016.05.010>.
- [31] M.A. Behnajady, H. Eskandarloo, N. Modirshahla, and M. Shokri. Investigation of the effect of sol–gel synthesis variables on structural and photocatalytic properties of tio2 nanoparticles. *Desalination*, pages 10–17, 2011. doi: doi:10.1016/j.desal.2011.04.019.
- [32] Yanlong Yu, Peng Zhang, Limei Guo, Zhandong Chen, Qiang Wu, Yihong Ding, Wenjun Zheng, , and Yaan Cao. The design of TiO₂ nanostructures (nanoparticle, nanotube, and nanosheet) and their photocatalytic activity. *J. Phys. Chem. C*, pages 12727–12733, 2014. doi: dx.doi.org/10.1021/jp500252g.
- [33] Cédric B.D. Mariena, Thomas Cottineau, Didier Robert, and Patrick Drogui. TiO₂ nanotube arrays: Influence of tube length on the photocatalytic degradation of paraquat. *Applied Catalysis B: Environmental*, pages 1–6, 2016. doi: <http://dx.doi.org/10.1016/j.apcatb.2016.04.040>.
- [34] Thammasak Rojviroon, Orawan Rojviroon, Sanya Sirivithayapakorn, and Sivakorn Anghong. Application of TiO₂ nanotubes as photocatalysts for decolorization of synthetic dye wastewater. *Water Resources and Industry*, pages 1–10, 2021. doi: doi:10.1016/j.wri.2021.100163.
- [35] Alice Mazzarolo, Kiyoungh Lee, Antonello Vincenzo, and Patrik Schmuki. Anodic TiO₂ nanotubes: Influence of top morphology on their photocatalytic performance. *Electrochemistry Communications*, pages 162–165, 2012. doi: doi:10.1016/j.elecom.2012.05.037.
- [36] D. Regonini, C.R. Bowen, Jaroenworarluck, and R. Stevens. A review of growth mechanism, structure and crystallinity of anodized TiO₂ nanotubes. *Materials Science and Engineering R*, pages 377–406, 2013. doi: <http://dx.doi.org/10.1016/j.mser.2013.10.001>.
- [37] M.L. Puga, J. Venturini, C.S. ten Caten, and C.P. Bergmann. Influencing parameters

- in the electrochemical anodization of TiO₂ nanotubes: Systematic review and meta-analysis. *Ceramics International*, pages 19513–19526, 2022. doi: <https://doi.org/10.1016/j.ceramint.2022.04.059>.
- [38] Hua Song, Kai Cheng, Haifeng Guo, Fang Wang, Junlei Wang, Ningfang Zhu, Mingxing Bai, and Xueqin Wang. Effect of ethylene glycol concentration on the morphology and catalytic properties of TiO₂ nanotubes. *Catalysis Communications*, pages 23–26, 2017. doi: [doi:10.1016/j.catcom.2017.04.005](https://doi.org/10.1016/j.catcom.2017.04.005).
- [39] Nisha T. Padmanabhan and Honey John. Titanium dioxide based self-cleaning smart surfaces: A short review. *Journal of Environmental Chemical Engineering*, 2020. doi: <https://doi.org/10.1016/j.jece.2020.104211>.
- [40] Mritunjaya Parashar, Vivek Kumar Shukla, and Ranbir Singh. Metal oxides nanoparticles via sol–gel method: a review on synthesis, characterization and applications. *Journal of Materials Science: Materials in Electronics*, pages 3729–3749, 2020. doi: <https://doi.org/10.1007/s10854-020-02994-8>.
- [41] Dmitry Bokov, Abduladheem Turki Jalil, Supat Chupradit, Wanich Suksatan, Mohammad Javed Ansari, Iman H. Shewael, Gabdrakhman H. Valiev, and Ehsan Kianfar. Nanomaterial by sol-gel method: Synthesis and application. *Advances in Materials Science and Engineering*, 2021. doi: <https://doi.org/10.1155/2021/5102014>.
- [42] Naghmeh Aboualigaedari and Mohammad Rahmani. A review on the synthesis of the tio₂-based photocatalyst for the environmental purification. *Journal of Composites and Compounds*, pages 25–42, 2021. doi: <https://doi.org/10.29252/jcc.3.1.4>.
- [43] Aravin Prince Periyasamy, Mohanapriya Venkataraman, Dana Kremenakova, Jiri Militky, and Yan Zhou. Progress in sol-gel technology for the coatings of fabrics. *Materials*, 2020. doi: [doi:10.3390/ma13081838](https://doi.org/10.3390/ma13081838).
- [44] Rita B. Figueira. Hybrid sol–gel coatings for corrosion mitigation: A critical review. *Polymers*, 2020. doi: [doi:10.3390/polym12030689](https://doi.org/10.3390/polym12030689).
- [45] Jenny Alongi and Giulio Malucelli. State of the art and perspectives on sol–gel derived hybrid architectures for flame retardancy of textiles. *J. Mater. Chem.*, pages 21805–21809, 2012. doi: [DOI:10.1039/c2jm32513f](https://doi.org/10.1039/c2jm32513f).
- [46] Xiaobo Chen and Samuel S.Mao. Titanium dioxide nanomaterials: Synthesis, properties, modifications, and applications. *Chem. Rev.*, pages 2891–2959, 2007.
- [47] Gareth J. Owens, Rajendra K. Singh, Farzad Foroutan, Mustafa Alqaysi, Cheol-Min Han, Chinmaya Mahapatra, Hae-Won Kim, and Jonathan C. Knowles. Sol–gel

- based materials for biomedical applications. *Progress in Materials Science*, pages 1–79, 2016. doi: <http://dx.doi.org/10.1016/j.pmatsci.2015.12.001>.
- [48] Muhammad A. Butt. Thin-film coating methods: A successful marriage of high-quality and cost-effectiveness—a brief exploration. *Coatings*, 2022. doi: <https://doi.org/10.3390/coatings12081115>.
- [49] Kashif Nawaz, Shelly J. Schmidt, and Anthony M. Jacobi. Effect of catalyst used in the sol–gel process on the microstructure and adsorption/desorption performance of silica aerogels. *International Journal of Heat and Mass Transfer*, pages 25–34, 2014. doi: <http://dx.doi.org/10.1016/j.ijheatmasstransfer.2014.03.003>.
- [50] Sara L. Isley and R. Lee Penn. Titanium dioxide nanoparticles: Effect of sol-gel ph on phase composition, particle size, and particle growth mechanism. *J. Phys. Chem. C*, pages 4469–4474, 2008. doi: <https://doi.org/10.1021/jp710844d>.
- [51] J S Appasamy and J C Kurnia. Synthesis and evaluation of novel tio2-based self-cleaning coating layer for buildings. *IOP Conf. Series: Earth and Environmental Science*, 2019. doi: [doi:10.1088/1755-1315/268/1/012049](https://doi.org/10.1088/1755-1315/268/1/012049).
- [52] Shuhadah A. Yazid, Zulkifli Mohd Rosli, and Jariah Mohamad Juoi. Effect of titanium (iv) isopropoxide molarity on the crystallinity and photocatalytic activity of titanium dioxide thin film deposited via green sol–gel route. *J. Mater. Res. Technol.*, pages 1434–1439, 2019. doi: <https://doi.org/10.1016/j.jmrt.2018.10.009>.
- [53] Orawan Wiranwetchayan, Surin Promnopas, Titipun Thongtem, Arnon Chaipanich, and Somchai Thongtema. Effect of alcohol solvents on TiO₂ films prepared by sol–gel method. *Surface & Coatings Technology*, pages 310–315, 2017. doi: <http://dx.doi.org/10.1016/j.surfcoat.2017.07.068>.
- [54] R. Parra, M. S. Góes, M. S. Castro, E. Longo, P. R. Bueno, , and J. A. Varela. Reaction pathway to the synthesis of anatase via the chemical modification of titanium isopropoxide with acetic acid. *Chem. Mater*, pages 143–150, 2008. doi: <https://doi.org/10.1021/cm702286e>.
- [55] Abbas Sadeghzadeh Attar, Morteza Sasani Ghamsari, Fereshteh Hajiesmaeilbaigi, and Shamsoddin Mirdamadi. Modifier ligands effects on the synthesized TiO₂ nanocrystals. *J Mater Sci*, pages 1723–1729, 2008. doi: [DOI10.1007/s10853-007-2244-z](https://doi.org/10.1007/s10853-007-2244-z).
- [56] Elim Albiter Escobar, Miguel Ángel Valenzuela Zapata, Salvador Alfaro Hernández, Sergio Odín Flores Valle, Omar Ríos Berny, Víctor Jesús González Ángeles, and

- Iván Córdova Reyes. Photocatalytic reduction of benzophenone on tio2: Effect of preparation method and reaction conditions. *J. Mex. Chem. Soc.*, pages 133–138, 2010. doi: DOI:10.29356/jmcs.v54i3.924.
- [57] Katarzyna Siwinska-Stefanska, Jakub Zdarta, Dominik Paukszta, and Teofil Jesionowski. The influence of addition of a catalyst and chelating agent on the properties of titanium dioxide synthesized via the sol–gel method. *J Sol-Gel Sci Technol*, pages 264–278, 2015. doi: DOI10.1007/s10971-015-3696-2.
- [58] Mohammad A. Behnajady, Hamed Eskandarloo, Nasser Modirshahla, and Mohammad Shokri. Sol-gel low-temperature synthesis of stable anatase-type TiO₂ nanoparticles under different conditions and its photocatalytic activity. *Photochemistry and Photobiology*, pages 1002–1008, 2011. doi: DOI:10.1111/j.1751-1097.2011.00954.x.
- [59] Mohammad Reza Golobostanfard and Hossein Abdizadeh. Effect of mixed solvent on structural, morphological, and optoelectrical properties of spin-coated tio2 thin films. *Ceramics International*, pages 5843–5851, 2012. doi: <http://dx.doi.org/10.1016/j.ceramint.2012.04.034>.
- [60] Changseok Han, Joel Andersen, Vlassis Likodimos, Polycarpos Falarasb, Jacob Linkugelc, and Dionysios D. Dionysioua. The effect of solvent in the sol–gel synthesis of visible light-activated, sulfur-doped tio2 nanostructured porous films for water treatment. *Catalysis Today*, pages 132–139, 2014. doi: <http://dx.doi.org/10.1016/j.cattod.2013.11.052>.
- [61] Mphilisi M. Mahlambi, Ajay K. Mishra, Shivani B. Mishra, Rui W. Krause, Bhekie B. Mamba, and Ashok M. Raichur. Comparison of rhodamine b degradation under uv irradiation by two phases of titania nano-photocatalyst. *J Therm Anal Calorim*, pages 847–855, 2012. doi: DOI10.1007/s10973-011-1852-7.
- [62] D. Spini. Green synthesis and characterization of TiO₂ sol-gel for self-cleaning surfaces. Master’s thesis, Politecnico di Milano, 2020-2021.
- [63] Stefano Brigatti. A comparative study over differently produced titanium dioxide photocatalyst. Master’s thesis, Politecnico di Milano, 2020-2021.
- [64] Carolina Cionti, Ewoud Cosaer, Gabriele Deshayes, Ermelinda Falletta, Daniela Meroni, Claudia L. Bianchi, and Dirk Poelman. Self-cleaning, photocatalytic films on aluminum plates for multi-pollutant air remediation: promoting adhesion and activity by SiO₂ interlayers. *Nanotechnology*, pages 1–10, 2021. doi: <https://doi.org/10.1088/1361-6528/ac1d76>.

- [65] Merck Life Science S.r.l. Merck life science s.r.l. Technical report, Titanium(IV) isopropoxide, 205273, Milano, IT, Released: 05.10.2022. URL <https://www.sigmaaldrich.com/IT/en/sds/aldrich/205273>.
- [66] Merck Life Science S.r.l. Acetic acid, $\geq 99.0\%$ (t), 45740. Technical report, Merck Life Science S.r.l., Milano, IT, Released: 05.10.2022. URL <https://www.sigmaaldrich.com/IT/en/sds/mm/8.18755>.
- [67] Merck Life Science S.r.l. Ethanol, 32221-m. Technical report, Milano, IT, Released: 07.10.2022. URL <https://www.sigmaaldrich.com/IT/en/sds/sial/32221-m>.
- [68] Michael F. Ashby. *Appendix A - Data for Engineering Materials*. Materials Selection in Mechanical Design (Fourth Edition). Butterworth-Heinemann, 2011. ISBN 9781856176637.
- [69] Fine ceramics (advanced ceramics, advanced technical ceramics) — determination of photocatalytic activity of surfaces in an aqueous medium by degradation of methylene blue. Technical report, BS ISO 10678:2010, Switzerland, 2010.
- [70] Yan Wang, Zhaoli Yan, and Xiaodong Wang. Photocatalytic degradation of rhodamine b dye over novel porous TiO_2 – SnO_2 nanocomposites prepared by hydrothermal method. *International Journal of Photoenergy*, 2014. doi: <http://dx.doi.org/10.1155/2014/928519>.
- [71] Yongfei Cui, Stephen M. Goldupb, and Steve Dunn. Photodegradation of rhodamine b over ag modified ferroelectric BaTiO_3 under simulated solar light: pathways and mechanism. *RSC Adv.*, 2015. doi: DOI:10.1039/c5ra00798d.
- [72] Kai Yu, Shaogui Yang, Huan He, Cheng Sun, Chenggang Gu, and Yongming Ju. Visible light-driven photocatalytic degradation of rhodamine b over nabio3: Pathways and mechanism. *J. Phys. Chem. A.*, pages 10024–10032, 2009.
- [73] Feng Chen, Jincal Zhao, and Hisao Hidaka. Highly selective deethylation of rhodamine b:adsorption and photooxidation pathways of the dye on the $\text{tio}_2/\text{sio}_2$ composite photocatalyst. *International Journal of Photoenergy*, 2003.
- [74] Tunde Lewis Yusuf, Benjamin O. Orimolade, Daniel Masekela, Bhekie Mamba, and Nonhlangabezo Mabuba. The application of photoelectrocatalysis in the degradation of rhodamine b in aqueous solutions:a review. *RSC Adv.*, pages 26176–26191, 2022. doi: DOI:10.1039/d2ra04236c.
- [75] Fiaz Ahmad, Daochen Zhu, and Jianzhong Sun. Environmental fate of tetracycline

- antibiotics: degradation pathway mechanisms, challenges, and perspectives. *Environ Sci Eur*, pages 1–17, 2021. doi: <https://doi.org/10.1186/s12302-021-00505-y>.
- [76] <https://lumstatic.com/J6/WF/3wicX8Kdn8qRraESjA.pdf>. Ncsu033c(t)-specifications for uv led. Technical report, Nichia Corporation, 2022.
- [77] K. Vasanth Kumar, K. Porkodi, and F. Rocha. Langmuir–hinshelwood kinetics – a theoretical study. *Catalysis Communications*, pages 82–84, 2008. doi: doi:10.1016/j.catcom.2007.05.019.
- [78] C. Cionti et al. Combining ph-triggered adsorption and photocatalysis for the remediation of complex water matrices. *J. Environ. Chem. Eng.*, 2022. doi: <https://doi.org/10.1016/j.jece.2022.108468>.
- [79] Applicazioni industriali uv led - hg 500. <https://www.jelosil.net/prodotti/applicazioni-industriali-uv-led/hg500/>, 2022. Accessed: 2022-12-19.
- [80] BS EN 15802:2009. Conservation of cultural property — test methods determination of static contact angle. Technical report, ISO, Switzerland, 2009.
- [81] Aurélien Stadler and Daniel Sage. Drop shape analysis-free software for high precision contact angle measurement. Technical report, <http://bigwww.epfl.ch/demo/dropanalysis/>, 2006.
- [82] Philip S. Brown and Bharat Bhushan. Durable, superoleophobic polymer–nanoparticle composite surfaces with re-entrant geometry via solvent-induced phase transformation. *Scientific reports*, 2016. doi: DOI:10.1038/srep21048.
- [83] Asier Martinez-Urrutia, Peru Fernandez de Arroiabe, Miguel Ramirez, Manex Martinez-Agirre, and M. Mounir Bou-Ali. Contact angle measurement for libr aqueous solutions on different surface materials used in absorption systems. *International Journal of Refrigeration*, pages 182–188, 2018. doi: <https://doi.org/10.1016/j.ijrefrig.2018.05.041>.
- [84] Ampol Kamnerdsook, Ekachai Juntasaro, Numfon Khemthongcharoen, Mayuree Chanasakulniyom, Witsaroot Sripumkhai, Pattaraluck Pattamang, Chamras Promptmas, Nithi Atthid, and Wutthinan Jeamsaksirid. Formation of double emulsion micro-droplets in a microfluidic device using a partially hydrophilic–hydrophobic surface. *RSC. Adv.*, pages 35653–35662, 2021. doi: DOI:10.1039/d1ra06887c.
- [85] Alison Gilchrist and Jim Nobbs. Colorimetry, theory. *Encyclopedia of Spectroscopy and Spectrometry (Third Edition)*, Academic Press, pages 328–333, 2017. doi: <https://doi.org/10.1016/B978-0-12-803224-4.00124-2>.

- [86] M. J. Delgado-González, Y. Carmona-Jiménez, M.C. Rodríguez-Dodero, and M.V. García-Moreno. Color space mathematical modeling using microsoft excel. *J. Chem. Educ.*, pages 1885–1889, 2018. doi: doi:10.1021/acs.jchemed.7b00681.
- [87] BS EN ISO/CIE 11664-4:2019. Standard: Colorimetry. cie 1976 l*a*b* colour space. Technical report, ISO, Switzerland, 2019.
- [88] Yumiko Hosoya, Takanobu Shiraishi, Tetsuo Odatsu, Toshiaki Ogata, Masashi Miyazaki, and John M. Powers. Effects of specular component on color differences of different filler type resin composites after aging. *Journal of Dentistry*, pages 585–590, 2009. doi: doi:10.1016/j.jdent.2009.03.018.
- [89] ASTM. Standard practice for identification of instrumental methods of color or color-difference measurement of materials. Technical report, ASTM E805 – 12, United States, 2012.
- [90] Maryam Mokhtarifar, Reyhaneh Kaveh, Mojtaba Bagherzadeh, Andrea Lucotti, MariaPia Pedferri, and Maria Vittoria Diamanti. Heterostructured $\text{TiO}_2/\text{SiO}_2/\gamma - \text{Fe}_2\text{O}_3/\text{rGO}$ coating with highly efficient visible-light-induced self-cleaning properties for metallic artifacts. *ACS Applied Materials & Interfaces*, pages 29671–29683, 2020. doi: doi:10.1021/acsami.0c06792.
- [91] ASTM Drr59-17. Standard test methods for rating adhesion by tape test. Technical report, ASTM, United States, 2017.
- [92] Hsuan-Fu Yu and Chao-Wei Cheng. Enhancing photocatalytic ability of tio_2 films using gel-derived P/Si – TiO_2 powder. *Journal of Sol-Gel Science and Technology*, pages 259–270, 2021. doi: <https://doi.org/10.1007/s10971-020-05450-5>.
- [93] A. Retolaza, P.T. Valentim, O. Bondarchuk, M.A. Freitas, D. Baptista, M. Amaral, and P.C. Sousa. A comparative study of the effect of different surface treatments on polymeric substrates. *Vacuum*, 2022. doi: <https://doi.org/10.1016/j.vacuum.2022.110918>.
- [94] NIST Inorganic Crystal Structure Database. Nist standard reference database number 3. Technical report, National Institute of Standards and Technology, Gaithersburg MD, 20899, Accessed: 09.03.2023. URL <https://doi.org/10.18434/M32147>.

A | Appendix A

A.0.1. Natural soiling

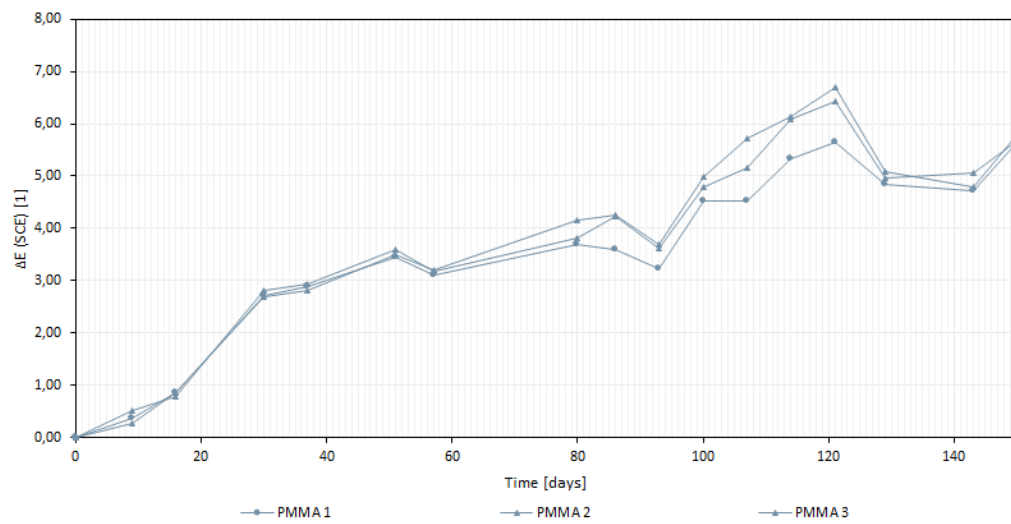


Figure A.1: Pattern behavior of PMMA samples exposed to natural soiling (SCE).

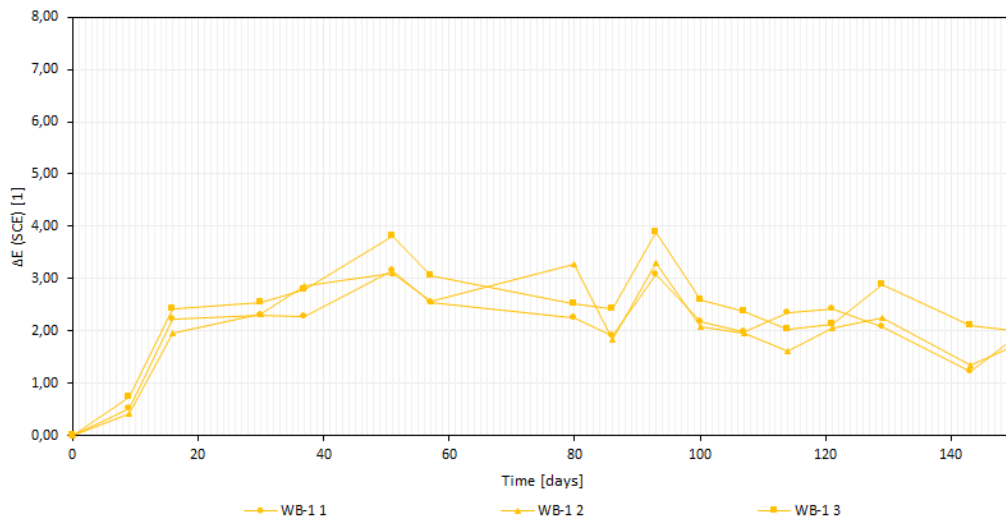


Figure A.2: Pattern behavior of *WB-1* exposed to natural soiling (SCE).

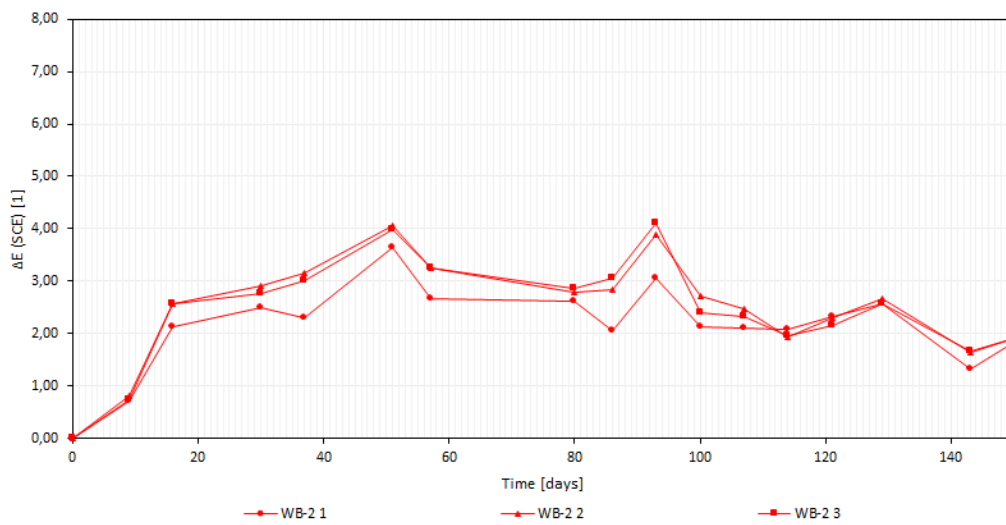


Figure A.3: Pattern behavior of *WB-2* exposed to natural soiling (SCE).

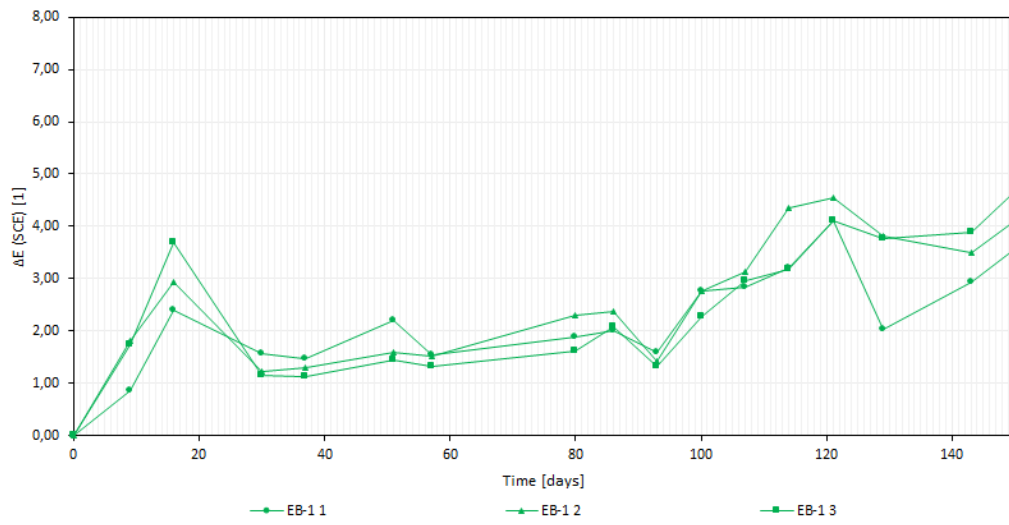


Figure A.4: Pattern behavior of *EB-1* exposed to natural soiling (SCE).

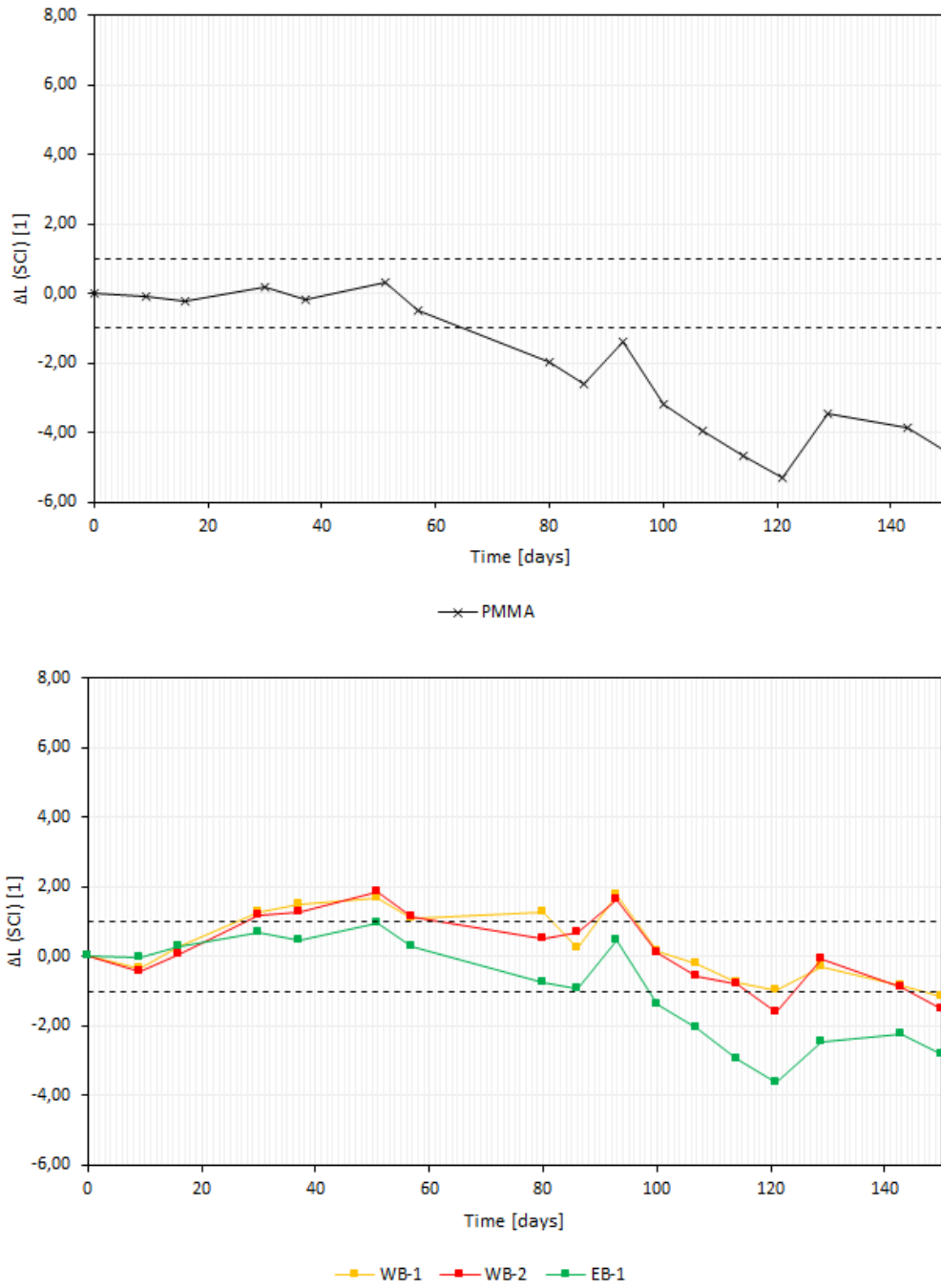


Figure A.5: Variation of L^* coordinate during natural soiling (SCI mode).

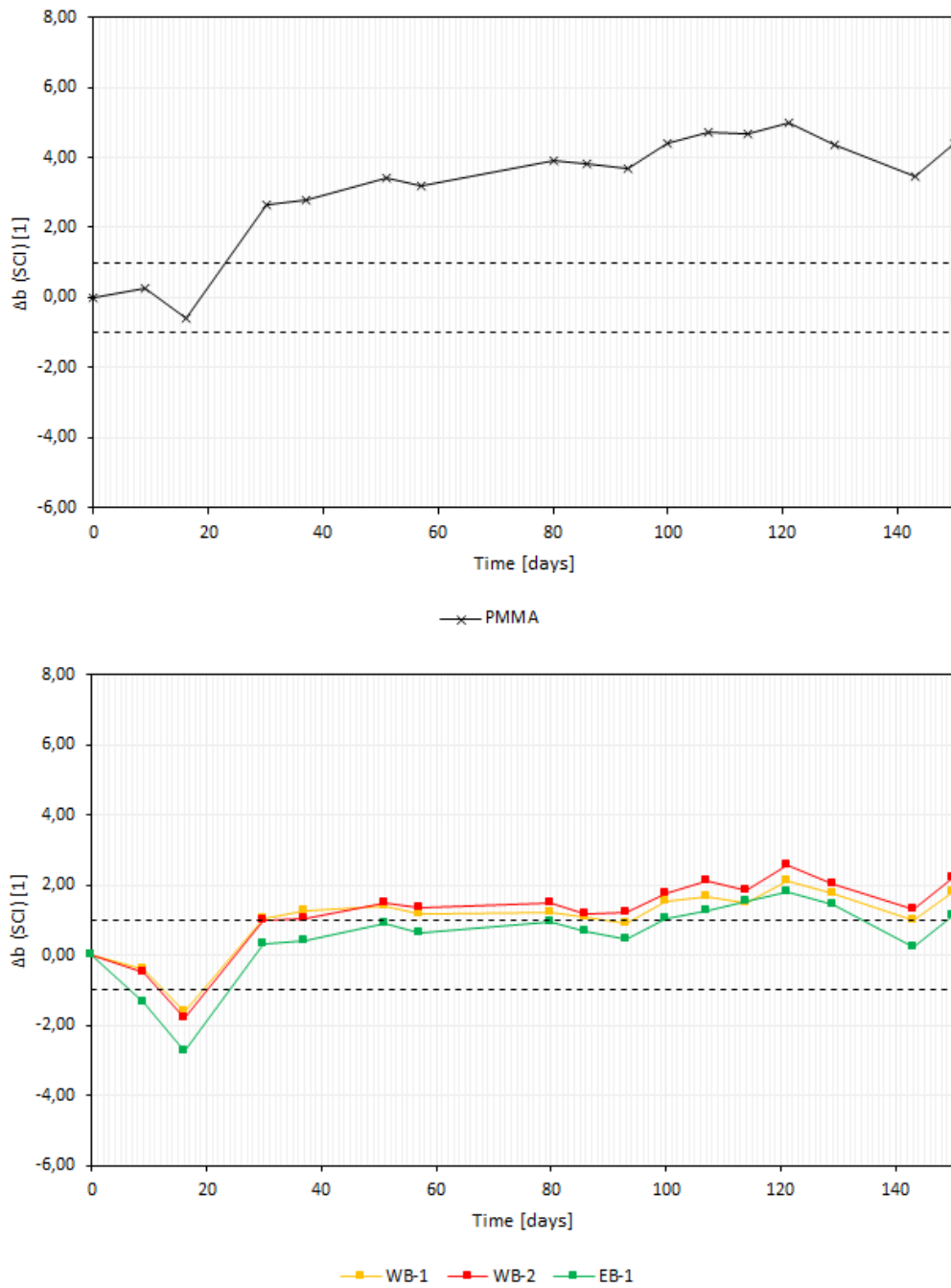


Figure A.6: Variation of b^* coordinate during natural soiling (SCI mode).

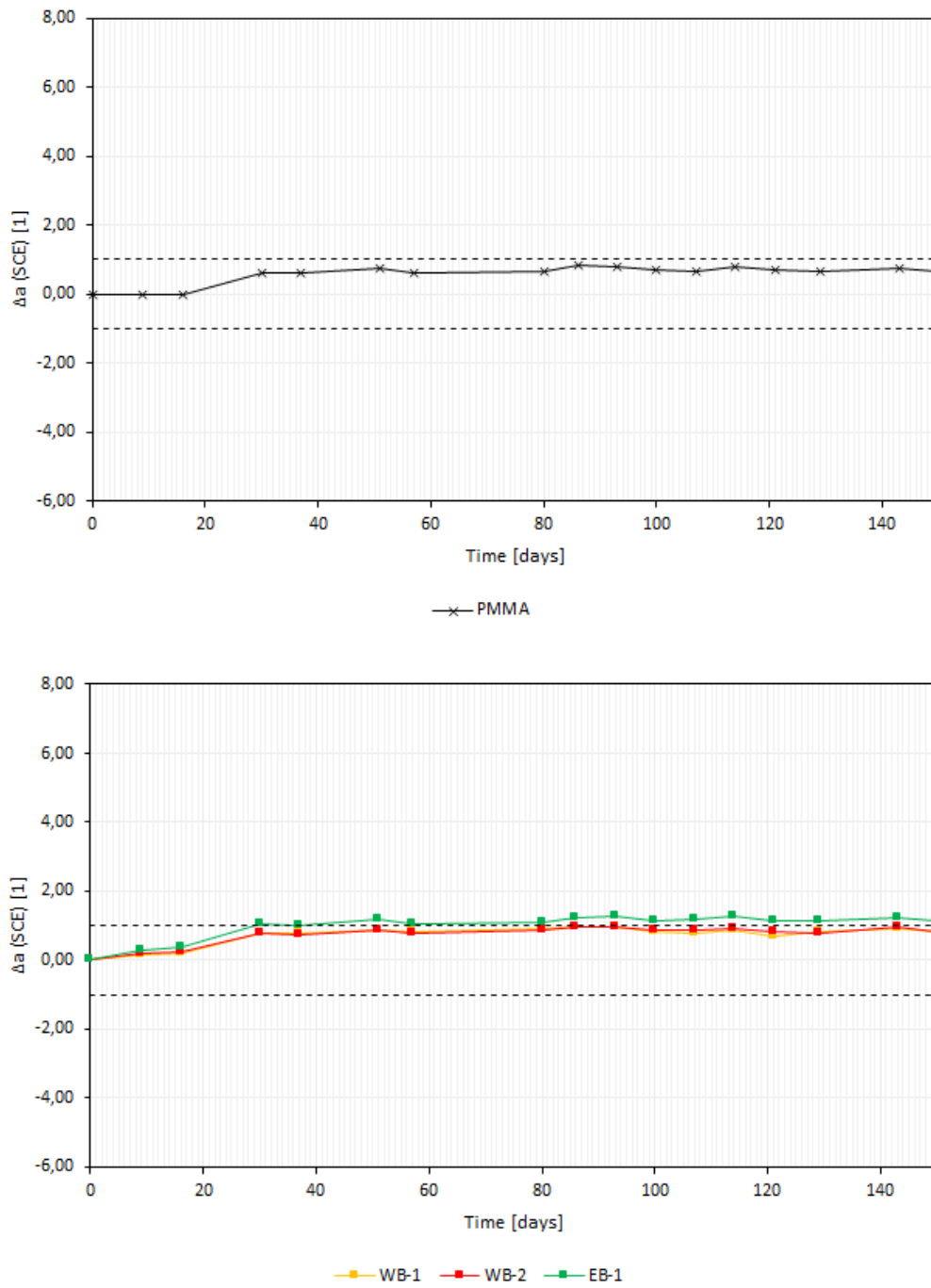


Figure A.7: Variation of a^* coordinate during natural soiling (SCE mode).

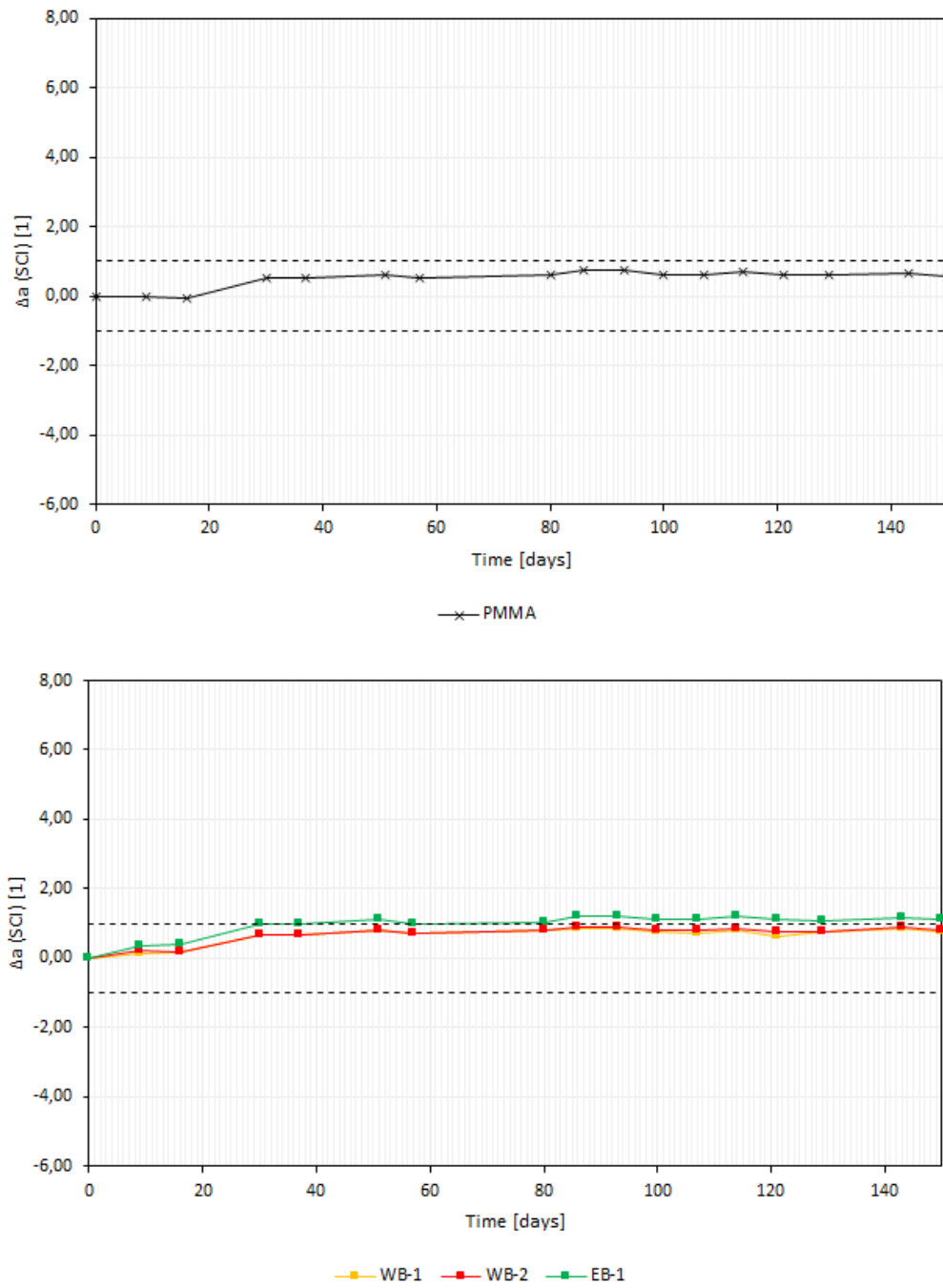
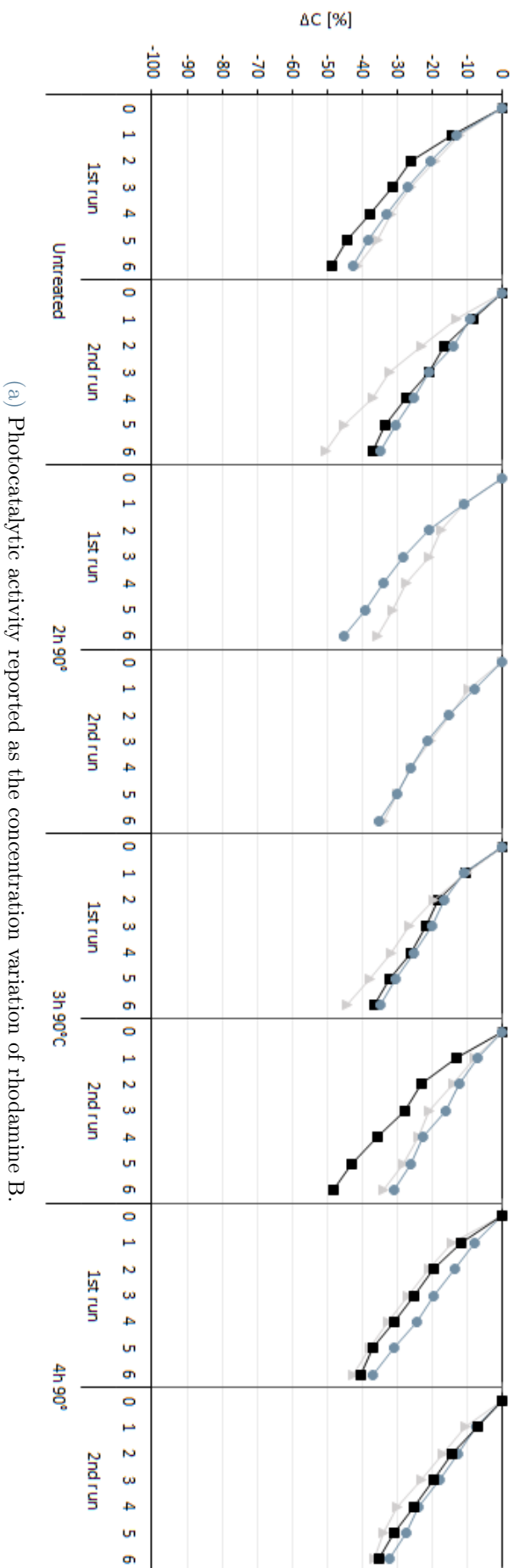
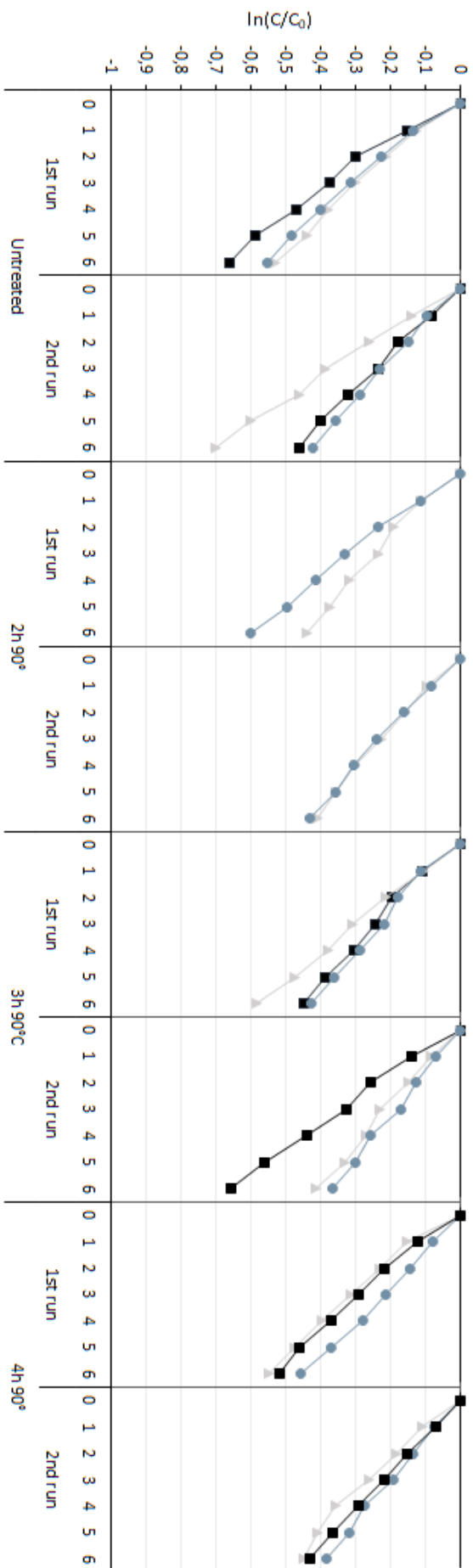


Figure A.8: Variation of a^* coordinate during natural soiling (SCI mode).

A.0.2. Annealing conditions

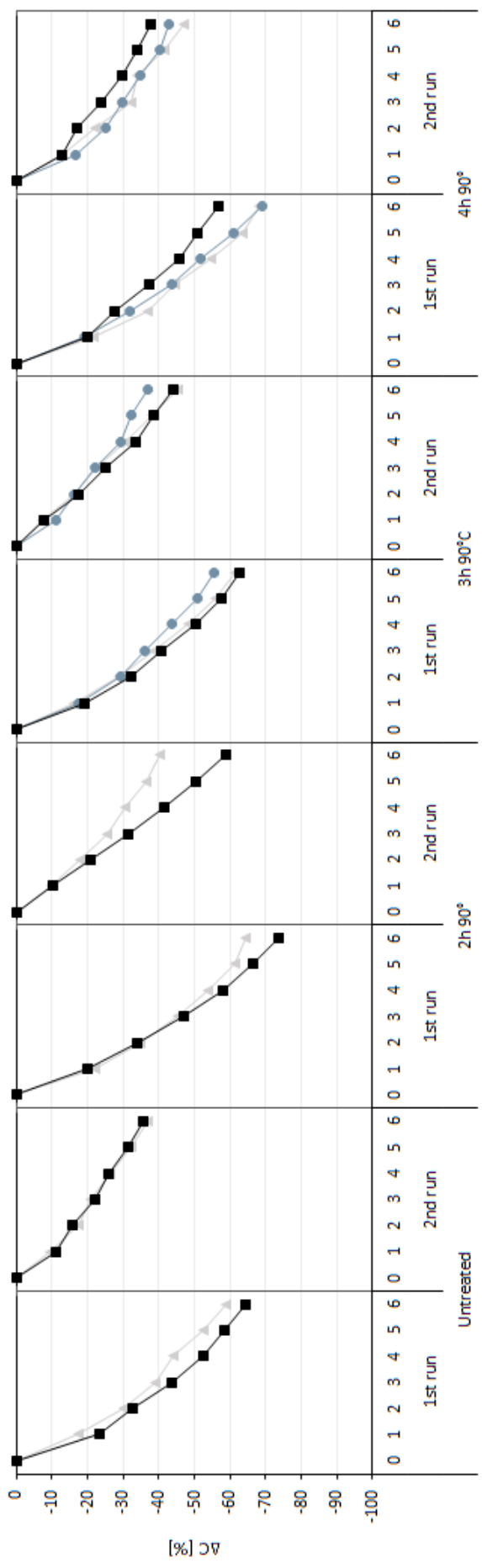


(a) Photocatalytic activity reported as the concentration variation of rhodamine B.

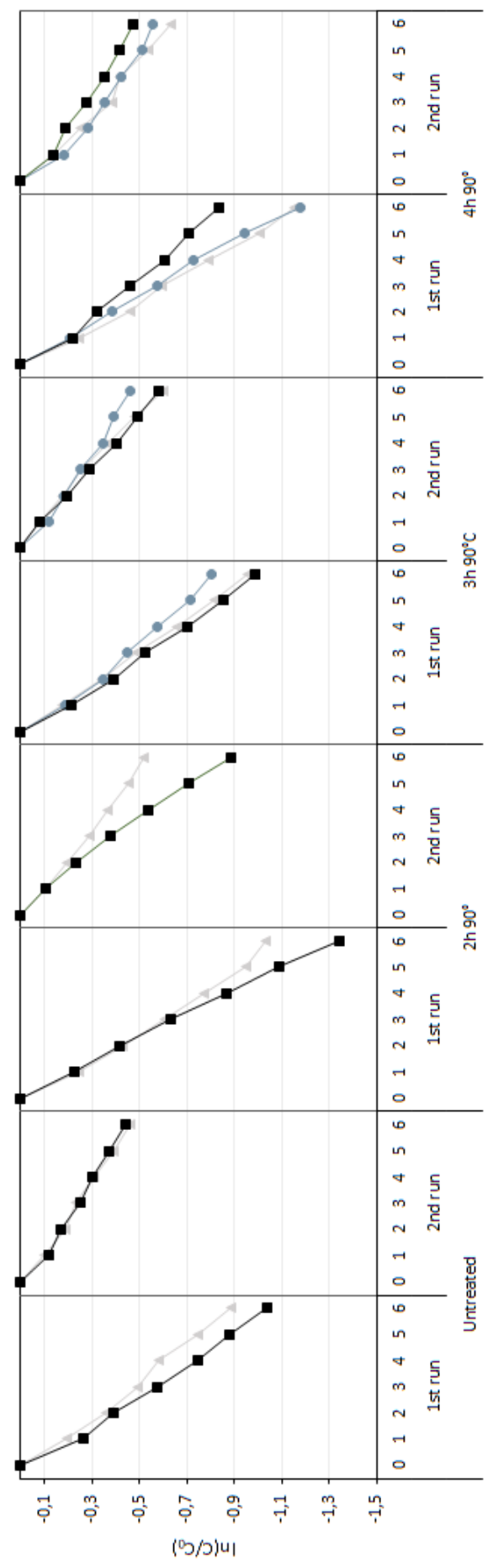


(b) Application of the pseudo-first order kinetics model to the results obtained during photocatalytic tests.

Figure A.9: Influence of duration of annealing treatment on the photocatalytic activity of spray-coated glass samples (complete graph).



(a) Photocatalytic activity reported as the concentration variation of rhodamine B.



(b) Application of the pseudo-first order kinetics model to the results obtained during photocatalytic tests.

Figure A.10: Influence of duration of annealing treatment on the photocatalytic activity of spray-coated PMMA samples (complete graph).

B | Appendix B

B.1. Dip-coater source code

```

int pulsante_Power = 2;
int pulsante_Direction = 3;
unsigned long lastDebounceTime = 0;
unsigned long debounceDelay = 100;
int buttonState;
int lastButtonState = LOW;
unsigned long lastDebounceTime_2 = 0;
unsigned long debounceDelay_2 = 100;
int buttonState_2;
int lastButtonState_2 = LOW;
int direzione = 8;
int stepp = 9;
int durata;
int distanza;
int rele = 4;

void setup() {
  pinMode(pulsante_Power, INPUT);
  pinMode(pulsante_Direction, INPUT);
  pinMode(direzione, OUTPUT);
  pinMode(stepp, OUTPUT);
  pinMode(rele, OUTPUT);
  Serial.begin(9600);
}

void loop() {

  int reading = digitalRead(pulsante_Power);
  if (reading != lastButtonState) {
    lastDebounceTime = millis();
  }

  if ((millis() - lastDebounceTime) > debounceDelay) {

    if (reading != buttonState) {
      buttonState = reading;
      if (buttonState == HIGH) {
        Serial.print("On");
      }
    }
  }
  lastButtonState = reading;
}

```

```

    int reading_2 = digitalRead(pulsante_Direction);
    if (reading != lastButtonState_2){
        lastDebounceTime_2 = millis();
    }

    if ((millis() - lastDebounceTime_2) > debounceDelay_2){

        if (reading_2 != buttonState_2){
            buttonState_2 = reading_2;
            if (buttonState_2 == HIGH){
                Serial.print("Up");
            }
            else{
                Serial.print("Down");
            }
        }
    }
    lastButtonState_2 = reading_2;

    if(lastButtonState == HIGH and lastButtonState_2 == HIGH){
        Serial.print("UP");
        digitalWrite(rele,HIGH);
        digitalWrite(direzione,HIGH);
        digitalWrite(step,HIGH);
        delayMicroseconds(5040);
        digitalWrite(step,LOW);
        delayMicroseconds(5040);
    }
    else if(lastButtonState == HIGH and lastButtonState_2 == LOW){
        Serial.print("DOWN");
        digitalWrite(rele,HIGH);
        digitalWrite(direzione,LOW);
        digitalWrite(step,HIGH);
        delayMicroseconds(5280);
        digitalWrite(step,LOW);
        delayMicroseconds(5280);
    }
    else{
        digitalWrite(rele,LOW);
    }
}

```

B.2. LED

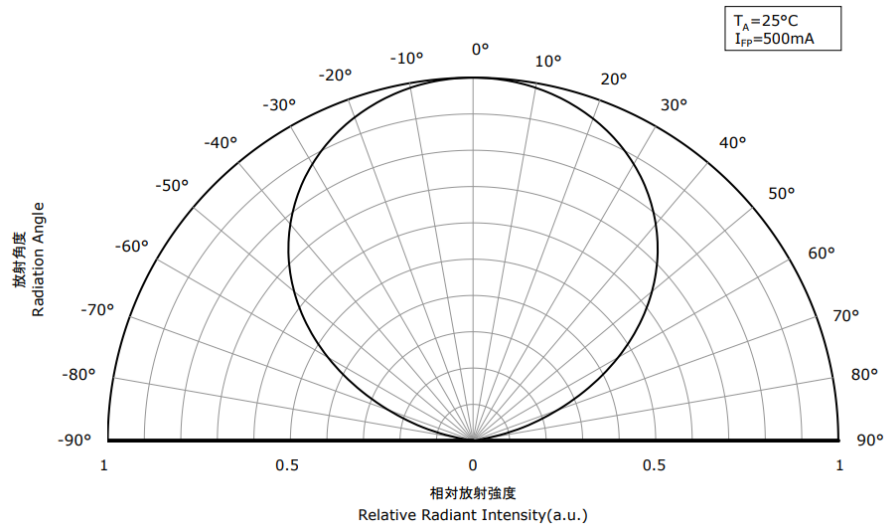


Figure B.1: LEDs directional emission [76].

B.3. Calibration curves for T.O.C. Analyzer

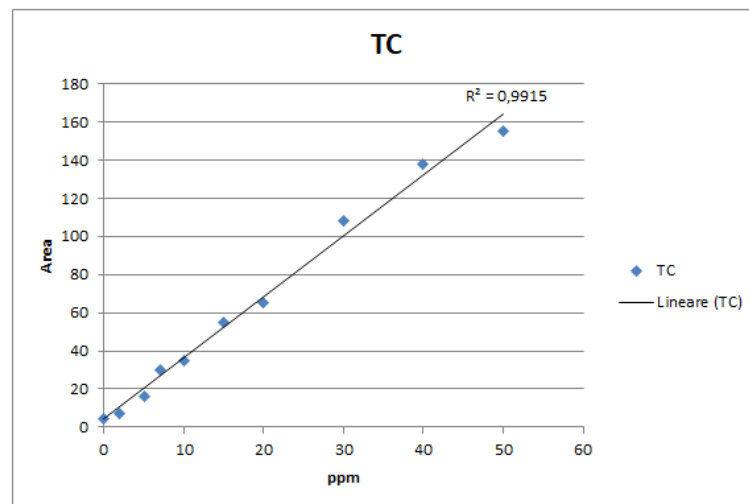


Figure B.2: TC calibration curve.

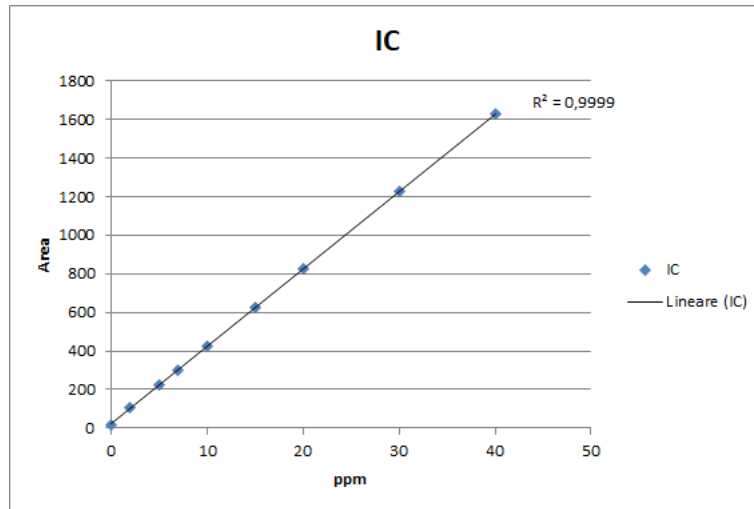


Figure B.3: IC calibration curve.

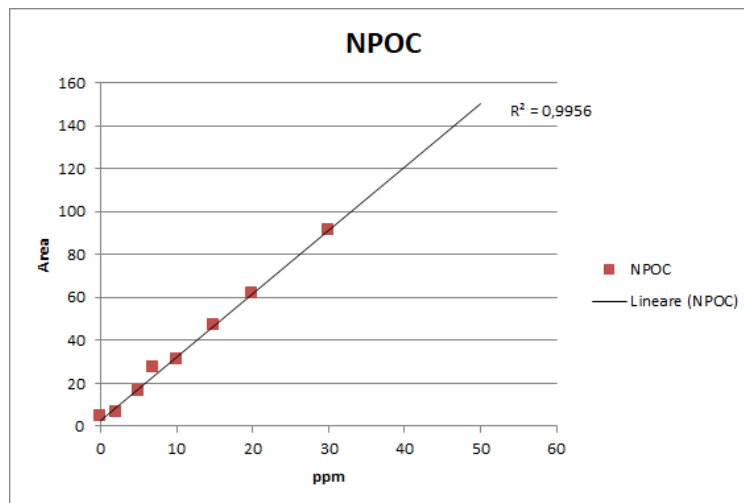


Figure B.4: NPOC calibration curve.

List of Figures

1.1	Crystal structures of TiO ₂ polymorphs [3]	3
1.2	Comparison between Wenzel's and Cassie-Baxter's model [14]	6
1.3	Photoinduced hydrophilicity.	8
1.4	Superhydrophilic conversion phenomenon [13].	8
1.5	Water contact angle variation on different single-crystal rutile faces [18].	9
1.6	(a) Linear conversion rate under different UV irradiation intensities: (a) 0.2 (b) 0.7 (c) 1.0 mW/cm ² [19]; (b) Linear dependency between conversion rate and UV irradiation [19].	10
1.7	Hydrophilization model [19]	10
1.8	Representation of exciton generation, charge transfer, electron-hole recombination, electron and hole driven reactions at the surface of a photocatalist particle [26]	14
1.9	Efficiency comparison between suspended and immobilized TiO ₂ photocatalysts [27].	15
1.10	Photocatalytic activity difference among TiO ₂ polymorphs [26]	16
1.11	Influence of calcination temperature on phase and crystallite size [31].	17
1.12	Influence of calcination temperature on photocatalytic activity [31].	17
1.13	Comparison of photocatalytic efficiency between different TiO ₂ nanostructures.	18
1.14	Illustration and interpretation of the correlation between photocatalytic activity and anodized TiO ₂ nanotubes [33].	19
1.15	Current density variation registered during anodization of titanium in glycerol/NaF [36].	21
1.16	Illustration of titanium oxide growth mechanism[36]: a) formation of the barrier film; b) formation of pits on the surface due to dissolution induced by fluoride ions; c-d) alignment of the cavities which leads to the formation of self-ordered nanotube arrays; e) formation of longer channels due to the collapse of adjacent cavities; f) final structure.	23
1.17	Effects of aging on a sol-gel formula	27

1.18	Dip-coating method for thin film deposition [48].	28
1.19	Spray-coating method for thin film deposition [48].	29
1.20	Spin-coating method for thin film deposition [48].	29
1.21	Effect of chelating agent on powder microstructure [55].	32
2.1	Spray-coating deposition pattern.	38
2.2	Corona treatment.	39
2.3	Anodized mesh sample.	41
2.4	Emission spectrum of employed UV-LED [76].	42
2.5	Design of the employed batch reactor.	43
2.6	Absorbance spectrum of degrading rhodamine B.	43
2.7	Set-up of photocatalytic test.	45
2.8	ImageJ software interface.	48
2.9	Representation of Cartesian and polar coordinates in the $CIEL^*a^*b^*$ color space [85].	49
2.10	Evolution of PM10 concentration in air in 2022.	52
2.11	Set-up and samples used for the natural soiling tests.	53
2.12	Relative humidity data acquired during the natural soiling test.	54
2.13	Precipitation data acquired during the natural soiling test.	54
2.14	Global radiation data acquired during the natural soiling test.	55
2.15	Classification of X-cut test results [91]	56
2.16	Classification of cross-cut test results [91].	57
3.1	Appearance of dip-coated glass samples.	59
3.2	Appearance of spray-coated glass samples.	60
3.3	Appearance of spray-coated PMMA samples.	60
3.4	Example of absorbance variation during photocatalysis tests.	61
3.5	Example of concentration variation during photocatalysis tests.	61
3.6	Example of application of the pseudo first-order kinetic model on photocatalysis data.	62
3.7	Concentration variation during preliminary photolysis tests.	63
3.8	Application of the pseudo-first order kinetic model on preliminary photolysis tests.	63
3.9	Average rate coefficients of preliminary photolysis tests.	64
3.10	Comparison of concentration variations induced by photolysis and adsorption tests.	65
3.11	Concentration variation during degradation of rhodamine B ($10^{-5}M$) performed by WB-2.	66

3.12	Photocatalytic activity variation in time of WB-2.	66
3.13	Concentration variation during degradation of rhodamine B ($10^{-5}M$) performed by WB-1.	67
3.14	Photocatalytic activity variation in time of WB-1.	67
3.15	Concentration variation during degradation of rhodamine B ($10^{-5}M$) performed by EB-1.	68
3.16	Photocatalytic activity variation in time of EB-1.	68
3.17	Evolution of photocatalytic activity in time.	69
3.18	Comparison of degradation efficiency between spray- and dip-coated samples.	70
3.19	Comparison of photocatalytic activity between spray- and dip-coated samples.	70
3.20	Reaction rate constants of spray- and dip-coated samples.	71
3.22	Comparison of reaction rate constants of untreated and annealed dip-coated glass samples.	72
3.21	Effects of annealing treatment, performed at $500^{\circ}C$ for two hours, on the coatings' photocatalytic activity.	73
3.23	Influence of duration of annealing treatment on the degradation efficiency of spray-coated glass samples.	74
3.24	Influence of duration of annealing treatment on the photocatalytic activity of spray-coated glass samples.	74
3.25	Thermal treatment assessment of coated glass samples.	75
3.26	Influence of annealing treatment on the degradation efficiency of spray-coated PMMA.	76
3.27	Influence of annealing treatment on the photocatalytic activity of spray-coated PMMA.	76
3.28	Thermal treatment assessment of coated PMMA samples.	77
3.29	Assessment of corona treatment on the degradation efficiency of PMMA samples spray-coated with (a) <i>WB-1</i> , (b) <i>WB-2</i> , and (c) <i>EB-1</i>	78
3.30	Assessment of corona treatment.	79
3.31	Comparison of photocatalytic activity of different batches after a 4 month aging process.	80
3.32	Application of pseudo-first order kinetics on the degradation efficiency of different batches after a 4 month aging process.	80
3.33	Reaction rate constants of different batches after a 4 month aging process.	81
3.34	Wettability before and after UV irradiation of dip-coated glass samples.	82

3.35 Comparison between wettability of coatings deposited with different methods.	84
3.36 Wettability before and after UV irradiation of spray-coated samples.	85
3.37 Photoinduced hydrophilicity of spray-coated glass samples.	86
3.38 Substrate influence on wettability.	87
3.39 Wettability before and after UV irradiation of spray-coated PMMA samples.	88
3.40 Photoinduced hydrophilicity of spray-coated PMMA samples.	89
3.41 Photoinduced hydrophilicity of glass spray-coated with <i>EB-1</i>	90
3.42 Photoinduced hydrophilicity glass sprat-coated with <i>WB-1</i>	91
3.43 Photoinduced hydrophilicity of glass spray-coated with <i>WB-2</i>	91
3.44 Variation in the L^* coordinate following coating deposition.	94
3.45 Variation in the a^* coordinate following coating deposition.	94
3.46 Variation in the b^* coordinate following coating deposition.	95
3.47 Variation in the L^* coordinate following thermal treatment.	95
3.48 Variation in the a^* coordinate following thermal treatment.	96
3.49 Variation in the b^* coordinate following thermal treatment.	96
3.50 Variation of CIELAB coordinates following sample soiling (SCI mode).	98
3.51 Coating appearance at the beginning (a) and at the end (b) of the natural soiling tests.	99
3.52 Color variation during natural soiling (SCI mode).	100
3.53 Color variation during natural soiling (SCE mode).	101
3.54 Pattern behavior of PMMA samples exposed to natural soiling (SCI).	102
3.55 Pattern behavior of <i>WB-1</i> exposed to natural soiling (SCI).	102
3.56 Pattern behavior of <i>WB-2</i> exposed to natural soiling (SCI).	103
3.57 Pattern behavior of <i>EB-1</i> exposed to natural soiling (SCI).	103
3.58 Variation of the L^* coordinate during natural soiling (SCE).	104
3.59 Variation of the b^* coordinate during natural soiling.	106
3.60 Correlation between precipitation and sample soiling (SCI).	107
3.61 Global radiation and precipitation data, with highlighted the areas where precipitations is anticipated by high global irradiation.	108
3.62 Global radiation and relative humidity data, with highlighted the area where no precipitation was recorded.	109
3.63 X-Cut adhesion test results for sample <i>EB-1</i>	111
3.64 X-Cut adhesion test results for sample <i>WB-1</i>	111
3.65 Comparison between tested sample and removed tape.	112
3.66 Thickness of sol-gel coatings deposited by immersion.	114

3.67	Thickness of <i>WB-1</i> (top), <i>EB-1</i> (left), <i>WB-2</i> (right), deposited by spray-coating on glass and annealed at 90°C for two hours.	115
3.68	Influence of annealing treatment on coating morphology.	116
3.69	<i>WB-1</i> (top), <i>EB-1</i> (left), <i>WB-2</i> (right) dip-coated on glass and annealed at 500°C for two hours.	117
3.70	<i>WB-1</i> spray-coated on glass (left) and PMMA (right).	118
3.71	Dip-coated glass with solutions <i>WB-1</i> (top left), <i>WB-1</i> An. (top right), <i>WB-2</i> An. (bottom left), <i>EB-1</i> An. (bottom right). The An. samples were annealed for two hours at 500°C.	119
3.72	Spray-coated glass with solutions <i>WB-1</i> (top left), <i>WB-1</i> An. (top right), and <i>WB-2</i> An. (bottom). The An. samples were annealed for two hours at 90°C.	120
3.73	XRD spectrum of <i>WB-1</i> deposited on glass.	121
3.74	XRD spectrum of <i>WB-2</i> deposited on glass.	121
3.75	XRD spectrum of the ethanol-based coating (<i>EB-1</i>).	122
3.76	Correlation between peak intensity and photoactivity.	122
3.77	XRD spectra of <i>WB-2</i> coatings subjected to different thermal treatments.	123
3.78	Monitored degradation of tetracycline in Milli-Q water.	124
3.79	Monitored degradation of tetracycline in simulated tap water.	125
3.80	Absorption spectra of the monitored degradation of tetracycline in Milli-Q water promoted by (A) photolysis, (B) anodized coating, and (C) sol-gel coating.	126
3.81	Absorption spectra of the monitored degradation of tetracycline in simulated tap water promoted by (A) photolysis, (B) anodized coating, and (C) sol-gel coating.	127
3.82	Repeatability tests conducted on the anodized coating and carried out in simulated tap water.	128
3.83	Repeatability tests conducted on the sol-gel coating and carried out in simulated tap water.	129
3.84	SEM images of the anodized coating.	130
3.85	SEM images of the sol-gel coating.	131
3.86	Mineralization values acquired during the degradation of tetracycline in Milli-Q water.	132
3.87	Mineralization values acquired during the degradation of tetracycline in simulated tap water.	133
3.88	Mineralization values acquired during repeatability tests conducted on the anodized coating and carried out in simulated tap water.	134

3.89	Mineralization values acquired during repeatability tests conducted on the sol-gel coating and carried out in simulated tap water.	134
3.90	Application of the pseudo first-order reaction kinetic model on the data acquired during degradation tests conducted on the Milli-Q water solution.	135
3.91	Application of the pseudo first-order reaction kinetic model on the data acquired during repeatability tests conducted on the sol-gel coating and carried out in simulated tap water.	135
3.92	Application of the pseudo first-order reaction kinetic model on the data acquired during repeatability tests conducted on the anodized coating and carried out in simulated tap water.	136
3.93	Reaction rate constants computed from the slope of the curves plotted as $\ln(CC_0^{-1})$ against time.	137
A.1	Pattern behavior of PMMA samples exposed to natural soiling (SCE).	151
A.2	Pattern behavior of <i>WB-1</i> exposed to natural soiling (SCE).	152
A.3	Pattern behavior of <i>WB-2</i> exposed to natural soiling (SCE).	152
A.4	Pattern behavior of <i>EB-1</i> exposed to natural soiling (SCE).	153
A.5	Variation of L^* coordinate during natural soiling (SCI mode).	154
A.6	Variation of b^* coordinate during natural soiling (SCI mode).	155
A.7	Variation of a^* coordinate during natural soiling (SCE mode).	156
A.8	Variation of a^* coordinate during natural soiling (SCI mode).	157
A.9	Influence of duration of annealing treatment on the photocatalytic activity of spray-coated glass samples (complete graph).	158
A.10	Influence of duration of annealing treatment on the photocatalytic activity of spray-coated PMMA samples (complete graph).	159
B.1	LEDs directional emission [76].	163
B.2	TC calibration curve.	163
B.3	IC calibration curve.	164
B.4	NPOC calibration curve.	164

List of Tables

2.1	Formula of sol-gel solutions, where <i>WB</i> and <i>EB</i> stand for water- and ethanol-based solutions, respectively.	35
2.2	Unit conversion values for the dip-coater [62].	37
2.3	Employed reagents for the anodizing solution.	40
2.4	List of reagents necessary to synthesize two liters of the tap water solution [78].	45
3.1	CIELAB coordinates of PMMA samples following coating deposition by spray-coating and annealing treatment (SCI mode).	93
3.2	CIELAB coordinates following accelerated soiling tests (SCI mode).	97
3.3	Adhesion test results.	110

